DOCTORAL THESIS

Press Cycle Time Reduction of A Reinforced Epoxy Resin and the Influence On Its Mechanical/Thermal Properties

Qi TAO

A thesis submitted in fulfillment of the requirements for the degree of Dr.mont.

at the

Montanuniversitaet Leoben

Chair of Materials Science and Testing of Polymers

Leoben, May 2018

AFFIDAVIT

I declare in lieu of oath that I wrote this thesis and performed the associated research myself, using only literature cited in this volume.

Signed:

_____

Date:

_____

“小车不倒只管推”

“As long as the wheelbarrow has not fallen down, simply push it.”

杨水才 / Shuicai Yang

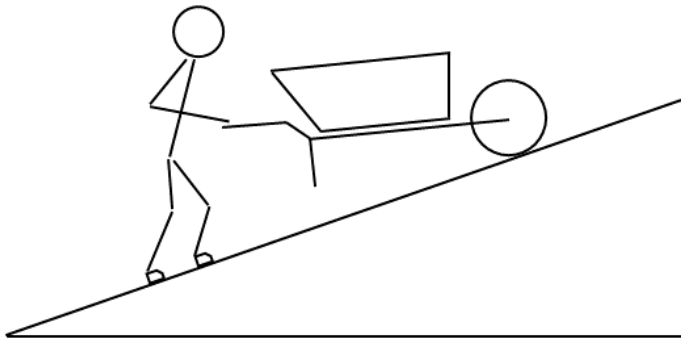

Dedicate to my family…

ABSTRACT

Lamination or pressing is one of the most important processes in the printed circuit board (PCB) manufacturing, because the reinforced epoxy resin (prepreg) will be cured and consequently relevant mechanical and thermomechanical properties, such as stiffness, glass transition temperature (Tg) and coefficient of thermal expansion (CTE) etc., of the PCBs are formed during this procedure. However, this process is also time-consuming. Although material suppliers will normally offer the manufacturer's recommended cure cycles (MRC) for every specific material to the PCB manufacturers, these MRCs often need to be adapted in terms of cycle time and/or temperature in order to reduce the production time and/or enhance the utilization of the press machine.

In this thesis the mechanism of the epoxy curing kinetics was first studied in order to understand its polymerization procedure during lamination. Afterwards, the way to reduce the press cycle time of a reinforced epoxy resin, CE688, at the lamination process based on the study and the influence on its mechanical, thermal, fracture mechanical properties, as well as on the reliability performance, are presented.

Since the main function of the lamination process is to cure the epoxy resin at elevated temperatures with high pressure, the evolution of the curing degree during this heating process is one of the key indicators for press cycle time reduction. Therefore, the well-known model free kinetics (MFK) approach was applied first to a model resin for the feasibility study of the method and then to the CE688 epoxy resin. Although small deviations to the experimental curves were found in the predicted ones due to the absence of diffusion correction in the MFK approach, the results can be well accepted. However, this commonly applied MFK approach can only predict the curing under either isothermal or non-isothermal (i.e., with fixed heating rate) heating conditions, which cannot be directly used for predicting a real case. Meanwhile, due to the lag of the heat transfer within a press book, the curing degree of the epoxy will vary depending on the location. For instance, the closer to the heating plate, the faster the curing advances. Hence, a mathematical algorithm was proposed by the author to couple the MFK with the powerful finite element approach (FEA) in order to predict the curing behavior more accurately.

The proposed algorithm was eventually implemented in Abaqus® by integrating the discretized analytical solution of the MFK into its user subroutines. This method was verified by non-isothermal and isothermal differential scanning calorimetry (DSC) experiments. By means of this method, the real manufacturing press cycle can be simulated regarding the temperature distribution within the whole press book and the curing degree of the epoxy resin at every location. Besides, in contrast to other FEA curing simulations, the present method can easily simulate arbitrary geometries with advanced curing degree-dependent material properties, such as density, CTE, thermal conductivity, specific heat and even the chemical shrinkage during polymerization. Moreover, the developed MFK can also be used for the decomposition study which is very important for characterizing the thermal stability of the material.

DSC is one of the most commonly used methods for obtaining the necessary parameters required by the MFK approach. But sometimes the reaction peaks of polymerization in the DSC thermographs are not discernable due to higher filler content or whatever other reasons. In these cases, the Fourier transform infrared (FTIR) spectroscopy can be utilized as a complementary method. Therefore, the FTIR curing kinetics for CE688 was studied and compared to the DSC one in this PhD work in order to develop an alternative method for the future application.

Based on the curing kinetics study for CE688, samples produced with different press cycle time (standard, -30min and -60min/-90min) were prepared. Half of these samples were further subjected to 10x lead-free reflow tests, i.e., a special heating process used to melt the lead-free solders at a maximum temperature of 260°C in order to connect the components to the PCB. Afterwards, the effects of press cycle time reduction on the three main material properties were examined: 1) mechanical properties were checked by monotonic tensile tests and dynamic mechanical analysis (DMA); 2) thermal properties were tested by DSC, thermal mechanical analysis (TMA) and thermogravimetric analysis (TGA); 3) fracture toughness were measured by monotonic and cyclic double cantilever beam (DCB) tests. Meanwhile, six typical reliability tests were performed: moisture uptake, peel strength, delamination by capacitance, interconnection stress test (IST), highly accelerated stress test (HAST) and warpage.

Finally, a general procedure for optimizing the press cycle time as an important output of the PhD work was established according to the fundamental studies and the testing results. This procedure aimed at offering a fast response when a new material is introduced into the production. The warpage performance was chosen as the primary criterion to judge the optimization procedure due to the following two factors: 1) the warpage issue is becoming more prominent along with the reduction of the PCB thickness, which might cause serious assembly issues or reliability issues in the PCB lifetime. 2) the diffusion effect, the lamination pressure, the chemical shrinkage and the stress relaxation at hot stage were not considered in the simulation at the moment.

Zusammenfassung

Die Laminierung oder die Verpressung ist einer der wichtigsten Prozesse in der Leiterplattenherstellung, da das verstärkte Epoxidharz (Prepreg) ausgehärtet wird und damit relevante mechanische und thermomechanische Eigenschaften wie Steifigkeit, Glasübergangstemperatur (Tg) und Wärmeausdehnungskoeffizienten (CTE) usw. der PCBs während dieses Vorgangs festgelegt werden. Dieser Prozess ist jedoch auch zeitaufwendig. Obwohl Materiallieferanten den Leiterplattenherstellern normalerweise die vom Hersteller empfohlenen Aushärtungszyklen (MRC) für jedes spezifische Material anbieten, müssen diese MRCs oft in Bezug auf Zykluszeit und/oder Temperatur angepasst werden, um die Produktionszeit zu verringern und/oder Auslastung der Presse zu verbessern.

In dieser Arbeit wurde zunächst der Mechanismus der Epoxidaushärtungskinetik untersucht, um den Polymerisationsprozess während der Laminierung zu verstehen. Anschließend wird der Weg zur Verkürzung der Presszykluszeit eines verstärkten Epoxidharzes, CE688, dargestellt, basierend auf Untersuchungen des Laminierungsprozesses und des Einflusses auf seine mechanischen, thermischen, bruchmechanischen Eigenschaften sowie auf die Zuverlässigkeit.

Da die Hauptfunktion des Laminierungsprozesses darin besteht, das Epoxidharz bei erhöhten Temperaturen mit hohem Druck auszuhärten, ist die Entwicklung des Härtungsgrads während dieses Erwärmungsprozesses einer der Schlüsselindikatoren für die Reduktion der Pressenzykluszeit. Daher wurde der bekannte Modellfreie Kinetik-Ansatz (MFK) zunächst auf ein Modellharz für die Machbarkeitsstudie der Methode und dann auf das CE688-Epoxidharz angewendet. Obwohl aufgrund der fehlenden Diffusionskorrektur im MFK-Ansatz kleine Abweichungen der prognostizierten gegenüber den experimentellen Kurven gefunden wurden, können die Ergebnisse gut akzeptiert werden. Dieser allgemein angewendete MFK-Ansatz kann jedoch nur die Härtung unter entweder isothermen oder nicht-isothermen (d.h. mit einer festen Erwärmungsrate) Erwärmungsbedingungen vorhersagen und kann daher nicht direkt zur Vorhersage eines realen Falls verwendet werden. Aufgrund der Verzögerung der Wärmeübertragung innerhalb des Pressbuchs variiert der Aushärtungsgrad des Epoxids abhängig vom Ort. Je näher zum Beispiel die Heizplatte ist, desto schneller schreitet die Aushärtung voran. Daher wurde vom Autor ein mathematischer Algorithmus entwickelt, um die MFK mit einer leistungsfähigen Finite-Elemente-Analyse (FEA) zu koppeln, um so das Aushärteverhalten genauer vorhersagen zu können.

Dieser Algorithmus wurde schließlich in Abaqus® implementiert, indem die diskretisierte analytische Lösung des MFK in die Benutzer-Subroutinen integriert wurde. Diese Methode wurde durch nicht-isotherme und isotherme Differenzialrasterkalorimetrie (DSC) Experimente verifiziert. Mit diesem Verfahren kann der reale Herstellungspresszyklus hinsichtlich der Temperaturverteilung innerhalb des gesamten Pressbuches und der Aushärtungsgrad des Epoxidharzes an jedem Ort simuliert werden. Außerdem kann das vorliegende Verfahren im Gegensatz zu anderen FEA-Aushärtungssimulationen einfach beliebige Geometrien mit fortgeschrittenen, vom Aushärtungsgrad abhängigen Materialeigenschaften wie Dichte, CTE, Wärmeleitfähigkeit, spezifische Wärme und sogar die chemische Schrumpfung während der Polymerisation simulieren. Darüber hinaus kann

die entwickelte MFK auch für die Abbauuntersuchung verwendet werden, die zur Charakterisierung der thermischen Stabilität des Materials sehr wichtig ist.

DSC ist eine der am häufigsten verwendeten Methoden, um die notwendigen Parameter zu erhalten, die der MFK-Ansatz benötigt. Aber manchmal sind die Reaktionspeaks der Polymerisation in den DSC-Thermographen aufgrund eines höheren Füllstoffgehaltes oder aus anderen Gründen nicht erkennbar. In diesen Fällen kann die Fourier-Transformations-Infrarot (FTIR) -Spektroskopie als eine komplementäre Methode verwendet werden. Daher wurde die FTIR-Härtungskinetik für CE688 untersucht und mit der DSC-Methode in dieser Doktorarbeit verglichen, um eine alternative Methode für zukünftige Anwendungen zu entwickeln.

Basierend auf der Aushärtungskinetik-Untersuchung für CE688 wurden Proben hergestellt, die mit unterschiedlichen Presszykluszeiten (Standard, -30min und -60min/-90min) hergestellt wurden. Die Hälfte dieser Proben wurde weiters einem 10-fachen bleifreien Reflow-Test unterzogen, bei dem es sich um ein spezielles Erhitzungsverfahren handelt, mit dem die bleifreien Lötmittel bei einer maximalen Temperatur von 260°C geschmolzen werden, um die Komponenten mit der Leiterplatte zu verbinden. Anschließend wurden die Auswirkungen der Reduktion der Presszykluszeit auf die drei wichtigsten Materialeigenschaften untersucht: 1) Mechanische Eigenschaften wurden durch monotone Zugprüfung und eine dynamisch-mechanische Analyse (DMA) überprüft; 2) die thermischen Eigenschaften wurden mittels DSC, thermomechanischer Analyse (TMA) und thermogravimetrischer Analyse (TGA) getestet; 3) die Bruchzähigkeit wurde durch monotonen und zyklischen Doppelausleger (DCB) -Test gemessen. In der Zwischenzeit wurden sechs typische Zuverlässigkeitstests durchgeführt: Feuchtigkeitsaufnahme, Schälfestigkeit, Delamination durch Kapazitanz, Verbindungsspannungstest (IST), hoch beschleunigter Stresstest (HAST) und Verwerfung.

Schließlich wurde ein allgemeingültiges Verfahren zur Optimierung der Presszykluszeit als zentrales Ergebnis der vorliegenden Doktorarbeit auf Basis von umfassenden Forschungsarbeiten und den Testergebnissen entwickelt. Dieses Verfahren reagiert schnell, wenn ein neues Material in die Produktion eingeführt wird. Die Krümmung wurde als Hauptkriterium für die Beurteilung des Optimierungsverfahrens aufgrund der folgenden zwei Faktoren gewählt: 1) Das Krümmungsproblematik verschärft sich mit der Reduktion der Leiterplattendicke, was zu ernsthaften Problemen bei der Bestückung und somit hinsichtlich der Zuverlässigkeit einer Leiterplatte führen kann. 2) Der Diffusionseffekt, der Laminationsdruck, die chemische Schrumpfung und die Spannungsrelaxation im heißen Zustand wurden in der Simulation nicht berücksichtigt.

ACKNOWLEDGEMENTS

First of all, I would like to thank my academic advisors, Prof. Dr. Gerald Pinter and Prof. Dr. Wolfgang Kern, who supported me for all the scientific-related discussions and the thorough reviewing of my dissertation. I also would like to thank Dr. Michael Feuchter Prof. Dr. Thomas Antretter, who spent their time on reviewing my work and advising me in the field of curing kinetics and finite element simulation respectively. I appreciate Dr. Steffen Stelzer and Dr. Santhosh Ayalur Karunakaran for sharing their expertise with respect to the double cantilever beam test and the nuclear magnetic resonance analysis respectively. In addition, I appreciate Dr. Peter Fuchs for helping me to facilitate my PhD study in the university and spending his time on some technical discussions.

Special thanks go to AT&S Austria Technologie & Systemtechnik AG for providing me the opportunity and transferring my family from China to Austria to do the PhD study at the Montanuniversität. I really appreciate Dipl. Ing. Thomas Krivec serving as supervisor in the company. With his great support, I could settle down my life in Austria much easier and start my study earlier. I am grateful to Ms. Anke Steinberg and Dr. Petra Staberhofer for their constant concern about my life and study. Meanwhile, I thank Mr. Hyung Wook Park for providing me the model epoxy resin. I thank Mr. Markus Frewein and the team members in the AT&S laboratories of Shanghai and Leoben for their support regarding the experiments.

Special gratitude goes to my family as well. I thank my wife, Ms. Jie Zhou, who supported me by taking most of the responsibilities for the family. I thank my dear son, Leran, who left me alone when I needed time for study and played with me when I was tired. I thank my parents-in-law for taking care of my health and shipping us the delicious foods from time to time. I also thank my parents for cultivating my interest in science when I was still a child and teaching me to never give up. Without their love and steady backup, I cannot finish this PhD study.

Moreover, I want to take this chance to thank Dr. Qi Zheng, who was my first manager in my career and guided me to the way of studying science.

Finally, I would like to express my appreciation to Ms. Marian Pink and Dr. Petra Staberhofer who helped me to review my dissertation in terms of English grammar and to translate the English abstract to German.

Contents

AFFIDAVIT i

ABSTRACT iv

Zusammenfassung vi

ACKNOWLEDGEMENTS viii

1 Introduction 1

1.1 Electronics and manufacturing procedures 1

1.2 Epoxy resin related reliability issues of a PCB 5

1.3 Importance of the lamination process to the reliability of the epoxies 7

1.4 Motivation and objectives 8

2 Background 9

2.1 Epoxy resins 9

2.2 Curing agents 11

2.3 Glass fibers 12

2.4 Fillers and other agents 13

2.5 Curing mechanism 14

2.6 Ageing mechanism 18

3 Methodology 21

3.1 Curing kinetics by DSC 21

3.2 Curing kinetics by FTIR 26

3.3 Decomposition kinetics by TGA 28

3.4 Model free kinetics (MFK) 31

3.5 Coupling of MFK and FEA 34

3.6 Delamination kinetics by fracture 39

4 Experiments 50

4.1 Materials 51

4.1.1 Model epoxy resin 51

4.1.2 Commercial epoxy resin 51

4.2 Process conditions 52
4.2.1 Lamination process 52
4.2.2 Reflow process 53
4.3 Test coupons 53
4.4 Test plan 55
4.4.1 Kinetics study with a model resin 55
4.4.2 Curing kinetics 56
4.4.3 Mechanical properties 60
4.4.4 Thermal properties 61
4.4.5 Fracture toughness 64
4.4.6 Reliability test 67
5 Results and discussion 71
5.1 Kinetics study with a model resin 71
5.1.1 Decomposition and heat flow of DGEBA and DICY 71
5.1.2 Non-isothermal curing of resins belonging to group M1, M2 and M3 .. 72
5.1.3 Curing kinetics of resins belonging to group M3 77
5.2 Curing kinetics of CE688 80
5.2.1 DSC curing kinetics 80
5.2.2 FTIR curing kinetics 84
5.2.3 Curing prediction in the press book 88
5.3 Effect of press cycle time reduction 91
5.3.1 Mechanical properties 91
5.3.2 Thermal properties 99
5.3.3 Fracture mechanics 113
5.3.4 Reliability 119
5.4 General procedure for optimizing the press cycle time of a new material .. 127
6 Conclusion and future work 130

1 Introduction

1.1 Electronics and manufacturing procedures

Thanks to the ubiquitous availability of electronic devices, modern society is getting smarter and more convenient. The demands on these devices are growing all the time because thinner tablets, smartphones with more functions and more intelligent cars, etc., are desired. Paul Glenn [1] summarized some of the most anticipated technology trends in the 2016 consumer electronics such as drones, virtual reality, cars, robots, smart wears, improved smartphones and appliances for smart home.

Figure 1-1 presents an example of the internal parts of a smartphone [2]. The highlighted part is a printed circuit board assembly (PCBA), or the so-called master board which carries out most of the functions in the background.

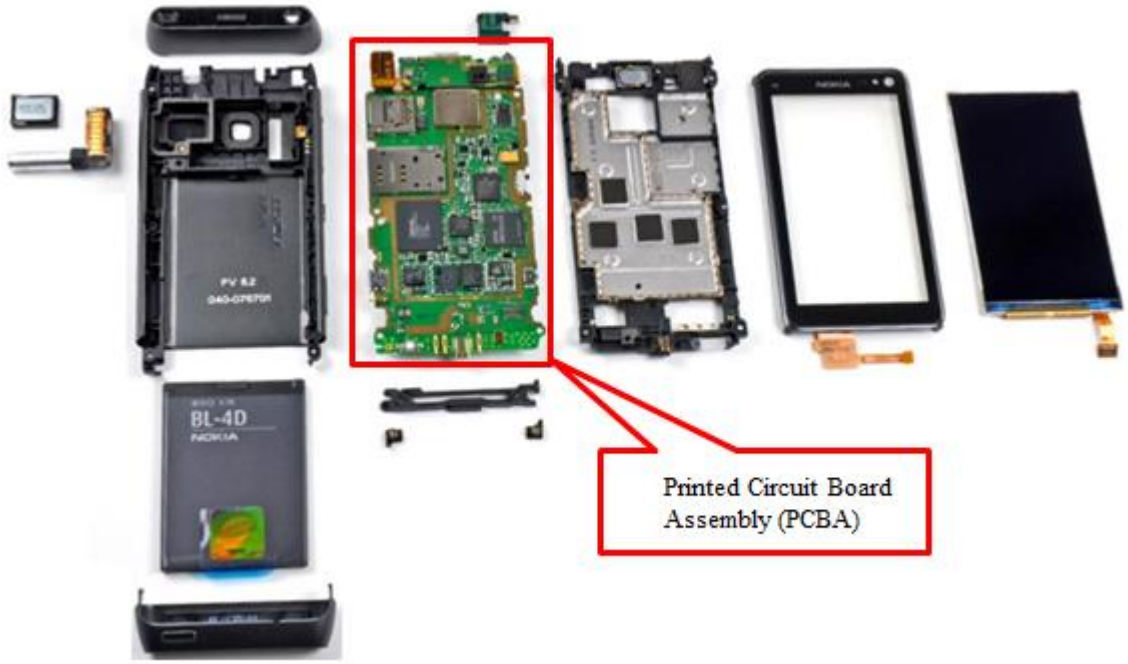

Figure 1-1 Teardown of a smartphone. Adapted from [2].

Principally, all electronics need PCBAs. The application and type of the electronic devices are very diverse; however, the fabrication procedure of a PCBA can be illustrated by a simple flow chart as shown in Figure 1-2. The raw material suppliers produce the prepregs (PPs) and cores for the printed circuit board (PCB) manufacturers from uncured epoxy resins ("A staged" state), glass fibers and/or copper foils. PP is a kind of glass-fiber reinforced dielectric material with a pre-determined curing degree up to 30% ("B staged" state) [3, 4, 5]. The core is a big panel that consists of one or more plies of fully cured PPs and copper claddings.

Based on various interconnection technologies (e.g., photolithography, copper plating, drilling and lamination), PCB makers create connections for the surface-mounted devices (SMDs), such as resistors, capacitors, inductors and integrated circuits. Finally the connections are completed in the assembly plants.

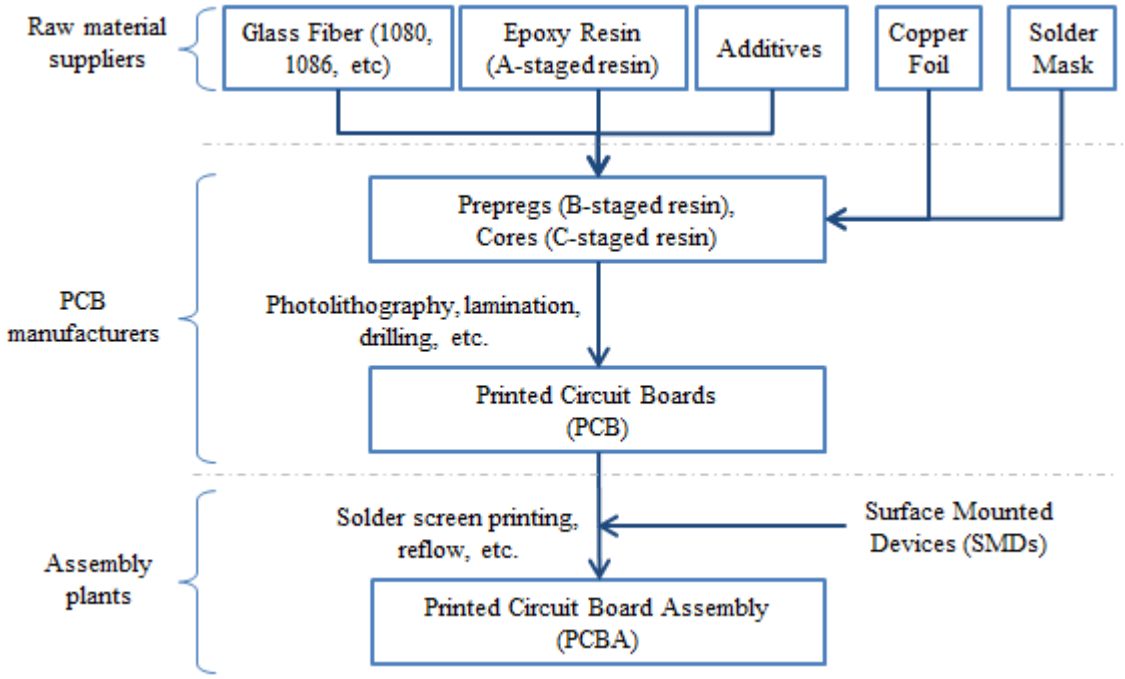

Figure 1-2 Fabrication flow of a printed circuit board assembly

To form the lamination, PCB manufacturers laminate the PPs with outer layers of copper foils by applying programmed pressure and temperature. Subsequently, the PPs are fully cured ("C staged" state). Figure 1-3 shows a typical printed circuit board [6].

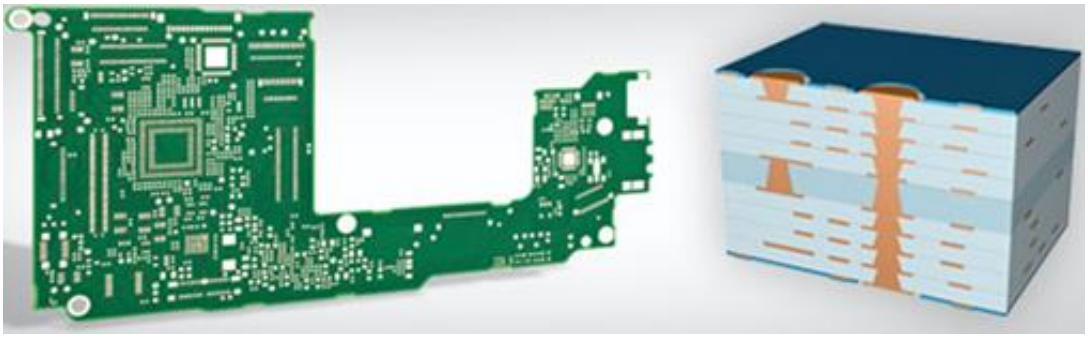

Figure 1-3 Typical printed circuit board (left) and its cross-section model (right) [6]

PCB manufacturing is a very complicated technology, which includes many mechanical (drilling, routing, etc.) and chemical (e.g., photo, etching.) processes. In order to illustrate

the whole process in a simply way, we categorize it into 4 steps using the example of a 6-layer PCB:

1) Inner layer imaging

   The production starts with cores. By means of a photo process, the designed images are transferred to both sides of the cores, as shown in Figure 1-4 (1) to (6).

2) Lamination

   The patterned cores are stacked with uncured prepregs and copper foils, as shown in Figure 1-4 (7), and pressed at elevated temperatures until the prepregs are fully cured.

3) Drilling and panel plating

   The step (8) and (9) in Figure 1-4 creates the electrical connections between the inner and outer layers.

4) Outer layer imaging and solder mask coating

   Similar to the inner layer imaging, the outer layers are also patterned. Meanwhile, the solder mask is applied so as to protect the PCB from corrosion and electrical shorts, as shown in Figure 1-4 (10).

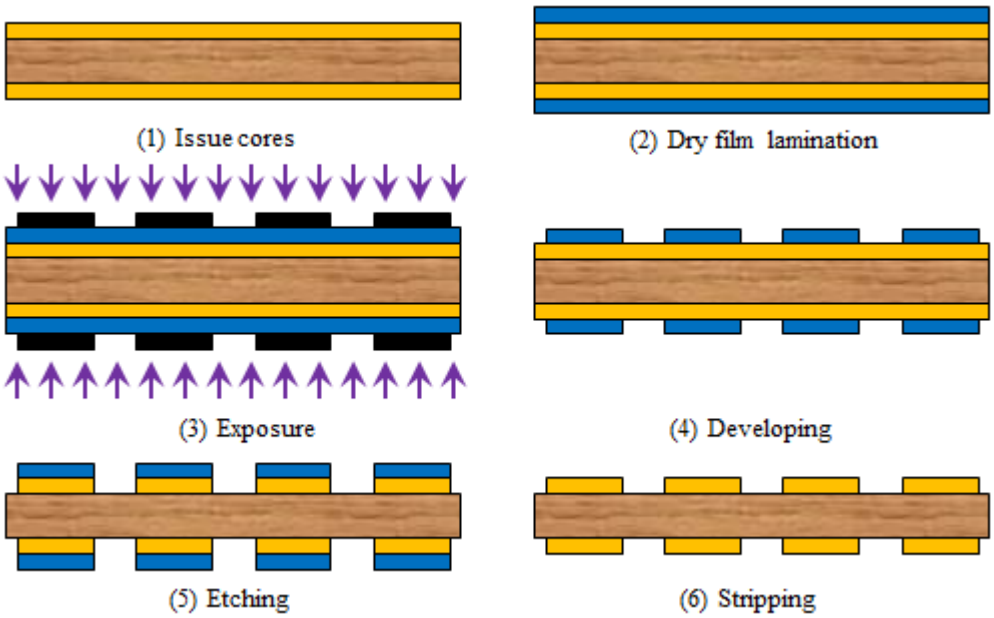

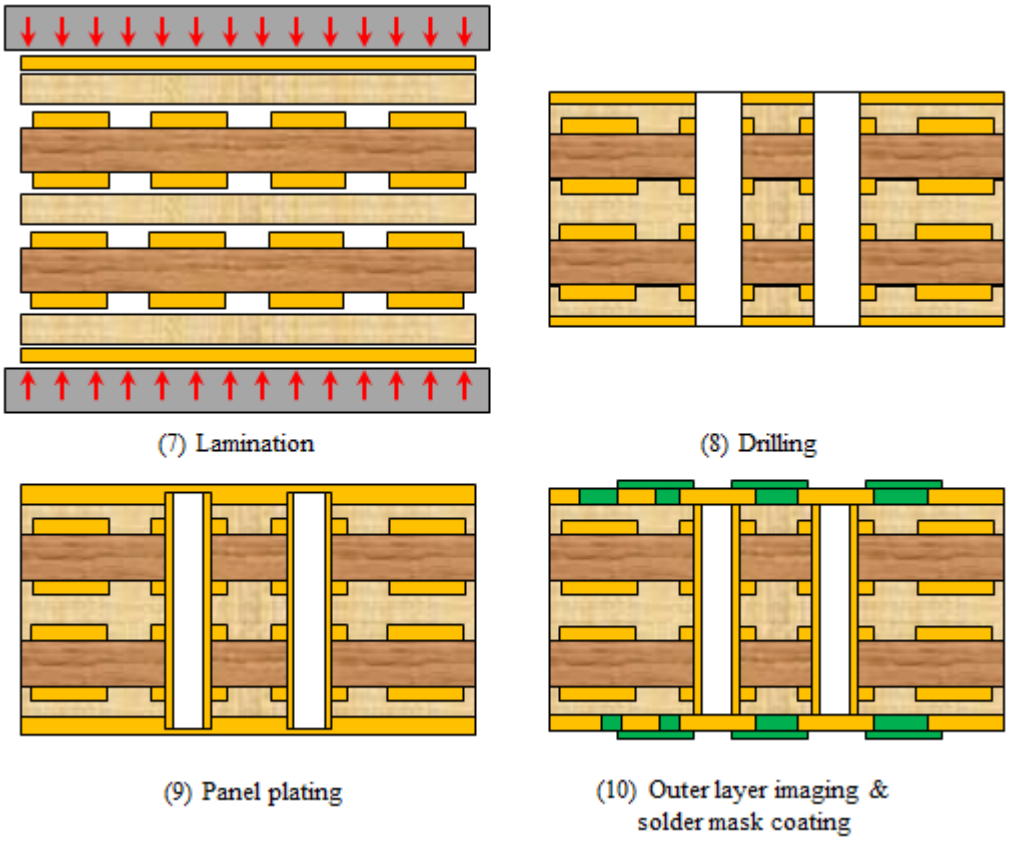

Figure 1-4 A typical manufacturing process for a 6-layer PCB

For the purpose of illustrating the procedure in the assembly plants, as described in Figure 1-2, a typical assembly process is depicted in Figure 1-5:

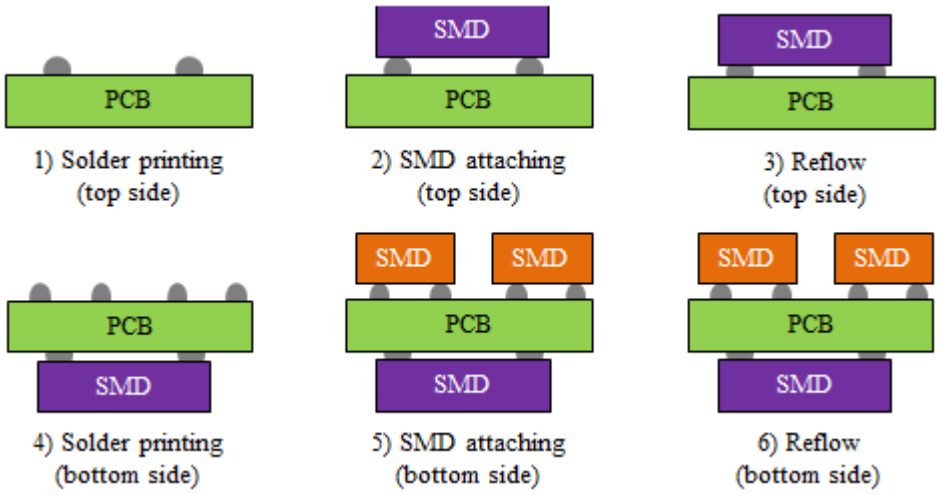

Figure 1-5 A typical simplified assembly process

During the reflow process in Figure 1-5, the printed solder paste is molten and becomes solid afterwards in order to connect the SMDs to the pads on PCB both mechanically and electrically. This process is performed two times if there is no rework in the assembly. But

in reality this process is often repeated 3 to 6 times due to rework. A schematic drawing of a reflow profile according to IPC/JEDEC [7] is depicted in Figure 1-6. The liquidous temperature T_L is normally 217°C for the lead-free product. The solder paste is in solid form below T_L and all the to-be-assembled parts are more slowly heated up. There is a temperature ramp-up (up to 3°C/min) after T_L until the peak temperature T_P is reached. Afterwards, there is a controlled section of temperature ramp-down (max. 6°C/min) till T_L. Since T_P is as high as 260°C for the lead-free reflow process, reflow becomes one of the most critical moments for a PCB, with regard to heating, in its life period.

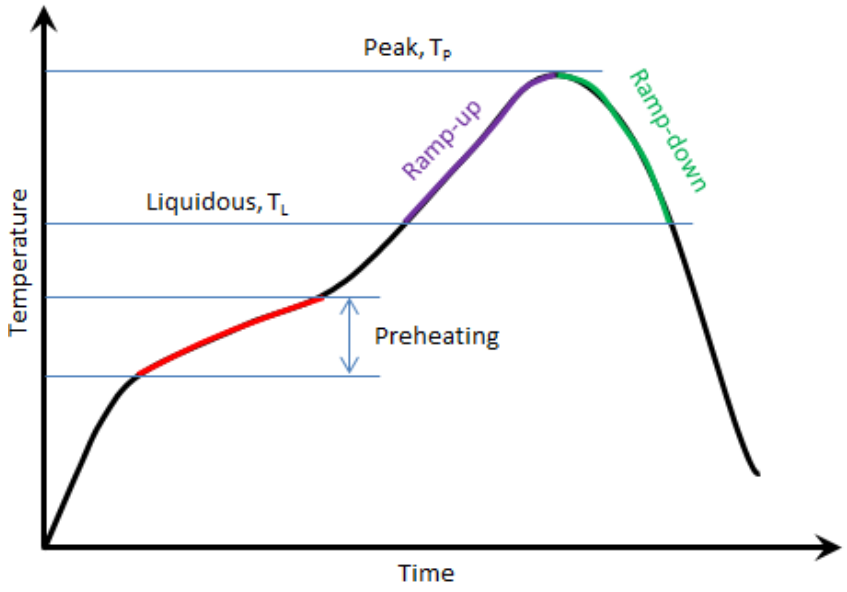

Figure 1-6 Schematic drawing of a lead-free reflow profile

1.2 Epoxy resin related reliability issues of a PCB

In 1925 Charles Ducas first submitted a patent which revolutionarily conceived of the idea to create electrical paths directly on an insulated surface. At early times, the insulation materials could be almost anything, such as Bakelite and wood. Until the 1950s, different resins began to be utilized as PCB materials [8]. These thermoset epoxy laminates are essential parts of a PCB, and most often appear as glass fiber-reinforced boards for printed circuit manufacturing in the electronics industry due to their high performance in specific stiffness, electrical insulation, corrosion resistance, chemical compatibility with reinforced fibers, and relative ease-of-manufacture.

There are many factors which will finally contribute to the lamination quality of a PCB: the resin content of the PPs, the curing degree of the PPs as received, the chemical structure of the resin, the distribution of the glass fibers and fillers, the interface between fiber and

resin, the architecture of reinforcement and the amount of heat transferred to the resin or generated by the polymerization reaction during lamination, etc [9]. A good understanding of the resin curing and ageing behavior and afterwards the ability to predict and monitor the lamination/curing process of the PPs is crucial for the PCB manufacturer, since only the last factor can be optimized for a specific PP. The other factors are controlled by the raw material suppliers.

The PCB mechanical properties are influenced strongly by the final conversion degree, the uniformity of curing, the residual stresses introduced by the thermal and crosslink-shrinkage strains and the mechanical constrains imposed during lamination [10].

According to the IPC standard [11], the reliability of a PCB can be defined as "the ability of a PCB to function under given conditions and for a specified period of time without exceeding acceptable failure levels". Correspondingly, a wide variety of PCB related reliability tests have been designed to assure the quality of the products from different points of view: the thermal cycling test (TCT) and the thermal shock test (TST) are intended to accelerate the potential failures caused by repeated temperature variations during normal use conditions; the conductive anodic filament test (CAF) and the highly-accelerated temperature and humidity stress test (HAST) aim to assess the propensity of inner-laminate electro-migration under high humidity and high bias voltage; the warpage test is often used to evaluate the dimensional stability during and/or after the reflow process. Although most of the PCB-related reliability tests were performed in this study, only those which have a direct link to the curing degree of the PPs are discussed here.

This PhD work focuses on the epoxy curing procedure and the effect of the reduction of the press cycle time on the reliability of PCBs and the relevant reliability tests. Therefore the further development of the existing model free kinetics (MFK) theory, which couples MFK with a finite element approach (FEA), can be treated as one of the key contributions of this study. This is because the current MFK approach can only predict the curing procedure with non-isothermal (at fixed heating rates) or isothermal conditions. However, the newly developed method extends the application of MFK to curing at arbitrary heating rates. Meanwhile, the geometry of the whole heating system can be taken into account, which provides another big advantage.

1.3 Importance of the lamination process to the reliability of the epoxies

Lamination or pressing is one of the most important processes in PCB manufacturing, since the relevant mechanical and thermomechanical properties of the PCB are formed during this procedure. This process involves three steps: 1) Temperature ramp-up. The stacked-up layers are heated up in the press book according to the program. Meanwhile, high pressure will be applied before the gelation temperature in order to squeeze the melted resin and force it to flow and fill in the gaps in the patterns of the inner layers. 2) Isothermal heating. The curing procedure will be completed in this stage. Normally the holding time is set much longer than the time required for curing for the purpose of stress relaxation. At the end of this stage, the high pressure is gradually released. 3) Temperature ramp-down. The cured stacked-up layers are cooled down to room temperature according to the program.

Usually the glass transition temperature (Tg) of the cured PPs is measured after pressing and is used to evaluate the quality of the lamination, because Tg is a property of thermosetting polymers which depends on the curing degree [12] and the one-to-one relation can be described by the empirical DiBenedetto equation [13]. Not only the Tg, but also coefficient of thermal expansion (CTE), density, hardness, tensile storage modulus above Tg and dimensional stability, etc. will all be more or less affected by the cure state of the material [14, 15, 16].

Due to the mismatch of thermal expansion and cure-induced/chemical shrinkage, residual stresses will be produced in epoxies which can result in cracks, voids, delamination, warpage and various other defects. Therefore many authors have studied ways to optimize the press cycle for minimizing the undesirable stresses. White and Hahn [17] studied the processing conditions for a graphite/BMI polymer material in terms of the influence of holding temperature/time, cooling-down rate/pressure and post-cure on the residual stresses and found that curing at lower temperatures for longer times would reduce the stresses by as much as 25-30% while maintaining the transverse mechanical properties. Naito and Todd [18] investigated the effects of curing parameters on the properties development of a model epoxy/anhydride integrated circuit (IC) encapsulant material and concluded that step curing (adding an intermediate dwell at low temperature prior to the isothermal heating step) can reduce shrinkage and the extended time at high temperature can anneal stresses built into the polymer, which finally reduces the device warpage significantly without affecting the development of Tg, CTE or flexural properties. Based on Bogetti and Gillespie's model of curing kinetics and a viscoelastic material model, Gopal et al. [19] researched the

development of thermally-induced residual stresses during the curing process of a polymer composite for the purpose of minimizing these stresses. They determined that the temperature gradients of the holding times and the cooling down period have significant influence and thereafter they could reduce not only the residual stresses but also the cure cycle time by virtue of optimizing the temperature profile.

1.4 Motivation and objectives

Normally the material suppliers are obliged to study the properties of their products and offer the so-called manufacturer's recommended cure cycles (MRC) for every specific PP to the PCB manufacturers. However, these MRCs are often suggested based on their experiences to meet the reliability requirements for most applications [18] and probably most of them are not achieving the optimum performance with regard to residual stresses [19]. Moreover, the material suppliers need not consider the production cost as carefully/precisely as the PCB manufacturers do: the total cycle time could be extended half an hour more and the heating rate/ temperature could be varied to achieve the best general properties.

Depending on the specific application case, a PCB engineer has to decide which material properties are more import and adapt the MRC accordingly. For example, if the final PCB is relatively thicker and the warpage issue is not critical compared with the thin PCBs, the holding time at the hot stage might be reduced to enhance the productivity. In other cases, such as in the application of Embedded Component Packaging (ECP®), the PPs are expected to be cured in two separated press cycles: The first pressing (soft-relam) is used to soften the resin at elevated temperatures and force it to fill the cavities. In this step, the MRC has to be modified to exploit the gelation property to the maximum without affecting the curing degree of the PPs. After some other processes in between, the second pressing (final-relam) will be applied to cure the PPs completely as usual. Furthermore, it will also be beneficial in terms of the machine utilization if one press program can be used for more materials.

The motivation of this PhD work originated from the strong demands of the PCB production with respect to cost-saving, productivity as well as quality control in the lamination process. A good and comprehensive understanding of the curing behavior of the epoxy resin based on the literature and the further development of curing kinetics theories are the base and starting point. Afterwards a variety of reliability tests have been investigated regarding different press cycle times in order to have a deeper insight into the influence of the press cycle time reduction on the material properties.

2 Background

2.1 Epoxy resins

The word “polymer” originates from the Greek words “poly” and “mer”, which mean “many” and “parts” respectively. Polymers are macromolecules consisting of a large number of repeating units and can be categorized into elastomers, thermoplastics and thermosets based on their thermal processing behavior [20]. Epoxy resins are a family of thermoset materials containing oxirane rings as their basic chemical structures as shown in Figure 2-1.

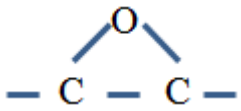

Figure 2-1 Oxirane ring

Epoxy resins are extensively used as adhesives, coatings, dielectrics, encapsulates and matrices in polymer composites because they have a unique combination of properties among all the thermosetting resins thanks to following factors [21, 22]: they are available from low-viscosity liquid to high-melting solids; they are amenable to a wide range of processes; they have a controllable degree of crosslinking by judicious selection of curing agents; minimum pressure is required for manufacturing; they show low shrinkage and hence low residual stress in the cured product; they exhibit excellent performance in terms of adhesion, electrical insulation and chemical resistance, etc.

Glycidyl and non-glycidyl epoxies are the two main family members of epoxy resins and the former can be further classified as glycidyl-ether, glycidyl-ester and glycidyl-amine [23, 24]. Depending on the number of reactive sites per monomer (functionality), they can be categorized into difunctional and multifunctional epoxies as shown in Figure 2-2. Monofunctional reactants cannot form a polymer because the polyreaction will be interrupted; difunctional reactants will generate linear polymers; at least one of the monomers with a functionality higher than two is necessary for obtaining cross-linked polymers. Difunctional epoxies are utilized as a matrix in most of the composite applications [22], but in the PCB industry, they are used in comparatively unsophisticated products such as double-sided boards [25]. In order to improve the performance, either blended difunctional or multifunctional epoxies are used.

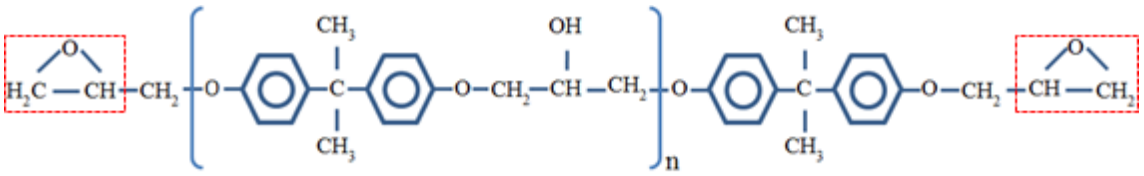

Difunctional: DGEBA (DiGlycidyl Ether of Bisphenol A)

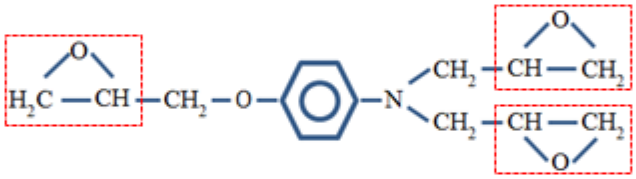

Trifunctional: TGAP (Triglycidyl para-amino phenol)

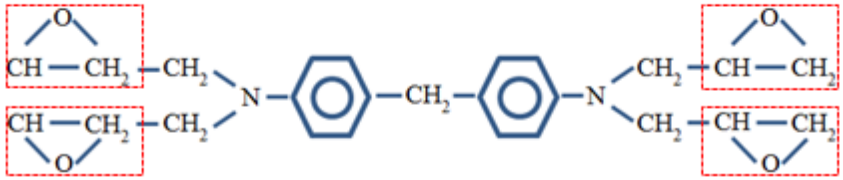

Tetrafunctional: TGDDM (Tetraglycidylether of 4,4' diaminodiphenyl methane)

Figure 2-2 Di- and multi-functional epoxy resins

The structure and functionality of the epoxy monomer will determine its reactivity and the properties of the final product. A representative example of this relationship based on DGEBA is presented in Figure 2-3 [26]: chemical shrinkage is driven by the oxirane ring-opening during curing. Chemical-resistance and elasticity can be improved by the ether linkages in the main chain; chemical/heat-resistance, adhesiveness, durability and electrical properties are provided by the benzene rings in bisphenol A group; the adhesiveness to various adherends is enhanced by the coexistence of hydrophilic groups (-OH) with hydrophobic groups (-CH3).

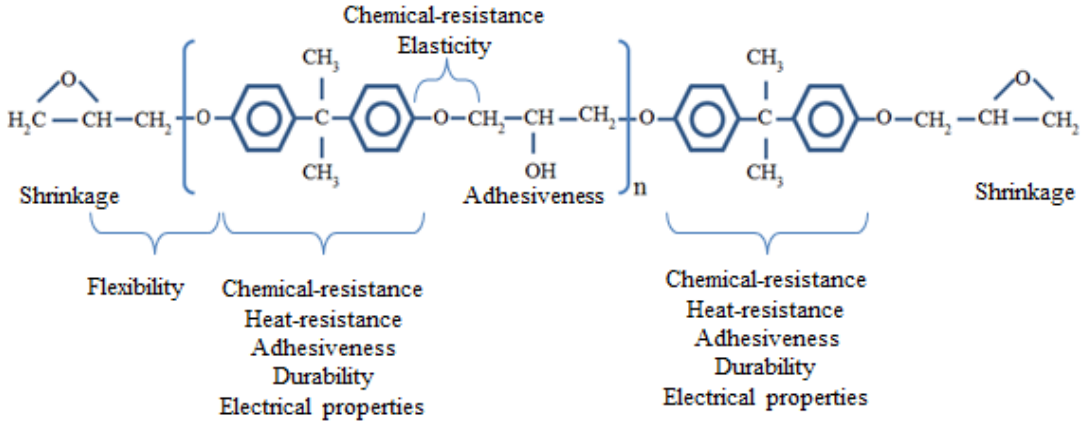

Figure 2-3 Structure and properties of DGEBA. Adapted from [26].

The glass transition temperature (Tg) is an important and primary indicator of the service temperature of a cured epoxy resin product. The state of the polymer is described as glass when its temperature is lower than Tg where only vibrational motion is allowed due to the limitation of the free volume, whereas above Tg it is in the rubbery state where the long-chain molecular segments are able to move owing to the significantly increased free volume. Correspondingly, massive changes in physical properties, such as thermal expansion coefficient (CTE) and modulus, are observed and lead to reliability issues. Normally every resin system should have an ultimate Tg dictated by its formulation. However this final Tg will normally not be used as a specification for quality control in the PCB industry. On the one hand, it is difficult to achieve since the diffusion effect will dominate the kinetics at the end of the curing process which will dramatically extend the curing time; on the other hand, other reliability problems might arise from the increased brittleness of the cured resins. Instead, a min Tg is often being defined as the criteria. For example, Tg > 150°C after lamination might be required for a material with a max Tg of 170°C measured in the laboratory. Furthermore, the Tg of the epoxy resin utilized in PCB has a close relation to the curing temperature [21]: a PP will have a relatively lower Tg with lower curing temperature, and vice versa.

2.2 Curing agents

Curing agents or hardeners are a significant part of the epoxy resin products. The combination of epoxy resin and judiciously selected curing agents provide a wide range of options for viscosity, reactivity, working time, curing rate, thermal resistance, adhesion, flexibility and other mechanical, chemical and optical properties required to meet specific end-use requirements. For example, the curing times can vary from seconds to days; the uncured resins can appear in the form of solid, rubbery or liquid states; the curing temperatures could range from 5 to 260°C; the Tg of the final cured products could alter from room temperature to 260°C and the tensile elongation from 1% to over 100%. [21]

Epoxy resins can react with amines, anhydride, polyamides, imidazoles, etc [21, 22, 27]. Amines are the most widely used curing agents for epoxy resin and are classified into aliphatic, cycloaliphatic and aromatic according to the types of hydrocarbons involved. Acid anhydrides are the next most common hardeners for epoxy resin. They are used as encapsulating material for integrated circuits or as insulators in power current components [22].

Uncured prepregs are a kind of one-component epoxy resin, i.e., the curing agents have been mixed with the epoxy resins at the raw material supplier side. These types of curing agents are also called latent curing agents. They can be stably stored at room temperature and rapidly cured at elevated temperatures or cured by light, pressure or moisture [26, 27].

Dicyandiamide (DICY) is a widely used representative latent curing agent for epoxy resins existing in the form of fine white crystal powder. When dispersed in epoxy resins, its particle size distribution may have a significant effect on the reactivity and the final cured product [21]. The formula of DICY is $C_2N_4H_4$ and its chemical structure is [28]:

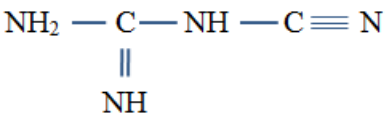

Figure 2-4 Chemical structure of DICY

Zhang et al. [29] studied the thermochemical properties of DICY and found the following: DICY is stable in the temperature range 80-250K (-193.15 – -23.15°C); a reversible phase transition starts at 265K (-8.15°C) and ends at 274K (0.85°C) which may be caused by the change of the crystalline structure; melting starts at 481.59K (208.44°C) with a peak at 487.56K (214.41°C); decomposition starts at about 495K (221.85°C) and 2.3% weight loss below 520K (246.85°C) is caused by the sublimation and evaporation of DICY.

Compared with other curing agents, DICY features low volatility, improved adhesion, good flexibility and toughness [22]. However, DICY is hard to mix and tends to be insoluble in epoxy at room temperature and tends to sediment due to its high specific gravity. No reaction will initiate until solubility is achieved (between 80 and 90°C in most epoxy resins). DICY requires heating at 160 to 180°C for 20 to 60 minutes for curing accompanied by a large amount of reaction heat. In many cases, accelerating agents are applied in order to decrease the curing temperature. For example, when substituted ureas are added, curing will take place at 120 to 175°C over a period of minutes to hours. [21, 26, 27]

2.3 Glass fibers

Glass fiber is a lightweight and extremely strong material typically with greater than 50%wt silica. Since Owens-Corning introduced the long continuous fiber drawn from glass and named it fiberglass in the 1930's, it has become the most prevailing fiber used in the reinforced polymer industry. [30]

The properties along and across a glass fiber are similar because it has an amorphous structure. The filament diameters range typically from 3μm to 20μm. The thinner fibers are

more flexible and ductile. Although its tensile strength is lower than carbon fiber, it is typically far less brittle and cheaper. The tensile strength of a glass fiber is susceptible to its surface quality: the more the surface is scratched, the less the strength. Meanwhile, high humidity can accelerate the degradation of a glass fiber which has micro cracks or defects on the surface by means of moisture adsorption. [31]

Based on the application, glass fibers can be categorized into general-purpose fibers, which comprise 90%, and special-purpose fibers. According to the ASTM D578 standards, the former are designated as E (Electrical) which means low electrical conductivity; the latter include all the remaining, such as S (Strength) with high strength, C (Chemical) with high chemical durability and D (Dielectric) with low dielectric constant, etc. [32]

2.4 Fillers and other agents

Fillers are commonly used in the polymer composites in order to decrease the costs and improve their physical properties such as mechanical strength, elastic modulus and thermal conductivity.

Low [33] studied the influence of residual stresses introduced by the thermal expansion mismatch between epoxy and fillers on the fracture toughness (K_{IC}) of the epoxy system and demonstrated that controlled residual stresses can be exploited to improve the K_{IC} and the crack growth stability of toughened epoxies.

Chauhan et al. [34] developed a semi-empirical model for predicting the effective thermal conductivity (λ_{eff}) of filled polymer composites. The model was validated by the earlier experimental data based on four different composite/filler systems: Phenol-Formaldehyde/Graphite, Phenol-Formaldehyde/Aluminium Oxide, Polypropylene/ Alumninium and Polypropylene/Copper. Both analytical prediction and experimental data show that λ_{eff} is in proportion to the volume fraction of the fillers, especially when it is greater than 0.3, there is a rapid increase of λ_{eff} as the particles come closer and thus the interaction between filler particles become stronger.

In order to impart specific physical and chemical properties to the prepregs, some other agents are often applied: an accelerator might be used together with DICY so that a lower curing temperature and a shortened curing time are possible [27]; rubber additives might be added to improve the flexibility, fatigue and crack resistance in epoxy resins [21]; diluents are usually required to adjust the viscosity of the uncured resin system [26].

2.5 Curing mechanism

The curing of an epoxy resin system proceeds through the cleavage of the oxirane rings and the nucleophilic addition reactions [22]. For example, in the curing procedure of an epoxy / DICY system, the epoxides first react with the four reactive hydrogen atoms, then the hydroxyl group (-OH) of the intermediate reactant reacts with the cyanogen group (-C≡N) of another, as shown in Figure 2-5. As the procedure iterates, a highly cross-linked 3D network will eventually be formed [35].

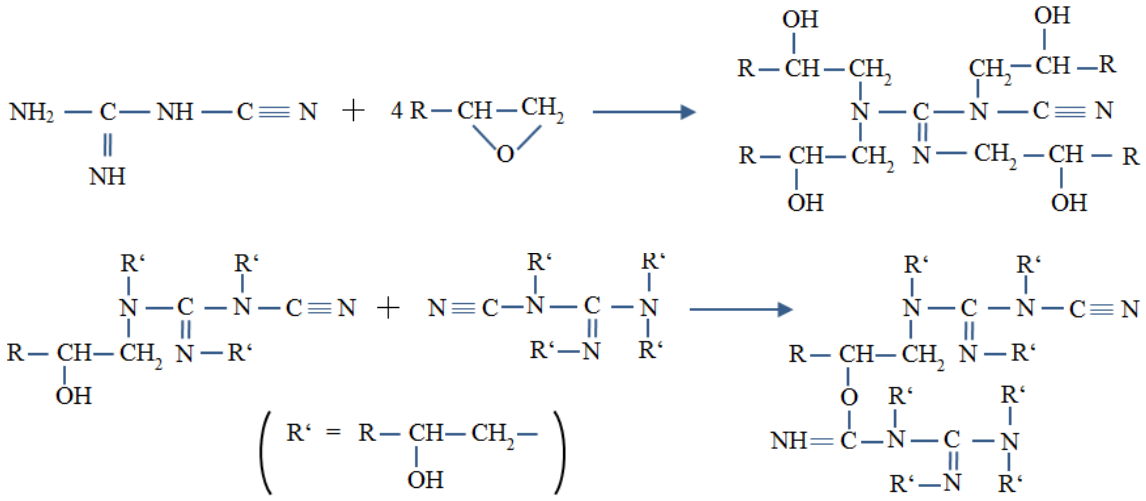

Figure 2-5 Reaction mechanism of DICY with epoxide

A more comprehensive understanding of the curing behavior of thermosetting materials can be established based on the Time-Temperature-Transformation (TTT) cure diagram which can be drawn through measuring the times to events, such as gelation, vitrification, full cure and devitrification, etc., during isothermal curing at different temperature levels [36]. A generalized TTT cure diagram is presented in Figure 2-6.

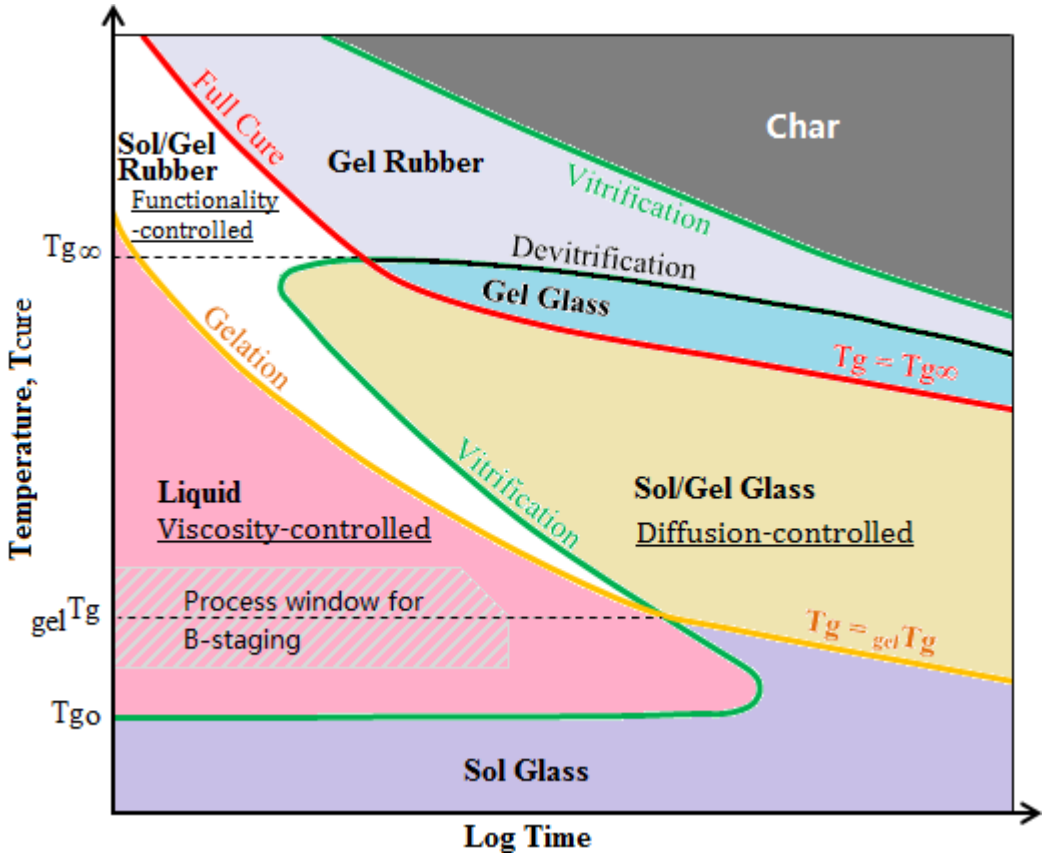

Figure 2-6 Time-Temperature-Transition (TTT) diagram. Adapted from [36, 37, 5].

No reaction will occur if the curing temperature (Tcure) is below the glass transition temperature of the reactants (Tgo) and the resin system is called sol glass because it is soluble in an appropriate solvent. Above Tgo, the sol glass will change to the liquid form and the polymerization process starts, which features raising the number of chemical bonds and the rising of viscosity. There will be a so-called gel point (refer to Figure 2-6, points on the orange line) where a macroscopic network is formed as curing develops, in which all monomers and hardeners are bonded to each other. At gel point, the system has been transferred from the sol state to the gel state which means at least part of the polymer is not soluble in any solvent [22]. This transition is known as the gelation transition or the sol-gel transition. [38]

Analytically, the Flory-Stockmayer model can be used to describe the gelation phenomenon [38]: assume each bond point of a resin system before curing is independent from each other and can connect to maximum z other points with the probability f. A simple example with three times of evolution is presented in Figure 2-7 by means of a Cayley tree. In this case, 1 and 4 are assigned to f and z respectively. For each advancement, the number of newly generated bonds at each bond point will be f(z-1). Hence the total number of bonds

after n times evolution will be $N=[f(z-1)]^n$. As n goes to infinite, N will be finite if f(z-1) is less than 1, i.e., the solution is a sol. Otherwise, the solution will be a gel if f(z-1) is greater than 1 since N will go to infinite as well, which means the weight-average molecular weight becomes infinite while the number-average molecular weight is very low.

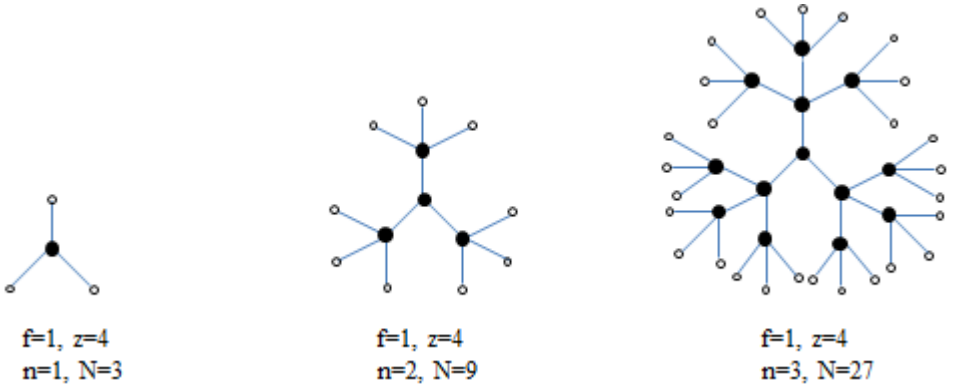

Figure 2-7 Evolution of a Cayley tree from the 1st generation to the 3rd

The PCB manufactures must receive the prepregs in the solid form and in a state prior to gelation at room temperature so that they can be transported in the production and still stay in the liquid region at elevated temperatures (>Tgo) and flow during the lamination process. Therefore there are two key aspects of the prepregging process at the material supplier side [5]: 1) a partially cured resin system so that at RT it can be in the solid state (this step is also called B-staging and the process window is shown in Figure 2-6); 2) the B-staged resin system must be cooled to below Tgo and the material be transformed to an ungelled glass.

The Tg of the reacting system will continuously increase until the final glass transition temperature (Tg∞) is achieved because of the increase in the weight-average molecular weight before gelation and the increase in the cross-link density after gelation. If Tcure < Tg∞, there will be a moment that the Tg rises to the isothermal curing temperature, which is defined as vitrification, as shown by the green curves in Figure 2-6. If it happens that the Tg of the uncured polymer at the composition corresponds to gelation, it is called $_{gel}$Tg which is important for determining the upper limit of the storage temperature. After full cure, the polymer can be thermally deteriorated because of the reduction of the cross-linking or the formation of the low molecular weight plasticizing materials. This degradation will give rise to the decrease of Tg through the isothermal curing temperature which is referred to as devitrification, as presented in Figure 2-6. Once these plasticizing materials volatize during further heating, the Tg can increase through Tcure again and that causes a second time vitrification which is followed by a char region. [37]

The TTT diagram may be exploited to provide a framework for understanding the curing kinetics as shown in Figure 2-8: A strip of the TTT diagram in the vicinity of Tg∞ region is extracted and linked to a typical isothermal curing kinetic curve with a Tcure right below Tg∞.

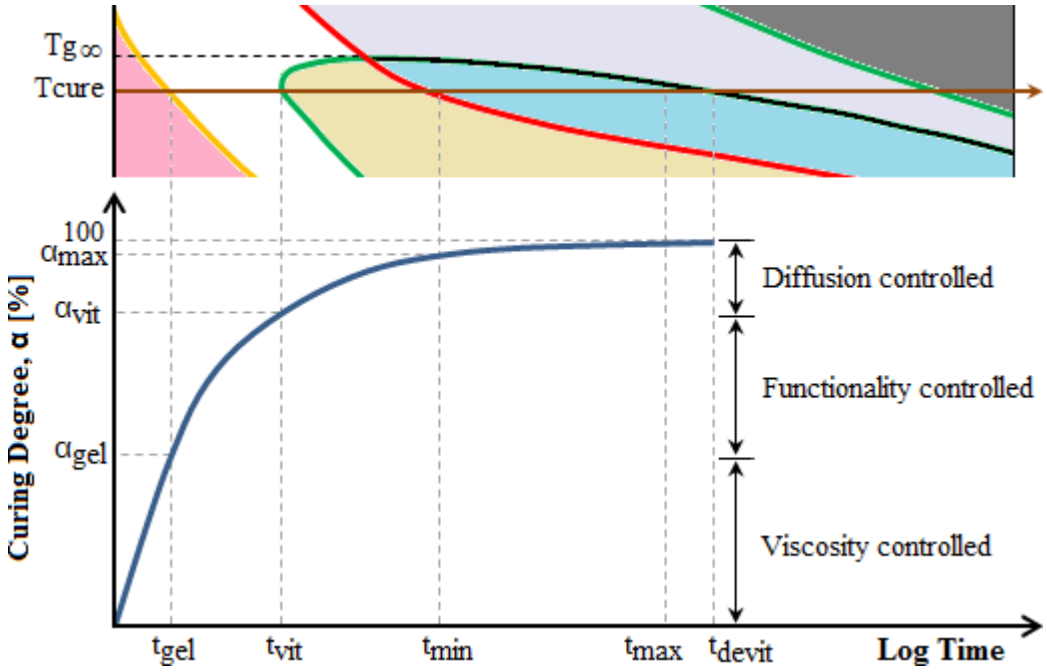

Figure 2-8 Relationship between curing kinetics and TTT diagram (partially drawn)

An isothermal curing kinetic curve describes the one-to-one relationship between the curing degree (α) and the curing time at a fixed isothermal temperature. Vertically it can be divided into 3 main regions according to the reaction mechanism: 1) Viscosity controlled region ($\alpha<\alpha_{gel}$): No macroscopic network is formed before gelation, the viscosity of the reacting system is relatively low, and therefore, the monomers and the hardeners have higher mobility than in the other two regions. If a suitable pressure is applied, the reaction can be accelerated due to density increase [39]. Moreover, gelation is considered to be iso-conversional, i.e., α_{gel} is constant for a given thermoset. For a stoichiometrically mixed reacting system consisting of an f-functional monomer and a g-functional hardener, $\alpha_{gel} = [(f-1)(g-1)]^{-1/2}$. In case of reacting DGEBA (f=2) with a diamine (g=4), $\alpha_{gel} = 0.577$, which aligns well with the experimental values (0.58~0.60) [40]. 2) Functionality controlled region ($\alpha_{gel}<\alpha<\alpha_{vit}$): Beyond gelation the reacting system becomes very viscous, which retards the movement of the reactants, and thus in this regime the reaction is controlled by the functionality rather than viscosity. This confirms the fact that the TGDDM (Tetraglycidylether of 4,4' diaminodiphenyl methane) / DETDA (Diethyltoluene diamine)

system vitrifies sooner than TGAP (Triglycidyl p-amino phenol) / DETDA where the former is a tetrafunctional and the latter is a trifunctional epoxy system [22]. 3) Diffusion controlled region ($\alpha_{vit}<\alpha<100\%$): Owing to the increasing cross-link density after gelation, the rigidity of the formed 3D network increases. Once the Tg of the reacting system is higher than Tcure, the whole system transforms to the glassy state which means that diffusion of the monomers will dominate the further reaction. In this case, the applied pressure will slow down the movement velocity of the monomers inside the 3D network and cause the reduction of the reaction rate [39].

On the time scale of the curing kinetic curve, the time to gelation (t_{gel}) and the time to vitrification (t_{vit}) correspond to the α_{gel} and α_{vit} respectively, both decrease with increasing functionality of the reactants. In practice, it is difficult to fully cure epoxy: on the one hand, the dominant diffusion effect after vitrification slows down the reaction rate significantly which weakens exothermal signals and makes it harder to be detected by a normal differential scanning calorimeter (DSC); on the other hand, cure and thermal degradation compete with each other for high Tg systems. Therefore, α_{max} measured by DSC is often used as 100% cured and its corresponding time (t_{min}) defines the minimum time to full cure. An extended holding time until t_{max} after full cure is typically used in practice in order to release the residual stresses occurred after gelation above $_{gel}$Tg due to volumetric shrinkage. However there must be a safe distance between t_{max} and t_{devit} to avoid the deterioration of the material. [37]

2.6 Ageing mechanism

Ageing refers to the property changes, such as Tg, stiffness and CTE, etc., of a material versus time. In terms of thermosetting materials, their ageing can be categorized into two separate and complementary parts, i.e., chemical and physical ageing [41]. Irreversible modification of the chemical bonds is the main characteristic of the former. And the latter features the reversible procedure of molecular movement and structural relaxation in the vitreous phase.

With regard to the chemical ageing, the oxidative degradation is one of the most often occurring cases which could be caused by using the material at elevated temperatures (thermo-oxidation) or exposing it to UV radiation (photo-oxidation). Both oxidations need free radicals $P^{\bullet}$ to react with oxygen in the environment in order to form peroxide radicals:

$$P^{\bullet} + O_2 \rightarrow POO^{\bullet}$$

Equation 2-1

These free radicals exist in all polymers due to the polymerization and processing history. Alternatively, they can be generated by the dissociation of the C-H bonds in the presence of radiation. Once the peroxide radicals are formed, they will start to propagate in the bulk and breakdown the polymer chains [42]. This degradation process consists of two stages under service temperatures: a relatively long induction period which may be regarded as the service lifetime since very little degradation occurs during this stage; and a drastically increased degradation process at the end of the first stage which will reduce the material properties significantly [43]. At elevated temperatures, the degradation process can be accelerated and therefore two strong exothermic reactions may be observed [44, 45]: the first is caused by the scission of large polymer chains which results in low molecular weight products; the second is associated with the oxidation of the fragments. In the presence of high humidity at high temperatures, or the so-called hygrothermal ageing, water molecules will diffuse into the bulk leading to a reversible plasticization effect on re-drying [46]. However, the Tg of the polymer will be reduced due to the increase of the molecular mobility [47]. Besides, the crosslinking density can be modified due to the absorption of water and significantly affect the material performance [41].

In a pioneering work Struik determined the influence of structural recovery on the viscoelastic properties of glassy polymers and labeled it as physical ageing [47]. It can be generally characterized as an increase in mass density (volumetric relaxation) and/or a decrease in molecular configurational energy (enthalpy relaxation) of amorphous or semi-crystalline materials under sub-Tg temperatures for an extended period of time (annealing) [48]. Based on the characteristics of the physical ageing, it might be helpful to consider it from the specific enthalpy point of view, which is a measurement of energy in a thermodynamic system and defined as:

$$H \equiv U + pV$$

Equation 2-2

Where, H is the specific enthalpy, [J/kg];

U is the specific internal energy, [J/kg];

p is the pressure, [Pa];

V is the specific volume, [m^3/kg].

In reality, it is more useful to calculate its change from a reference point. Therefore Equation 2-2 is modified as:

$$dH = dU + p \cdot dV + V \cdot dp$$

Equation 2-3

It makes sense to assume $dp = 0$ in Equation 2-3 since the process of ageing normally happens under constant pressure in practical conditions. Hence,

$$dH = dU + p \cdot dV$$

Equation 2-4

In Equation 2-4, dU refers to the volume-independent change of configuration and dV stands for the change of the free volume in a molecular network. [48]

The reduction of the free volume can be described by the lattice contraction process, i.e., the chain segments collectively become closer to each other [49]. Kovacs [50] proposed a simple but useful first-order isothermal volume relaxation equation:

$$\frac{dV_f}{dt} = -\frac{V_f - V_{f\infty}}{\tau[V_f, T]}$$

Equation 2-5

Where, V_f is the momentary free volume at ageing time t, [m^3/kg];

$V_{f\infty}$ is the free volume of equilibrium at temperature T, [m^3/kg];

τ is the relaxation time which depends on both V_f and T, [s].

The well-known Struik model [51] describes physical ageing as a self-retarding process where the relaxation time of a bulk polymer will drastically increase as its free volume decreases and makes an additional assumption that τ in Equation 2-5 varies with V_f according to:

$$\tau = \frac{\tau_\infty}{e^{\gamma[V_f - V_{f\infty}]}}$$

Equation 2-6

Where, τ_∞ is the relaxation time of equilibrium at temperature T, [s];

γ is a constant, [kg/m^3].

3 Methodology

3.1 Curing kinetics by DSC

Differential Scanning Calorimetry (DSC), which was developed by Emmett S. Watson and Michael J. O'Neill of Perkin-Elmer in 1962 [52], is a technique in which the heat flow difference into a substance and a reference material is measured as a function of temperature while the substance and reference material are subjected to a controlled-temperature program [53]. It can be used for the determination of the glass transition temperature, the heat capacity, and the melting and crystallization temperatures. Meanwhile, it can also be used to measure the reaction heat. There are two types of DSC instruments, the power compensated DSC and the heat-flux DSC [54]. The following discussion mainly focuses on the latter since it was used in this study.

One of the most important user-related parts of a DSC is the testing chamber, which is a housing that contains the heat sink, heater, thermocouples, two pans or crucibles denoted as sample and reference separately, and the heat leak which is a directional heat pathway formed by the temperature difference. A schematic drawing of the heat-flux type DSC testing chamber and the corresponding thermal model are shown in Figure 3-1 and Figure 3-2 respectively:

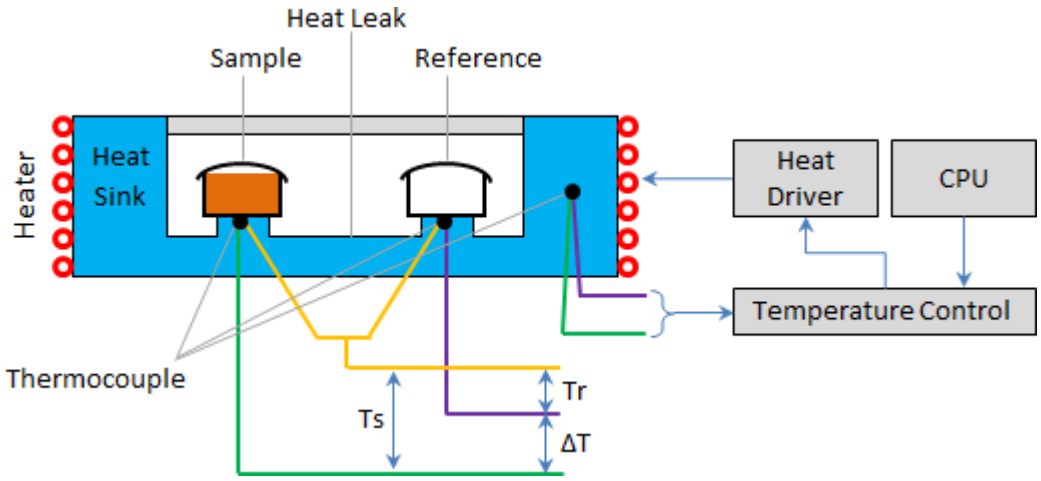

Figure 3-1 A schematic drawing of the testing chamber of a heat-flux DSC. Adapted from [55].

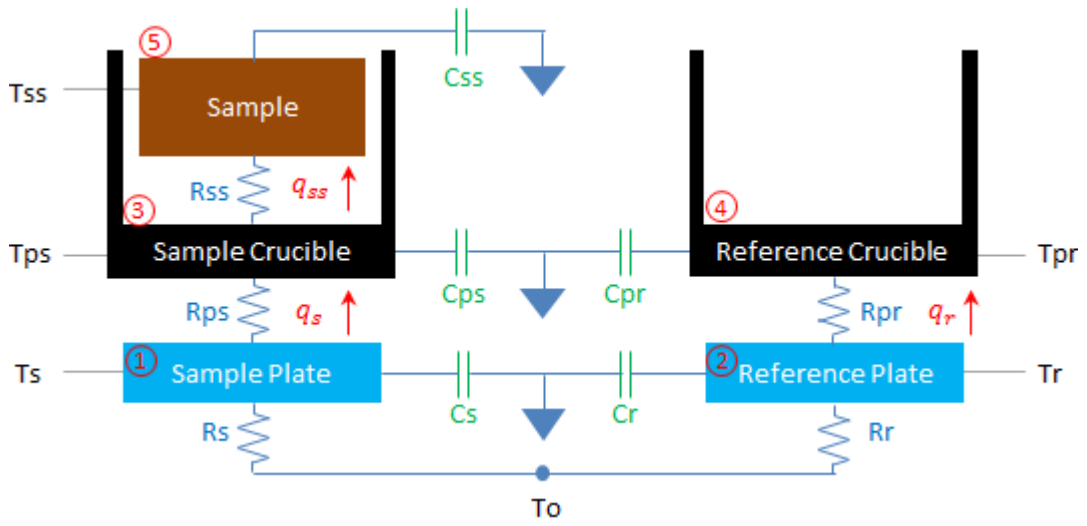

Figure 3-2 Thermal model of the testing chamber of a heat-flux DSC with junction 1 – 5 marked in red. Adapted from [56].

The heat flow rate between the sample and the reference crucibles can be obtained based on the thermal equivalent of Ohm's law [54]:

$$\dot{Q} = \frac{\Delta T}{R} = \frac{T_s - T_r}{R_s + R_r}$$

Equation 3-1

Where, $\dot{Q}$ is the heat flow rate, [J/s];

ΔT is the temperature difference between sample and reference plate, [K].

T_s/T_r is the temperature of the sample/reference plate, [K];

R is the thermal resistance of the heat leak disk, [K/W];

R_s/R_r is the thermal resistance of the sample/reference calorimeter, [K/W].

Equation 3-1 describes a basic understanding of the DSC. However, a further analysis of the thermal model as shown in Equation 3-2 is essential to accurately interpret the DSC results. Analogous to the Kirchhoff's current law (KCL), below thermal equations of balance can be obtained at each junction point in Figure 3-2:

$$\begin{cases} Junction\ 1: \dot{q}_s = \dfrac{T_o - T_s}{R_s} - C_s \dfrac{dT_s}{dt} \ldots\ldots\ldots (1) \\ Junction\ 2: \dot{q}_r = \dfrac{T_o - T_r}{R_r} - C_r \dfrac{dT_r}{dt} \ldots\ldots\ldots (2) \\ Junction\ 3: \dot{q}_{ss} = \dot{q}_s - C_{ps} \dfrac{dT_{ps}}{dt} \quad \ldots\ldots\ldots (3) \\ Junction\ 4: \dot{q}_r = C_{pr} \dfrac{dT_{pr}}{dt} \quad \ldots\ldots\ldots (4) \\ Junction\ 5: \dot{q}_{ss} = C_{ss} \dfrac{dT_{ss}}{dt} - \dfrac{dh}{dt} \quad \ldots\ldots\ldots (5) \end{cases}$$

Equation 3-2

Where, $\dot{q}_s$ is the heat flow rate between sample plate and sample pan, [J/s];

$\dot{q}_r$ is the heat flow rate between reference plate and reference pan, [J/s];

$\dot{q}_{ss}$ is the heat flow rate between sample pan and sample, [J/s];

$T_o/T_s/T_r$ is the temperature of the oven/sample plate/reference plate, [K];

$T_{ps}/T_{pr}/T_{ss}$ is the temperature of sample pan/reference pan/sample, [K];

C_s/C_r is the heat capacity of the sample/reference calorimeter, [J/K];

$C_{ps}/C_{pr}/C_{ss}$ is the heat capacity of the sample pan/reference pan/sample, [J/K];

h is the reaction heat of the sample, [J].

Replacing the heat capacities in Equation 3-2 (3) and (4) with their specific heat capacities and combining both:

$$\dot{q}_{ss} = \dot{q}_s - \dot{q}_r \frac{m_{ps}}{m_{pr}} \left(\frac{dT_{ps}/dt}{dT_{pr}/dt} \right)$$

Equation 3-3

Where, m_{ps}/m_{pr} is the mass of the sample/reference pan, [Kg].

q_{ss} is the actual heat energy which has been transferred into the sample. In order to obtain the reaction heat, replace $\dot{q}_{ss}$ in Equation 3-3 with items (5) in Equation 3-2:

$$-\frac{dh}{dt} = \dot{q}_s - \dot{q}_r \frac{m_{ps}}{m_{pr}} \left(\frac{dT_{ps}/dt}{dT_{pr}/dt} \right) - C_{ss} \frac{dT_{ss}}{dt}$$

Equation 3-4

To simplify Equation 3-4, assign $\gamma = \frac{m_{ps}}{m_{pr}}\left(\frac{dT_{ps}/dt}{dT_{pr}/dt}\right)$. Meanwhile, T_{ps} and T_{pr} may be expressed according to the equation below by means of applying the thermal equivalence of Ohm's law in the thermal model:

$$\begin{cases} T_{ps} = T_s - \dot{q}_s R_{ps} \\ T_{pr} = T_r - \dot{q}_r R_{pr} \end{cases}$$

Equation 3-5

Combined with items (1) and (2) in Equation 3-2, γ can be rewritten as:

$$\gamma = \frac{m_{ps}\left[-\frac{dT_o}{dt}\frac{R_{ps}}{R_s} + \left(1 + \frac{R_{ps}}{R_s}\right)\frac{dT_s}{dt} + C_s R_{ps}\frac{d^2T_s}{dt^2}\right]}{m_{pr}\left[-\frac{dT_o}{dt}\frac{R_{pr}}{R_r} + \left(1 + \frac{R_{pr}}{R_r}\right)\frac{dT_r}{dt} + C_r R_{pr}\frac{d^2T_r}{dt^2}\right]}$$

Equation 3-6

Where, γ is a correction factor, [-].

Similarly, replacing $\dot{q}_s$ and $\dot{q}_r$ in Equation 3-4 and rearranging it result in the following five-term heat flow expression:

$$-\frac{dh}{dt} = -\gamma\frac{\Delta T}{R_r} + (T_s - T_o)\left(\frac{\gamma}{R_r} - \frac{1}{R_s}\right) + (\gamma C_r - C_s)\frac{dT_s}{dt} - \gamma C_r\frac{d\Delta T}{dt} - C_{ss}\frac{dT_{ss}}{dt}$$

Equation 3-7

Eventually, Equation 3-6 and Equation 3-7 can be used for the application since the temperatures (T_o, T_s, T_r) and the masses (m_{ps}, m_{pr}) can be measured during the experiments; the thermal resistances and heat capacities of the sample and reference calorimeters (R_s, R_r, C_s, C_r) can be obtained via a specific calibration procedure for the DSC instrument; the contact resistances between the plates and pans (R_{ps}, R_{pr}) can be calculated based on certain semi-empirical functions [56]. The three items on the right side of Equation 3-7 without α have been interpreted by [54]: $-\Delta T/R_r$ is the principal heat flow rate which roughly equals to $-\Delta T/(R_s+R_r)$ for certain DSC devices, $(C_r-C_s)(dT_s/dt)$ is the thermal capacitance related imbalance, and $C_r(d\Delta T/dt)$ is the heating rate related imbalance. Before and after a chemical reaction ($-dh/dt=0$), the last item, $C_{ss}(dT_{ss}/dt)$, describes the base line of the DSC curve. The heat capacity of an epoxy system C_{ss} would first increase almost linearly with the conversion from the start of the chemical reaction until the onset of the vitrification and then decrease sharply due to the significantly reduced molecular mobility after vitrification [57, 58]. Therefore, taking a straight line as the base line for an exothermal peak

to calculate the reaction energy is not exact although it is generally accepted. Moreover, the temperature changes inside the sample (dT_{ss}/dt) should be as constant as possible.

Normally there are two kinds of thermal profiles: one is dynamic scanning by heating up the sample from a start temperature to a final one with a fixed heating rate; another is isothermal scanning by keeping the sample at a constant temperature in the whole test procedure. DSC is one of the most commonly used methods to obtain the cure kinetics of epoxy by assuming that the heat of the cure reaction equals the total area under the heat flow-time curve, as shown in Figure 3-3. With the known total heat of the reaction, H_T, and the heat at any time, H_t, the conversion degree can be easily defined as:

$$\alpha = \frac{H_t}{H_T}$$

Equation 3-8

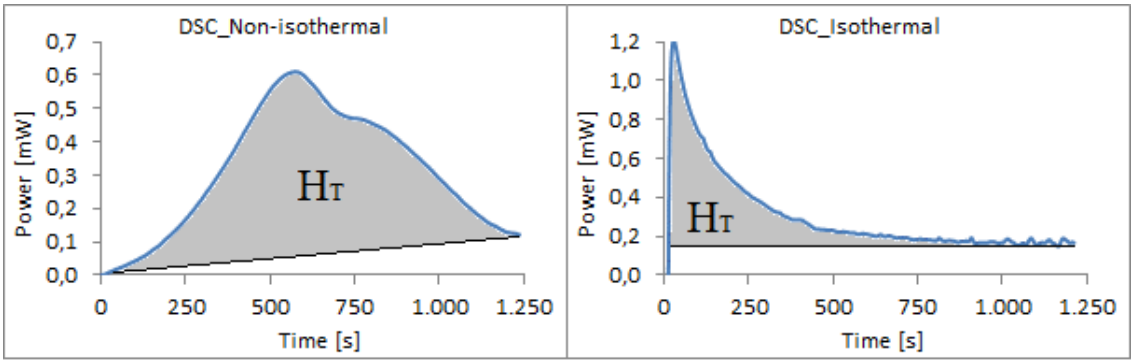

Figure 3-3 Typical DSC curves and their corresponding total reaction of heat for (a) the non-isothermal scan and (b) the isothermal scan

Moreover, there are two important factors in the practice of quantitatively determining the reaction energy from an isothermal DSC measurement: [59, pp. 89-91]

1) Since there is a short time gap (~10s) between the placement of the sample in the DSC chamber and the starting of the recording, the reaction time should be longer than two minutes in order to reduce the negative influence introduced by the uncertainty at the beginning of the reaction. Therefore, the isothermal temperature should not be too high. Some authors [60] suggest that the maximum temperature should not be higher than the one halfway to the peak of the thermogram scanned at 5°C/min.
2) The isothermal DSC thermogram should be recorded long enough to determine the reaction energy more accurately by applying the horizontal baseline at the end of the curve.

3.2 Curing kinetics by FTIR

Infrared spectroscopy studies the interaction of infrared light with matter and one of its most widely used types is Fourier Transform Infrared (FTIR). Compared with other chemical analysis techniques, infrared spectroscopy is sensitive, fast and easy, relatively inexpensive, information-rich and can be applied for all substances which consist of polar molecules. [61]

The measured light waves are usually characterized by the wavenumber, cm^{-1}, which means the number of cycles a wave undergoes per centimeter. Due to the periodic motion of the atoms, the molecules will have constant translational and rotational motion with certain vibration frequencies which typically range from 500 to 5000cm^{-1}. Generally, a lighter mass or a stronger bond will result in higher frequency. At room temperature, most bonds will vibrate with the lowest possible energy. However, in the presence of IR radiation, the bond can absorb energy and vibrate with greater amplitude. The absorbance spectrum of a sample indicates its molecular structure. Since more and more material structures of interest have become known over the last 100-plus years, the peak positions of known molecules derived from these spectra can be utilized to identify the molecules in an unknown sample [61].

The first generation of infrared spectrometers emerged in the 1940's, based on the dispersive technology as shown in Figure 3-4: light from the IR source is split into two beams of equal intensity which are allowed to pass through the sample and reference separately. The chopper then makes the sample and the reference beam fall on the monochromator alternatingly, so that the difference in intensity between the two beams at each wavelength can be measured by the detector. The monochromator consists of a prism or diffraction grating and a moving slit. The former disperses the light according to wavelength or frequency; the latter allows light in just a narrow frequency range to hit the detector permitting the separation of absorption bands that are close in frequency. Eventually, the amount of light that has been absorbed at each frequency can be calculated by comparing intensity differences between the sample and the reference beams. [62]

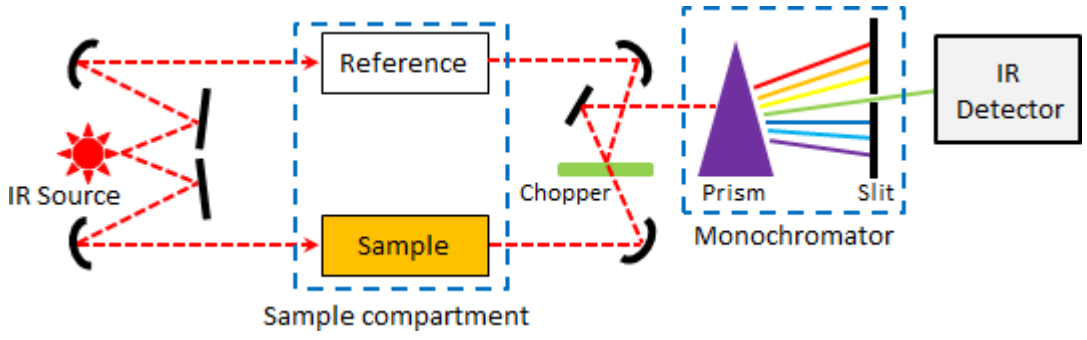

Figure 3-4 Schematic drawing of a dispersive infrared spectrometer. Adapted from [62].

However the dispersive IR spectrometer lacks in efficiency because of its scanning speed, throughput and manual operation. Gradually, the FTIR spectrometer, which was developed in the 1960's based on the interference technology, has become more popular for organic compound identification. The key part of the spectrometer is the interferometer which contains a beam-splitter and two mirrors. The assembly of an interferometer is depicted in Figure 3-5. The IR light from the source strikes the beam-splitter first and is then split into two beams of equal intensity. One beam is reflected to a fixed mirror; another one is transmitted to a moving mirror that oscillates at a constant velocity timed according to the frequency of the IR light. Once the two reflected beams meet at the beam-splitter, they will recombine constructively if the distances they travel are the same, otherwise they will result in some destructive interference. The recombined IR beam next passes through the sample or the reference and the transmitted portion will finally reach the detector and is recorded as a total intensity in the so-called interferogram. [62]

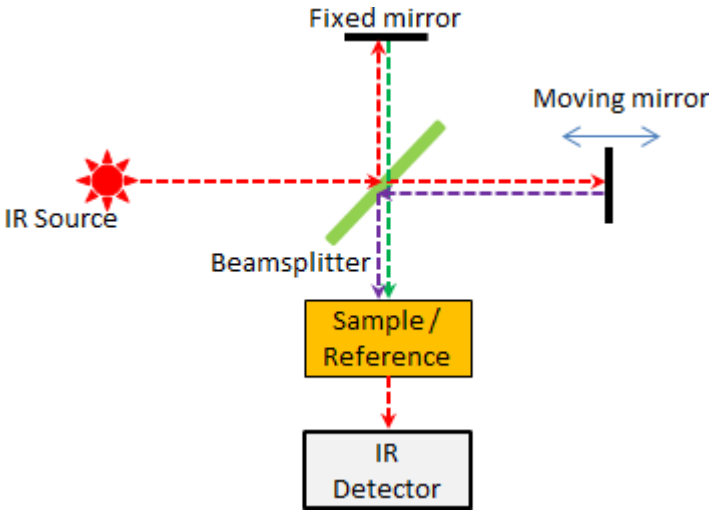

Figure 3-5 Schematic drawing of an interferometer. Adapted from [62].

The interferogram is actually the intensity of the interfering wave versus the optical path difference. A decoding process must be performed in order to extract the actual spectrum of the sample. The intensity collected by the detector at a certain read point can be expressed as [63]:

$$I(p,\bar{v}) = I(\bar{v})[1+\cos(2\pi\bar{v}p)]$$

Equation 3-9

Where, I is the intensity of the received light, [arb. unit];

p is the optical path length difference, [nm];

$\bar{\nu}$ is the wavenumber of the received light, [1/cm].

Thus, the total intensity at p is:

$$I(p) = \int_0^\infty I(\bar{\nu})[1 + \cos(2\pi\bar{\nu}p)]d\bar{\nu}$$

Equation 3-10

Finally, the desired spectrum can be resolved by conducting an inverse Fourier transform:

$$I(\bar{\nu}) = 4\int_0^\infty [I(p) - \frac{1}{2}I_0]\cos(2\pi\bar{\nu}p)\,dp$$

Equation 3-11

Once the IR spectrum of an epoxy resin sample is measured, its conversion degree α can be calculated according to [64, 65]:

$$\alpha = 1 - \frac{A_{epo}(t)/A_{ref}(t)}{A_{epo}(0)/A_{ref}(0)}$$

Equation 3-12

Where, $A_{epo}(t)$ is the absorbance of epoxide group at time t, [-];

$A_{ref}(t)$ is the absorbance of reference at time t, [-];

$A_{epo}(0)$ is the absorbance of epoxide group at beginning, [t];

$A_{ref}(0)$ is the absorbance of reference at beginning, [t].

Although Equation 3-12 is written in terms of the absorbance of an epoxide group, the application is not limited to the epoxy. Depending on the needs and the convenience of the characterization process, the absorbance of the hardener, for example, can also be used to replace the $A_{epo}(0)$/ $A_{epo}(t)$ in the equation.

3.3 Decomposition kinetics by TGA

Thermogravimetric analysis or "TGA" is a technique in which the mass of a substance is measured as a function of temperature or time as the sample specimen is subjected to a controlled temperature program. The graphic presentation of the data obtained in thermogravimetry is referred to as a "TG thermal curve" which may be expressed as either

the weight or weight percent of the original sample remaining versus temperature or time, as shown in Figure 3-6. [66]

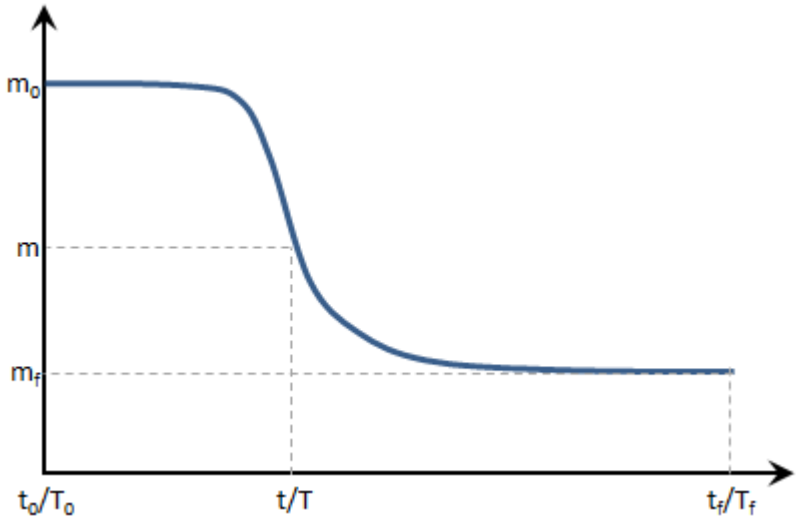

Figure 3-6 A typical TG thermal curve

TGA measurements are very useful for the study of polymeric materials in terms of determining the properties of thermal and/or oxidative stabilities. Polymers will exhibit either mass loss or gain due to decomposition, loss of volatiles or oxidation. In the PCB industry, TGA is primarily applied for the mass loss study of prepregs, solder masks or finished PCBs which can arise from [67]: 1) volatile components, such as absorbed moisture, solvents, low-molecular-mass additives or oligomers, that generally evaporate between ambient and 300°C; 2) reaction products, such as water and formaldehyde (CH_2O) from the curing of phenolic and amino resins, which generally form between 100°C and 250°C; 3) volatile degradation products resulting from chain scission at temperatures above 200°C but not more than 800°C. The characterization of these mass loss processes is essential to PCB manufacturers, because it offers very important information such as resin content, moisture and volatiles content, extent of cure, decomposition kinetics and thermal stability.

One of the key parts of the TGA is the thermobalance, which enables the measurement of the sample mass as a function of temperature and time. A simple schematic representation of the thermobalance is shown in Figure 3-7. The sample is first encapsulated in a crucible outside of the device and then placed on a small ceramic or metal pan. The pan is suspended in the furnace and connected to one side of the thermobalance. A weight hangs on the other side of the balance in order to offset the mass of the apparatus. The photodiodes determine the weight of the sample by measuring the offset angle according to the amount of received light. Equal amounts of light will shine on the photodiodes at zero position. Once the sample

has been balanced, the sample is heated according to the predetermined heating program. Due to the mass change of the sample during heating, a current will be applied to the meter movement trying to maintain the balance at zero position. This applied current is proportional to the weight loss or gain of the sample. [68]

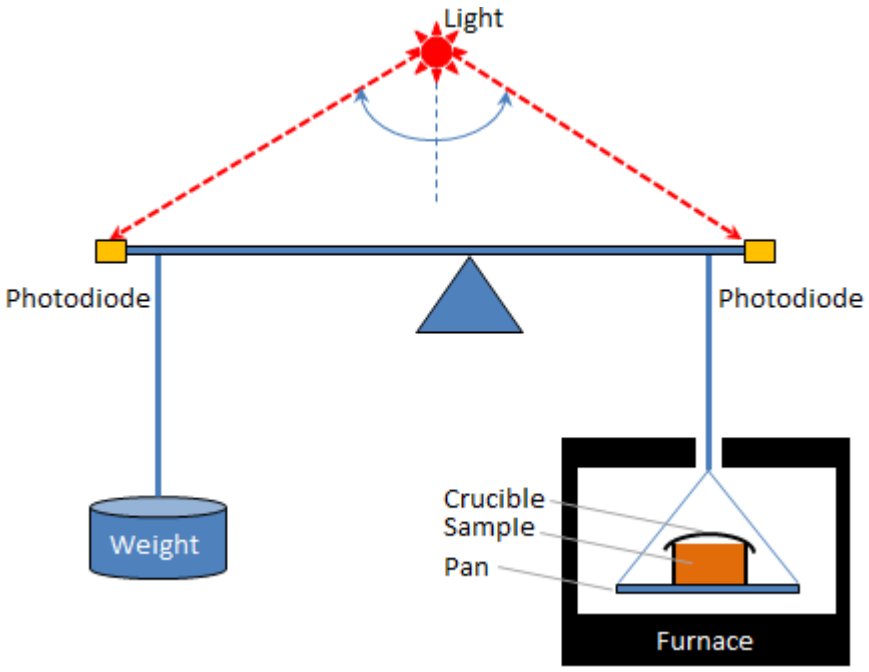

Figure 3-7 Schematic drawing of a thermobalance in TGA. Adapted from [68].

The property of thermal resistance of an epoxy resin is crucial for the PCB industry since PCBs have to endure extreme thermal histories such as the reflow process during manufacturing and harsh environmental thermal stresses in service. The degradation kinetic study is therefore important because it can be used to predict the PCB lifetime or the time to a certain conversion degree at given non-/isothermal temperatures. Similar to the curing kinetics, both dynamic and isothermal heating methods can be utilized. However, there are two different ways to define the conversion degradation degree α [67, 69]:

$$\alpha = \frac{m_0 - m}{m_0 - m_f}$$

Equation 3-13

$$\alpha = \frac{m_0 - m}{m_0}$$

Equation 3-14

Where, m_0, m_f, m are the initial weight, final weight and weight at time t or temperature T as shown in Figure 3-6, [mg];

3.4 Model free kinetics (MFK)[1]

Thermal kinetics deals with the measurement of how fast a chemical reaction reaches equilibrium, i.e., the reactants change to products, assuming that the activation energy supplied to the reactants was enough to guarantee a forward reaction procedure. There are normally three major variables which have to be considered: the temperature T, the conversion degree α, and the pressure P. Putting all together, the reaction rate can be parameterized as follows [70]:

$$\frac{d\alpha}{dt} = \kappa(T)f(\alpha)h(P)$$

Equation 3-15

Equation 3-15 is a general description of the thermal kinetics. Depending on the application cases, it can be used for describing the polymerization process of an epoxy resin as well as the decomposition process of a cured epoxy resin. In other words, α could be either the transformation extent of the reaction heat measured in DSC or the mass loss in TGA.

However, in this present work, the pressure will not be taken into account for the following reasons:

1) The polymerization of the epoxy used here was mainly solid-to-solid, there was a certain outgassing/ gaseous product but at a very low level (<0.5%wt);
2) All the thermal kinetics related experiments were performed in a normal DSC/TGA at atmospheric pressure;
3) All the DSC samples were sealed in the aluminum crucibles with a hole in the lids, the outgassing/gaseous product could be released during the reaction.
4) Although the applied pressure in the lamination process will accelerate the reaction in the viscosity-controlled region and will decelerate it in the diffusion-controlled region [39], it is generally acceptable in the PCB industry to study the curing kinetics without applied pressure for the lamination process.

Hence, simply taking away the pressure part, Equation 3-15 is rewritten to represent a single-step reaction as follows:

$$\frac{d\alpha}{dt} = \kappa(T)f(\alpha)$$

Equation 3-16

[1] This chapter and chapter 3.5 have been elaborated in the author's paper [109] during his PhD study.

The temperature dependency of the conversion rate is depicted by the rate constant κ(T), and the conversion degree dependency by the so-called reaction model f(α). Typically κ(T) is expressed empirically by the Arrhenius equation, and then Equation 3-16 is written as:

$$\frac{d\alpha}{dt} = \mathrm{A}e^{-\frac{E_a}{RT}}f(\alpha)$$

Equation 3-17

Where, A is the pre-exponential factor, [1/s];
E_a is the activation energy, [J/mol];
R is the gas constant, 8.31446 [J/mol/K];
T is the temperature, [K].

These three components A, E_a and f(α) in Equation 3-17 are called the "kinetic triplet" [70, 71]. A can be considered as the total number of collisions (leading to a reaction or not) per second in a chemical reaction [72] and $e^{-\frac{E_a}{RT}}$ the probability that such collisions will lead to a reaction. Therefore, increasing the temperature and/or decreasing the activation energy will result in an increase in reaction rate.

In terms of f(α), many different reaction models are available, such as n-th order $(1-\alpha)^n$, power law $\alpha^{(n-1)/n}$ and Prout-Thompkins $\alpha^m(1-\alpha)^n$, etc [73]. The traditional model-fitting analysis forces the experimental data to fit certain assumed models, which has intrinsic flaws to develop authentic models regardless of how well the goodness-of-fit is. Vyazovkin and Wight compared the Arrhenius parameters, based on 12 different models for the thermal decomposition of ammonium dinitramide (AND) [71]: 1) for the isothermal decomposition, both A and E_a were almost independent of the reaction model applied; 2) for the non-isothermal case, both exhibited a strong dependence on the models. Nevertheless, in all cases, the goodness-of-fit was quite high, most were higher than 0.99 and the worst case was 0.9783. That means, the model fitting approach is unable to determine the reaction model uniquely.

Therefore, in this study, the only feasible alternative was the model-free or iso-conversional kinetics approach, which assumes that the reaction rate at a constant extent of conversion is only a function of temperature. This approach can be derived from Equation 3-17 by taking the logarithm derivative at a constant α [70]:

$$\left(\frac{dln\left(\frac{d\alpha}{dt}\right)}{d\left(\frac{1}{T}\right)}\right)_{\alpha} = -\frac{E_\alpha}{R}$$

Equation 3-18

Obviously, the first step was to acquire the activation energy at each corresponding conversion degree in order to apply the iso-conversional method according to Equation 3-18. Hence the heating rate $\beta = \frac{dT}{dt}$ was defined and the rate of reaction was rewritten as $\beta \frac{d\alpha}{dT}$. And then taking the natural logarithm on both sides of Equation 3-17, the Ozawa-Flynn-Wall Equation is obtained:

$$ln\,\beta = \left(-\frac{E_\alpha}{R}\right)\frac{1}{T} + \left[lnA + lnf(\alpha) - ln\left(\frac{d\alpha}{dT}\right)\right]$$

Equation 3-19

Given a set of non-isothermal experiments, the conversion degree (α_i) at each heating rate (β_j) and its corresponding temperature (T) can be obtained according to Equation 3-8 and Figure 3-3(a). By fitting the lnβ-(1/T) plots with linear least squares regression, the slope ($-E_a/R$) at each α_i can be drawn and consequently E_a, as shown in Figure 3-8:

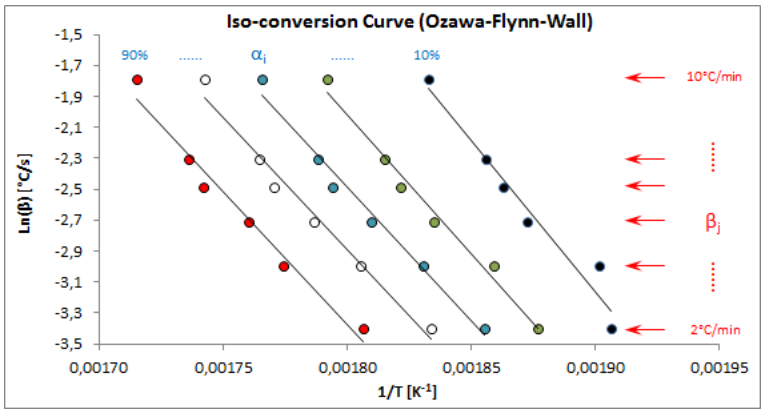

Figure 3-8 Iso-conversion curve for calculating the activation energy E_a

Back to Equation 3-17, it could be rearranged into the forms of isothermal and non-isothermal heating. Let us consider an infinitesimal development of the conversion degree from α_i to α_{i+1} in a time span of Δt_i:

1) Isothermal condition with the temperature T_{iso}

$$\int_{\alpha_i}^{\alpha_{i+1}} \frac{1}{f(\alpha)} d\alpha = \left(Ae^{-\frac{E_\alpha}{RT_{iso}}}\right)\Delta t_i$$

Equation 3-20

2) Non-isothermal condition with a corresponding temperature increase from T_i to T_{i+1}

$$\int_{\alpha_i}^{\alpha_{i+1}} \frac{1}{f(\alpha)} d\alpha = \frac{A}{\beta}\int_{T_i}^{T_{i+1}} e^{-\frac{E_\alpha}{RT}} dT$$

Equation 3-21

Equating the right terms of Equation 3-20 and Equation 3-21 will yield:

$$\Delta t_i = \frac{\int_{T_i}^{T_{i+1}} e^{-\frac{E_\alpha}{RT}}\, dT}{\beta e^{-\frac{E_\alpha}{RT_{iso}}}}$$

Equation 3-22

Equation 3-22 was first derived by Vyazovkin and Lesnikovich [74]. It allows to compute the transient time for the evolution of the conversion degree at an arbitrary constant temperature T_{iso} without knowledge of the reaction model and the pre-exponential factor.

Even though the increment from α_i to α_{i+1} is quite small, averaging of the activation energy will offer a better approximation, i.e., E_α in Equation 3-22 could be replaced by $\frac{E_{\alpha_i}+E_{\alpha_{i+1}}}{2}$. Then we apply the trapezoidal rule to the integral term in Equation 3-22:

$$\Delta t_i \approx \frac{\left(e^{-\frac{E_{\alpha_i}+E_{\alpha_{i+1}}}{2RT_{i+1}}} + e^{-\frac{E_{\alpha_i}+E_{\alpha_{i+1}}}{2RT_i}}\right)(T_{i+1}-T_i)}{2\beta e^{-\frac{E_{\alpha_i}+E_{\alpha_{i+1}}}{2RT_{iso}}}}$$

Equation 3-23

Finally, let us consider m (normally, m = 4~6) times non-isothermal experiments with different heating rates, and denote the slope at α_i in the lnβ-(1/T) plots as B_i ($E_{\alpha_i} = -RB_i$). Then Equation 3-23 can be converted to:

$$\Delta t_i \approx \frac{1}{m}\sum_{j=1}^{m}\left\{\left[e^{\left[\frac{B_{i+1}+B_i}{2}\left(\frac{1}{T_{i+1,j}}-\frac{1}{T_{iso}}\right)\right]} + e^{\left[\frac{B_{i+1}+B_i}{2}\left(\frac{1}{T_{i,j}}-\frac{1}{T_{iso}}\right)\right]}\right]\left(\frac{T_{i+1,j}-T_{i,j}}{2\beta_j}\right)\right\}$$

Equation 3-24

3.5 Coupling of MFK and FEA

To implement Equation 3-24 in a finite element program, the conversion degree was equidistantly divided into 100 pieces, that means, the letter "i" is an integer between 0 and 100 and stands for i% of the conversion degree. Meanwhile, the time interval between i% and (i+1)% was denoted as Δt_i. A schematic diagram for the algorithm of the conversion degree is presented in Figure 3-9.

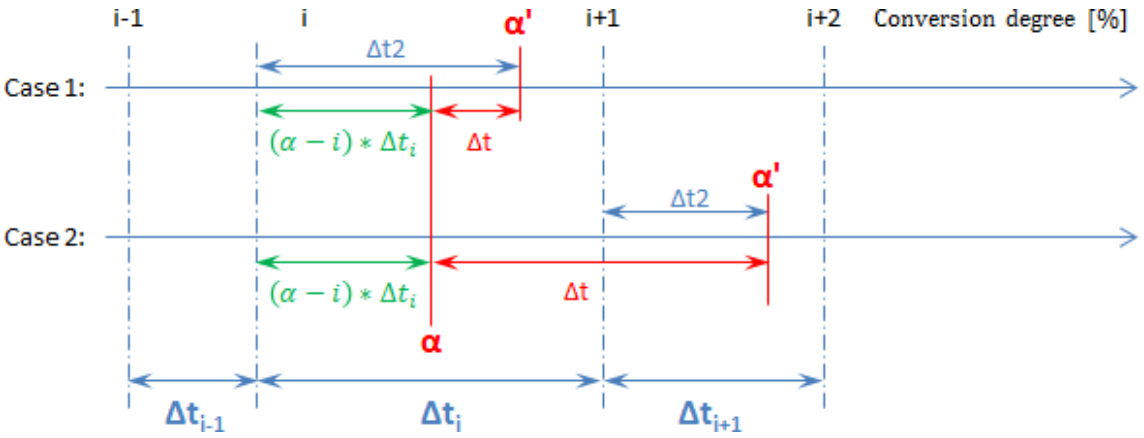

Figure 3-9 Schematic diagram for the algorithm of the conversion degree

Assume currently the conversion degree is α, which falls into the interval of [i, i+1]. In the next moment, the time increment is Δt, and the conversion degree is α'. If Δt2 is introduced as the time difference between the time at α' and the one at Int(α'), or the integer part of α', then by applying a linear interpolation:

$$\alpha' = i + \frac{\Delta t2}{\Delta t_i}$$

Equation 3-25

and:

$$\Delta t2 = (\alpha - i) * \Delta t_i + \Delta t - \sum_{j=0}^{n} \Delta t_{i+j}$$

Equation 3-26

In Equation 3-26, n should be taken in such a way that Δt2 can reach a minimum non-negative value. Replace Δt2 in Equation 3-25 by Equation 3-26:

$$\alpha' = \alpha + \frac{\Delta t - \sum_{j=0}^{n} \Delta t1_{i+j}}{\Delta t1_i}$$

Equation 3-27

The next step is to calculate the internal heat generated due to the evolution of the curing at this increment. From the above-mentioned DSC runs, the total enthalpy of reaction H_T is known, for simplicity, we took 1% of H_T, δH, for the calculation of the volumetric heat flux r by applying the linear interpolation rule:

$$r = \frac{\alpha' - \alpha}{\Delta t} * \rho * \delta H$$

Equation 3-28

Where, r is the volumetric heat flux, [J/s/m^3]

ρ is the density of the resin, [kg/m^3]

δH is 1% of the total reaction energy, [J/kg]

The numerical algorithm was implemented in the Abaqus® finite element software by utilizing two of its user subroutines and one external subroutine with the strategy shown in Figure 3-10.

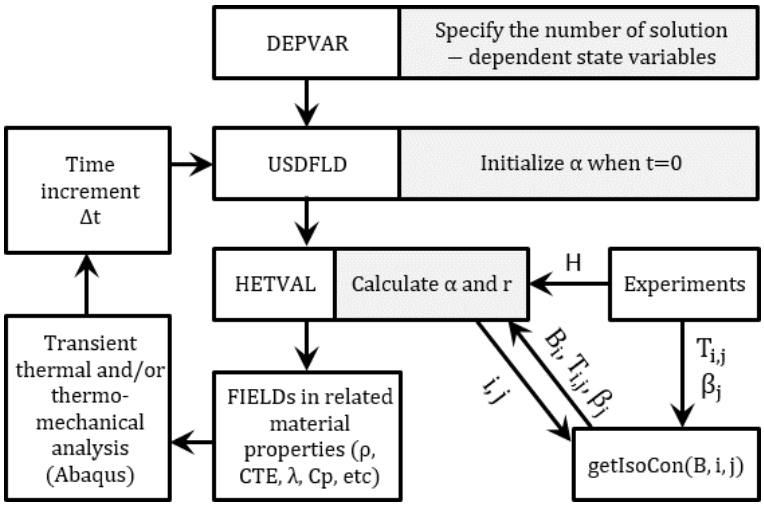

Figure 3-10 Strategy for the implementation of the subroutines

During simulation, subroutine USDFLD is called first to initialize α and then HETVAL to update α and calculate the heat flux, meanwhile getIsoCon(B, i, j) will be called in HETVAL for Δt1:

1) User subroutine: USDFLD

   The main field variable to be defined here is the conversion degree, α, which is a governing parameter of the material properties. By adding a FIELD array for each related material property in Abaqus®, it is possible to consider the property evolutions during simulation. Practically, the number of solution-dependent state variables has to be specified previously in the DEPVAR material behavior in Abaqus®, which is in this case, one variable. Afterwards, the variable STATEV(1) can be used for storing/updating the conversion degree and is available for both user subroutines. In USDFLD, it initializes α to zero at the starting point, since we consider the status of the as-received prepregs is considered as 0% cured. Furthermore, no material property is linked to the conversion degree at the moment owing to the lack of experimental data. However, this work offers an opportunity so that, depending on the application cases and the availability of the material properties, the modulus, CTE, specific heat,

thermal conductivity and even the chemical shrinkage during polymerization can all be considered as conversion-degree dependent.

2) User subroutine: HETVAL

   This subroutine is utilized to define the heat flux due to the thermosetting reaction at each material calculation point and the variable FLUX(1) in Abaqus® is used for its storing/updating. Since the heat generation is proportional to the change of the conversion degree, as implied by Equation 3-28, both STATEV(1) and FLUX(1) will be updated at each time increment.

3) External subroutine: getIsoCon(B, i, j)

   This subroutine is used for storing the experimental data acquired from the non-isothermal DSC runs, i.e., the heating rates of the j-th DSC run β_j and the temperature $T_{i,j}$ at the i% conversion degree of the j-th DSC run; and solving the slope B_i at the i% conversion degree in the iso-conversion curve using a least squares fit:

$$B_i = \frac{m \cdot \overline{\left(\frac{1}{T_{i,J}}\right)} \cdot \overline{(ln\beta_j)} - \sum_{j=1}^{m}\left(\frac{1}{T_{i,j}} \cdot ln\beta_j\right)}{m \cdot \left(\overline{\frac{1}{T_{i,J}}}\right)^2 - \sum_{j=1}^{m}\left(\frac{1}{T_{i,j}}\right)^2}$$

Equation 3-29

   Where: m is the number of the non-isothermal DSC runs, normally m=4 – 6.

The flowchart for the implementation of these subroutines is presented in Figure 3-11.

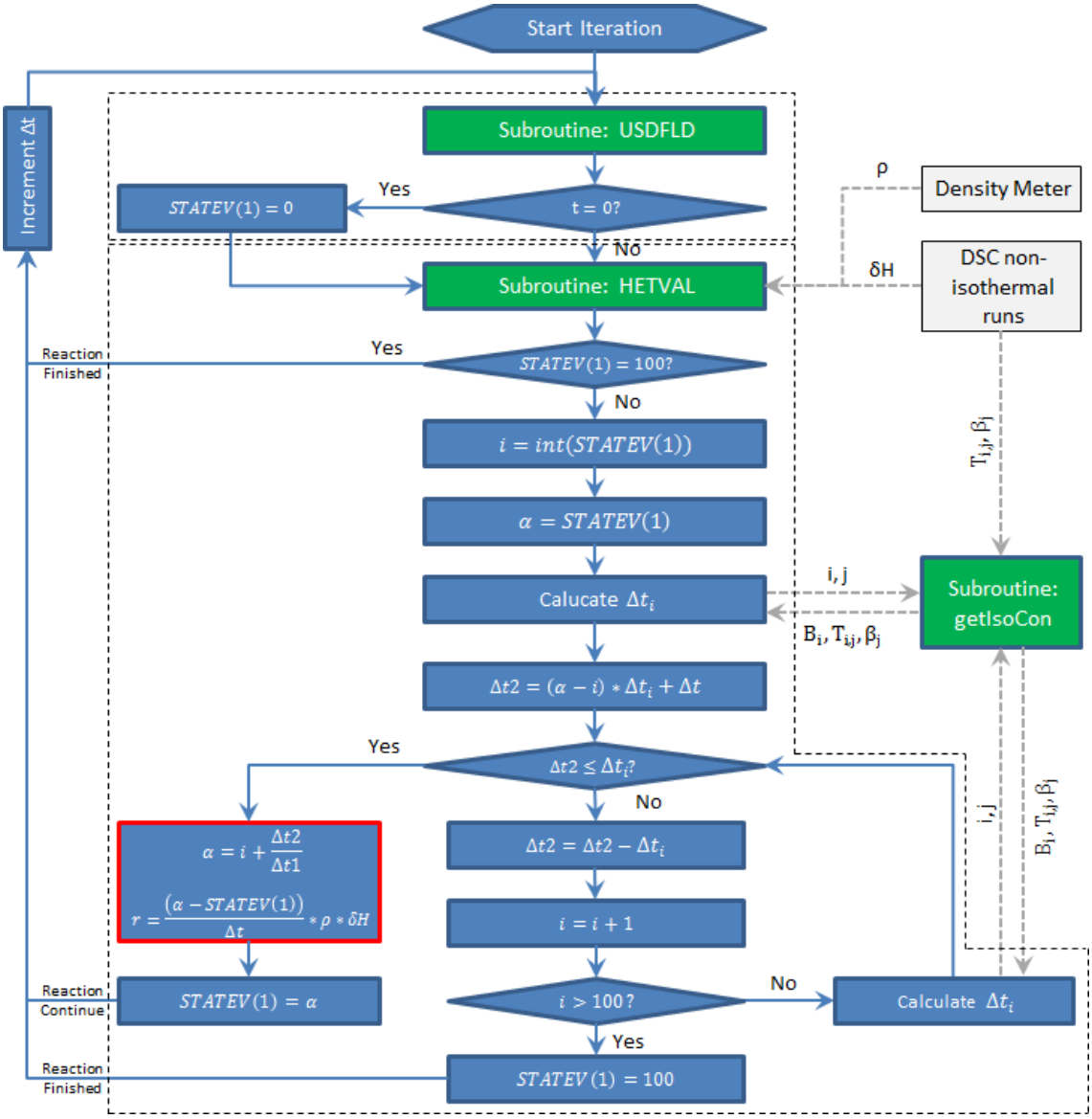

Figure 3-11 Flowchart for the implementation of the subroutines

Another key point that has to be emphasized in terms of the application of the subroutines is the time increment Δt: it must be relatively small, for example 1 sec, for the epoxy resin used in this study. As implied by the term of T_{iso} in Equation 3-24, the solution is principally only applicable for the case of isothermal heating. If we apply it for predicting the non-isothermal case, the smaller time increment will provide a better approximation. Indeed, the solution for the single step non-isothermal heating with a fixed heating rate β can directly be drawn from the iso-conversion curve (refer to Figure 3-8) and used for the simulation:

$$T_i = \frac{B_i}{ln\beta - C_i}$$

Equation 3-30

However the utilization of Equation 3-30 is limited, since it is only valid for a single step non-isothermal heating case. As shown in Figure 3-12, the expected heating rate in the ramp-up stage meets the prerequisite of using Equation 3-30, but the real measured temperature profiles will never be a single step heating due to the medium between the heating plate and the pressed resin, such as the paper cushion used for stabilizing the contacts. Very often the known condition is the setting profile of the heating plate in a press book, which is also not a single step.

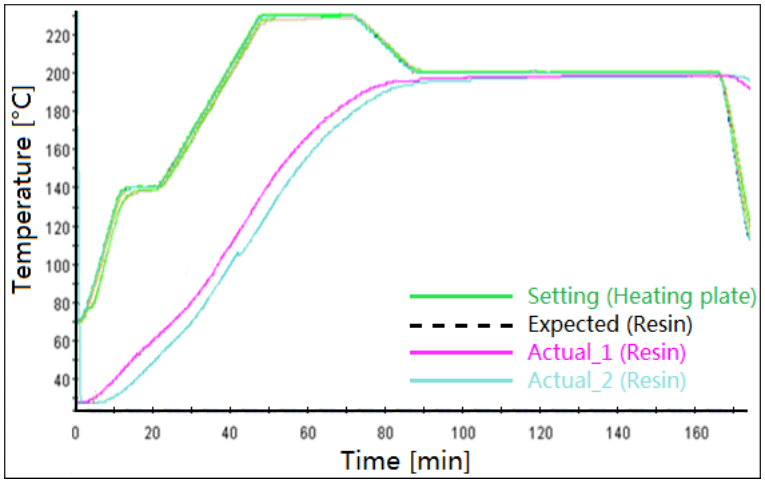

Figure 3-12 Temperature setting vs. actual profiles in a press book

3.6 Delamination kinetics by fracture

The monotonic tensile test measures the material properties regarding tensile strength, elastic modulus, failure stress/strain, etc. in the light of ASTM [75] or ISO [76] standards. The tested general deformation behavior of the materials is traditionally used for designing a structure or for material selection. However, the performance of the engineering materials in service normally cannot reach their theoretical yield or tensile strengths which are determined from these laboratory tests, due to several factors such as inherent material properties, loading and environmental conditions [77]. Therefore, the fracture mechanics approach utilizes flaw size and fracture toughness, instead of yield or tensile strength for failure prediction. The comparison of both approaches is shown in Figure 3-13.

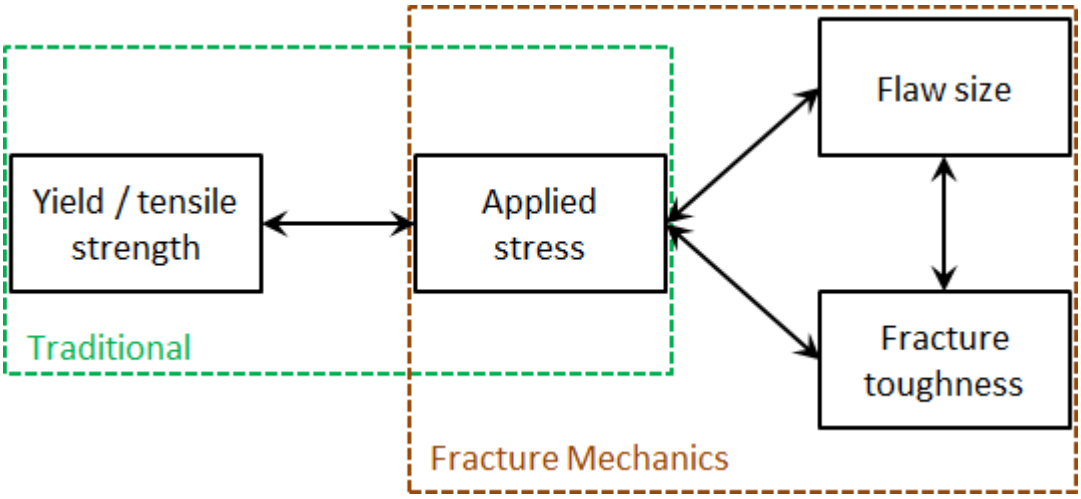

Figure 3-13 Traditional and fracture mechanics approaches for structure design or material selection. Adapted from [78].

Toughness is the energy absorbed by the material during deformation before failure. A material with high strength or ductility alone does not make it tough. The key to toughness is a good combination of both strength and ductility. In polymer science, it is usually defined as the energy required for the crack to grow and create an increase in the surface area of cracked material. [79] Energy balance criterion and the stress intensity approach are the two alternative approaches to fracture analysis.

In terms of the frequently encountered fact that the fracture strength is always lower than the theoretical cohesive strength, Griffith explained that the discrepancy is due to the inherent defects in brittle materials which lower the fracture strength of the materials and suggested two necessary conditions for crack growth [80]:

1) The applied stress must be sufficient to stress the bonds at the crack tip to the point of failure.
2) The strain energy released by an increment of crack extension must be equal to or exceed the required energy for generating two new crack surfaces. It might be expressed mathematically as:

$$\frac{dU_s}{da} \geq \frac{dU_\gamma}{da}$$

Equation 3-31

Where, U_s is the strain energy, [J/m];

U_γ is the surface energy, [J/m];

da is the crack length increment, [m].

If a remote tensile stress $\sigma_a$is applied to an infinite plate of unit width which contains a very narrow elliptical crack of a length of 2a in the middle, the strain energy released is [81]:

$$U_s = \frac{\pi \sigma_a^2 a^2}{E}$$

Equation 3-32

Let γ be the fracture surface energy of the plate, the surface energy of the two new opened surfaces with length 2a can be then expressed as:

$$U_\gamma = 4\gamma a$$

Equation 3-33

Thus, putting Equation 3-32 and Equation 3-33 into Equation 3-31, the well-known Griffith criterion for crack growth can be deduced as shown below in [80]:

$$\frac{\pi \sigma_a^2 a}{E} \geq 2\gamma$$

Equation 3-34

The left side in Equation 3-14 is defined as being equal to the strain energy release rate per crack tip:

$$G = \frac{\pi \sigma_a^2 a}{E}$$

Equation 3-35

The Griffith equation shows that doubling the applied stress has the same effect of increasing the crack length by 4 times. Griffith also presented good agreement between this theory and experimental results on glass [81]. However, the prediction could not be applied to not ideally brittle materials, such as metals, since the observed fracture stresses were much higher. Therefore, Orowan proposed to replace the 2γ in Equation 3-34 by the critical strain energy release rate per crack tip, Gc, which takes into account plastic deformation [82]. Accordingly, Equation 3-34 is modified to be:

$$\frac{\pi \sigma_a^2 a}{E} \geq G_c$$

Equation 3-36

The stress intensity factor K, which was developed in 1957 by G. R. Irwin [83], is one of the most fundamental and useful parameters in fracture mechanics, since it completely defines the crack tip conditions. That means it is possible to solve for all components of stress, strain and displacement as a function of the position relative to the crack tip. Irwin's near crack tip solution is an approximation to Westergaard's complete solution [84] for the stress field surrounding a crack if the element in an elastic material is near the tip of a crack as shown in Figure 3-14.

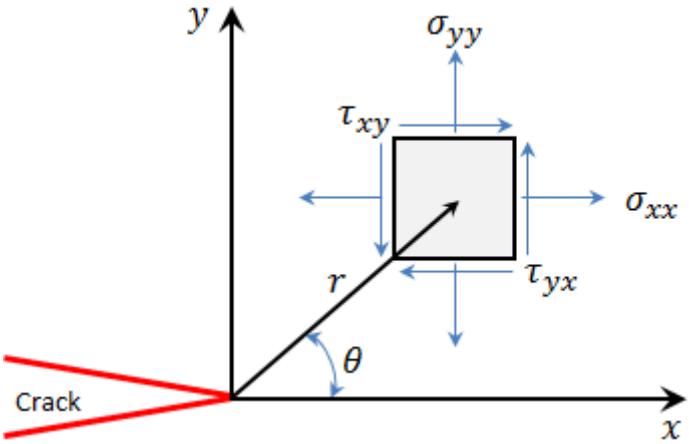

Figure 3-14 Stresses acting on an element close to the tip of a crack

In terms of a straight double-ended crack in an infinite solid, the stress components in Figure 3-14 can be expressed as:

$$\begin{cases} \sigma_{xx} = \dfrac{\sigma_a\sqrt{\pi a}}{\sqrt{2\pi r}}\cos\dfrac{\theta}{2} = \left(1 - sin\dfrac{\theta}{2}sin\dfrac{3\theta}{2}\right) \\ \sigma_{yy} = \dfrac{\sigma_a\sqrt{\pi a}}{\sqrt{2\pi r}}\cos\dfrac{\theta}{2} = \left(1 + sin\dfrac{\theta}{2}sin\dfrac{3\theta}{2}\right) \\ \tau_{xy} = \dfrac{\sigma_a\sqrt{\pi a}}{\sqrt{2\pi r}}\cos\dfrac{\theta}{2}sin\dfrac{\theta}{2}cos\dfrac{3\theta}{2} \end{cases}$$

Equation 3-37

The stress intensity factor in this case is defined as:

$$K_I = \sigma_a\sqrt{\pi a}$$

Equation 3-38

A clear relationship between K_I and G can be found by comparing Equation 3-35 and Equation 3-38:

$$G = \frac{K_I^2}{E}$$

Equation 3-39

Thus, the energy balance criterion and the stress intensity approach are essentially equivalent for linear elastic materials. At the onset of a crack extension, K_I is normally denoted by K_{Ic}. The subscript I in K_I is associated with tensile loading (Mode I), which is one of the three basic loading modes in linear elastic fracture mechanics (LEFM) that can cause crack growth [80]. Figure 3-15 shows the three basic loading modes.

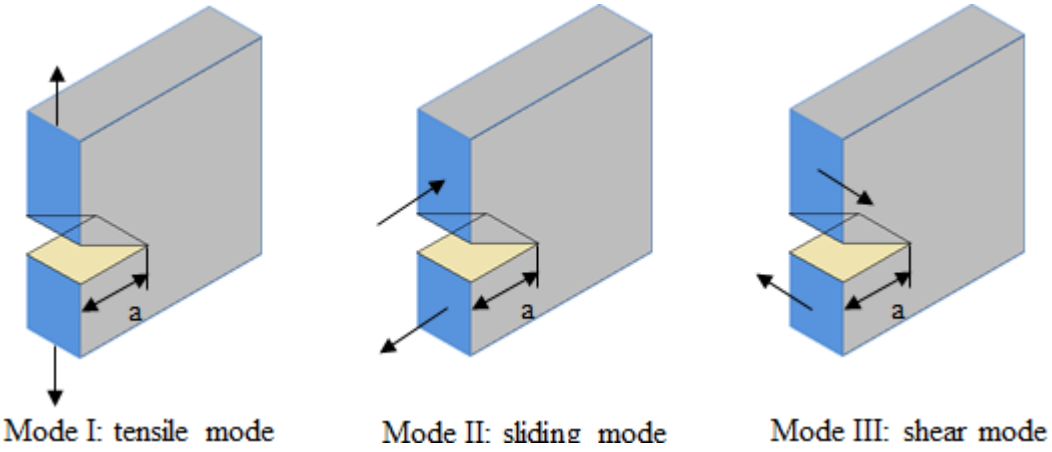

Figure 3-15 Three basic loading modes in LEFM

Many different experimental techniques can be used to characterize the fracture toughness of epoxy resins. One of them is the compact tension (CT) testing coupon according to ASTM standard [85] as presented in Figure 3-16. Its toughness in terms of critical stress intensity factor at fracture initiation is given by:

$$K_{Ic} = \frac{P_{max}}{B\sqrt{W}}\left[\frac{2+\alpha}{(1-\alpha)^{1.5}}(0.886 + 4.64\alpha - 13.32\alpha^2 + 14.72\alpha^3 - 5.6\alpha^4)\right]$$

Equation 3-40

Where, K_{Ic} is the plane-strain fracture toughness, [MPa·m$^{1/2}$]

P_{max} is the maximum load during test, [N];

α is the ratio a_0/W, [-];

a_0 is the initial crack length, [m];

B, W are the dimensions of specimen in Figure 3-16, [m].

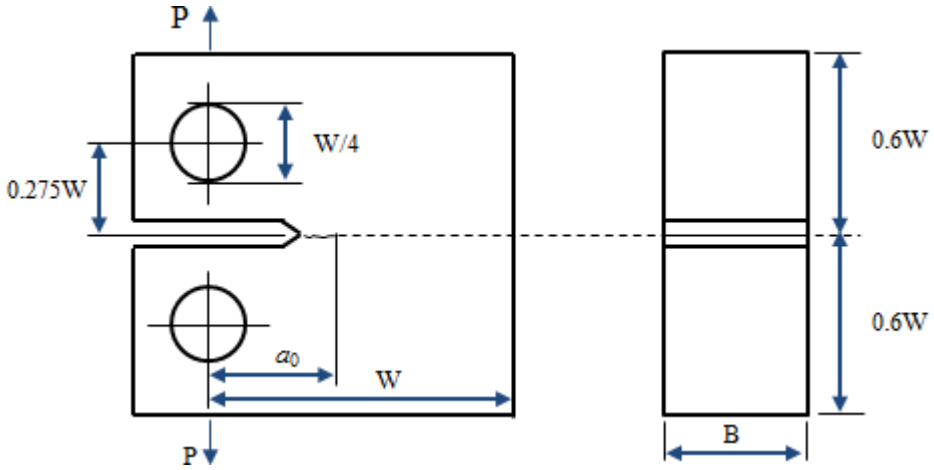

Figure 3-16 CT specimen according to ASTM standard

K_{Ic} is an important factor for quantifying the reliability and crack extension conditions of existing cracks. However, cyclic loads can cause crack extension at K values less than K_{Ic}. Epoxy resins usually perform under cyclic loading at various stress amplitudes and mean stresses during service.

For linear-elastic materials, the stress intensity factor range (ΔK) can be used to characterize the fatigue crack growth rate under cyclic loading. Based on ASTM E647 (Standard Test Method for Measurement of Fatigue Crack Growth Rates), ΔK of a CT specimen is given by:

$$\Delta K = \frac{\Delta P}{B\sqrt{W}}\left[\frac{2+\alpha}{(1-\alpha)^{1.5}}(0.886 + 4.64\alpha - 13.32\alpha^2 + 14.72\alpha^3 - 5.6\alpha^4)\right]$$

Equation 3-41

Where, $\Delta P (= P_{max} - P_{min})$ is the loading range, [N];

α, B, W are the same as in Equation 3-40.

The double cantilever beam (DCB) specimen is one of the most commonly used types for determining mode I interlaminar fracture toughness of fiber reinforced composite materials [86, 87, 88], because delamination is often caused by interlaminar normal (peel) stress, rather than interlaminar shear stress [86].

Figure 3-17 shows the dimensions of the DCB used in this study according to the ASTM standard [89]. Two plies of prepreg sample sheets are placed in the middle of two cores. Meanwhile, a Teflon® film is inserted into the 2 layers of the prepregs so that a precrack can be introduced after lamination.

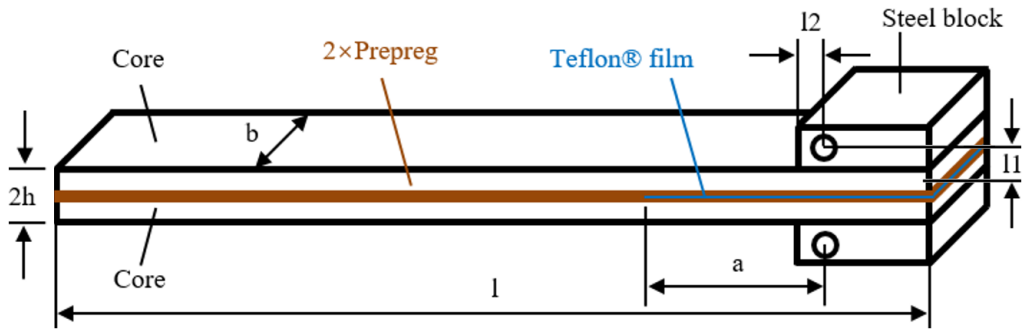

Figure 3-17 DCB specimen according to ASTM standard

The monotonic and cyclic DCB test procedures are described in the ASTM standards [89] and [90] respectively. Equation 3-42 to Equation 3-47 are used for calculating the fracture toughness, G_{Ic}, in terms of the beam theory (BT), corrected beam theory (CBT) and modified compliance calibration (MCC). The compliance C can be directly calculated from the force P and the displacement δ which are recorded by the test device. Crack length a is manually measured by suspending the test at certain checking points. The sample width b, sample height 2h, sample length l, distance from loading block pin to center line of top specimen arm l1, and half width of loading block l2 are the dimensions marked in Figure 3-17. F is a correction factor for large displacements and N is a correction factor for load blocks (as they lead to falsified stiffness), Δ is a correction factor for the parabolic shape of the plastic zone (and therefore a correction factor of the crack length).

The detailed procedure for calculating the G_{Ic} for the monotonic DCB test is displayed in Figure 3-18. The parameters listed in the parentheses are the ones required for calculating the corresponding variables. In terms of the cyclic DCB test, the number of manually recorded crack lengths is limited since the tests normally take days to complete. Therefore, the compliance calibration (CC) is applied to relate the compliances, which are calculated by those automatically recorded P and δ, to the crack length as shown in Figure 3-19. Afterwards, the same procedure as shown in Figure 3-18 can be utilized for calculating the G_{Ic} for the cyclic DCB test.

$$C = \frac{\delta}{P}$$

Equation 3-42

$$F = 1 - 0.3\left(\frac{\delta}{a}\right)^2 - 1.5\left(\frac{\delta l_1}{a^2}\right)$$

Equation 3-43

$$N = 1 - \left(\frac{l_2}{a}\right)^3 - \frac{9}{8}\left[1 - \left(\frac{l_2}{a}\right)^2\right]\frac{\delta l_1}{a^2} - \frac{9}{35}\left(\frac{\delta}{a}\right)^2$$

Equation 3-44

$$G_{Ic} = \frac{3P\delta}{2ba} \dots\dots (BT)$$

Equation 3-45

$$G_{Ic} = \frac{3P\delta}{2b(a+\Delta)}\frac{F}{N} \dots\dots (CBT)$$

Equation 3-46

$$G_{Ic} = \frac{3m_2}{2(2h)}\left(\frac{P}{b}\right)^2\left(\frac{bC}{N}\right)^{\frac{2}{3}} F \dots\dots (MCC)$$

Equation 3-47

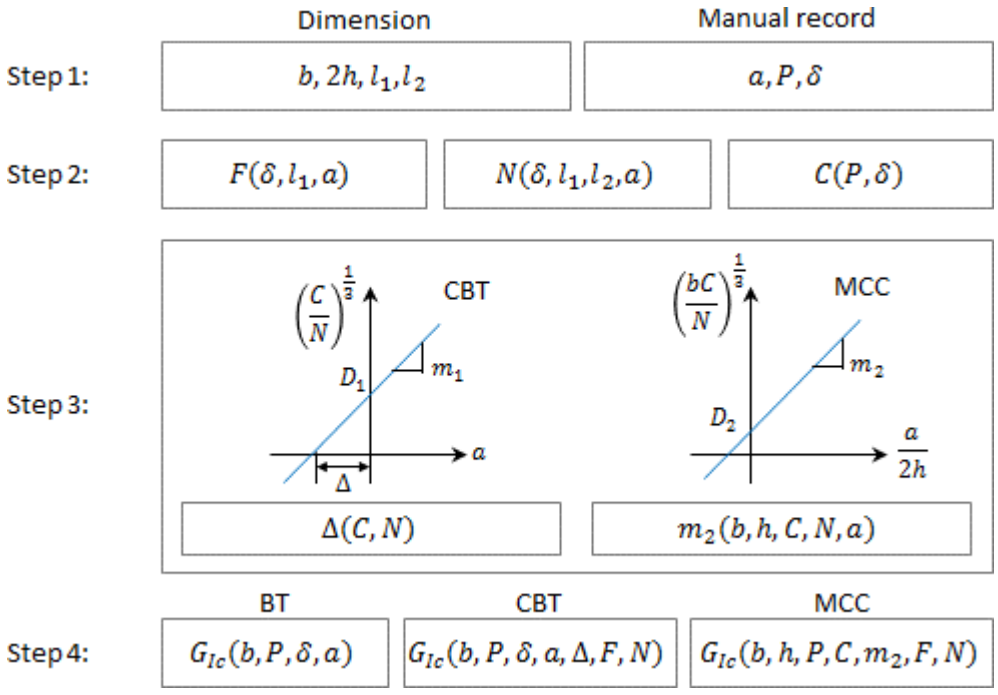

Figure 3-18 Procedure for calculating G_{Ic} for monotonic DCB test

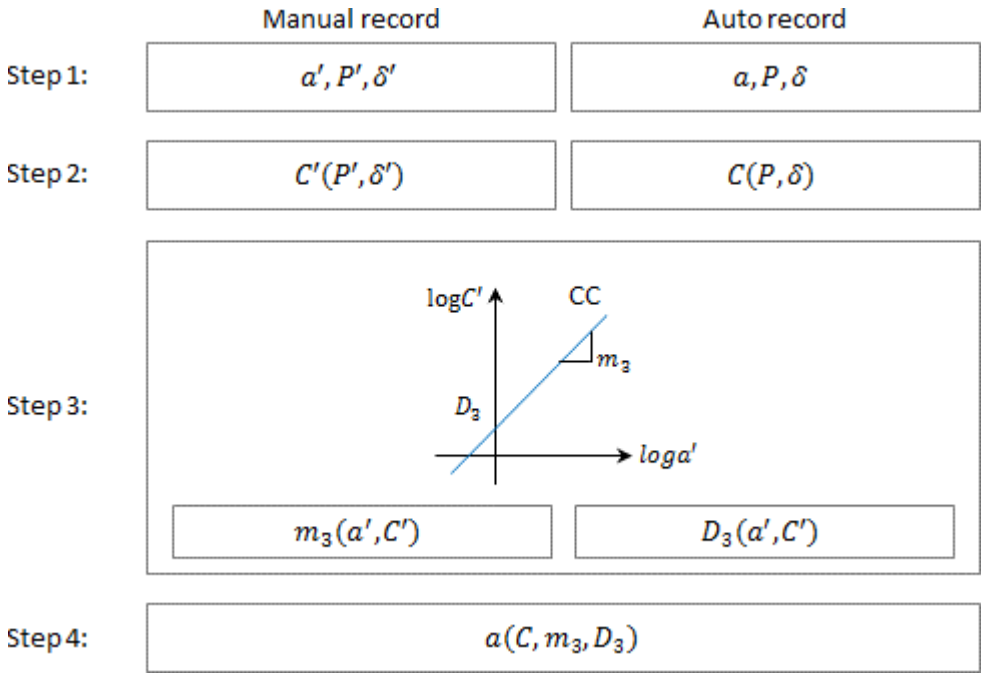

Figure 3-19 Procedure for calculating crack length for cyclic DCB test

The data obtained from the test machine normally needs to be reduced. A different algorithm was developed and implemented in an excel-based software in this study: First, the number of data points per fitting, n, should be defined. For example, n=8 as shown in Figure 3-20. Second, the quadratic fitting rule will be applied for each set of data points. But there will be an overlap of 25% of the data points for the adjacent two sets. (2 data points will be the common ones in case of n=8). Third, the fitted data will be recorded from the first set to the last. But except for the last one, only the first 75% of the fitted data points will be used (the first 6 will be used in case of n=8).

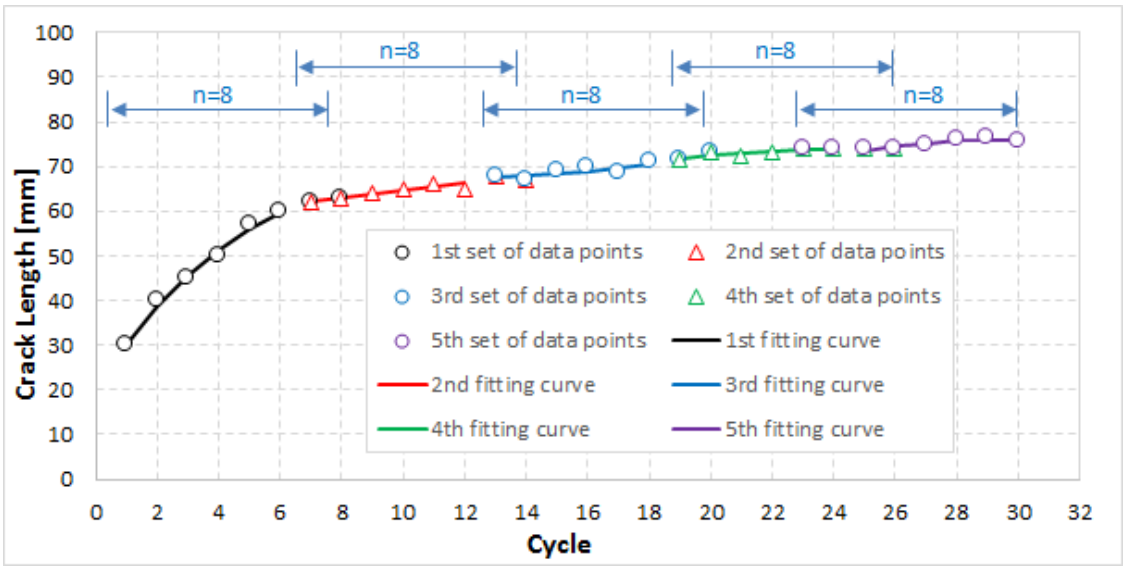

Figure 3-20 Example of data reduction for calculating crack growth rate (da/dN)

Moreover, considering that the crack grows very fast at the beginning of the test and tends to be constant at the end, because the driving force in the DCB configuration decreases with crack growth in the displacement controlled mode, the value of n should be smaller at the beginning and could be greater when the crack growth rate (da/dN) is stable. And in fact, relatively more data points to be fitted in one set can reduce the data noise as well. Therefore, in this algorithm, a second parameter, m, needs to be specified. That means the fitting will be processed m times with a number of n data points. Afterwards, n will be doubled and m will be halved. An example is given in Figure 3-21: the raw data is crack length a vs. cycle N (grey curve). The fitting curve (red) is obtained with n=7 and m=64. The fitting is very successful because the noise at the end of the raw data is eliminated. Subsequently the da/dN vs. N (light green) is obtained based on the red curve. Since the raw da/dN curve contains much noise before the crack growth rate becomes stable, a fitting with n=7 and m=1 is applied and the green curve shows the result. Finally, Figure 3-22 presents a comparison between the one with the fitting procedure applied to the raw da/dN curve and the one without. The effect is obvious; the tendency of the delamination growth rate can only be seen on the curve with the fitting procedure.

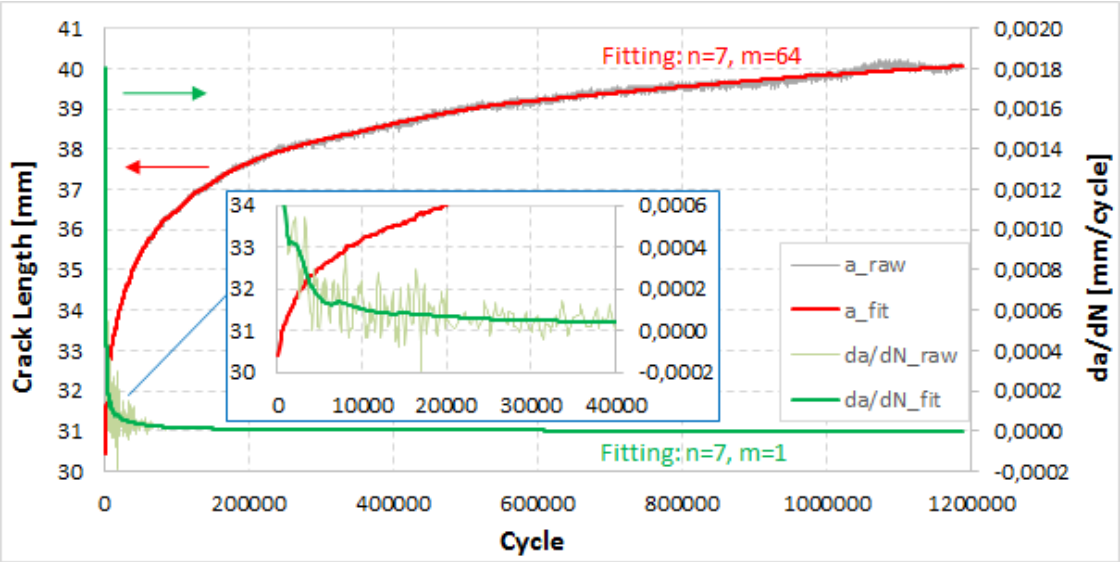

Figure 3-21 Example of data reduction for calculating crack growth rate (da/dN)

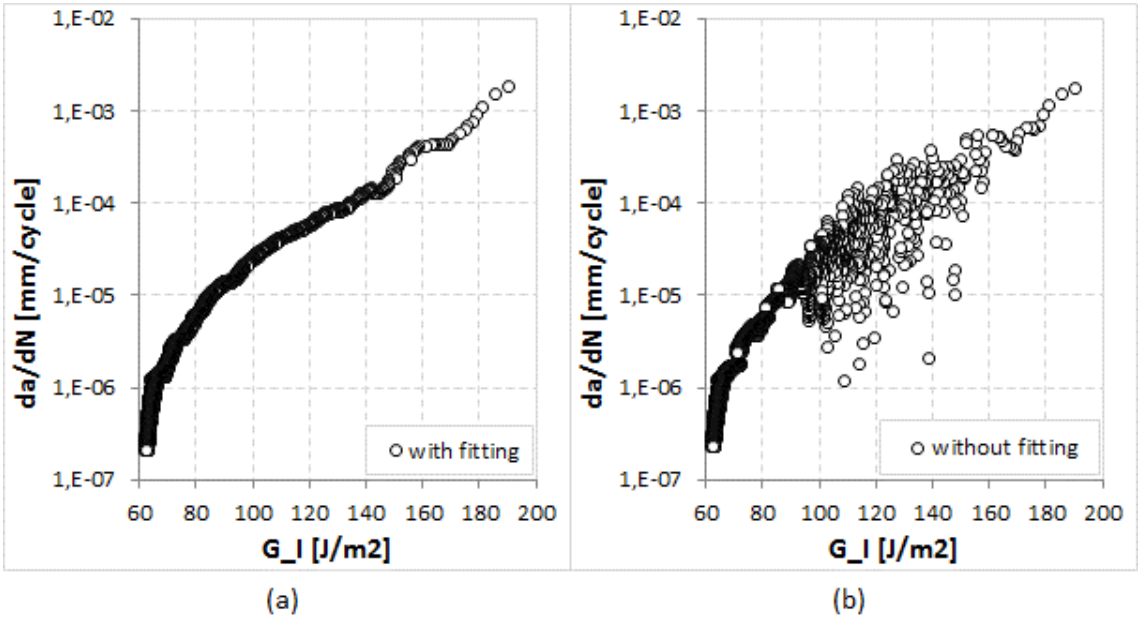

Figure 3-22 Example of data reduction for calculating crack growth rate (da/dN): (a) with the fitting procedure and (b) without the fitting procedure

4 Experiments

One purpose of this study was to evaluate how much the press cycle time of a commercial prepreg, CE688, can be reduced without or with acceptable negative subsequent influences on the reliability of the final products. Accordingly 4 steps were designed in order to achieve this goal: First, to figure out a reliable methodology to characterize the curing/decomposition kinetics of the epoxy resin based on a model epoxy resin which consists of chemical components similar to CE688, i.e., DICY-based epoxy resin system. Second, to study the curing/decomposition kinetics of the CE688 based on the fixed methodology. Third, to cure the CE688 prepregs with 3 different press cycle times (standard, -30min and -90min) according to the results of the kinetics study and afterwards certain reliability tests would be performed on these 3 groups of cured samples for the purpose of checking their thermal and fracture mechanic properties. Finally, a test PCB was designed according to the real product and 3 groups of such PCB were produced with 3 different press cycle times (standard, -30min and -60min) respectively. All these PCB samples were subjected to the standard reliability tests in line with the requirement of the PCB industry. Furthermore, in order to investigate the ageing effect, each group of the PCB samples was split into 2 parts: directly after pressing or as received and after 10x reflowed. For convenience, the samples are labelled, based on the curing and ageing conditions, as shown in Table 4-1.

Table 4-1 Sample labelling

Curing Condition			Model Resin	CE688		
				Resin Powder	Prepreg	PCB
DSC Cured			M	A	--	--
Press Book Cured	As received	Standard	--	A00	B00	C00
		-30 min	--	A30	B30	C30
		-60 min	--	A60	B60	C60
		-90 min	--	A90	B90	C90
	After 10x reflowed	Standard	--	A00R	B00R	C00R
		-30 min	--	A30R	B30R	C30R
		-60 min	--	A60R	B60R	C60R
		-90 min	--	A90R	B90R	C90R

4.1 Materials

4.1.1 Model epoxy resin

For a better understanding of the curing kinetics of the DICY-based epoxy resin system, a simple model epoxy resin system was designed which contains only DGEBA epoxy and DICY as hardener.

The liquid DGEBA (type: SE-187) was a kind of low chlorine (≤900ppm) epoxy with epoxy equivalent weight of 187g/eq and was supplied by Shin-A T&C Co., Ltd (Seoul, Korea). The very fine DICY powder (type: DicyanexTM 1400B curing agent; the approximate particle size was 1μm) was supplied by Air Products & Chemicals, Inc (Pennsylvania, USA). All reactants were used as received without further purification.

4.1.2 Commercial epoxy resin

The commercial CE688 epoxies were received in the form of prepreg (glass fiber type: #1080) and pure resin powder (except that the glass fiber is excluded, other components are identical to the prepreg) with a nominal DSC Tg of 150°C. Its pronounced absorbance bands at 2125–2225 cm^{-1} in the FTIR spectra, as shown in Figure 4-1, disappeared after the curing process. This indicates a high concentration of the functionality of N=C=N (near 2165 cm^{-1}) and cyano (near 2210 cm^{-1}), which means CE688 is dicyandiamide-epoxy resin system.

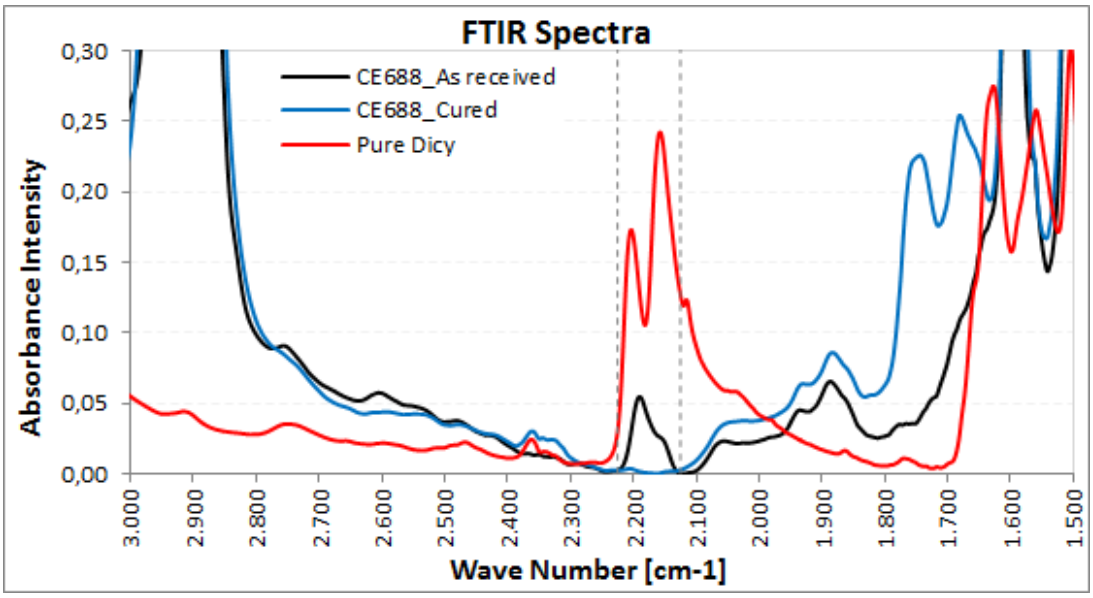

Figure 4-1 FTIR spectra of the pure DICY, fresh CE688 and cured CE688

4.2 Process conditions

As schematically presented in Figure 1-4 and Figure 1-5, a complete PCBA process consists of many processes, such as dry film lamination, exposure, developing, etching, lamination and reflow, etc. However, only the lamination and reflow processes are directly related to this study.

4.2.1 Lamination process

The standard curing condition of CE688, which is based on the suggested lamination program from the material supplier, is presented in Figure 4-2: a ramp-up from room temperature (RT) to 200°C with ~2.4°C/min heating rate and then 75min at 200°C followed by a slow cooling down to the RT with 2°C/min cooling rate. Meanwhile a pressure of 8.8MPa is slowly applied during the temperature ramp-up before the gelation and is released before the cooling process.

In the following experiments, only the holding time at 200°C was varied or reduced. The standard, 30min, 60min and 90min reduced press cycle program was recorded as Norm, -30m, -60m and -90m respectively.

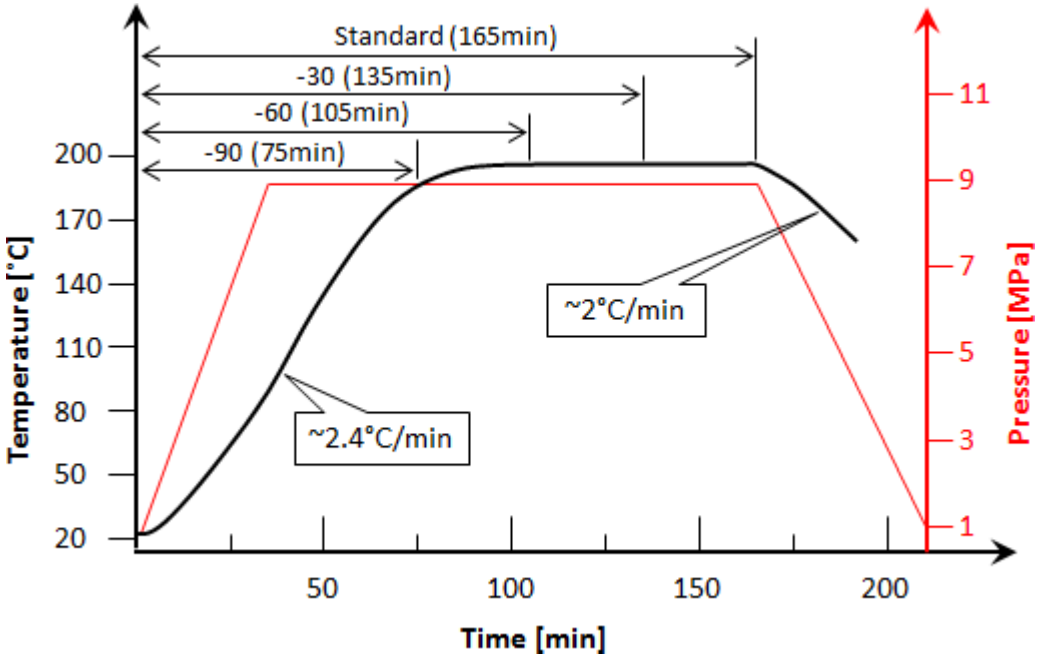

Figure 4-2 Schematic drawing of the lamination program

4.2.2 Reflow process

The lead-free reflow process as shown in Figure 4-3 was referred to IPC/JEDEC [7]. The total reflow time was a little bit more than 8 min with a peak temperature at 260°C. The cooling rate after the liquidous temperature was greater than 100°C/min.

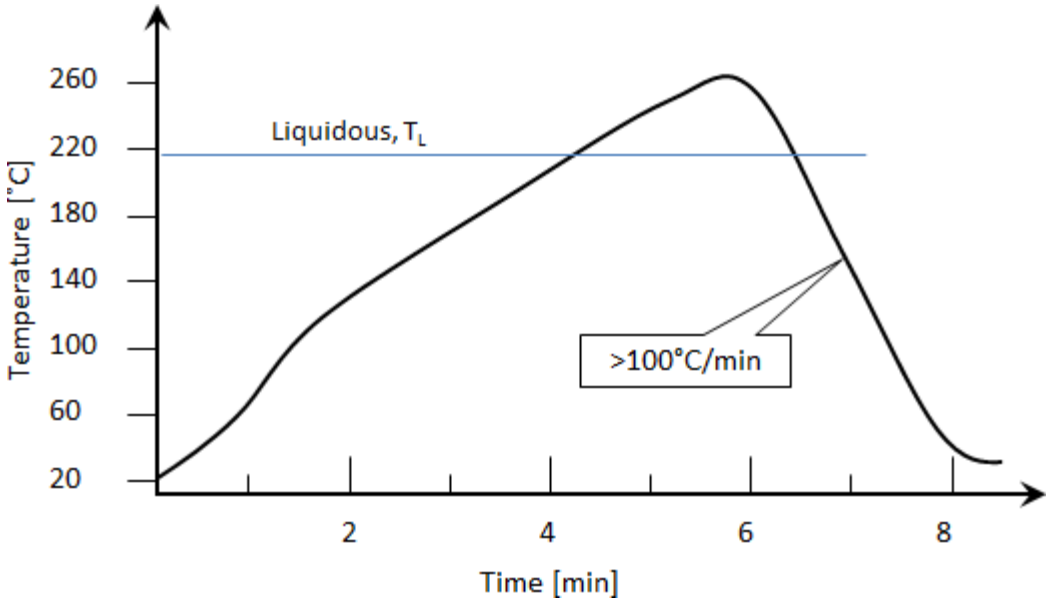

Figure 4-3 Schematic drawing of the lead-free reflow profile used in this study

4.3 Test coupons

The generalized methodologies described in Chapter 3 are not dependent on specific application cases, since they were all focused on the study of the material itself. Accordingly, the sample forms as well as their preparation were relatively simple. For example, in order to validate the predicted curing parameters via Tg measurements, only one time press was required for the sample preparation. However, the multiply layered PCBs required two or more press cycles. Whether these extra press cycles would influence the Tg values needed to be confirmed as well. Moreover, some properties can only be tested in the form of PCB. Such as the warpage performance which is relevant not only to the curing status but also to the copper ratio of each layer and the geometric symmetry of the PCB stack-up. Therefore, a commonly used 8-layer PCB design with 3x press cycle was chosen. Figure 4-4 depicts its stack-up: it starts with a core; each press cycle adds two more prepreg and copper layers. Meanwhile five test coupons according to the most important reliability tests, as shown in Figure 4-5, were chosen for the purpose of further validation: peel strength, delamination, IST (Interconnection Stress Test), HAST (Highly Accelerated Temperature and Humidity Stress Test) and warpage coupon.

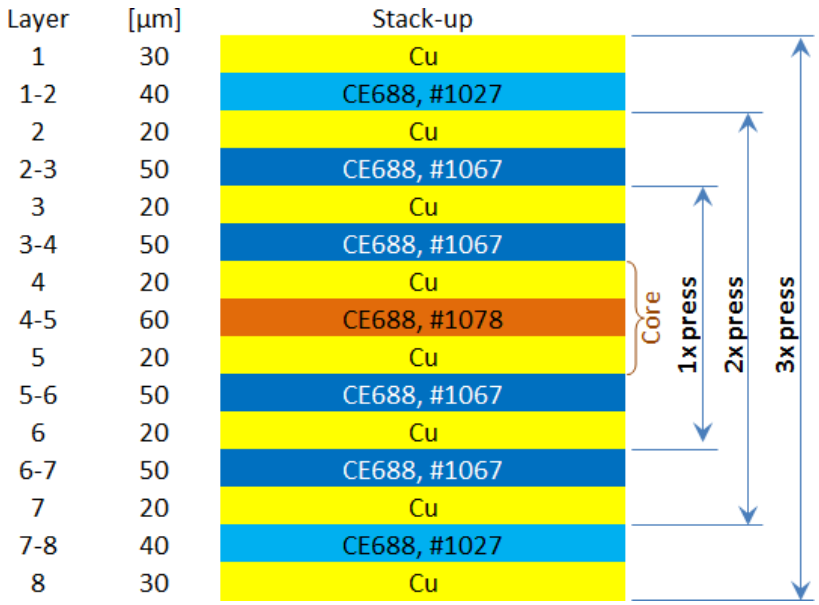

Figure 4-4 PCB stack-up and layer thickness

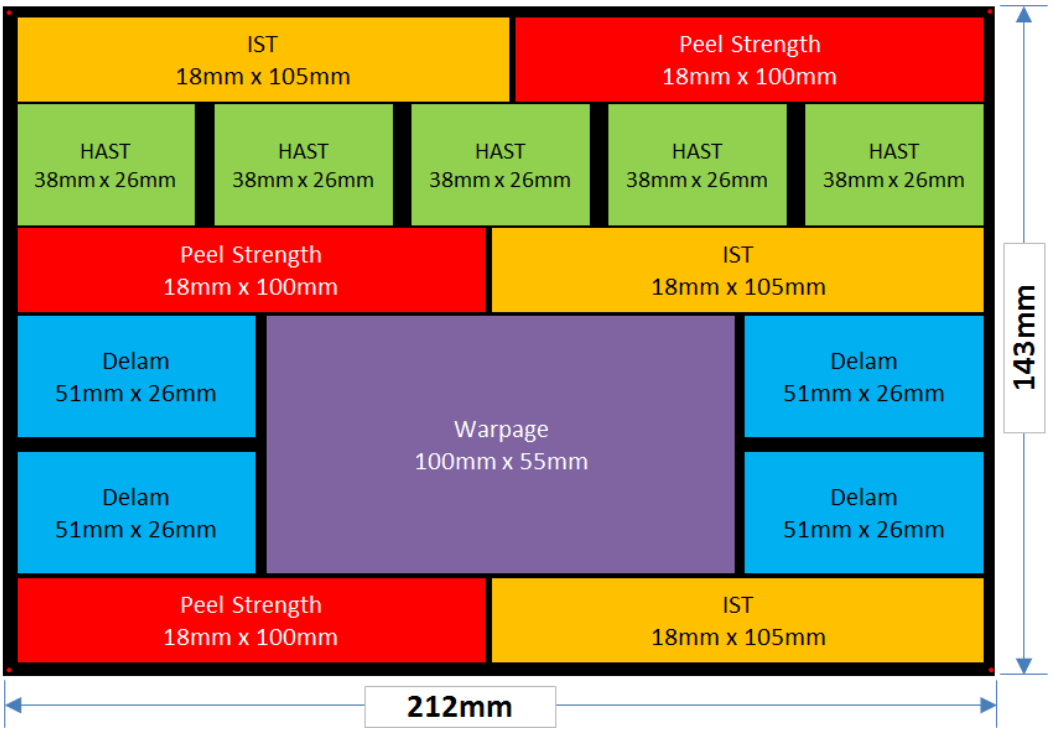

Figure 4-5 Layout of a single test coupon card

4.4 Test plan

4.4.1 Kinetics study with a model resin

There are many different models available for the epoxy kinetics study which can be applied to both curing and decomposition kinetics of an epoxy resin. This step aims of finding the best suitable one for the current application, i.e., the DGEBA/DICY model epoxy resin system.

First, the thermal decomposition properties of both monomer and hardener were determined by a Mettler-Toledo TGA/SDTA851e under 50ml/min nitrogen atmosphere. One sample for each was tested and the weight of DGEBA and DICY were 10.175 mg and 16.683mg weighed by the TGA device. Samples were put into 70µl alumina crucibles with lids and were heated from 30°C to 800°C with 10°C/min heating rate.

Second, the heat flows of both components were measured by a Mettler-Toledo DSC823e/400 instrument under nitrogen atmosphere with a flow rate of 50ml/min. One sample for each was measured and the mass of DGEBA and DICY were 5.06mg and 12.40mg weighed by a Mettler-Toledo Balance/AE260 with 0.1mg accuracy. Samples were sealed in 40µl aluminum crucibles with lids. A hole was made in each lid before sealing. Samples were heated from 30°C to 300°C with 10°C/min heating rate.

Third, the mixture ratio and the sample weights had to be fixed. Assume that all four hydrogen atoms of DICY take part in the reaction and react with one epoxide each, then the ideal stoichiometric PHR (parts by weight per 100 parts resin) of amine is ($\frac{Amine\ H\ eq\ wt \times 100}{Epoxide\ eq\ wt\ of\ resin} = \frac{21.2 \times 100}{100} =$) 11.24. Afterwards three groups of mixtures were prepared: group M1 with excess DICY (PHR=14.29, $\frac{Weight\ of\ resin}{Weight\ of\ DICY} = 7$), group M2 with exact DICY (PHR=11.24, $\frac{Weight\ of\ resin}{Weight\ of\ DICY} = 9$), group M3 with less DICY (PHR=9.09, $\frac{Weight\ of\ resin}{Weight\ of\ DICY} = 11$). The heat flows of the three groups were measured by DSC in the temperature range from 30°C to 260°C with 3°C/min, 5°C/min, 8°C/min and 10°C/min heating rates. Three measurements were made for each condition. The mass of the samples was not specially controlled at this stage, they varied from 7.5mg to 23.0mg.

Finally, based on the results from the third step, the curing kinetics study in the temperature range from 30°C to 260°C was conducted with DSC for group M3. The selected heating rates were 1°C/min, 2°C/min, 3°C/min, 5°C/min, 8°C/min and 10°C/min. Each heating rate was repeated 3 times. Moreover, one group of isothermal curing at 180°C/2hr, 190°C/2hr, 200°C/1hr, 210°C/1hr and 220°C/1hr were conducted for the purpose of

validating the prediction. The mass of the samples were controlled between 3.0mg and 5.5mg. After the experiments, the raw data of the sample temperature and its corresponding curing degree was exported from the DSC and the sample temperature. The curing kinetics was then calculated according to the averaged values by means of a self-programmed MFK software in Excel on the basis of an Ozawa-Flynn-Wall equation.

4.4.2 Curing kinetics

4.4.2.1 DSC curing kinetics

The pure epoxy resin samples (A) were heated up from 30°C to 260°C under different heating rates for DSC curing kinetics study, i.e., 2°C/min, 3°C/min, 5°C/min, 8°C/min and 10°C/min. Each heating rate was repeated three times. Afterwards, four samples were isothermally cured at different temperatures based on the prediction, i.e., 220°C/0.5hr, 210°C/0.5hr, 200°C/0.5hr, 190°C/1hr and 180°C/1hr in order to validate the prediction. The sample weights were controlled within 3.0±0.1mg. Other procedures followed the ones in chapter 4.4.1.

4.4.2.2 FTIR curing kinetics

IR spectra (16 scans) were collected at 4cm^{-1} resolution using the transmission mode of the versatile FTIR spectrometer VERTEX 70 from Bruker Optik. The FTIR curing kinetics study was conducted as a complementary part of the DSC method. Since no additional heating device was equipped to the IR spectrometer, no in-situ measurement could be performed. Therefore, only isothermal curing kinetics could be studied and the samples were cured in the Nabertherm TR240 oven.

Compared to the DSC samples, the sample preparation of the pure epoxy resin powders (A) for the FTIR curing kinetics was relatively complicated, as described below:

1) The resin powder was spread onto a PTFE film evenly and then covered with another PTFE film.
2) The sandwich-like structure was put onto a hotplate maintained at 110°C with slight pressure applied by a glass plate for few seconds until the resin powder melted.
3) The sandwich-like structure was taken away from the hotplate and peeled off the top film, as depicted in Figure 4-6 A.

4) The resin film was cut into 27 small pieces for the measurements at 3 different temperature levels (T=190, 200, 220°C) and 9 different curing times (t=0, 2, 4, 6, 8, 10, 12, 15, 30min) respectively.
5) Each piece was wrapped by a PTFE film (Figure 4-6 B) and placed between two glass plates (Figure 4-6 C).
6) The glass plates with the wrapped resin film was put into the oven maintained at a specified temperature for a defined time.
7) The sample set was removed and the partially/fully cured resin film was attached directly onto the steel sample holder of the FTIR and the transmission mode measurement was done (Figure 4-6 D).

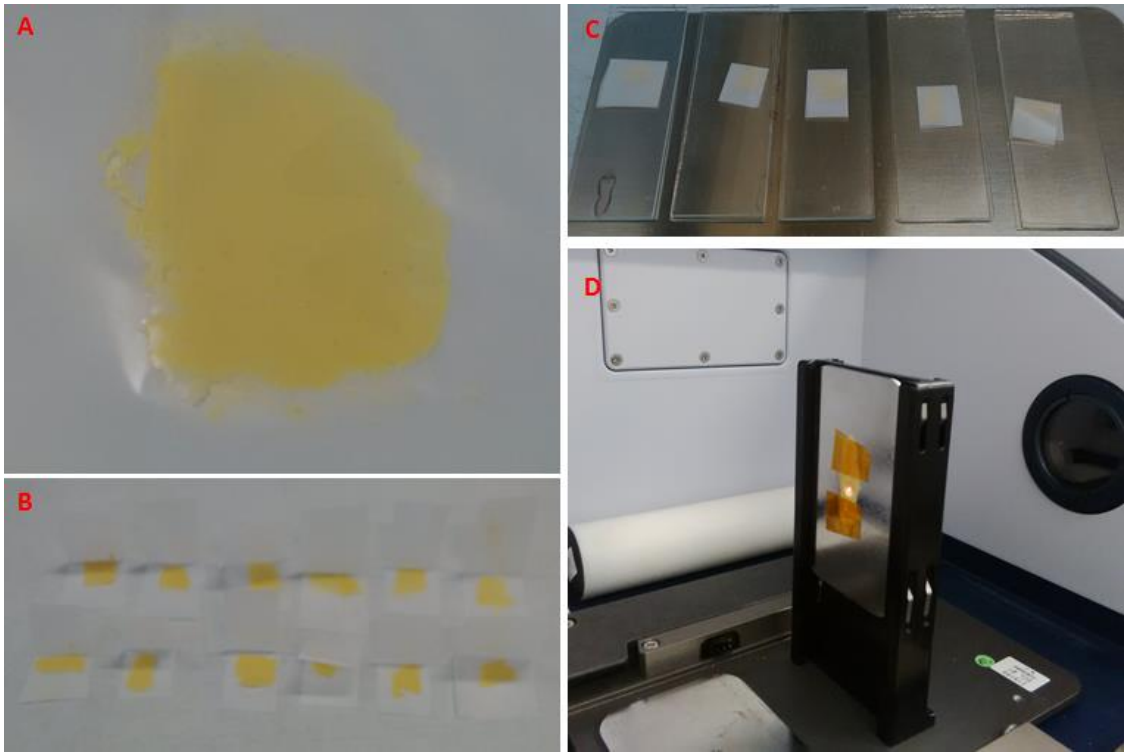

Figure 4-6 Sample preparation for FTIR isothermal curing kinetics

4.4.2.3 Coupling of MFK and FEA

During the DSC curing kinetics, all the resin samples were cured in the DSC crucibles and their temperatures were very well controlled by the DSC device: the heating and cooling of the resin would exactly follow the program profile. In reality, due to the stack-up of the press book, the temperature of the prepregs will not follow the preset program. Therefore, the coupling of MFK with a finite element approach (FEA) was implemented in order to simulate the real curing conditions.

Four-node two dimensional solid elements (DC2D4) were used for the modelling of the quarter-sized press book in Abaqus® as presented in Figure 4-7. 8 layers of CE-688 prepregs were pressed in a press book separated by steel plates. The top and bottom of each prepreg were covered by a thin copper foil. The cushion paper below the heating plate acted as a stabilizer when the pressure was applied. Two thermocouples were placed near node 1 and 2, between which the biggest temperature differences during curing were expected. The material properties used for the simulation are listed in Table 4-2. The temperature setting for the heating plates and the measured temperatures at the locations near the two nodes are depicted in Figure 4-8. The total time of a standard press cycle without cooling was 165min, but only the first 120min are presented in Figure 4-8, because after that all curves remained constant. The temperature profile of the heating plates was used as an input for the simulation. The outputs of the simulation were the transient temperature distribution in the press book and the evolution of the curing degree of each node.

Table 4-2 Material properties used for the press cycle simulation

Material	Density [g/cm^3]	Conductivity [W/m/K]	Specific Heat [J/kg/K]
Paper	0.70 [91]	0.05 [92]	1340 [93]
Steel	7.85 [94]	15 [95]	502 [96]
Copper	8.59	400	585
Prepreg	1.38	0.25	1200

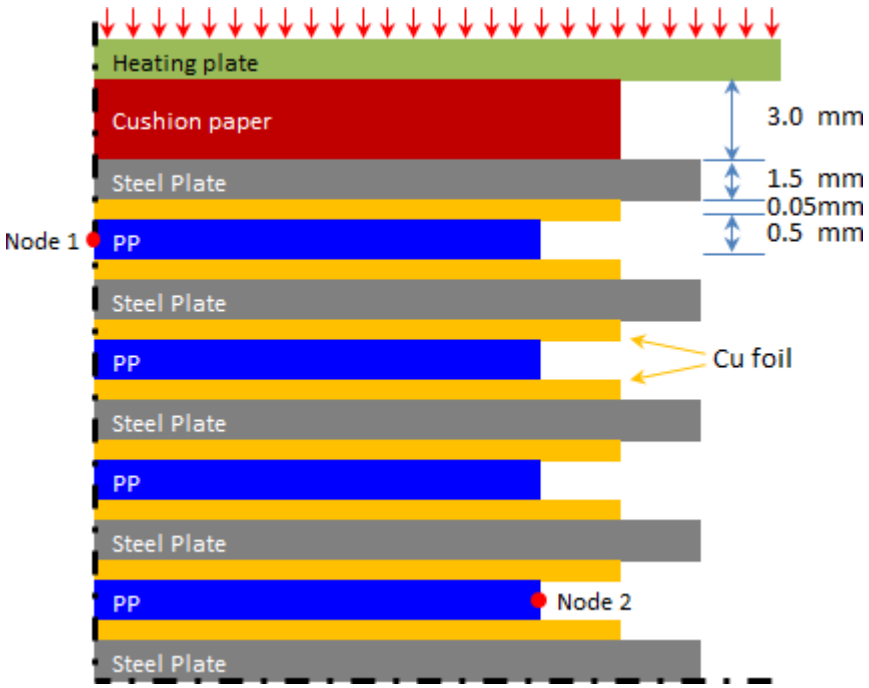

Figure 4-7 Schematic drawing for the stack-up of the press book which was used in the study for sample preparation (quarter-sized, not in scale)

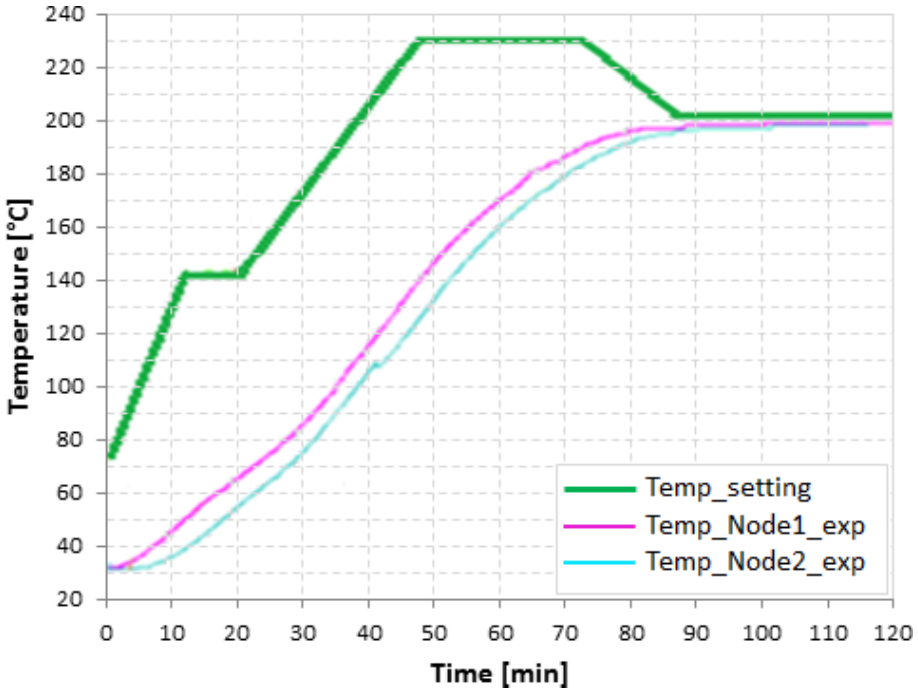

Figure 4-8 Temperature setting for the heating plates and the measured temperatures at the locations near node1 and node2

4.4.3 Mechanical properties

4.4.3.1 Monotonic tensile (Dumbbell)

The mechanical properties of the materials under study, such as Young's modulus (E), fracture strain/strength, were evaluated through tensile testes following the guidelines of ISO [97] on standard dumbbell specimens (Type 5A) as shown in Figure 4-9. The pure resin samples were produced by pressing the powder into a 1.0mm thick plate. The glass fiber type of the prepregs was #1080 and the resin content was 62%. Since one sheet of the prepreg was only 80µm, seven such plies were stacked and pressed into a panel with an average thickness of 0.53mm. The dumbbell specimens were routed out from the pure resin plate or the prepreg panel in order to obtain smooth edges. Only warp directions of the prepreg specimens were manufactured. Half of the prepreg specimens were subjected to 10x reflow test. The lamination and reflow procedures followed the description in Chapter 4.2.1 and 4.2.2 respectively.

The tensile tests were performed in an electromechanical testing machine Zwick (Z250, Zwick GmbH & Co. KG, Ulm, DE) combined with a digital image correlation system (Aramis, GOM mbH, Braunschweig, DE) for the purpose of determining the local strain, as shown in Figure 4-10. The load was applied with a test rate of 10mm/min under laboratory ambient. For each condition, six replicas were measured.

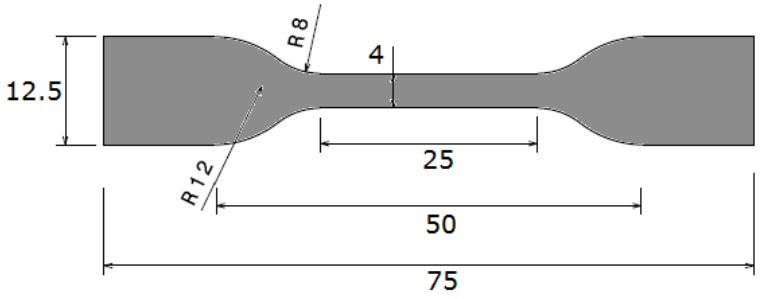

Figure 4-9 Standard dumbbell tensile test specimen (unit: mm)

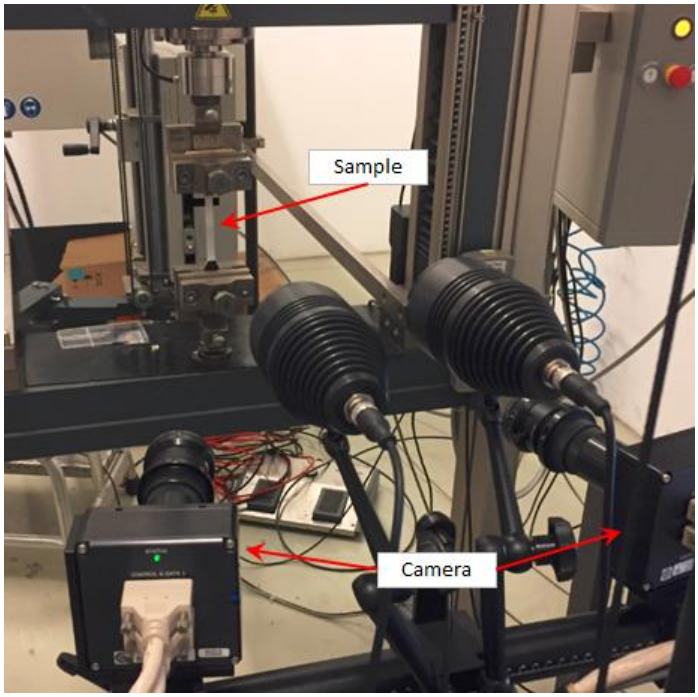

Figure 4-10 Tensile test setup

4.4.3.2 Dynamic Mechanical Analysis (DMA)

The DMA used in this study measured the changes in the viscoelastic response of the material under mechanical oscillation at fixed frequency as a function of temperature. The measurements were performed in a displacement-controlled tensile mode in a Mettler Toldedo DMA/SDTA861. Calibrations were conducted for each different type of sample in order to ensure that the maximum strain amplitude was within the linear viscoelastic range of the material. The pure resin (A00) and prepreg (B00, B30, B90, B00R, B30R and B90R) as well as the test PCB (C00, C30, C60, C00R, C30R and C60R) samples were prepared by using the same pressed plate/panel as for a monotonic tensile test. All samples were tested under Nitrogen atmosphere and were heated from 20°C to 250°C with 2°C/min heating rate at 10Hz. The nominal in-plane dimensions of the samples were 3.0mm x 9.0mm. For each condition, two to four replicas were measured.

4.4.4 Thermal properties

4.4.4.1 Differential Scanning Calorimetry (DSC)

All DSC measurements were performed on a Mettler-Toledo DSC823e/400 instrument under nitrogen atmosphere with a flow rate of 50ml/min. Samples were sealed in 40µl aluminum crucibles with lids. A hole was made in each lid before sealing.

There were four different DSC programs used in this study as shown in Figure 4-11: one DSC run includes a ramp-up from 50°C to 220°C with 20°C/min and a ramp-down back to 50°C with -20°C/min; P0 has two runs and the others have three; P105 and P130 have 10min preheating at 105°C and 130°C respectively in order to get rid of the possible moisture inside the sample; P105+ consists of additional 2hr preheating in an oven besides the 10min preheating in DSC. After measurement, Tg evaluations for each run were performed for the ramp-up stage according to the Mettler Toledo STAR^e procedure [59, pp. 72-77], i.e., the temperature at the intersection point of the bisector of the angle between the tangents above and below the glass transition on the heating scan was taken as the Tg value. Tg1, Tg2 and Tg3 stands for the Tg of the 1st, 2nd and 3rd run. The curing factor (ΔTg) is defined as the absolute temperature difference between the two successive runs [98] and hence $\Delta Tg1=|Tg2-Tg1|$ and $\Delta Tg2=|Tg3-Tg2|$. Based on the material specification of CE688, Tg should be >150°C and ΔTg must be <3°C.

The pure resin samples (group A) after the curing kinetics study were directly measured with the program P0. The prepreg (group B) and test PCB (group C) samples, both as received and after 10x reflowed, were measured initially with the program P130 (standard internal program). However, the DSC results of CE-688 showed that neither the Tg1 nor the ΔTg1 values were in spec for all the samples directly after lamination. Even after 10x reflow, both were still out of spec due to the dual-effect of cooling rate and annealing on the endothermic peaks in the DSC curves [99]. In order to tackle this problem, P105 and P105+ were specially designed.

The mass of the prepreg and test PCB samples were between 10mg and 15mg, which were not specially controlled as long as they fitted the size of the crucible. For each condition, three replicas were measured.

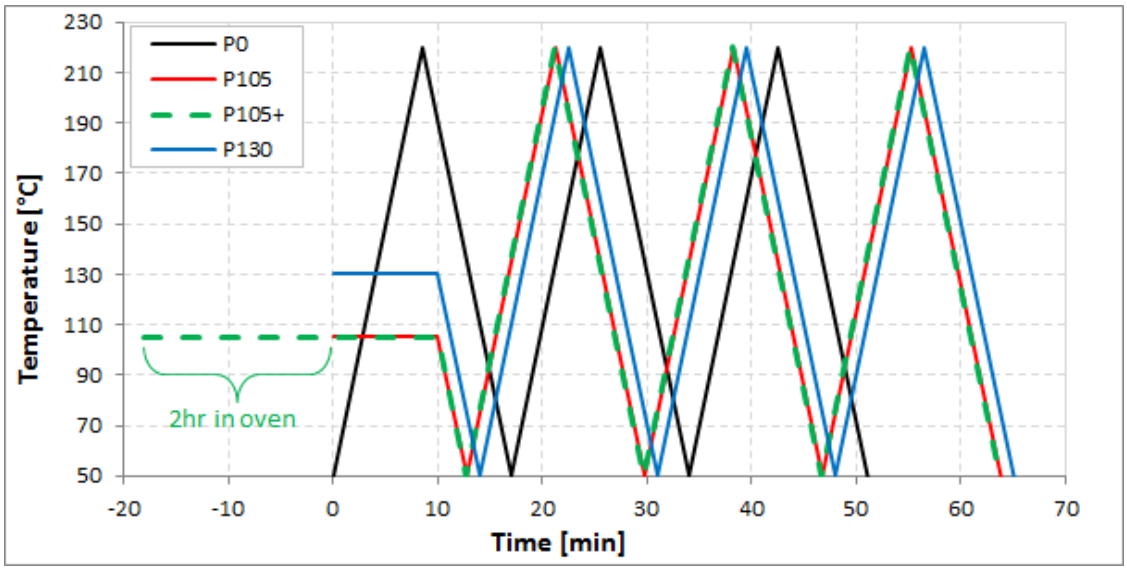

Figure 4-11 DSC programs used in this study

4.4.4.2 Thermal Mechanical Analysis (TMA)

All TMA measurements were performed on a Mettler-Toledo TMA/SDTA840 instrument under air atmosphere. Samples were measured between fused silica disks with 0.1N force applied. The standard internal TMA program, which was based on the IPC standard [100], was used in this study as shown in Figure 4-12: the program starts with a preheating of 10min at 130°C followed by three runs and each run includes a ramp-up from 50°C to 190°C with 10°C/min and a ramp-down back to 50°C with -10°C/min. The prepreg (B00, B30, B90, B00R, B30R and B90R) and test PCB (C00, C30, C60, C00R, C30R and C60R) samples were prepared by using the same pressed plate/panel as for the monotonic tensile test. For each condition, 2-4 replicas were measured.

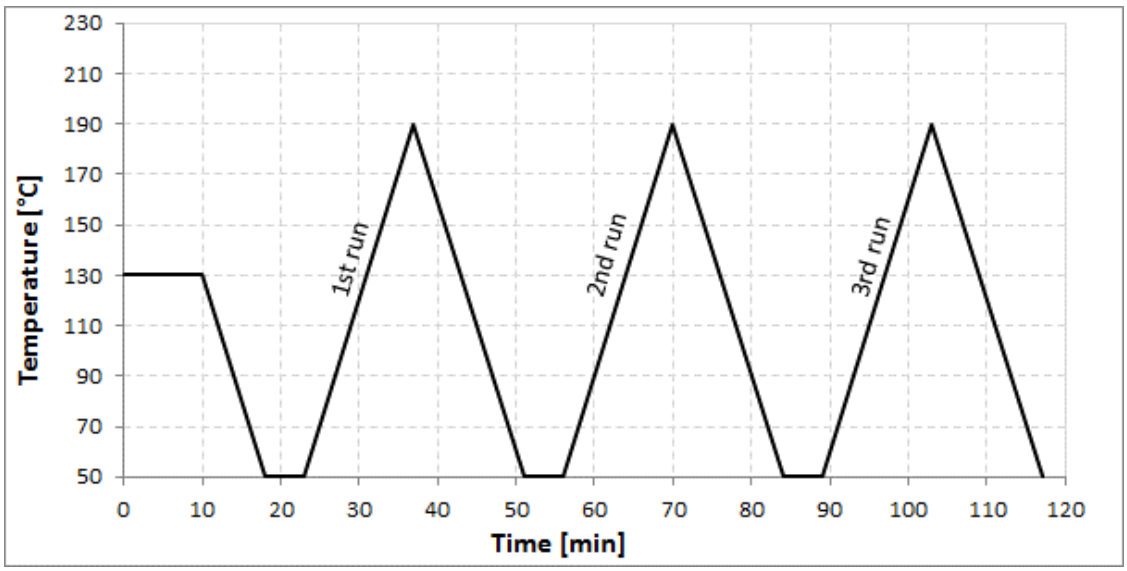

Figure 4-12 TMA programs used in this study

4.4.4.3 Thermogravimetric Analysis (TGA)

TGA decomposition kinetics was carried out for the prepreg samples pressed with 3 different conditions, i.e., normal (B00), -30min (B30) and -90min (B90). Furthermore, their 10x reflow aged counter parts (B00R, B30R and B90R) were included as well. The basic procedures were the same as the ones described in chapter 4.4.1.

The decomposition was determined by the Mettler-Toledo TGA/SDTA851e under 50ml/min nitrogen atmosphere. The sample weights were controlled at level of 12±3mg. Each group was measured twice for each condition with the temperature range between 30°C and 800°C, and the same heating rates were applied for all groups: 3°C/min, 5°C/min, 8°C/min, 10°C/min and 15°C/min.

4.4.5 Fracture toughness

In order to characterize the toughness of CE688 pure resin in terms of the critical-stress-intensity factor (K_{Ic}) and the critical strain energy release rate (G_{Ic}) at fracture initiation according to ASTM standard [85], pure resins were laminated with the standard (A00) and -90min (A90) programs with ~3mm thickness so that the compact tension (CT) specimens with a size of 50mm x 50mm could be machined out of the pressed plates. Unfortunately, all the samples failed during the sample preparation: either at the hole drilling process or at the step of introducing an initial crack mechanically, as shown in Figure 4-13. Obviously, this was caused by the high brittleness of the material.

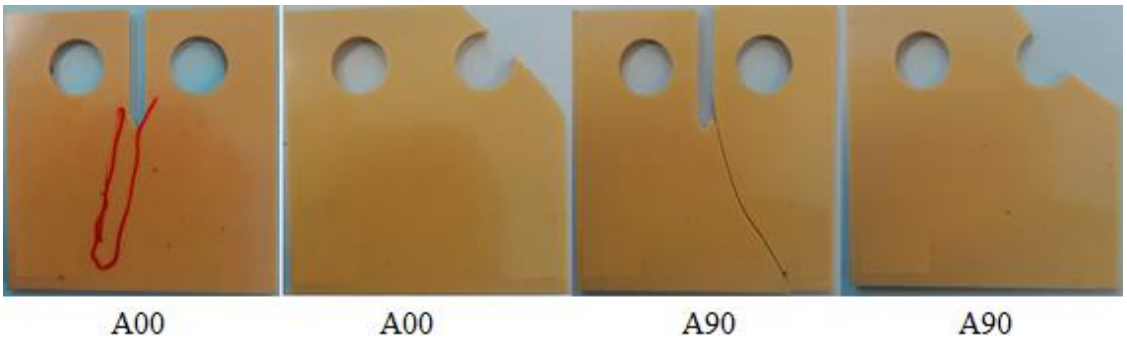

Figure 4-13 Compact Tension (CT) specimen failures during sample preparation

Another possibility to utilize the failed CT-specimens for the same purpose according to the same ASTM standard was to perform the Single-Edge-Notch Bending (SENB) test. Therefore, the undamaged parts from the failed CT-specimens were selected and ground to strips with a size of 50mm x 11mm. The next step was to create a V-cut in the middle of the strips and to introduce a pre-crack at the tip of the V-cuts. Because the samples were too brittle to be mechanically machined, a pico-laser cutting in a third-party laboratory was employed. However, the results were not satisfactory as shown in Figure 4-14 since the resins were burnt during the laser cutting.

Finally, both the CT- and SENB-specimens failed due to difficulties with the sample preparation procedure. Crack growth fatigue tests on the pressed pure resin samples of CE688 were impossible and thus abandoned.

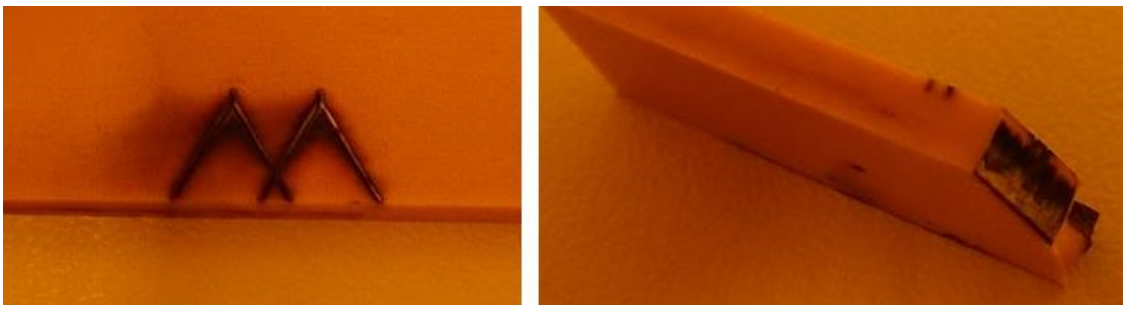

Figure 4-14 Pico-laser cutting for Single-Edge-Notch Bending (SENB) sample preparation

Considering the fracture mechanics, additionally a prepreg and a Teflon® film were pressed between two cores with standard, -30min and -90min conditions. After lamination, the Double Cantilever Beam (DCB) specimens were routed out and split into two groups: as received (B00, B30, B90) and after 10x reflowed (B00R, B30R, B90R). Two steel blocks with a pin hole were glued on the Teflon® film side for each DCB samples as shown in

Figure 3-17. To avoid introducing extra curing to the samples, the two-component glues were cured at room temperature. The total length l was 125mm, the width b was 20mm, the thickness 2h was between 3.30mm and 3.40mm. The servo-hydraulic test machine, MTS 858 Table Top System, was used for determining the opening Mode I interlaminar fracture toughness, G_{Ic}, of CE688 prepreg under both monotonic and cyclic loadings. For each condition, four replicate tests were carried out for each condition.

In terms of the monotonic DCB test, one side of the assembled DCB-specimens was painted with white color to enable an easier crack tracking. In order to follow the crack growth during testing, the painted side of the samples subject to monotonic loading was marked lengthwise with 5mm intervals as seen in Figure 4-15. The ends of the DCB are opened by controlling the opening displacement with a constant displacement rate of 5.0mm/min, while the load and delamination length are recorded.

Regarding the cyclic DCB test, an optical monitor with digital display was placed in front of the samples subject to cyclic loadings for the purpose of manually measuring the crack growth as shown in Figure 4-16. The testing was displacement controlled. The sinusoidal loading was applied with a ratio, R (=P_{min}/P_{max}), of 0.1. The loading frequency was set at10 Hz.

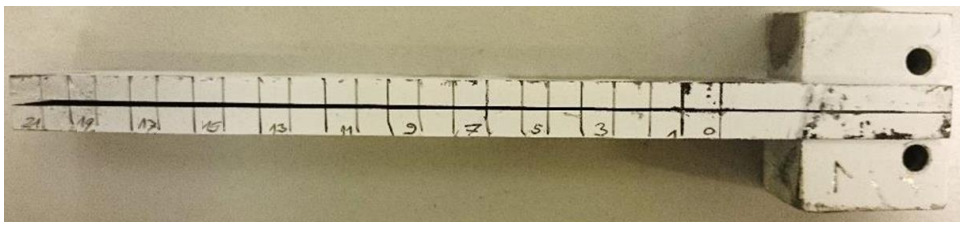

Figure 4-15 DCB specimen marking for crack tracking under monotonic loading

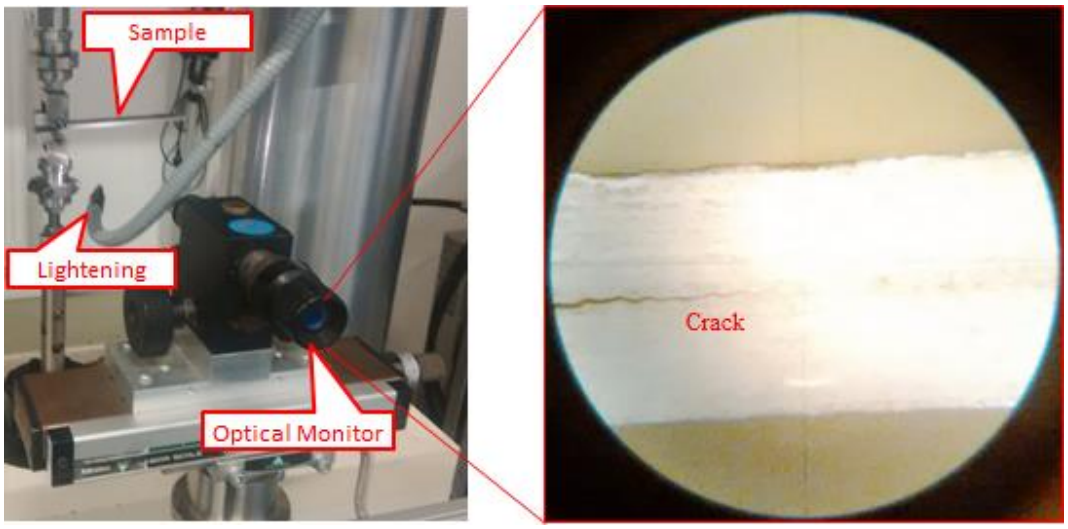

Figure 4-16 Setup for crack tracking under cyclic loading

4.4.6 Reliability test

4.4.6.1 Moisture uptake

The prepreg samples pressed with three different conditions (B00, B30 and B90) and their 10x reflowed counterparts (B00R, B30R and B90R) were subjected to moisture absorption under the hydrothermal condition of 85°C/85%RH in a climate chamber for 25 days. Three replicas for each condition were prepared with the size of 50mm × 50mm. All samples were prebaked at 120°C for 2hours. The weights after prebaking were recorded as the original ones. Samples were weighed within 30 min after the removal from the climate chamber and the measurement interval was one day.

4.4.6.2 Peel strength

The peel strength coupon according to IPC-TM-650 [101] was designed to determine the mechanical bonds between the cured CE688 prepreg and the external copper layers. All the eight layers of the peel strength coupon have the same design, as shown in Figure 4-17. It is a copper strip and only the external layers will be tested. Others are used for increasing the stiffness of the coupon.

30 samples were tested for each PCB group, i.e., C00, C30, C60, C00R, C30R and C60R. The tests were performed by a standard tensile test machine with a fixed cross head speed of 50.8mm/min.

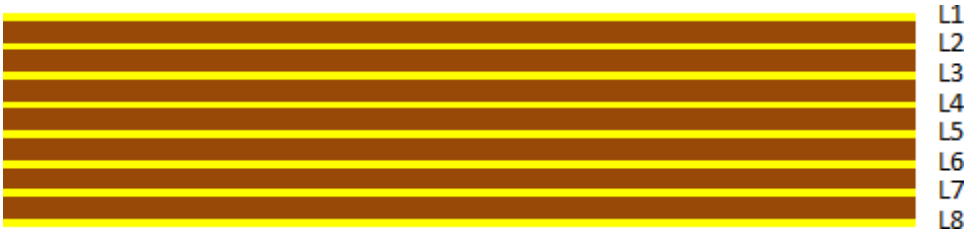

Figure 4-17 Design of the peel strength coupon (cross section). Only the outer layers (L1 or L8) are peeled off during testing.

4.4.6.3 Delamination

The delamination coupon is composed of eight plated through holes (PTHs) and 8 big copper areas on each layer. The design, which is based on IPC-TM-650 [102], ensures that

the big copper area of each layer is electrically connected only to one PTH, so that the capacitance between two adjacent layers can be measured via the corresponding PTHs. Figure 4-18 presents the copper structure of the first layer, whereby PTH_1 is connected to the big copper area.

One sample for C00 and one for C00R were subjected to the delamination test because the purpose was to evaluate the feasibility of this new method. A sample was placed on a hot plate maintained at the preset temperature. Once the sample temperature, which was measured by the attached thermocouple, reached the preset one, the counting of the heating time started. Considering that CE688 epoxy resin is quite stable at 260°C (it takes at least 50 min before it decomposes as shown in Figure 5-46 (b)), the isothermal heating temperature was set at 300°C. And after each 30/60 sec, the sample was removed from the hot plate and its capacitance was measured at room temperature.

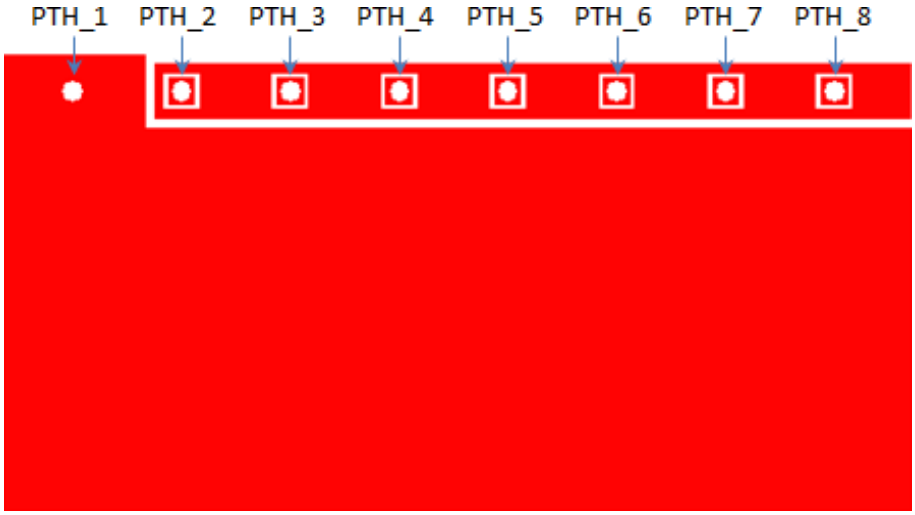

Figure 4-18 Delamination coupon design of layer 1

4.4.6.4 Interconnection Stress Test (IST)

Figure 4-19 presents the IST coupon design of layers 2 and 7 in line with IPC-TM-650 [103]. The laser vias sit in the middle of the pads (red dots with a diameter of 150µm) and stack on top of each other from the top layer to the bottom with a diameter of 70µm. All laser vias are connected to form a so-called daisy chain structure. There are six PTHs on the coupon: PTH_1/PTH_2 will act as anode and PTH_3/PTH_4 are cathodes, meanwhile, PTH_5 and PTH_6 are connected on layer 7 so that the DC current can pass through the lines on layer 2 and 7 in series in order to heat up the whole coupon homogeneously by applying the well-controlled current.

16 replicas for each PCB group (C00, C30, C60, C00R, C30R, C60R) were subjected to the IST test. One cycle of IST consists of a 3min temperature ramp-up (RT to 190°C) and a 2min cooling down (190°C to RT). The resistances were monitored in-situ. And once the resistance change is higher than 10%, the test will be automatically stopped so that the initiation of the failure can be analyzed afterwards.

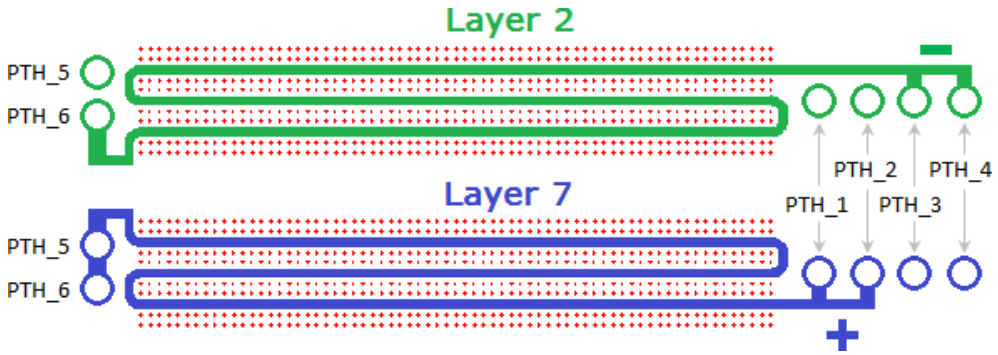

Figure 4-19 IST coupon design of layer 2 and layer 7

4.4.6.5 Highly-Accelerated temperature and humidity Stress Test (HAST)

The HAST procedure in the light of EIA/JEDEC [104] was carried out with the comb pattern design (both the line width and line space are 75µm) as shown in Figure 4-20. The comb patterns were placed on each inner layer, i.e., from layer 2 to layer 7. Ten samples of each PCB group (C00, C30, C60, C00R, C30R and C60R) were tested with a 5DV voltage bias applied at 110°C/85%RH. The test duration was 264 hours and the measurement interval was 1 hour.

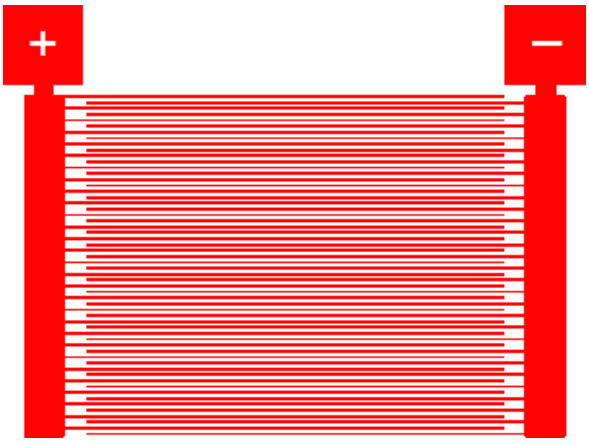

Figure 4-20 HAST coupon design of all layers

4.4.6.6 Warpage

Figure 4-21 presents the design of the warpage coupon. The patterns are identical for each layer. The square pads are 2x2mm with a distance (edge to edge) of 4mm away from each other. With the Shadow Moiré technology, the topographic changes can be recorded and the coplanarity of the sample will be used to describe the warpage.

Five samples for each PCB group (C00, C30, C60, C00R, C30R and C60R) were measured with the Akrometrix® PS400 equipment. The coplanarity of the samples were detected at elevated temperatures and the standard lead-free reflow profile, as shown in Figure 4-3, was applied. Furthermore, another five samples for each as-received group (C00, C30 and C60) were subjected to 10x reflow tests and their coplanarities were determined after each reflow at room temperature in order to see the evolution of the warpage over the reflow cycle.

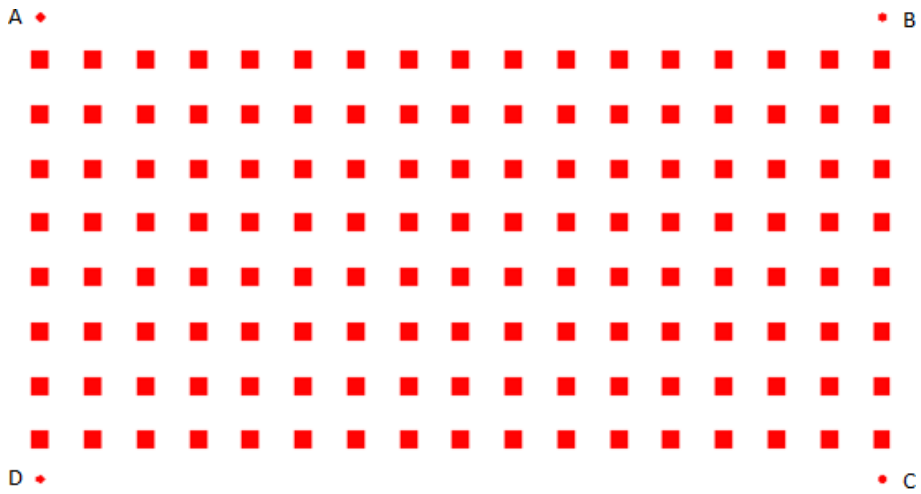

Figure 4-21 Warpage coupon design of all layers

5 Results and discussion

5.1 Kinetics study with a model resin

5.1.1 Decomposition and heat flow of DGEBA and DICY

As presented in Figure 5-1, DGEBA started to decompose at around 280°C and the decomposition ended at around 470°C. 5.70% weight remained at 800°C. The mass loss of DICY below 220°C was around 0.76% due to sublimation and evaporation [29]. DICY started to decompose at around 220°C, but very slightly, an obvious decomposition happened at around 300°C with 3.75% weight loss and ended at around 475°C, it remained 7.79% weight at 800°C.

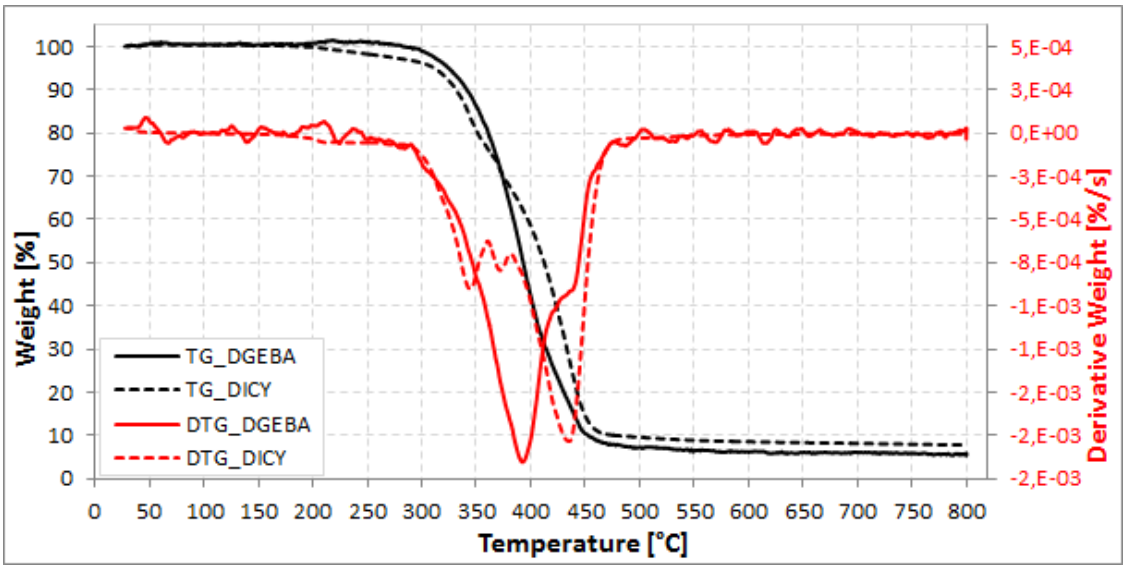

Figure 5-1 TG-DTG plots of DICY and DGEBA

The heat flow measurement results are shown in Figure 5-2. As expected, DGEBA was a quite stable epoxy below 300°C, the whole curve remained straight. A pronounced endothermic peak from the DSC curve of DICY starting at around 207°C and ending at around 220°C showed its melting behavior. The peak temperature of the melting was approximately 210°C. There are two strong exothermic peaks after the melting effect which means that DICY started to decompose at about 220°C releasing a large amount of energy. This is in accordance with the results obtained by TGA.

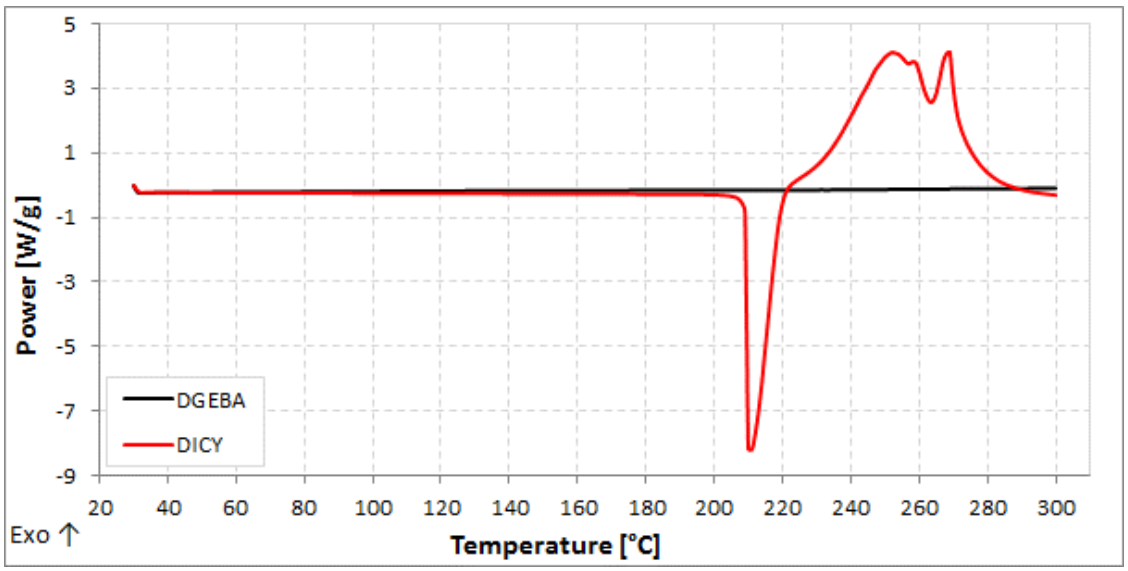

Figure 5-2 DSC heat flow curves of DICY and DGEBA

5.1.2 Non-isothermal curing of resins belonging to group M1, M2 and M3

In order to perform the curing kinetics study, the non-isothermal DSC scanning for each group of the model resins were conducted. From the curves in Figure 5-3 (a), it can be seen that all reaction curves contain only one pronounced exothermic peak whose intensity and temperature increase when the heating rate rises. This phenomenon was well reported in curing kinetics studies of other resin systems [105, 106, 107, 108]. Besides, a second small peak occurred in the temperature range between 202°C and 204°C for M1 and M2 at lower heating rates (3°C/min and 5°C/min) as seen in the inset of Figure 5-3 (a). This might be due to the melting of the excess of DICY. However all the peaks in Figure 5-3 (a) show a significant asymmetry with a positive slope on both sides: the faster the heating rate, the more the peaks of the curves shift/tilt to the higher temperatures. This finding was quite unexpected and not reasonable, because at a fixed temperature there should not be an ambiguous signal from the DSC machine.

There are two different temperatures in a DSC device, i.e., sample and reference temperatures as described in Figure 3-1. Since the heat leak permits a fast transfer of heat between the sample and reference crucible [54], there should be no obvious difference between the plots of power vs. sample temperature (the solid curves shown in Figure 5-3 (b)) and power vs. reference temperature (the dotted curves shown in Figure 5-3 (b)). However, this was not the case for the model resin system.

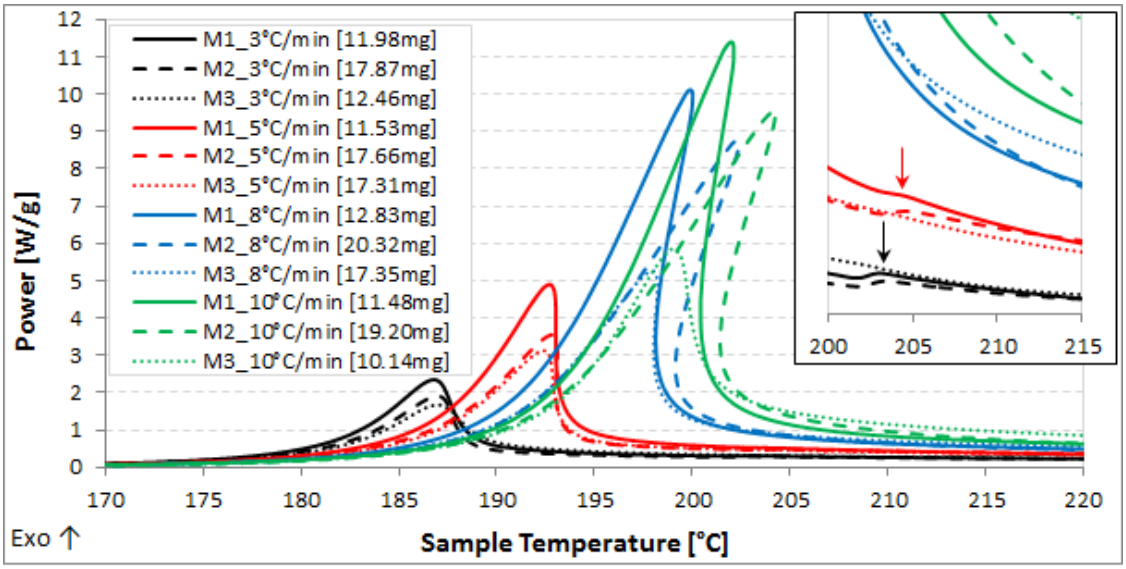

(a)

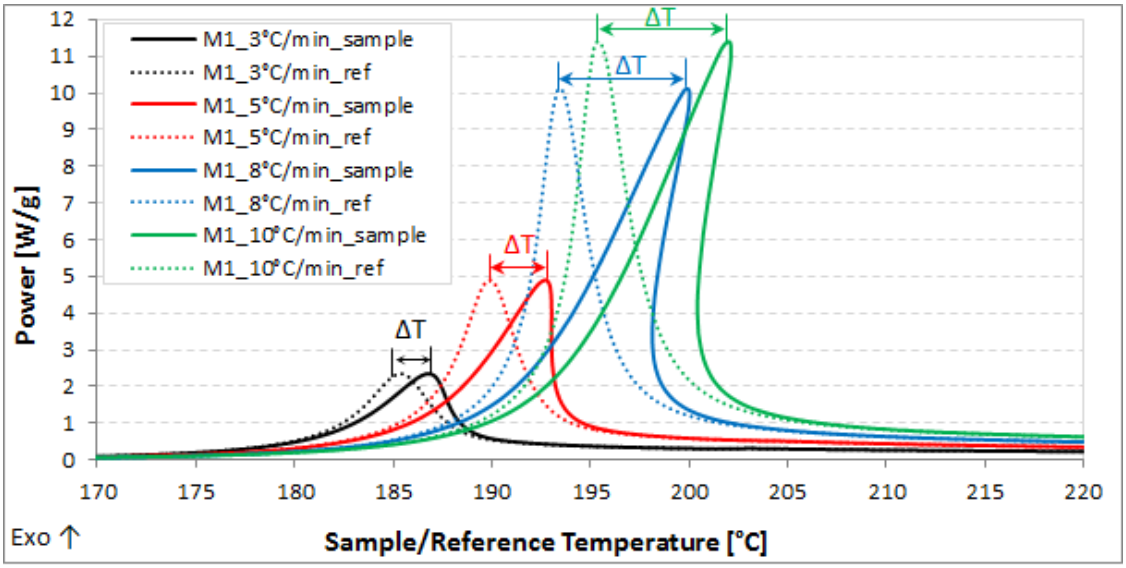

(b)

Figure 5-3 DSC heat flow curves: (a) Plots of power vs. sample temperature for group M1, M2 and M3; Inset: enlargement of the region between 200°C and 215°C. (b) Plots of power vs. sample temperature and power vs. reference temperature for group M1.

To figure out the root cause of the shifting and to quantify the extent of the shifting, the peak temperature differences, as described in Figure 5-3 (b), and the peak power were plotted against the sample weight as shown in Figure 5-4 (a) and (b) respectively. The circles stand for the measurement data and the lines are their corresponding best fitting lines. From the slopes of these lines, a clear conclusion can be drawn: the higher the sample weight and the faster the heating rate, the bigger the ΔT (i.e., the greater the shifting of the peak) and peak

power will be. If these lines in Figure 5-4 (a) are extrapolated to the X-axis, most will have the intercepts at around 5.0mg. That means, if the sample weight is controlled to be less than 6.0mg, it will have the least influence on the shifting of the sample peak with all heating rates. On the other hand, the weights should not be too small in order to generate a sufficient amount of reaction energy for the analysis.

Moreover, the peak power should be dependent on the heating rate but independent of the sample weight. Figure 5-4 (b) shows that only groups M2 and M3 at lower heating rates (3°C/min and 5°C/min) have such independence.

It is concluded that the shift of the DSC reaction curves was caused by the extremely fast reaction, or, the speed of the reaction was too fast to be followed/controlled by the DSC device. The excess of the reaction energy might cause the increment of the apparent peak power which was presented in Figure 5-4 (b). Then both the amount of the total released reaction energy and the ratio of DICY should be reduced to correct the shifted peaks and to make the peak power independent from the weight.

Additionally, in the attached paper [109], a FEA simulation based on two simple 4-node axisymmetric solid element (DCAX4) models in Abaqus® also confirms that a strong and fast release of the reaction energy during the DSC measurement will cause a big temperature gradient within the sample crucible, which will in turn give rise to the shift of the DSC curve.

Based on the above-mentioned points, group M3 (less DICY) was chosen with a sample weight between 3.0mg and 5.5mg for further curing kinetics studies. DSC scannings of group M3 with well-controlled sample weights between 3.0mg and 5.5mg are presented in Figure 5-5 (only one out of the three repeats is shown for each group in order to keep the chart clean): all the curves are “shifted” back to the normal shape; no second small peaks could be found in the temperature range of 202°C-204°C, which indicates that all the DICY have been consumed during the reaction. ΔTs at peaks all dropped to below 1°C with the sample weights near 3.0mg as shown in Figure 5-6 (a). Although there were still differences between the peak temperatures, it is better to accept the deviation (<1°C) than to further reduce the sample weights in order to obtain pronounced reaction peaks. Furthermore, Figure 5-6 (b) clearly shows that the peak power is only dependent on the heating rate and there is no influence from the sample weight if it is less than 6.0mg for group M3.

The reaction heat of M3 at various heating rates was determined by integrating the area under the exothermal peak in Figure 5-5 and dividing it by the sample weight as shown in Figure 5-7. It can be seen that the heat of reaction increases as the heating rate decreases and keeps constant at 572±28J/g once the heating rate is lower than or equal to 3°C/min.

Theoretically, the maximum reaction enthalpy should be independent of the scanning rate [110]. A reasonable explanation of the dependency might be related to the dissolution rate of the DICY during the polymerization reaction [111]; that means, at lower heating rates, DICY can be dissolved more effectively and therefore generates more reaction heat. A similar effect, which can be interpreted in the same way, has been found in terms of the isothermal curing of the epoxy/DICY system [112]: the curing heat increased with the curing temperature. This means that the resins which have been cured at higher heating rates or lower temperatures might have not been fully cured. However, these not fully cured resins are often defined as "fully cured" in the manufacturing of PCBs as long as their Tgs are above the minimum Tg criterion.

Based on the non-isothermal experiments of resins belonging to group M1, M2 and M3, it can be see that the sample weight is one of the most important factors for sample preparation. Considering both the shape and the intensity of the DSC peak, 3.0±0.1mg was finally chosen as the target weight for all the further experiments in the curing kinetics study. Meanwhile, the heating rates were limited between 1°C/min and 10°C/min.

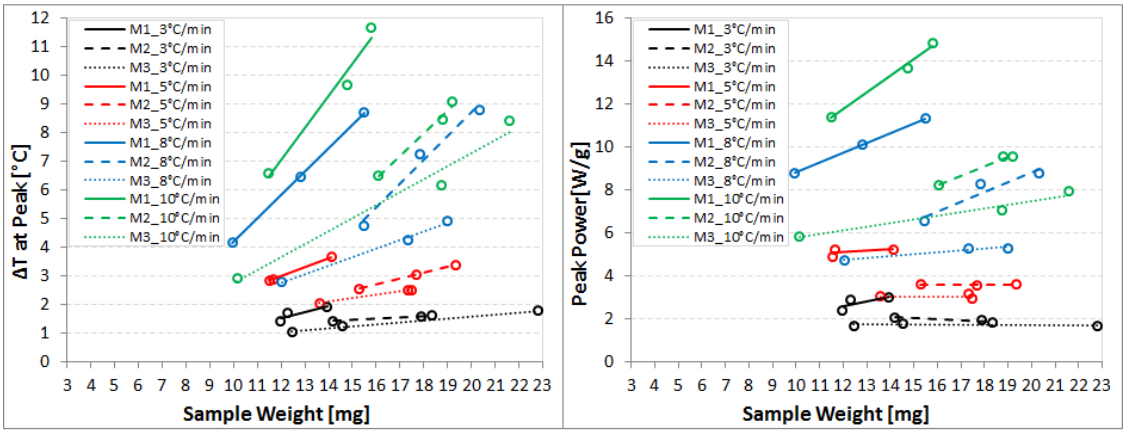

(a) (b)

Figure 5-4 Influence of the sample weight and the heating rate on the plot of power vs. sample temperature for group M1, M2 and M3: (a) Temperature deviation at the peak to the plot of power vs. reference temperature; (b) Peak power

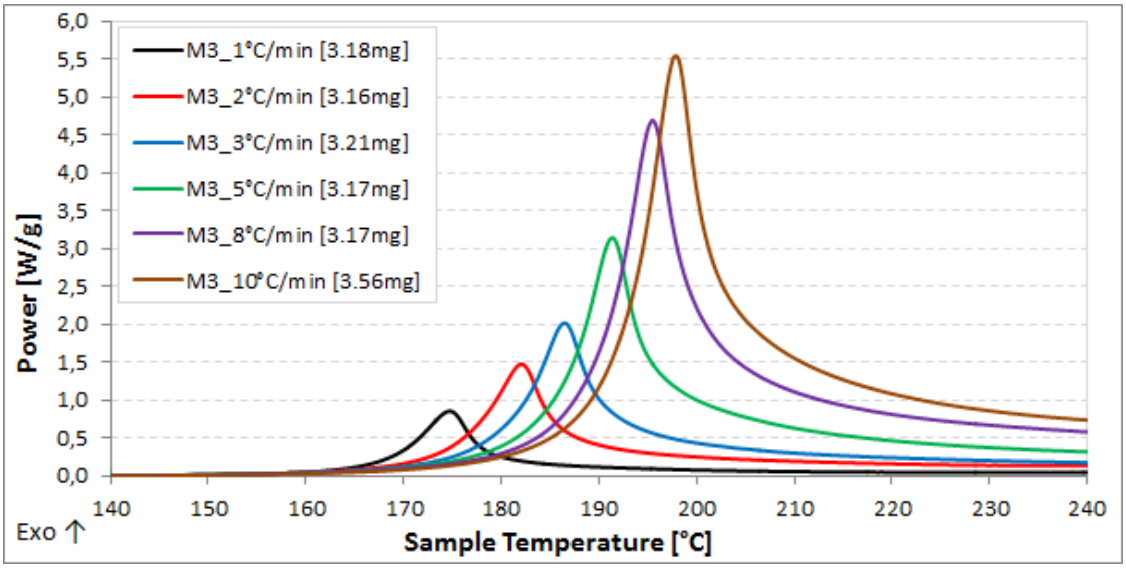

Figure 5-5 DSC non-isothermal heat flow curves of group M3 with well-controlled sample weights between 3.0mg and 5.5mg (only one out three repeats is shown for each group).

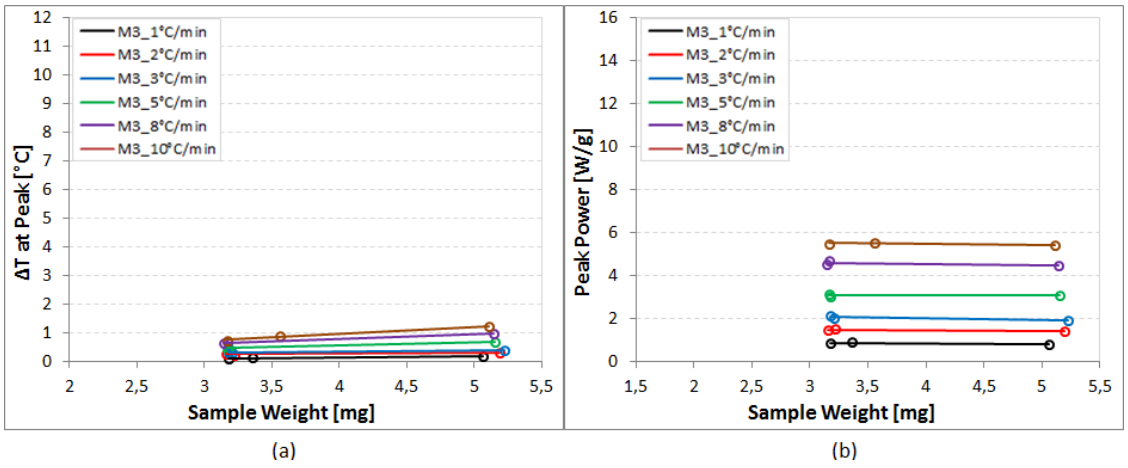

Figure 5-6 Influence of the sample weight and the heating rate on the plot of power vs. sample temperature for group M3 with well-controlled sample weights between 3.0mg and 5.5mg: (a) Temperature deviation at the peak to the plot of power vs. reference temperature; (b) Peak power

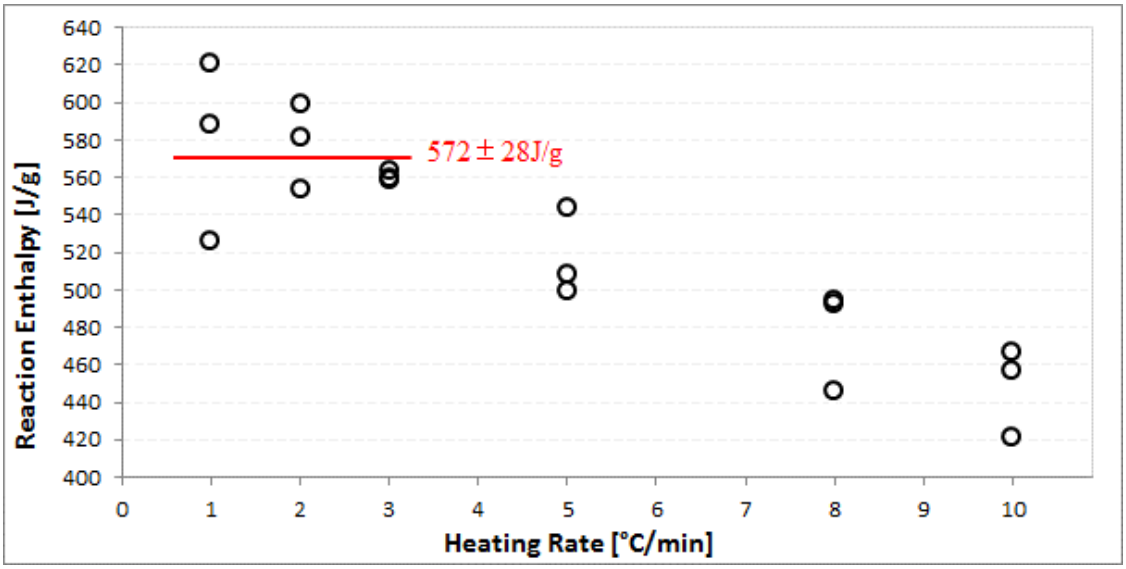

Figure 5-7 Reaction enthalpy of group M3 at various heating rates

5.1.3 Curing kinetics of resins belonging to group M3

Curing kinetics models can be categorized into mechanistic and pheonomenological models: the former is difficult to handle for the thermosetting chemical reactions due to their extremely high complexity and therefore the latter is more popular for curing kinetics modelling [113]. However, even for the pheonomenological method, there is no generalized cure kinetics model which can predict all epoxy systems and there is little hope to predict a commercial epoxy in an exact way. Nevertheless, kinetic models can still be useful in providing empirical parameters for predicting and controlling the curing process without requiring a thorough understanding of the cure chemistry [114].

A variety of kinetics models have been developed to relate the heating rate and conversion rate, such as the pheonomenological model proposed by Kamal and Sourour [115]. In this thesis, the model-free kinetics (MFK) method was used for the curing kinetics of the group M3. The Ozawa-Flynn-Wall equation (Equation 3-19) was first applied to each set of the non-isothermal DSC scans as shown in Figure 5-8 (a): the conversion degree (α_i) at each heating rate (β_j) and its corresponding temperature (T) can be obtained according to Equation 3-8 and Figure 3-3(a); the circles are the measured data; the lines are their corresponding best fitting lines and the lines which stand for the curing degrees at 10%, 50% and 90% are marked; the slope of the lines are related to the activation energy, E_a, at the specific conversion degree. Then the evolution of E_a against curing degree can be drawn, as shown in Figure 5-8 (b): the model epoxy resin M3 needed 150KJ/mol energy (below 150KJ/mol was excluded due to poor fitting) to start the reaction; then it continuously increased until

165KJ/mol at 15% curing degree and kept constant till 40% cured; afterwards, the required activation energy steadily dropped to around 120KJ/mol at the end of the reaction. The decrease of the activation energy at higher curing degrees might be due to the autocatalytic effect in the curing process [106]. Finally by utilizing Equation 3-19 and Equation 3-24, both non-isothermal and isothermal predictions could be executed as presented by the solid curves in Figure 5-9 and Figure 5-11 respectively.

Furthermore, experimental data of each heating condition (Figure 5-5 for non-isothermal and Figure 5-10 for isothermal) were added to the figures as well in order to validate the predictions. Both numeric predictions are acceptable from the engineering point of view and the non-isothermal prediction shows slightly better quality. It can be clearly seen from Figure 5-8 (a) that the goodness-of-fit is getting worse after 60% cured which leads to the relatively larger deviation (<5%) of the isothermal predictions above 60% curing degree in Figure 5-11.

Another important point is the way to construct the baselines for the isothermal thermograms. As described in chapter 3.1, the end of a horizontal baseline should be chosen at the end of the curve in order to reduce the tolerance. For instance, if we choose the right end point of the baseline at 5min for the green curve (190°C/120min) in Figure 5-10, the deviation of the calculated curing degree, as shown by the green circles in Figure 5-11, will be around 28% after 5min curing. Evidence of this can be seen by comparing the DSC curing kinetics to the FTIR one for CE688. Although, the green curve (190°C/60min) in Figure 5-12 (b) looks flat at 15min, the corresponding FTIR result (Figure 5-21) shows that the curing was not finished at that moment.

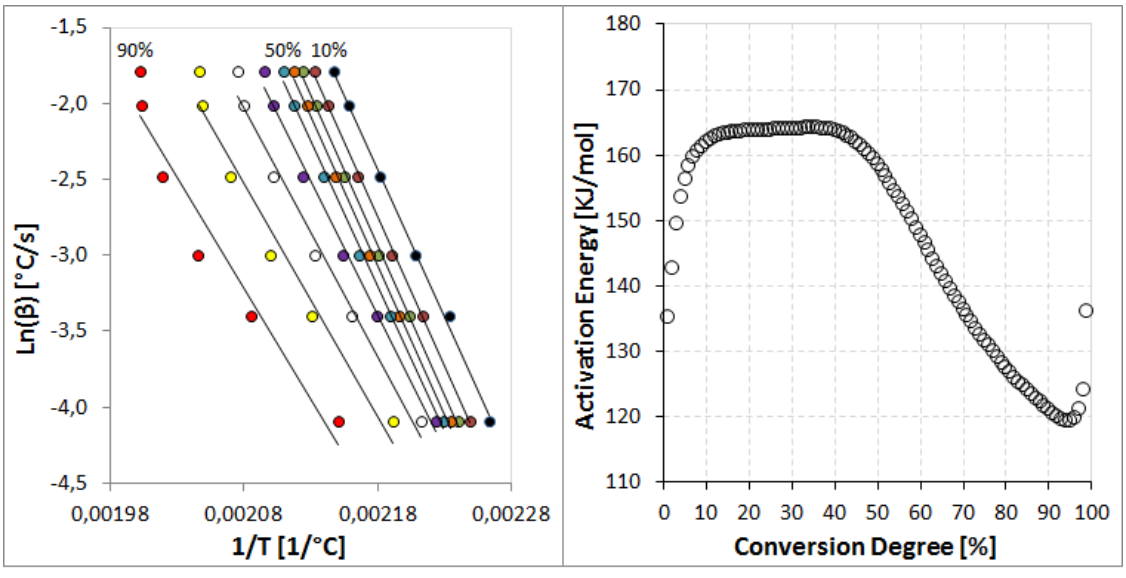

(a) (b)

Figure 5-8 MFK of group M3: (a) Isoconversion curves based on Ozawa-Flynn-Wall equation; (b) Activation energy at each conversion degree calculated based on the slope of the best fitting lines in (a).

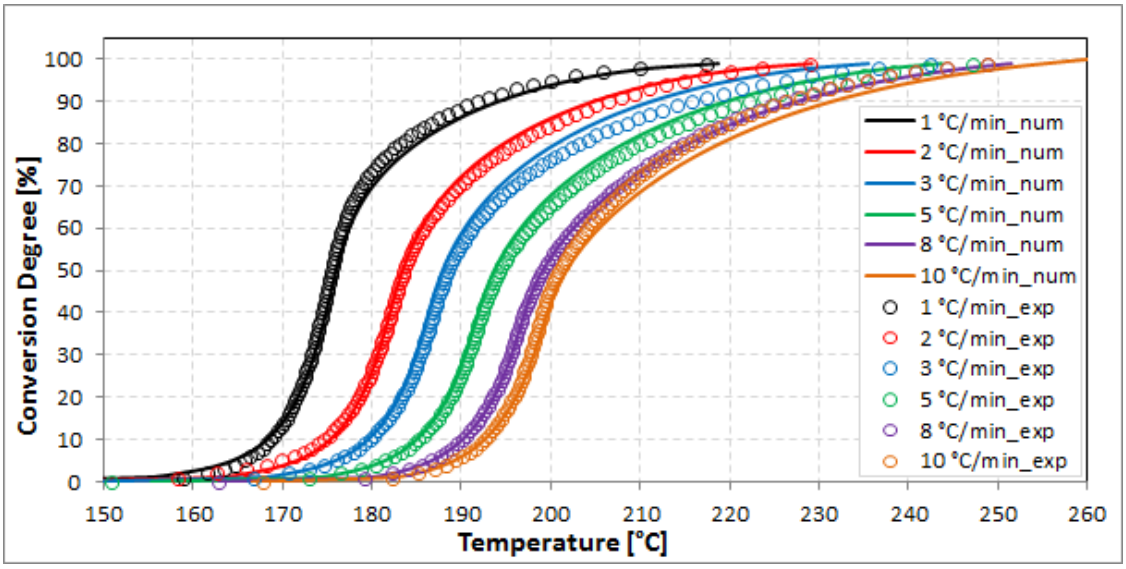

Figure 5-9 MFK non-isothermal numeric prediction vs. experiments for group M3 at various heating rates

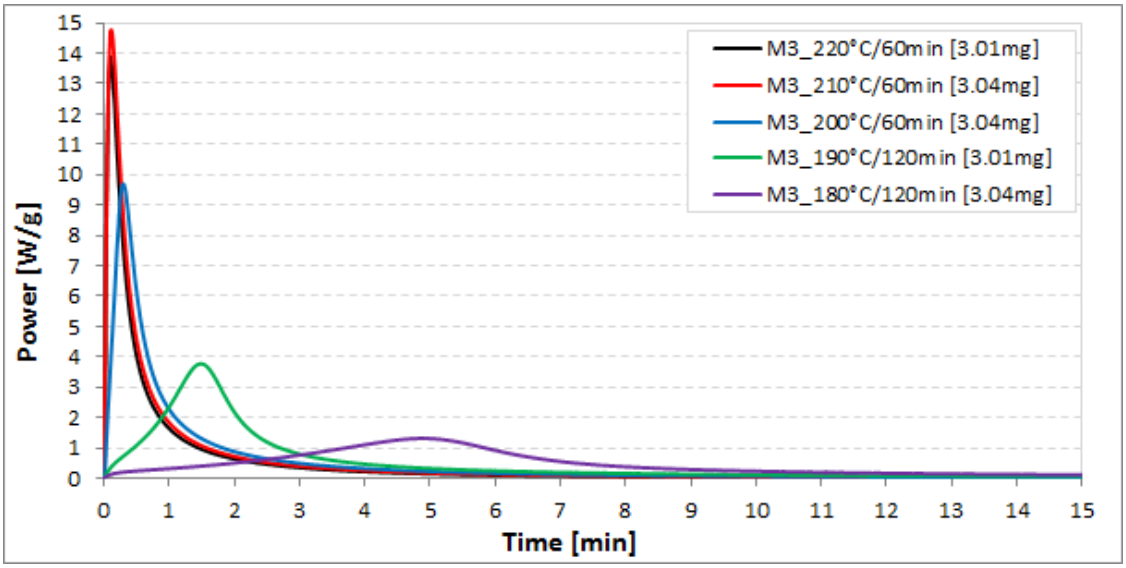

Figure 5-10 DSC isothermal heat flow curves of group M3 with well-controlled sample weights between 3.0mg and 5.5mg (only one out of three repeats is shown for each group to avoid crowding the diagrams).

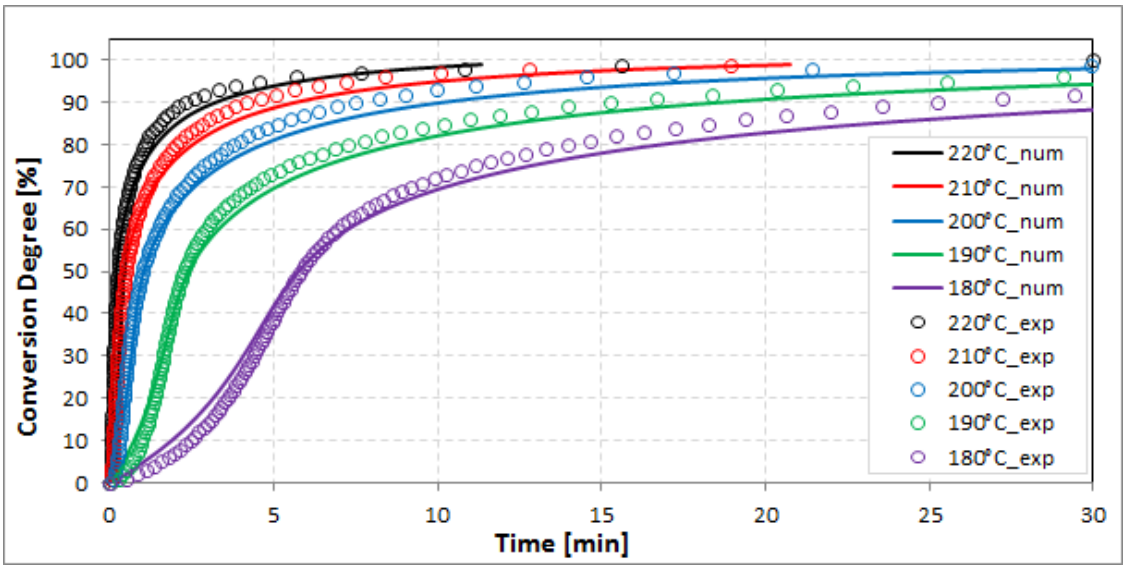

Figure 5-11 MFK isothermal numeric prediction vs. experiments for group M3 at various isothermal temperatures

5.2 Curing kinetics of CE688

5.2.1 DSC curing kinetics

The feasibility study of the MFK approach based on the model resin M3 was very successful because both the non-isothermal and isothermal predictions of M3 match its experimental data well, as shown in chapter 5.1. Therefore, the same methodology was applied to characterize the curing kinetics of the commercial epoxy system CE688. Figure 5-12 shows the non-isothermal and isothermal DSC heat flow curves respectively. Compared to the model resin M3 (Figure 5-5 and Figure 5-10), the reaction intensity of the commercial epoxy resin system CE688 was much less: e.g., the peak power at 6°C/min was only 0.23 W/g, as shown in Figure 5-12 (a), which was even less than the peak power of M3 at 1°C/min (0.85 W/g). The reaction rate of CE688 was much lower as well; it started at around 110°C and ended at 200°C-230°C, the required temperature increment was 90°C-120°C (M3 was 10°C-20°C). The lower intensity and bigger temperature range of reaction might contribute to the constant reaction enthalpy of cure at various heating rates since the hardener had more time to dissolve and react, as shown in Figure 5-13. Compared to the reaction enthalpy of group M3 (572±28J/g), CE688 showed very low enthalpy (37.51±1.15 J/g) which can be linked to its high amount of filler content (40~45%wt) and other possible additives. Another notable phenomenon is the relatively rougher heat flow curves in Figure 5-12 (a) compared to those in Figure 5-5 or to those in Figure 5-12 (b). It seems the reaction

speed was responsible for the smoothness: the polymerization is an exothermic reaction and the dissolution is endothermic; at higher heating rates or heating temperatures, polymerization will dominate the reaction and lead to smooth curves; however at lower heating rates, the influence from the dissolution becomes prominent and therefore rougher curves can be generated.

The isoconversion curves shown in Figure 5-14 (a) present very good linearity at each curing degree: the circles are the measured data; the lines are their corresponding best fitting lines and the lines which stand for the curing degrees at 10%, 50% and 90% are marked; the two grey vertical lines are the minimum and maximum isothermal temperatures predicted. The activation energy of CE688, as shown in Figure 5-14 (b), was lower than M3 and behaved differently with regard to curing degree: it needed 65KJ/mol energy to start the reaction; then it dropped quickly to a little bit below 64KJ/mol at 10% curing degree and kept constant till 30% cured; afterwards, the required activation energy increased constantly till the completion of the reaction and ended at 74KJ/mol.

The prediction of the non-isothermal reaction aligned very well with the experimental data, as shown in Figure 5-15. However, similar to the case of model resin M3, the isothermal prediction shows a relatively lower quality as presented in Figure 5-16. The prediction of curing at 220°C deviates most which was related to Figure 5-14 (a). The vertical line of 220°C has no intersection with those best fitting lines, which means that the prediction of 220°C was based on the extrapolation of those fitting lines and therefore was relatively inaccurate. The polymerization of epoxy resins is characterized by the gelation and the vitrification. Due to the formation of the 3D network, further progress of curing beyond vitrification will become more and more difficult. This event indicates that the cure kinetics at the later stage was subjected to diffusion control as a result of the vitrification. Experimental data after ~80% shows that a lower conversion degree is a sign of vitrification. This problem might be solved by introducing a diffusion factor, such as the semi-empirical relationship proposed by Fournier et al. [116] or Khanna and Chanda [117] based on the free volume consideration to extend the Kamal and Sourour model [115].

Furthermore, although it is common in the PCB industry to characterize the curing kinetics of prepregs via resin powder, especially in case of the presence of weak reaction peaks in the thermograms during polymerization, it might be better to use the prepregs directly since the influence from the glass-sizing composition on the epoxy curing behavior has been reported elsewhere [118, 119] despite the unclear mechanisms [119]. Therefore, for further work a closer study in this direction is recommended.

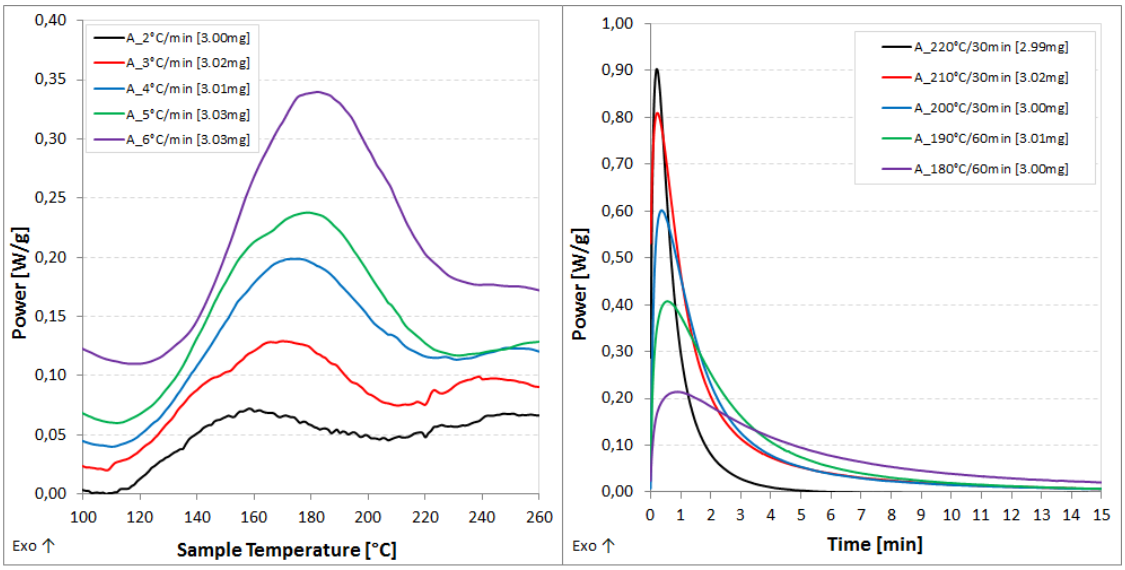

(a) (b)

Figure 5-12 DSC heat flow curves of CE688: (a) Dynamic heating (only one out three repeats is shown for each group to avoid crowding the diagrams); (b) Isothermal heating at various temperatures

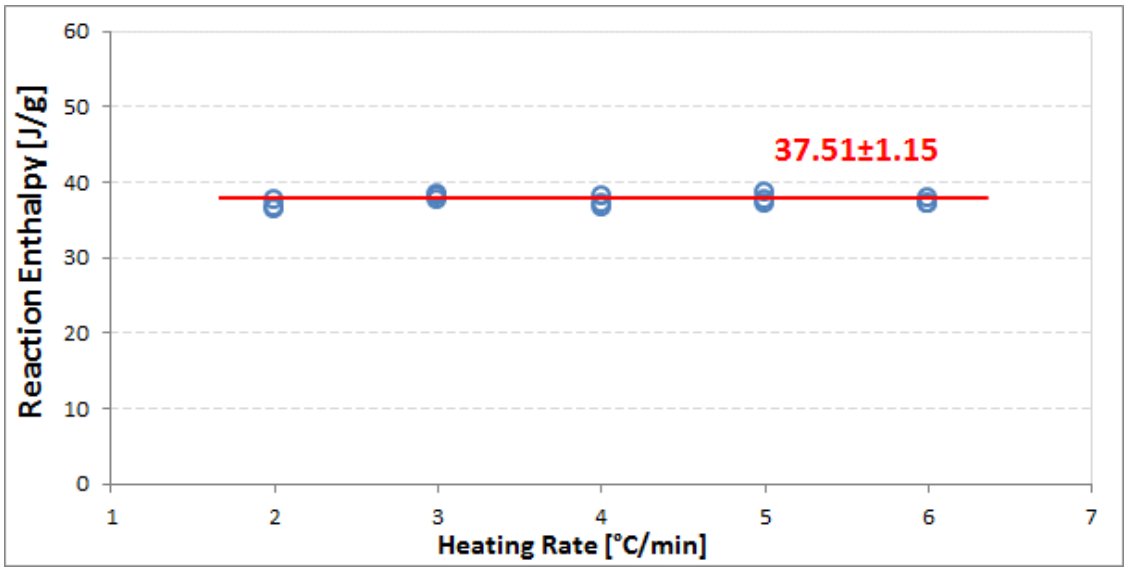

Figure 5-13 Reaction enthalpy of CE688 at various heating rates

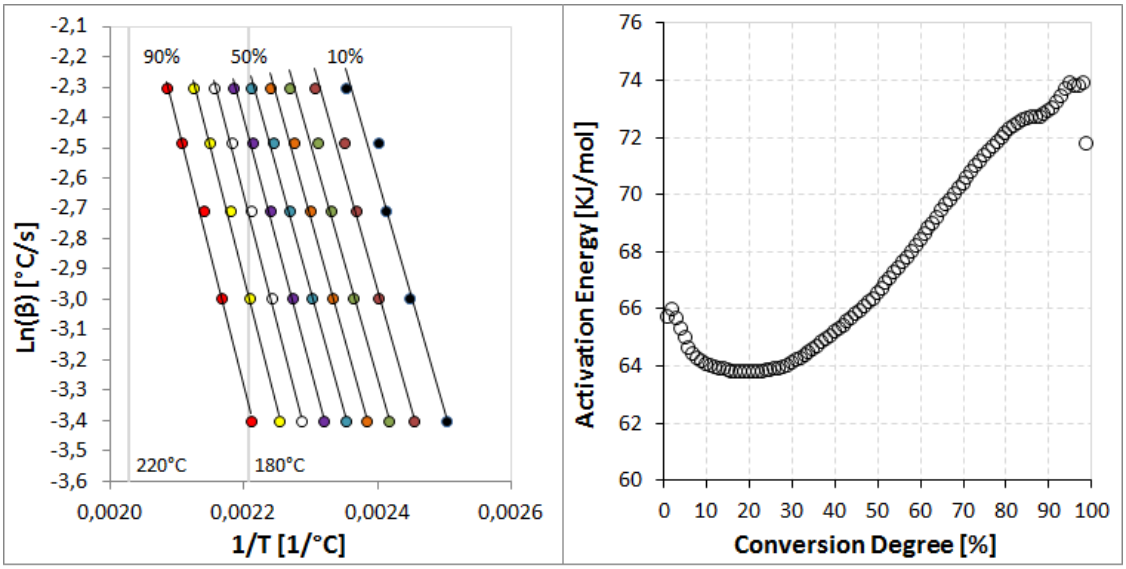

(a) (b)

Figure 5-14 MFK of CE688: (a) Isoconversion curves based on Ozawa-Flynn-Wall equation; (b) Activation energy calculated based on Ozawa-Flynn-Wall equation.

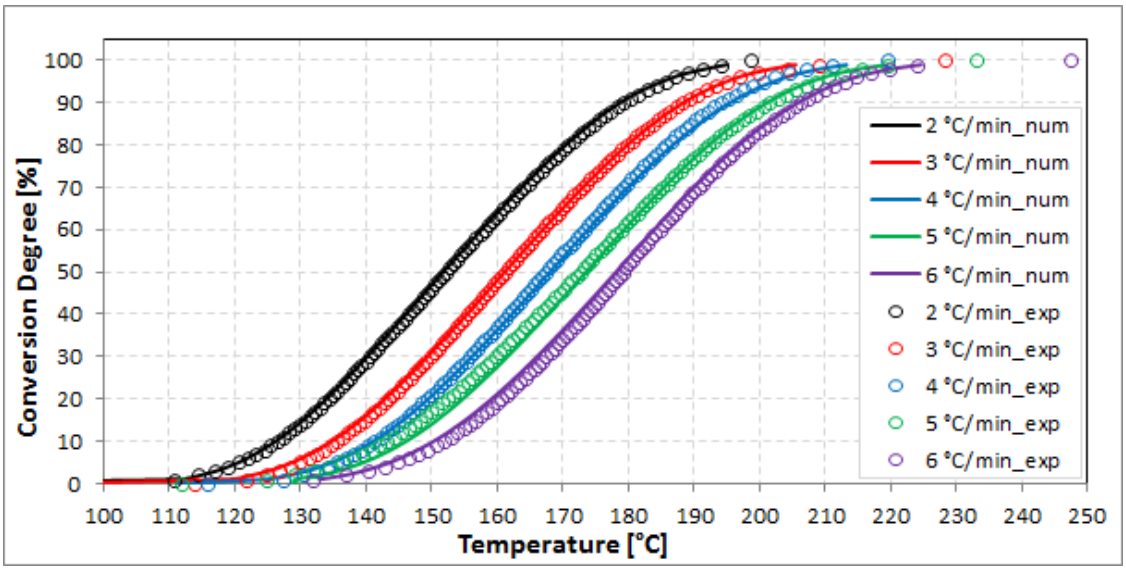

Figure 5-15 MFK non-isothermal numerical prediction vs. experiments for CE688 at different heating rates

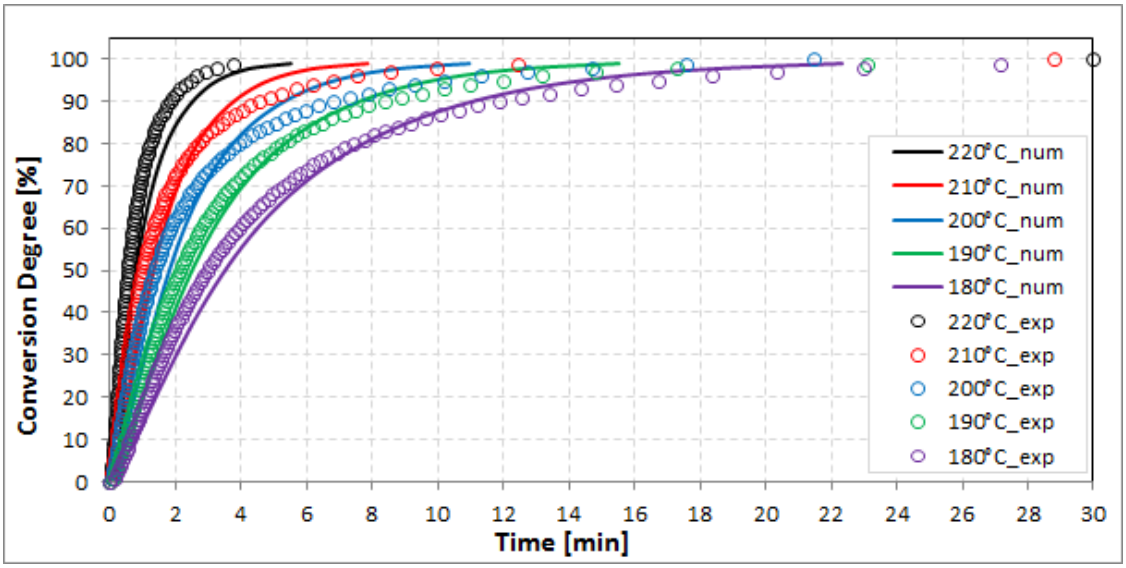

Figure 5-16 MFK isothermal numerical prediction vs. experiments for CE688 at various isothermal temperatures

5.2.2 FTIR curing kinetics

The development of the curing reactions can be identified in FTIR spectra. The representative IR spectra of CE688 at 190°C varying with time and the spectrum of pure DICY at RT are shown in Figure 5-17. The changes of absorption bands during curing can be clearly observed. There were three newly formed bands near 1650cm^{-1}, 1688cm^{-1} and 1728cm^{-1} as shown in Figure 5-18: the 1650cm^{-1} (c) band was assigned to an imino ester formed by the intermolecular addition of hydroxyl (a) to the DICY cyano (b) functionality (as shown in Figure 5-19), and/or by the intramolecular nucleophilic substitution of hydroxyl at the imide functionality; the absorption bands near 1688cm^{-1} and 1728cm^{-1} were assigned to carbonyls formed by the structural rearrangement of the imino esters into 2-oxazolidones and guanyl ureas, respectively [120, 112, 121].

The combination band of the second overtone of the epoxy ring stretching with the fundamental C-H stretching was centered at 4528cm^{-1} [23], as shown in Figure 5-20(a). The curing reaction also resulted in the shifts of the cyano group from 2205cm^{-1} to 2190cm^{-1} and N=C=N from 2158cm^{-1} to 2150cm^{-1} as presented in Figure 5-20(c). The band absorption intensities of both epoxy and DICY bands decreased as the curing developed. After 30min of curing at 190°C, the two peaks of DICY vanished and the epoxy peak remained slight. That means that DICY is stoichiometrically less than the epoxy in the chemical composition of CE688. Therefore, the two DICY bands at 2190 and 2150cm^{-1} were used as the reactant for the quantitative analysis.

Shrinkage during curing or initial sample thermostatting can lead to major errors in the integration of epoxy bands [23], hence, it is helpful to normalize the integrated areas to an invariable characteristic band in the curing, which corresponds to a chemical group not participating in the reaction. In this study, the band centered at 4070cm^{-1}, as shown in Figure 5-20(b), was chosen as the reference since its intensity stayed constant at 190°C. Although the chemical formula of the reference band was unknown since no information about the composition of CE688 could be obtained from the material supplier, it still enabled quantifying the evolution of the reaction according to Equation 3-12.

The peak areas of DICY and reference used for the kinetics study are 2125-2225 cm^{-1} and 4029-4105 cm^{-1} respectively. The obtained results are shown in Figure 5-21 as solid curves, and the dashed curves were the measured data from DSC for the purpose of comparison. The deviation of these two methods was very obvious if the kinetics curves were compared at the same temperature levels as shown in Figure 5-21(a), the conversion degree could have a difference of more than 20% which is not acceptable for engineering applications. However, if the comparisons were not performed at the same temperature levels, e.g., the FTIR curve measured at 190°C compared to the one at 170°C measured in DSC as seen in Figure 5-21(b), these two methods show very good alignment. The reason can be attributed to the effective curing temperature applied to the samples. The temperature control for the DSC-cured samples was normally accurate and reliable which was guaranteed by the design of the DSC device. However, the samples used for the FTIR analysis were cured in the big oven. There should be a certain temperature delay between the indicated value of the oven and the real temperature of the sample due to the time required for the heat transfer. Furthermore, the measurements of the FTIR samples at RT, instead of the curing temperature, also introduced another uncertainty to the measured data.

Nevertheless, the FTIR curing kinetics of CE688 was a valuable trial. It was not so successful, but it presented a good possibility for the future studies because there is still room for improvement.

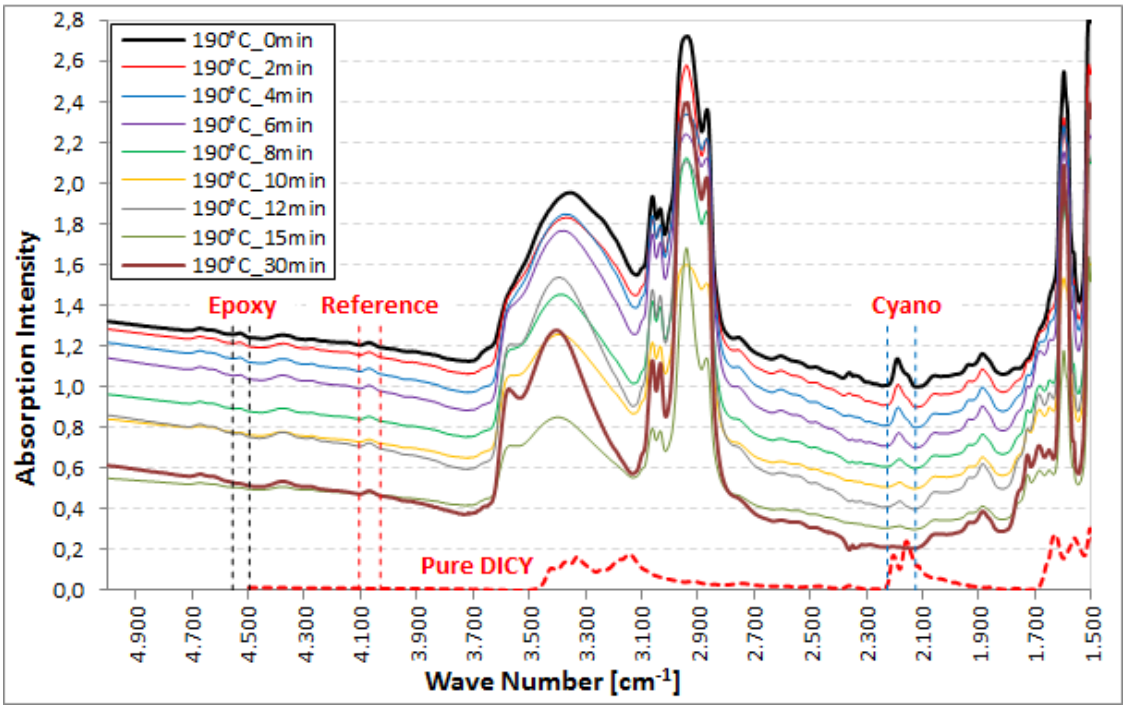

Figure 5-17 Evolution of the FTIR spectra of CE688 at 190°C and the pure DICY spectrum measured at room temperature as a reference

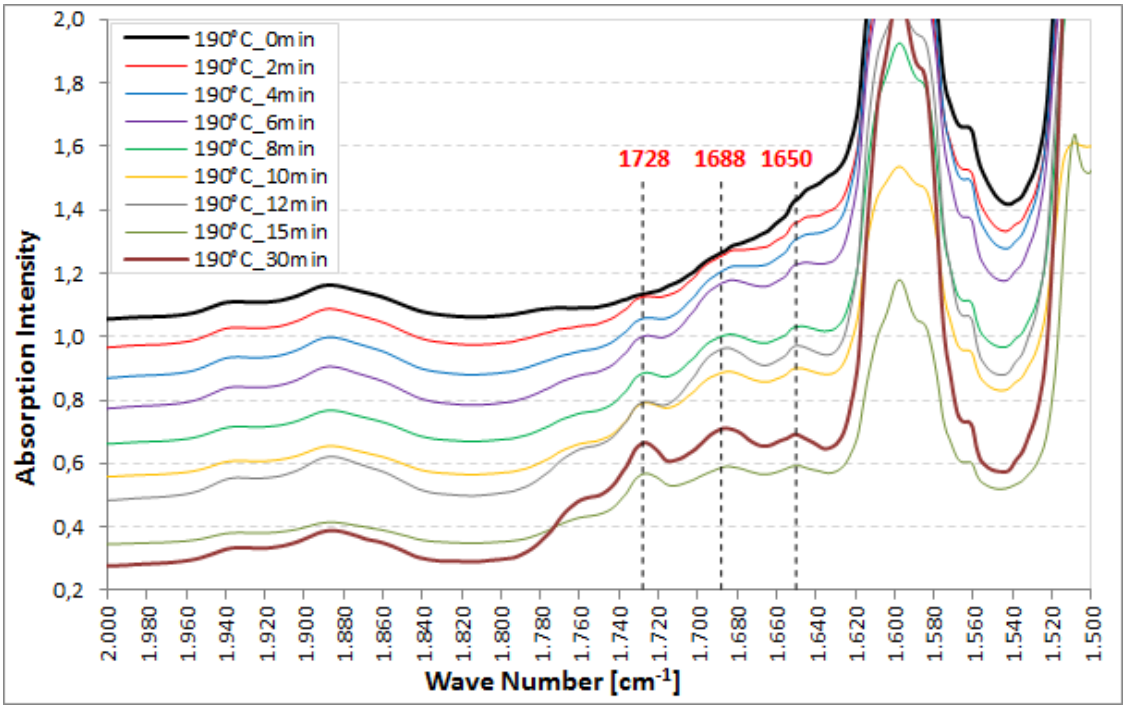

Figure 5-18 The formations of new absorbance bands near 1728, 1688 and 1650cm^{-1} during the isothermal curing of CE688 at 190°C

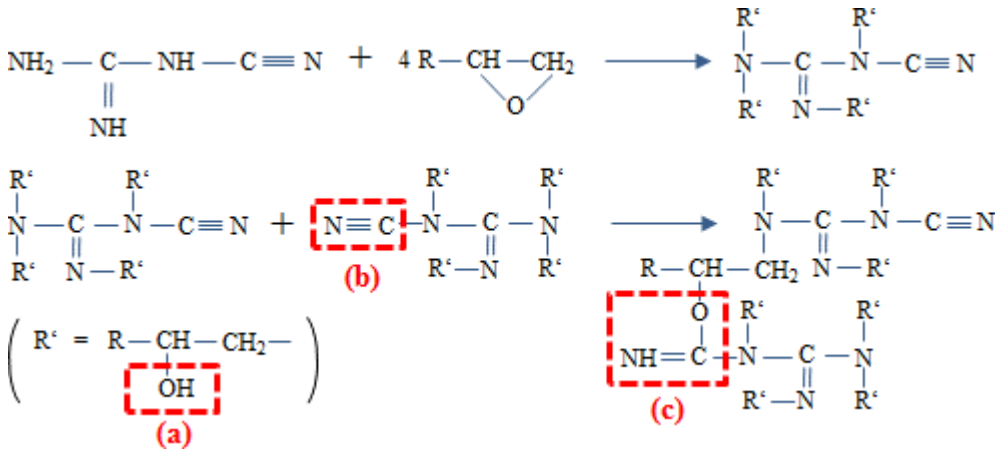

Figure 5-19 The formation of the 1650cm^{-1} band (c) in the reaction of DICY with epoxide

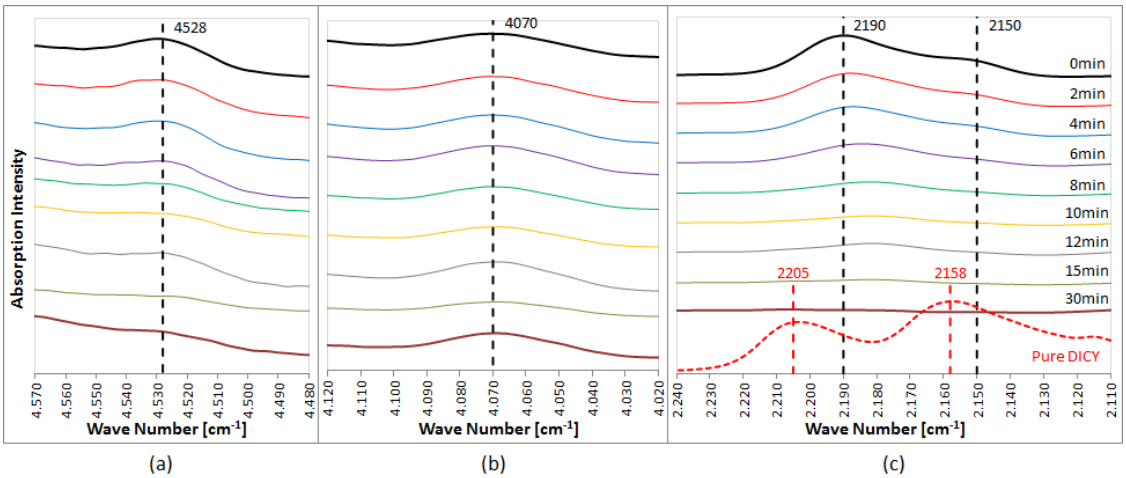

Figure 5-20 Evolution of the specific FTIR peaks of CE688 at 190°C: (a) Epoxy group centered at 4528cm^{-1}; (b) Reference group centered at 4070cm^{-1} (c) Shifts of cyano group from 2205cm^{-1} to 2190cm^{-1} and N=C=N from 2158cm^{-1} to 2150cm^{-1}

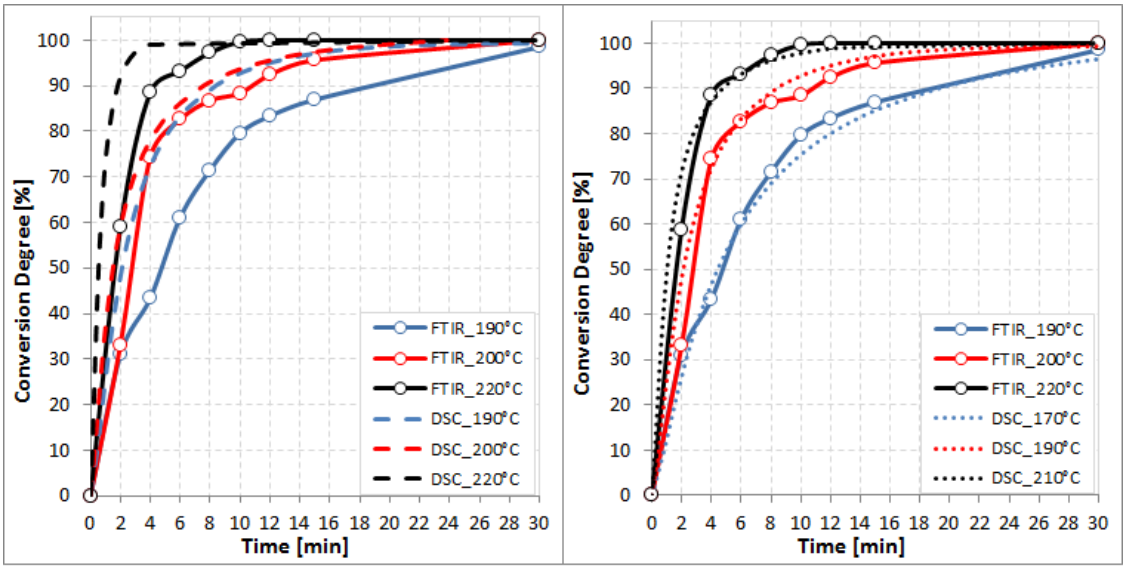

Figure 5-21 Comparison of isothermal curing prediction of CE688 between FTIR (based on the DICY peak at 2125 - 2150cm^{-1} and the reference peak at 4029-4105 cm^{-1}) and DSC: (a) at the same temperature levels; (b) at different temperature levels

5.2.3 Curing prediction in the press book

The predicted temperature profiles and the curing kinetics of both Node1 and Node2 (refer to Figure 4-7) are depicted in Figure 5-22. There are up to 10°C difference between the predicted and the measured temperatures in the range below 120°C. Afterwards, the prediction fits the measurements very well. Because the reaction started from >110°C according to Figure 5-15, the temperature discrepancy below 120°C can be ignored from the viewpoint of curing kinetics. It took around 90min to heat up the whole press book to the target isothermal temperature, i.e., 200°C. Since Node1 was closer to the heating plate, it was heated faster than Node2. The maximum temperature difference between both nodes in the ramp-up stage was around 10°C and there was no difference in the plateau stage. This was a quite satisfactory situation in terms of PCB lamination, because in some cases the maximum temperature difference between two laminates inside one press book can be up to 10-15°C in both ramp-up and holding stages [122].

The temperature increase between the 10th minute and the 60th was around 120°C; therefore the ramp-up speed was roughly 2.4°C/min. However, it can be clearly seen from both predicted and measured temperature profiles that the heating rate was not constant, which was mainly caused by the cushion papers. These special papers were placed between the heating plates and the stack-up of the laminates in order to stabilize the pressure when

the press book started to close.Their disadvantage lay in the fact that they hindered the heat transfer significantly because they were thick (3.0mm, refer to Figure 4-7) and were made of materials with low thermal conductivity (0.05W/m/K, refer to Table 4-2) materials. This was the reason that the setting temperature of the heating plates (solid green curve in Figure 5-22) was much higher.

The traditional MFK curing kinetics can predict the curing procedure of either non-isothermal heating with a fixed heating rate or isothermal heating. Nevertheless, with the newly developed methodology, as described in Chapter 3.5, it is possible to simulate the curing kinetics of the prepregs inside the press book. The curing kinetics of Node1 and Node2 were plotted in Figure 5-22 as examples, and the overview of the temperature and the curing status of the whole stack-up at three different moments were shown in Figure 5-23. The simulation results indicated that the curing started after about the 39min and stopped after about 88min. Due to the temperature difference between these two locations, their curing degrees deviated from each other by a maximum of 12.5%, which occurred after 55min. However, there was no difference among the whole stack-up after 90 minutes of curing. In terms of the samples prepared for the study, except the group pressed with a cycle time reduction of 90 minutes (or, when the cooling starts after 75min in Figure 5-22) showed slightly less curing (~97%), all others (standard, -30min, -60min) were fully cured according to the simulation.

The curing prediction of the CE688 in the press book showed a good overview of the curing status of the whole stack-up. It was also the basis for the design of the experiments in this study.

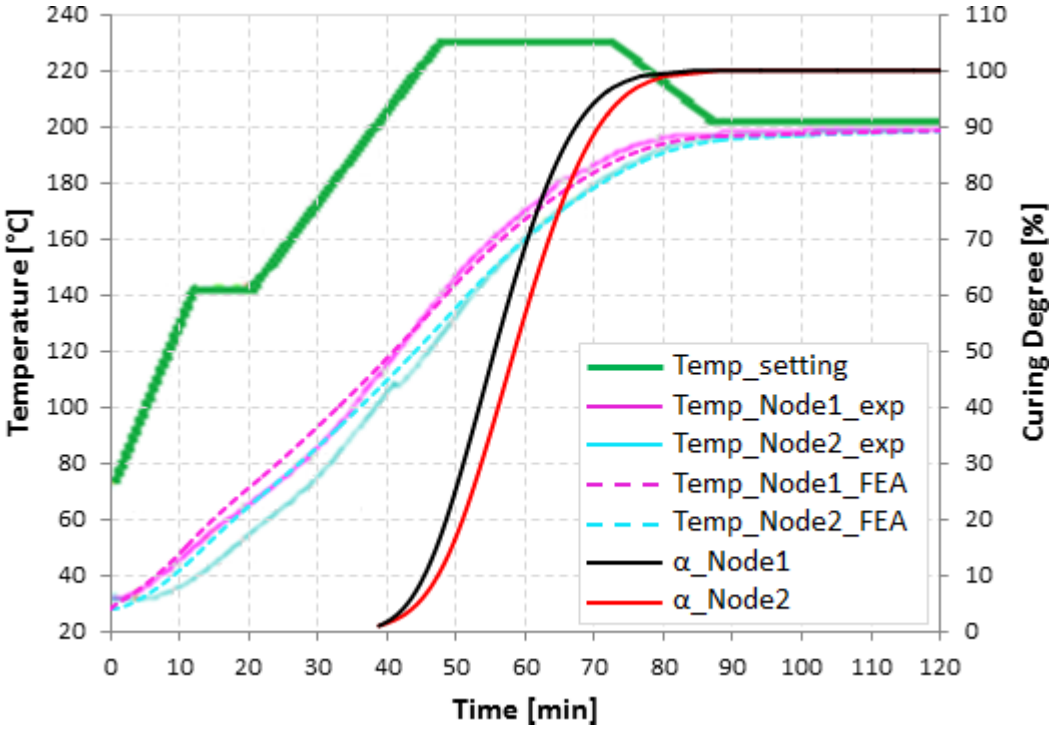

Figure 5-22 Simulation results for the curing kinetics of CE688 in the press book

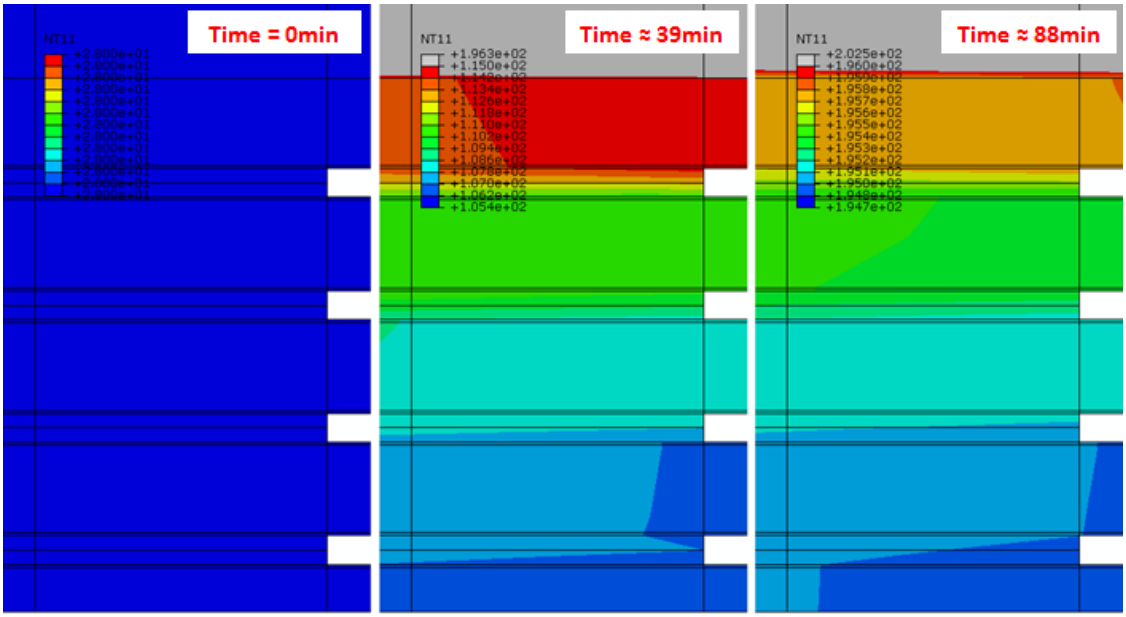

(a)

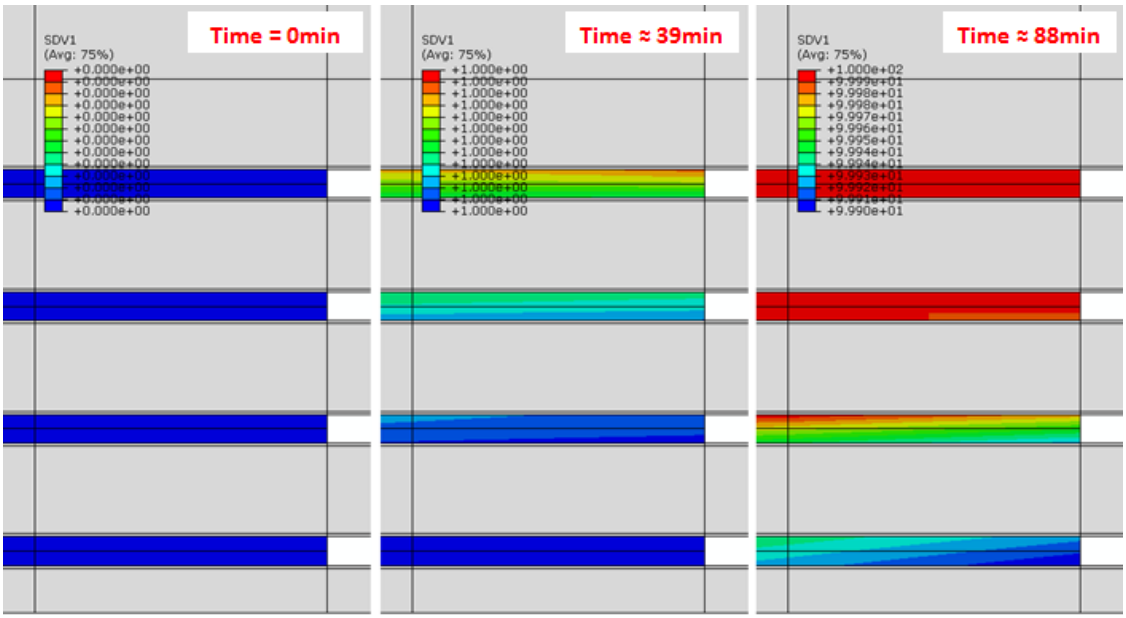

(b)

Figure 5-23 Simulation results of the CE688 prepregs in the press book in terms of (a) temperature and (b) curing degree at three different moments

5.3 Effect of press cycle time reduction

5.3.1 Mechanical properties

5.3.1.1 Monotonic tensile test (Dumbbell)

The tensile test results for all the specimens are depicted in Figure 5-24. Both pure resin (group A) and glass fiber reinforced prepreg (group B) behaved in a brittle manner under ambient conditions (Figure 5-24 (a)). Figure 5-24 (b) depicts the elastic moduli of all samples, i.e., the slopes of the least-squares regression lines fit to the deformation range between 0.05% and 0.25% [76]. The pure resin had a Young's modulus of around 5000MPa, which aligned quite well with the measured DMA storage modulus shown in Figure 5-27. The glass fibers enhanced the modulus almost by a factor of 3 and the average value was about 14000MPa. However, the fracture strains and stresses will be higher than the values shown in the chart, because all the samples failed at the areas near the shoulder of the dumbbell specimens as shown in Figure 5-25. All samples were routed out from their original sheet forms. To avoid being sucked away by the applied vacuum during routing, two bridges near the shoulders had to be kept. Although the burrs were manually ground off after removal of the specimens from the sheets, they obviously affected the tensile test results. These design-introduced failures have to be excluded in future studies. Nevertheless, the Young's moduli were still valid for the study.

No significant influence could be found among group B00, B30 and B90. This means that the Young's modulus will not vary with a slightly uncured status since B90 was ~97% cured and the other two were fully cured according to the curing kinetics study. Moreover, the 10x reflow did not change the moduli of any of the three samples, which showed a good resistance to thermal ageing.

The linear region of the stress-strain curve of the pure resin sample, which might consist of the region of elastic and linear viscoelastic deformation during tensile test, ends at around 1% as shown in Figure 5-26 (a): the former corresponds to changes in atomic distance and valence angle in the macromolecule while simultaneously storing elastic potential energy and is typically very small (<0.1%); the latter relates to the mechanically stimulated molecular rearranging processes in which the existing molecular links are not released [123]. The linear region of the curve from the prepreg sample is relatively smaller (0.6%) due to the influence of the glass fibers. Both secant moduli continuously dropped very fast as the strain increased, as shown in Figure 5-26 (b): it decreased from 15500MPa to 9600MPa with the increase of the strain from 0% to 1.8% for B30R and the changing rate was about 38%; the resin sample had a nearly 60% reduction of the secant modulus at failure. Normally, the calculated Young's modulus according to ISO meets the simulation requirement quite well, since the deformations of the resin/prepregs are small. But for large deformation cases, the Young's modulus might need to be adapted in order to reduce the error for simulation. For instances, there will be a 10% and 26% over-estimated stress at 1.5% and 2.2% of strain respectively by comparing the tangent line to the measured curve for the pure resin A00 in Figure 5-26 (a).

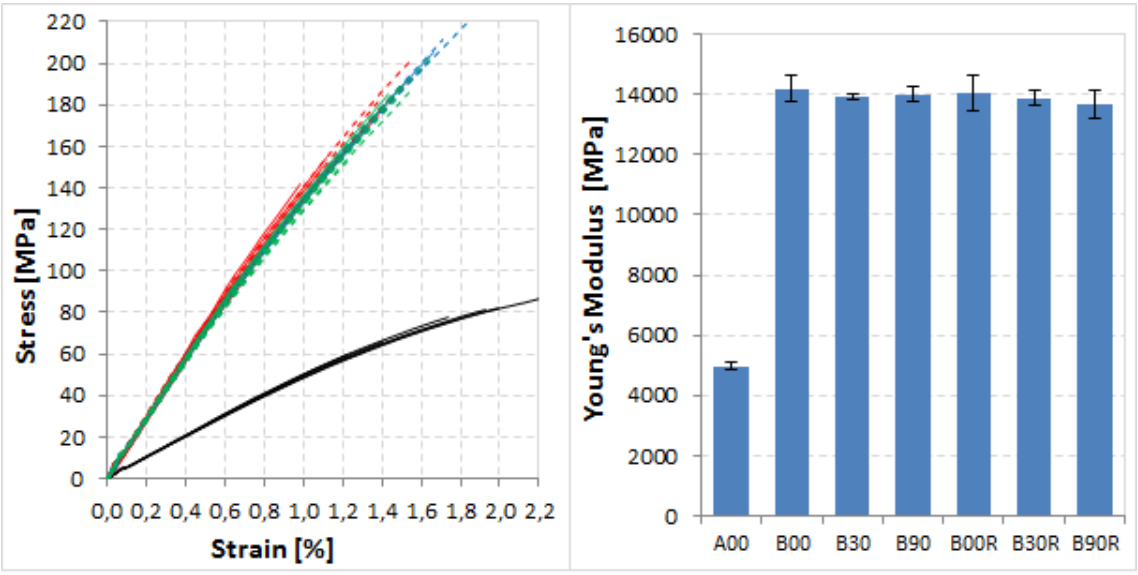

(a) (b)

Figure 5-24 Mechanical property – tensile test: (a) Stress-strain curve; (b) Young's modulus.

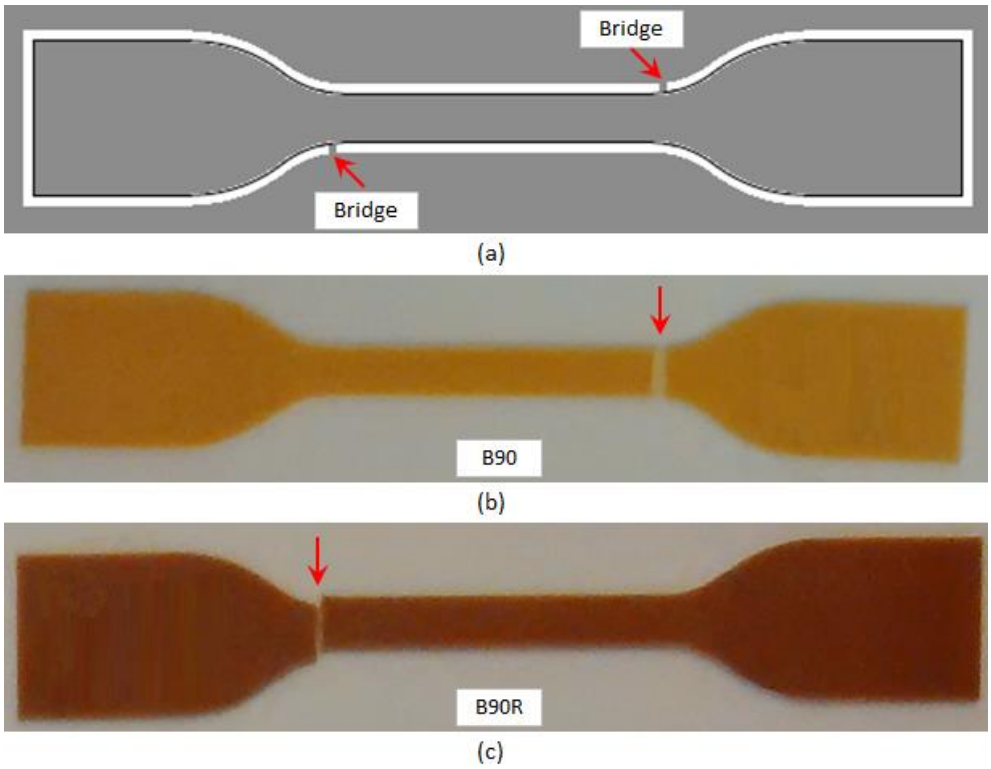

Figure 5-25 Tensile test samples: (a) two bridges near the shoulders remained after routing; (b) Sample failed near the right bridge; (c) Sample failed near the left bridge.

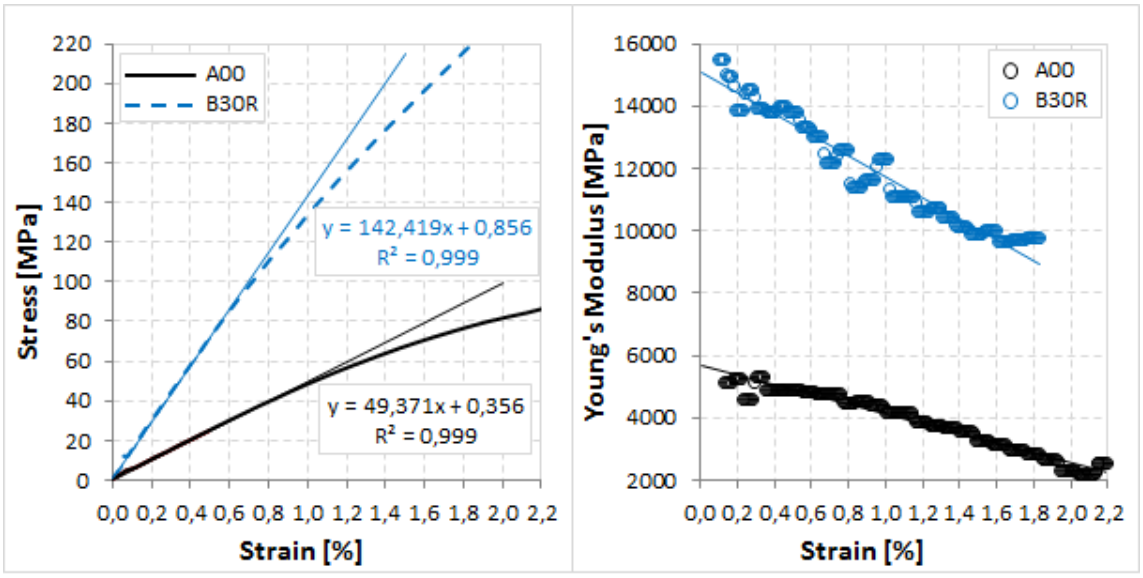

Figure 5-26 Mechanical property – tensile test: (a) Stress-strain curve of A00 and B30R and their tangent lines used for the calculation of the Young's modulus; (b) Secant E-modulus of A00 and B30R

5.3.1.2 Dynamic Mechanical Analysis (DMA)

The glass transition is one of the most important factors in the material characterization as the properties of the resins/prepregs are highly dependent on the relationship of the PCB end-use temperature to its Tg. Generally, three different glass transition temperatures can be calculated from the DMA analysis and each has its own physical meaning as exemplified in Figure 5-27, based on A00: 1) Tg_s is the extrapolated onset temperature of the decrease of storage modulus (E'), which defines the temperature at which the material strength will begin to decrease so that the material may no longer be able to bear a load without deformation; 2) Tg_l is the peak maximum of loss modulus (E''), which represents the temperature at which the polymer material undergoes the maximum change in mobility of the polymer chains and corresponds to the chemical definition of the glass transition temperature.; 3) Tg_t is the peak maximum of loss factor (tanδ), which characterizes the damping of a material and has its historical importance, since it was the very first property measured by DMA. Normally these temperatures are ranked in the order $Tg\_s < Tg\_l < Tg\_t$ and the first one, Tg_s, is recommended by the ASTM [124] standard.

However the measurements based on the extrapolated onset have greater uncertainty than those based on the peak maxima because the former rely on the selection of the starting points of the tangent lines and the latter are independent of the interpretation of the operator and rely on the physical changes of the material [125]. Hence, no Tg analysis based on Tg_s was made in this study.

Table 5-1 lists the average Tg values of all measured samples in terms of Tg_l and Tg_t. The DMA curves of the prepregs and test PCB samples are depicted in Figure 5-28 and Figure 5-29, respectively. Generally, it can be seen that the Tg values based on those peak maximums were quite reproducible within the same group. Depending on the sample form, the Tg values of the samples pressed by the standard program varies quite significantly: e.g., Tg_ls of A00, B00 and C00 were 159.2°C, 178.0°C and 185.7°C respectively. This can be related to the following two factors: 1) the difference in sample thickness. The thicker the sample, the longer it takes for reaching the programmed temperature. A00 had a thickness of 1mm, which was almost twice that of B00 and therefore more time is required for achieving the same cross-linking level. 2) the second factor is the number of pressings. A00

and B00 were pressed once, however, C00 was pressed three times and hence its Tg was the highest. Moreover, although the total thicknesses of C00 was similar to B00 (~0.53mm), each time only one layer of prepreg with 0.04 – 0.05mm was pressed, as shown in Figure 4-4. According to the prediction results in Figure 5-22, only B90 was not fully cured and therefore its Tg was 8.7°C lower than B00. But on the other hand, both B30 and C30 showed ~2°C lower Tgs than B00 and C00 respectively which conflicted with the simulation results. This might be linked to the sensitivity of the thermal analysis techniques. As concluded by Foreman et al. [125], based on their study of characterizing the Tg for amorphous polymers by means of five thermal analysis techniques (DSC, modulated DSC, TMA, DMA and Dielectric Analysis), DMA was the most sensitive technique for measuring the Tg. That means, the prediction on the basis of DSC curing kinetics might not be "correct" if validated with the DMA method. However, in terms of engineering applications, as long as the final Tg of the product is higher than the minimum Tg requirement, the slight differences can be ignored. Finally, it can be seen that the 10x reflow can increase the Tg_l temperature via enhancing the cross-linking density, but not significantly (~1°C) except that the sample was not fully cured (8.9°C for B90).

Table 5-1 Average Tg_l and Tg_t of each group based on the DMA analysis

Group	Tg_l	Tg_t	Group	Tg_l	Tg_t
A00	159.2	177.5	--	--	--
B00	178.9	186.0	B00R	178.5	185.6
B30	177.0	185.8	B30R	178.6	185.4
B90	170.2	178.1	B90R	179.1	188.7
C00	185.7	191.7	C00R	187.3	192.3
C30	181.8	188.5	C30R	182.5	190.3
C60	183.8	189.3	C60R	184.7	190.3

The tanδ/T curves of A00 samples were much higher and narrower than the samples from group B and C, indicating a more uniform network in pure resin samples [126]. Another noticeable difference to those from group C was that they all showed shoulders before the maximum peak which indicates that the curing status of the prepregs inside the PCB buildup varied from one to the other: the inner layers should have had higher Tgs than the outer layers since they were pressed one or two times more often.

Generally, the storage modulus matched the cross-linking status of the sample. That means the higher the Tg the greater the modulus, as shown in Figure 5-28 and Figure 5-29.

Meanwhile, the moduli were slightly higher after 10x reflow. However, the reproducibility of the DMA storage modulus was not good compared with the monotonic tensile test due to the influence of the clamping and in the real application, it is common to calibrate the DMA storage modulus curves based on the measured elastic modulus from the tensile test.

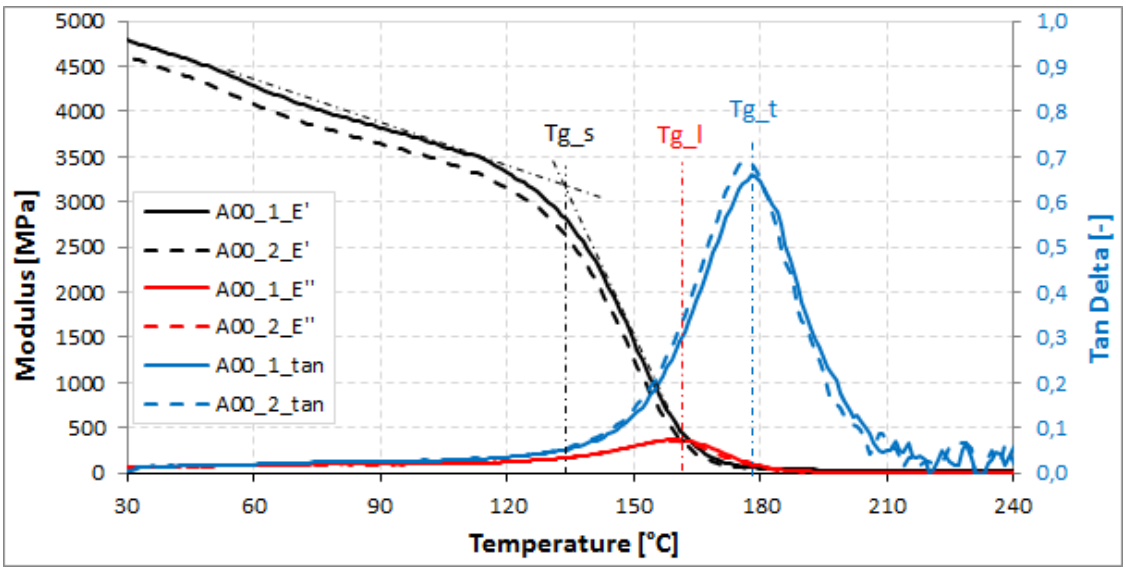

Figure 5-27 Mechanical property – DMA of A00 in terms of storage moduli (E'), loss moduli (E'') and tangents delta (tan)

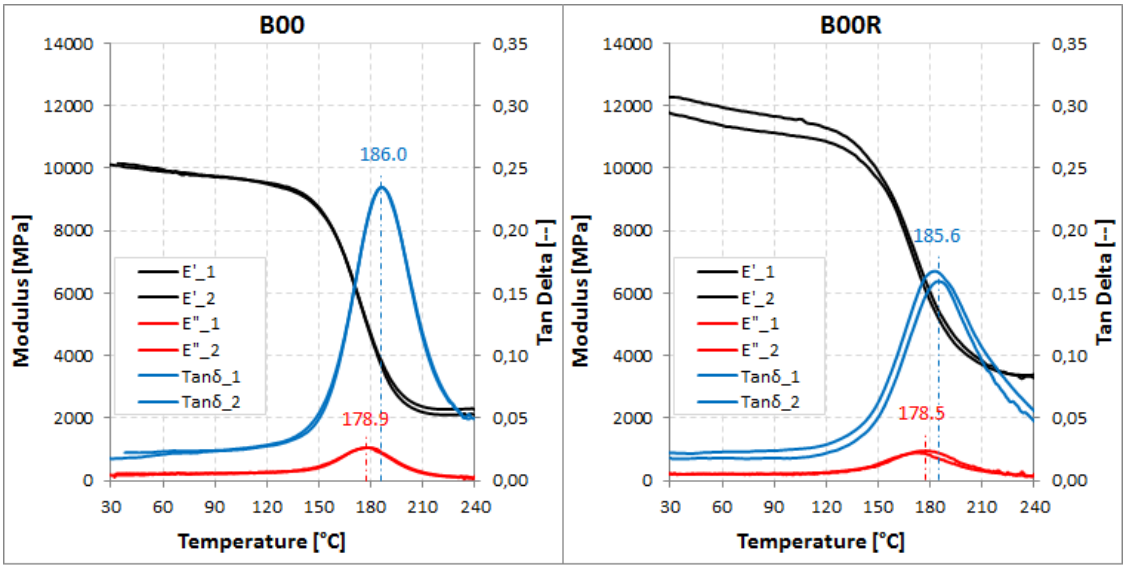

(a)

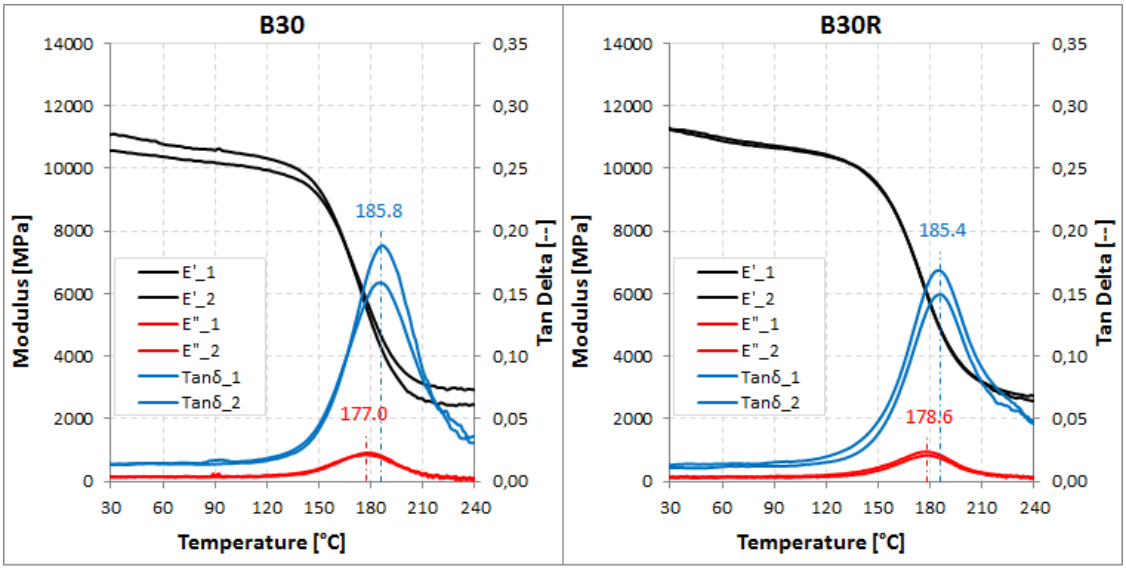

(b)

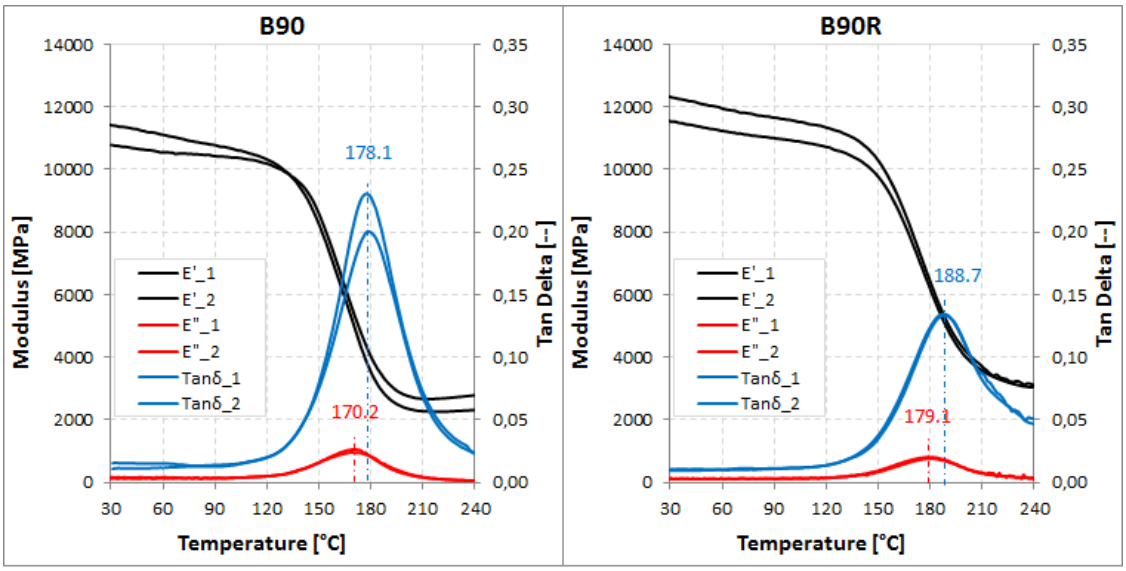

(c)

Figure 5-28 Mechanical property – DMA results of prepreg samples as received and after 10x reflowed: (a) B00/B00R, (b) B30/B30R and (c) B90/B90R

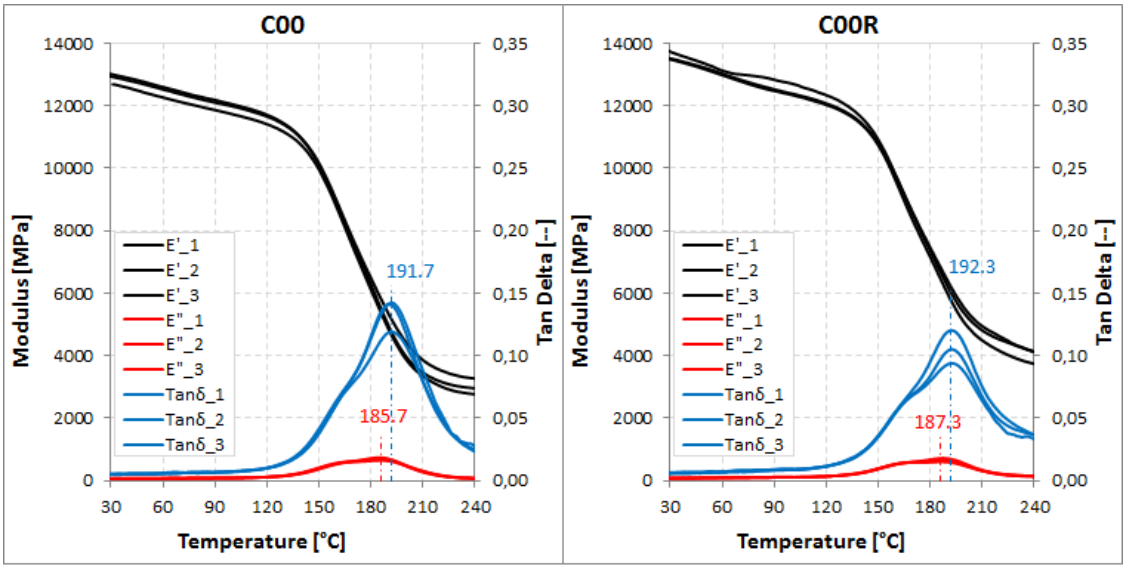
C00
C00R
Modulus [MPa]
Tan Delta [--]
Temperature [°C]
E'_1
E'_2
E'_3
E"_1
E"_2
E"_3
Tanδ_1
Tanδ_2
Tanδ_3
191.7
185.7
192.3
187.3

(a)

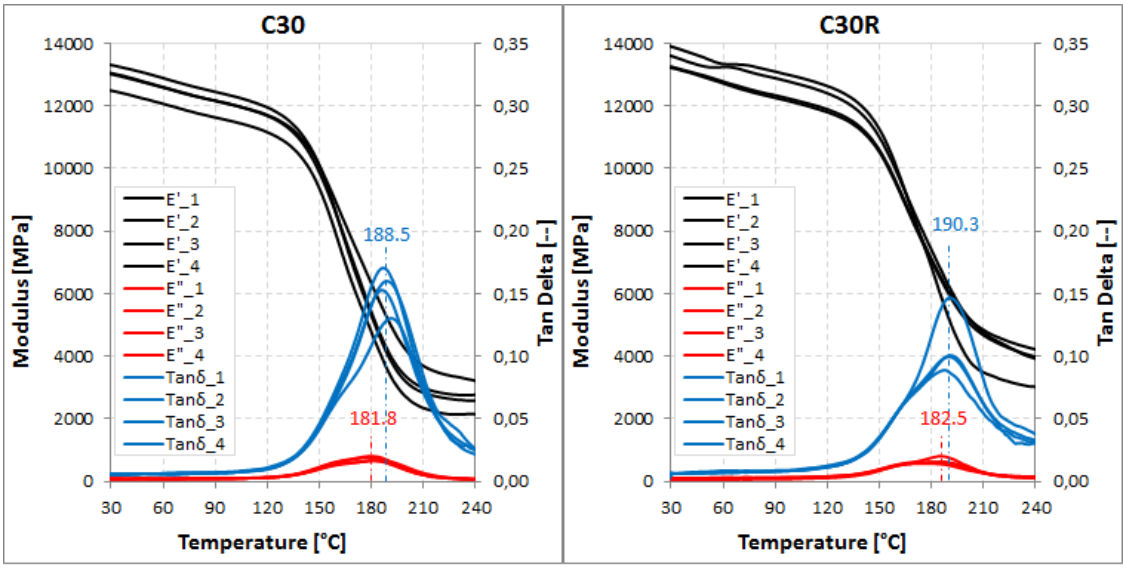
C30
C30R
Modulus [MPa]
Tan Delta [--]
Temperature [°C]
E'_1
E'_2
E'_3
E'_4
E"_1
E"_2
E"_3
E"_4
Tanδ_1
Tanδ_2
Tanδ_3
Tanδ_4
188.5
181.8
190.3
182.5

(b)

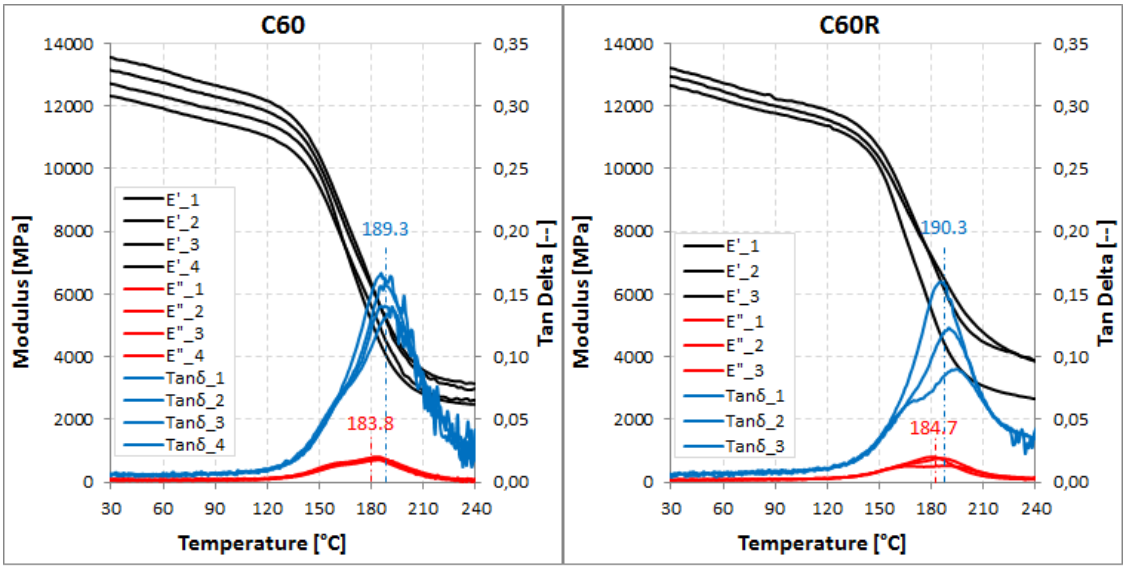
C60
C60R
Modulus [MPa]
Tan Delta [--]
Temperature [°C]
E'_1
E'_2
E'_3
E'_4
E"_1
E"_2
E"_3
E"_4
Tanδ_1
Tanδ_2
Tanδ_3
Tanδ_4
189.3
183.8
190.3
184.7

(c)

Figure 5-29 Mechanical property – DMA results of test PCB samples as received and after 10x reflowed: (a) C00/C00R, (b) C30/C30R and (c) C60/C60R

5.3.2 Thermal properties

Although DMA is a more sensitive technique than DSC and TMA in terms of the Tg measurement [125], DSC and TMA are more commonly used in the PCB industry owing to their easy operation, fast measurement and high reliability.

5.3.2.1 Differential Scanning Calorimetry (DSC)

Figure 5-30 shows the DSC Tg results of the pure resin samples non-isothermally and isothermally cured in the DSC, as described in chapter 4.4.2.1 and the Tg specification (>150°C) for the quality control. It is interesting to see that the Tg of CE688 epoxy resin grew with the increase of the curing time for non-isothermal heating (lower heating rates have longer heating times) or with the increase of the curing temperature for isothermal heating and all of them met the requirement specified by the data sheet. It is also clear that both the non-isothermal and isothermal DSC thermograms, as shown in Figure 5-12, indicate that the reactions had been completed (or, DSC could not detect anymore). This might be related to the dissolution rate of the hardener during the reaction. At higher heating rates or heating temperatures, the hardener could dissolve relatively faster and start to build up the 3D network earlier. As presented in Figure 5-16, once the curing progressed beyond vitrification (~80% curing degree), the further reaction will be dominated by the diffusion of the reactants and therefore the speed will be significantly reduced. The post heating, such as reflow, will increase the cross-link density. But in reality the effect will not be significant due to the limited time.

An additional confirmation experiment was performed in a third-party laboratory by nuclear magnetic resonance (NMR) with the magic sandwich echo (MSE) method on the standard pressed pure resin (A00) in order to check its cross-linking status, since NMR can detect the mobility of the side chains. The result impressively demonstrated that the mobility of the side chains continuously dropped at 200°C even after 200 minutes as depicted in Figure 5-31, which means that the curing process can last much longer than the standard lamination program suggested by the material supplier. However, this does not mean that the press cycle time must be extended, because the Tg temperatures were already above the criteria as shown by the red line in Figure 5-30.

Another remarkable phenomenon was that the first derivate of the DSC thermograms of the isothermally cured samples were much smoother than those of the non-isothermally cured one as exemplified in Figure 5-32. Further investigations should be carried out beyond this study since this might be an indicator of a different curing mechanism between these two heating schemes.

Figure 5-33 presents the Tg1, Tg2 and Tg3 from the 1st, 2nd and 3rd run respectively for all the samples based on the P130 DSC program (refer to Figure 4-11). According to the material specification, all Tg temperatures should be above 150°C (red line). But the results were rather frustrating, since almost no sample could pass the criteria in terms of Tg1. On the other hand there were also some unreasonable points which needed to be clarified. For example, if the Tg2 and Tg3 of the B00 samples were already in specification after the 1st run (50°C-220°C) in DSC, there was no reason why the Tg1 of B00R was out of specification after 10x reflow (30°C-260°C). This doubt triggered further investigations and it was interesting to see that the dual-effect of cooling rate and annealing on the endothermic peak in the DSC scan of CE688 epoxy resin played a big role in the DSC Tg evaluation. For instance, since B00 samples were cooled in the press book and B00R were cooled in the reflow oven, the former can be treated as slow-cooled (~2°C/min, refer to Figure 4-2) and the latter can be regarded as shock-cooled (>100K/min, refer to Figure 4-3). In terms of the slow-cooled samples (B00), the influence of the annealing, which was introduced by the DSC program P105 or P130, cannot be observed (solid curves in Figure 5-34). However, for the shock-cooled samples (B00R), it can be clearly seen that the intensity of the endothermic peak was in proportion to the annealing temperature and the position of the peak shifted to a higher temperature when the annealing temperature or time increased.

Based on the investigation of the dual-effects of cooling rate and annealing, it became clear that the different thermal history of the CE688 epoxy and different DSC method will produce different levels of enthalpy relaxation in the sample and result in different endothermic peaks in terms of intensity and position. Meanwhile, the closer the position to the Tg region and the greater the intensity of the peak, the bigger the influence on the Tg evaluation will be. The preheating at 130°C in P130 was too close to the Tg region and caused the lower Tg temperatures in Figure 5-33. Finally, P105 was chosen as the improved method. All the related details have been described in the attached paper [99], only the final results, which were much better and more reasonable, were presented in Figure 5-34. It can be clearly seen that except for the not fully cured B90, Tg1 from all other groups were within specification. This matches the MFK curing prediction very well. ΔTg1 from the as-received

groups (B00, B30, C00, C30, C60) were still obviously bigger than ΔTg2. This might be related to the curing pressure in the lamination process. As suggested by K. Nakamae, et al. [127], the high pressure would restrict the diffusion and collision of molecules and result in longer curing times. But the insufficiency would almost be recovered after the first run in the DSC measurement. That means only the freshly cured prepregs would have such "pressure" effects in the first DSC run, the 10x reflowed samples would not.

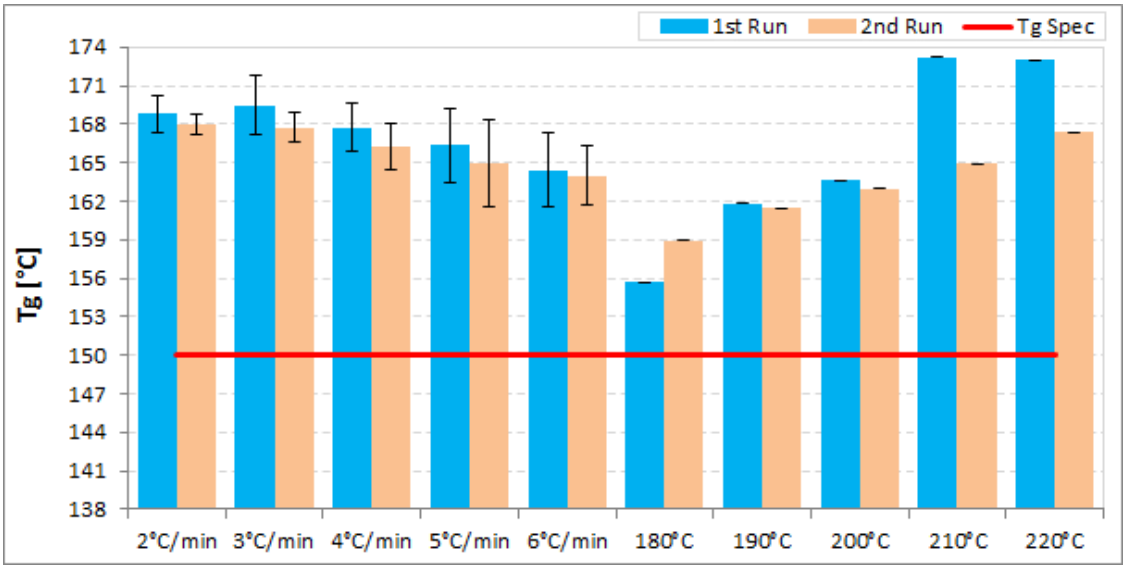

Figure 5-30 DSC Tg check for the pure resin samples directly after the non-isothermal and isothermal curing in DSC for curing kinetic studies

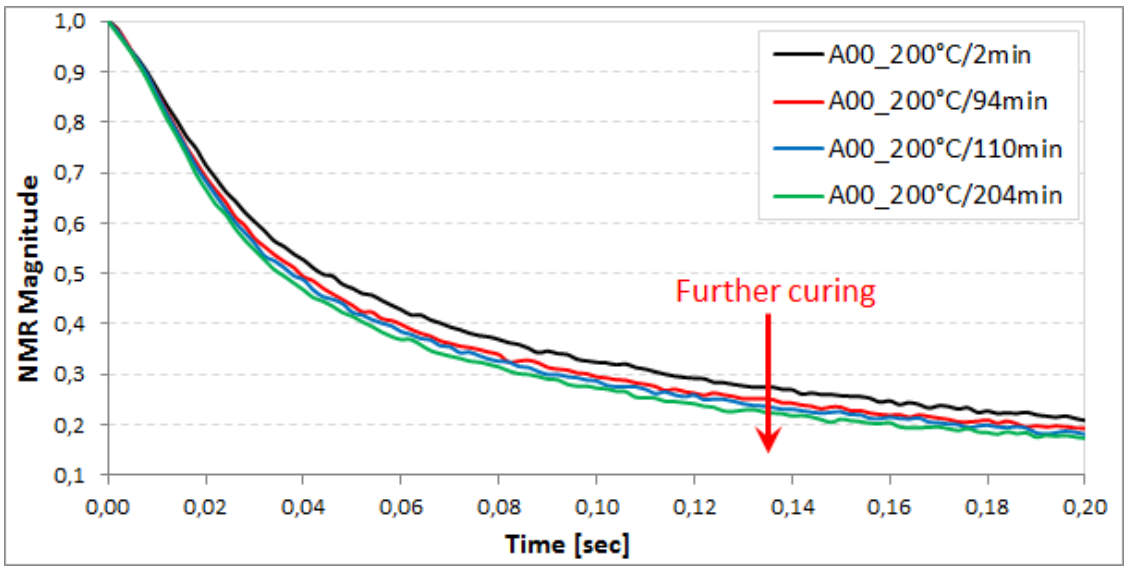

Figure 5-31 The NMR results show that the mobility of the side chains of the standard pressed pure resin sample (A00) continuously decreased at 200°C which evidenced further curing

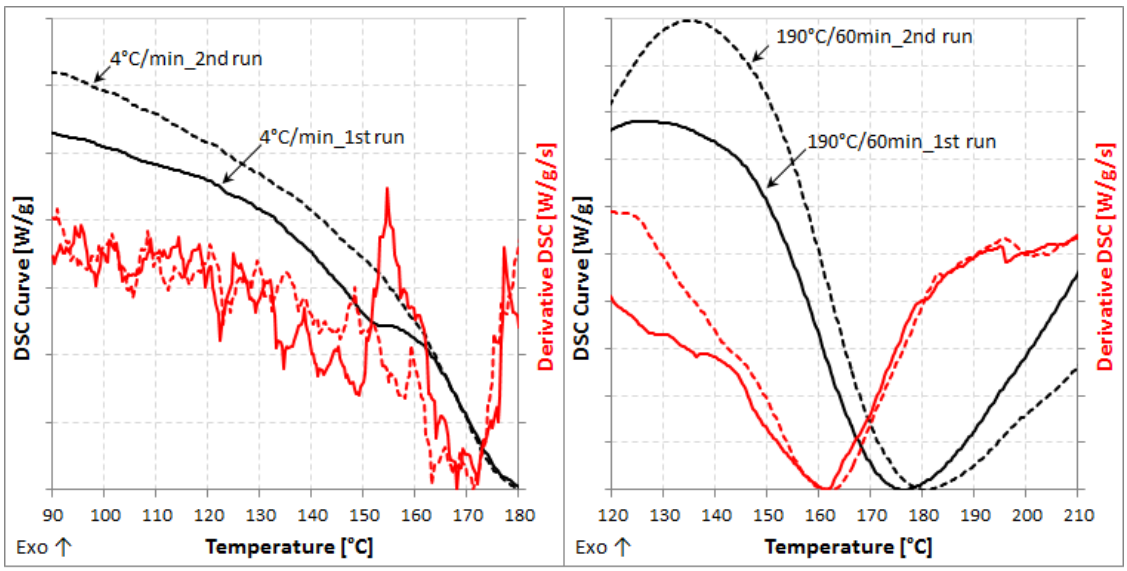

Figure 5-32 The first derivative of the DSC curves for (a) the samples non-isothermally and (b) isothermally cured in the DSC showed that the former is typically much rougher than the latter

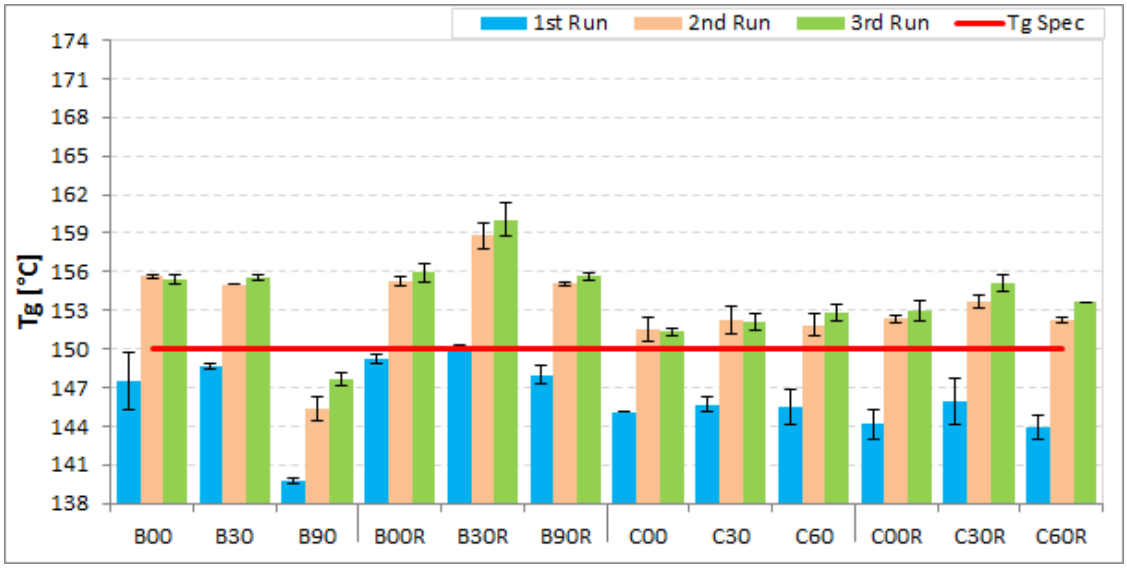

Figure 5-33 Thermal property – DSC Tg measured according to the standard internal test method (P130)

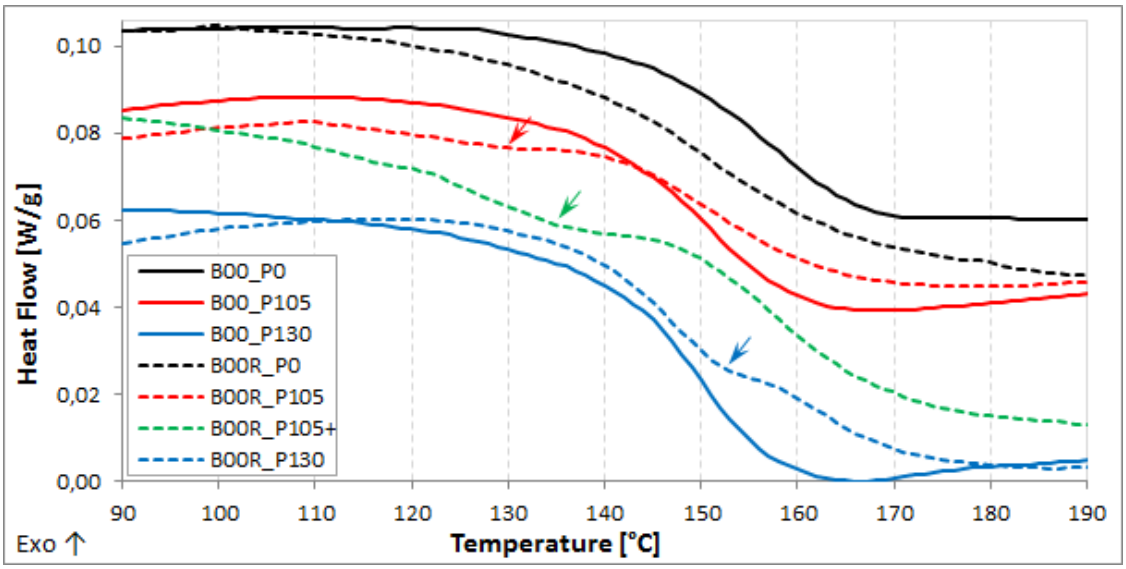

Figure 5-34 Dual-effect of cooling rate and annealing on the endothermic peaks in the DSC curves of CE688 prepreg samples which were cured in the press machine with 2°C/min cooling rate (B00) and reflowed with >100°C/min cooling rate (B00R)

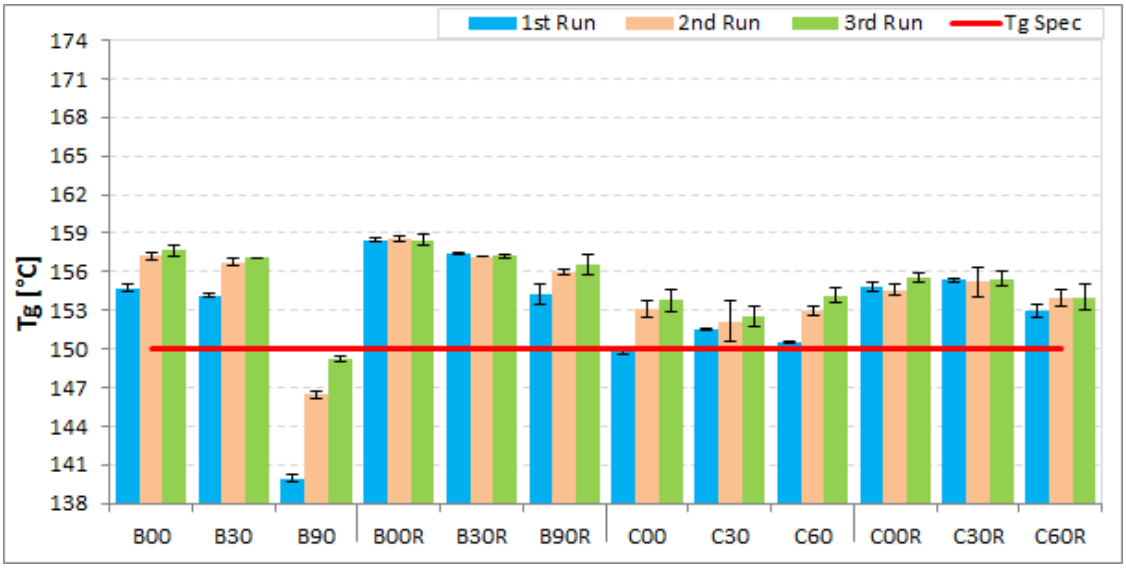

Figure 5-35 Thermal property – DSC Tg measured according to the improved test method (P105)

5.3.2.2 Thermal Mechanical Analysis (TMA)

A typical TMA scanning with three runs is depicted in Figure 5-36. The second and third runs presented a bilinear curve as expected. The first part can be used for calculating the coefficient of thermal expansion before Tg (CTE1) and the second part for CTE after Tg (CTE2) and their intersection is defined as Tg as exemplified by the third run in the figure.

The sharp drop from the 1st run (black curve) was observed for almost all the measurements. This phenomenon has been reported by other authors as well: Zarrelli et al. [14] reported that the partially cured epoxy resin will have a shoulder immediately after the Tg which indicates the onset of the residual reaction; Naito and Todd [18] studied the moisture penetration of the surface of an epoxy/anhydride material and found that the moisture will form a thermoplastic-like linear polymer on the surface which can be penetrated by the probe of the TMA at temperatures above its Tg; Salam et al. [128] pointed out that the segmental motion of molecules after Tg can be reduced by increasing the cross link density of epoxy polymer samples; Li et al. [129] considered the sharp drop as the consequence of the relaxation of the "frozen-in" free volume and internal stress in the epoxy sample once the sample was heated up to a certain temperature. Besides the sharp drop, there were shift-downs, i.e., the curves from the 2nd and 3rd runs shifted down a little bit compared to the 1st and 2nd runs respectively. In order to quantify the thickness changes, ΔL1 is defined as the sharp change of the sample in the Tg region during the 1st run; ΔL2/ΔL3 is the thickness difference between the 1st / 2nd and 2nd / 3rd run at 190°C. Taking the reference thickness, L0, from the one at 90°C in the 1st run, the dimension change rate can be calculated based on Equation 5-1:

$$D1 = \frac{\Delta L1}{L0} \times 100\%;\ D2 = \frac{\Delta L2}{L0} \times 100\%;\ D3 = \frac{\Delta L3}{L0} \times 100\%$$

Equation 5-1

Figure 5-37 summarizes the dimension change rates of the prepreg and test PCB samples. Before reflow, all samples had greater dimensional changes in the 1st run (D1) than the other two runs (D2, D3); after 10x reflow, the test PCB samples had much less D1s. The curing effect did not play a role in the dimension change, since B90 showed no difference from the others. However, this might be due to its relatively high curing degree (~97%, refer to Figure 5-22) as well. The large distribution of D1 in B00 and B90 showed that the homogeneity of curing condition in prepreg samples was worse than in the test PCBs. This can be attributed to the fact that the test PCBs had been pressed three times rather than one time which was the case of the prepreg samples. The D1s of C00, C30 and C60 showed an obvious tendency that the longer the press cycle the less the dimension change in the 1st TMA run. This can be related to the internal stress, as suggested by Li et al. [129], since a longer cycle time at high temperatures (200°C in this study) allows the polymer segments to relax more thoroughly. Furthermore, the small D2s and D3s (about 0.2%) might be an indicator of the free volume change due to further curing as depicted in Figure 5-38: the TMA Tg from the 3rd runs (Tg3) were all 1°C-3°C higher than the 2nd runs (Tg2) except B90 which was not fully cured.

Nevertheless, a further study beyond this work in terms of dimensional changes during TMA measurements is suggested because the conclusions mentioned above need to be validated with more samples.

If we ignore the dimension change between the 3rd and 2nd runs, in other words, if the curve of the 3rd run is shifted to the one from the 2nd run so that the thicknesses at the reference temperature (90°C) are the same, as shown in Figure 5-39, we can see that the two curves from each group almost overlap except the one from B90. This phenomenon was quite interesting and the reason was clear: the uncured part had more free volume and could expand more after Tg temperature. Moreover, this obvious difference in CTE2 due to insufficient curing can only be seen in this way, the calculated CTE values also showed a difference (~8 ppm/°C) but not that remarkable compared to the other groups as shown in Figure 5-40.

The same fact is shown in Figure 5-37 that Tg3 was higher than Tg2 for all samples. CTE2s from the 3rd runs were also higher than the ones from the 2nd runs. No differences in CTE1s were discernible which is logical since the free volume will expand much less below the Tg temperature. It seems that the mean CTE2 has a relation to the press cycle time as marked by the red arrows in Figure 5-40: for instance, a 30min reduction of the cycle time will cause the mean CTE2 increase of 18.5 ppm/°C for the prepreg samples and 6.0ppm/°C for the test PCBs. Besides, for both groups B and C, 10x reflow can significantly reduce the mean CTE2 values which shows the ageing effect. For example, the difference between B00/C00 and B00R/C00R was 21.5/19.7ppm/°C. However, in order to confirm the above-mentioned conclusion, more samples are required from the statistics point of view.

Finally, in order to have a good overview of the Tg measurements by these three different methods, the average measured values have been put together as shown in Figure 5-41: DMA Tgs are taken from the peak maximum of the loss modulus; DSC Tgs are calculated from the 2nd run for the purpose of excluding the influences from the pressure; TMA Tgs are extracted from Tg2 as well. Tgs from these three methods are ranked in the order Tg_DMA > Tg_DSC > Tg_TMA. Generally, these methods showed similar results: 1) Tg of B90 was always the lowest due to its insufficient curing; 2) 10x reflow increased the Tg temperatures more or less by introducing additional curing, as proved by the NMR measurements; 3) the reduction of press cycle time by 30min or 60min should influence the Tg of CE688, but this slight difference can be ignored since its DSC Tg is already above the criteria. However, there is a big difference between the DMA and DSC/TMA in terms of the Tg measurements for the test PCB samples. For example, C00 and C30 had higher DMA Tg temperatures

compared to their counter parts (B00 and B30), while their DSC/TMA measurements showed the opposite situation. This was caused by the different sensitivities of the devices. As mentioned by Foreman et al. [125], DMA was the most sensitive technique for measuring the Tg of amorphous polymers. The curing conditions in the C00/C30 samples were not homogenous thanks to the multiple press, and two peaks in both loss modulus and tangent delta curves could be detected by DMA as shown in Figure 5-29. However, the DMA Tg only considered the maximum peak temperatures by definition, which means the higher cross-linked part in the samples. In contrast, DSC/TMA measurements could not distinguish the cross-linking inhomogeneity in the sample, therefore their results were somehow "averaged" values of the Tg temperatures and should be relatively lower.

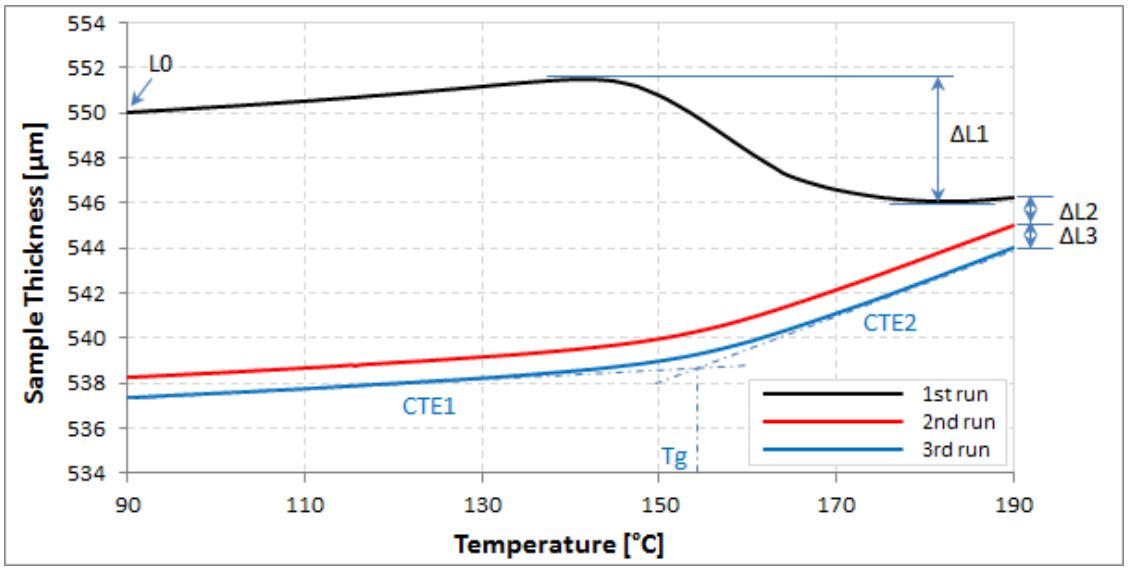

Figure 5-36 A typical TMA scanning with three runs

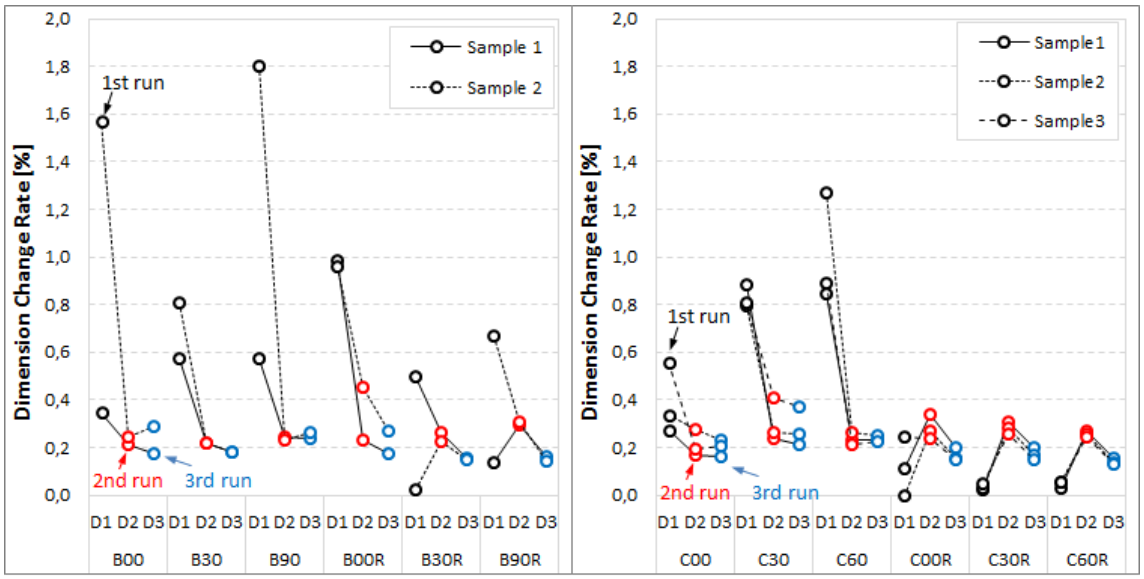

Figure 5-37 Dimension change rate of (a) each prepreg and (b) test PCB sample measured in TMA

Figure 5-38 Thermal property – TMA Tg values from the 2nd and 3rd runs

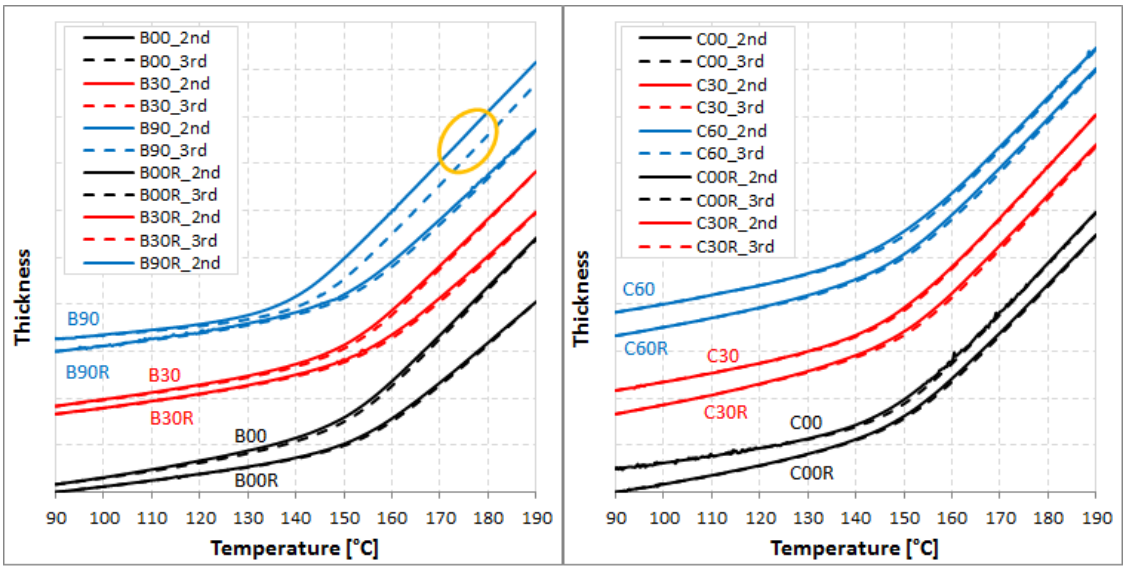

Figure 5-39 TMA curves by shifting the curves from the 3rd runs to the 2nd runs so that that the thicknesses at the reference temperature (90°C) were the same

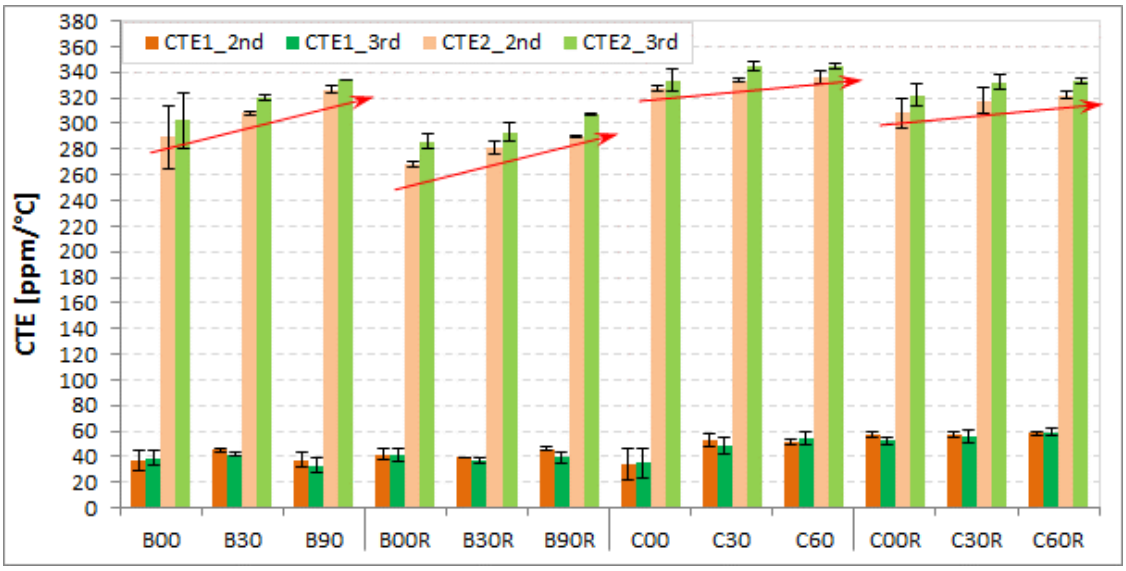

Figure 5-40 Thermal property – TMA CTE before (CTE1) and after (CTE2) Tg values from the 2nd and 3rd runs

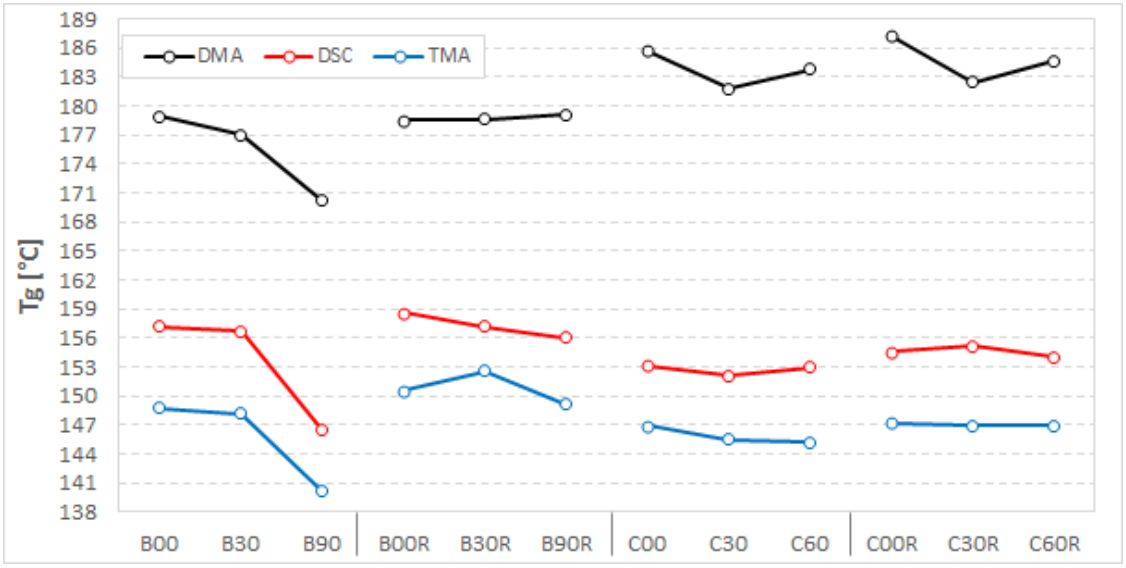

Figure 5-41 Average Tg values measured with DMA (from loss modulus), DSC (from 2nd run) and TMA (from 2nd run)

5.3.2.3 Thermogravimetric Analysis (TGA)

The TGA curves obtained at heating rates of 3, 5, 8, 10 and 15°C/min for the prepreg samples representing non-organic residual mass versus temperatures are shown in Figure 5-42 and Figure 5-43. In general all samples decomposed in a similar way and all curves show that the thermal degradation took place in one stage, which started at around 290°C and ended at around 540°C. Similar to the DSC non-isothermal heat flow curves as shown in Figure 5-5, all TGA curves shifted to higher temperatures with increasing heating rates which is common in polymer decomposition studies [69, 130, 131]. Although the final residual weights were quite similar for all samples (~ 63.5%), differences before and after 10x reflow can be seen as depicted in Figure 5-44. Assuming the residual weight at 800°C was independent of the heating rates, 10 measurement points (2 times 5 different heating rates) per sample type can be used for calculating the residual weight. Statistically the difference between B00 and B00R is significant and the 10x reflow reduced the organic ratio of B00 by ~2.5%. This might be linked to the change of the mass density of the epoxy resin system in the prepreg, because further curing [132] and physical ageing [48], which might have occurred based on the above-mentioned DMA, DSC and TMA measurements, will lead to an increase of the mass density. In contrast, the difference of the average residual weight between B30/B90 and B30R/B90R is not significant, which might be concealed by the relatively greater distribution of the measurements. However, it might be worth doing a

further investigation in order to have a closer look at the relationship between the residual weight and the mass density.

Model-free decomposition kinetics for all the prepreg samples were performed in line with chapter 3.4, but limited to max 30%, because in practice up to 5% decomposition is required according to IPC standards [133]. The isoconversion curves of B00, as an example, showed in Figure 5-45 (a) present very good linearity at each curing degree >1%: the circles are the measured data; the lines are their corresponding best fitting lines and the lines stand for the curing degrees at 1, 2, 3, 5, 10, 15, 20, 25 and 30% are marked. The activation energy for all samples, as shown in Figure 5-45 (b), behaves equally the same: it grew with increasing decomposition rate and the slope was steeper below 8% decomposition degree.; the activation energy started from ~ 120KJ/mol and ended at ~240KJ/mol on average.

The predictions of the non-isothermal and isothermal decomposition of all the prepreg samples are quite similar as well, especially in the range of interest (<5%) as shown in Figure 5-46. The prediction results show that CE688 has an excellent thermal stability: it will not decompose until 295°C if it is heated with 3°C/min; even at 260°C, it will take at least 50min for decomposition.

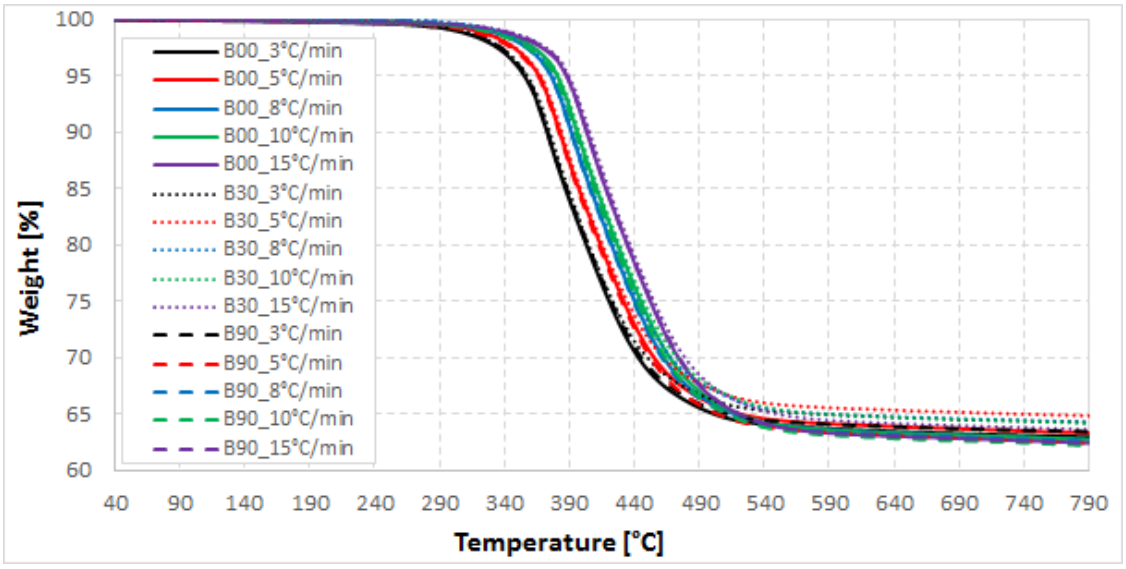

Figure 5-42 TGA curves for B00, B30 and B90 at various heating rates

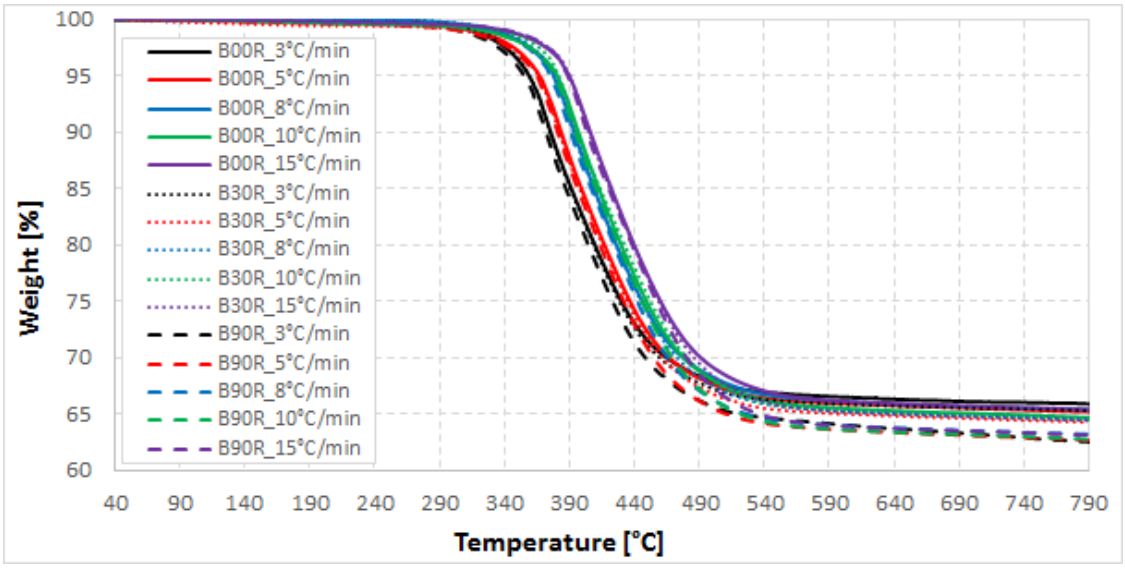

Figure 5-43 TGA curves for B00R, B30R and B90R at various heating rates

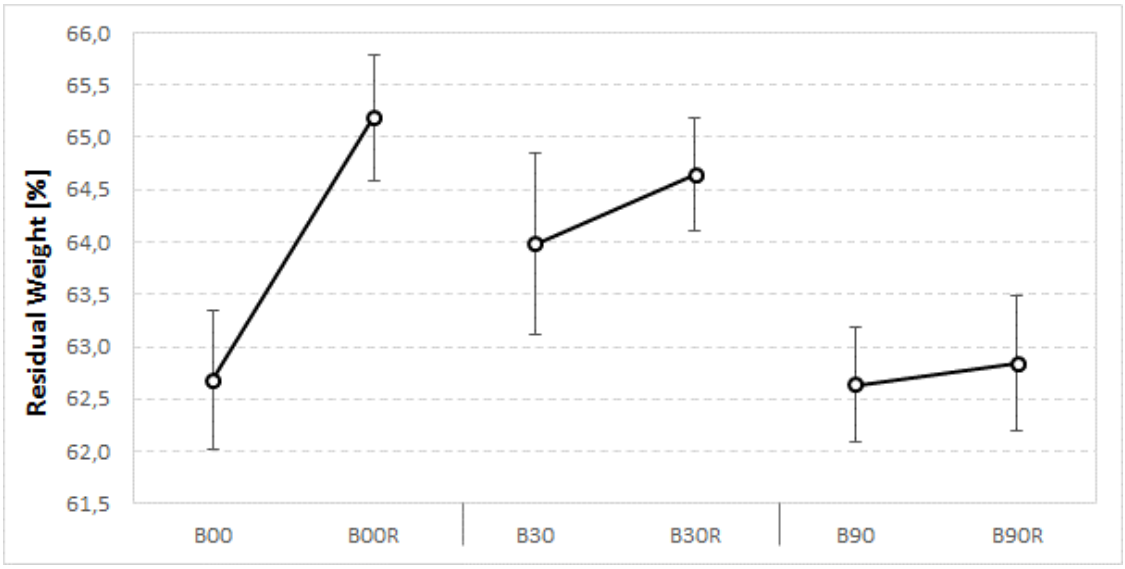

Figure 5-44 Residual weight of all prepreg samples after TGA measurements

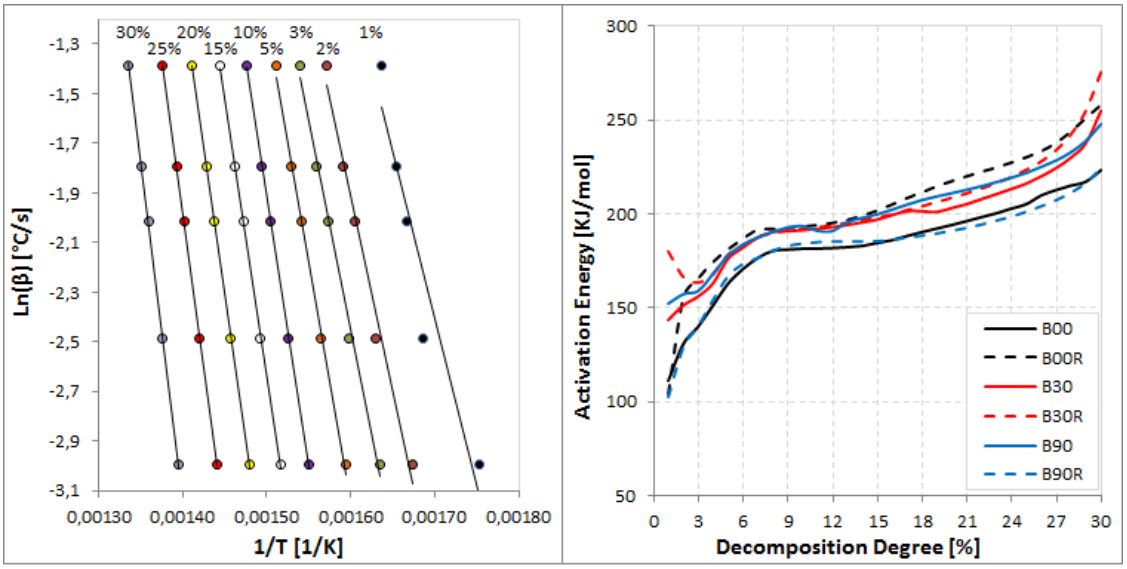

(a) (b)

Figure 5-45 Model-free decomposition kinetics of CE688: (a) isoconversion curves of B00 and (b) activation energy for all samples

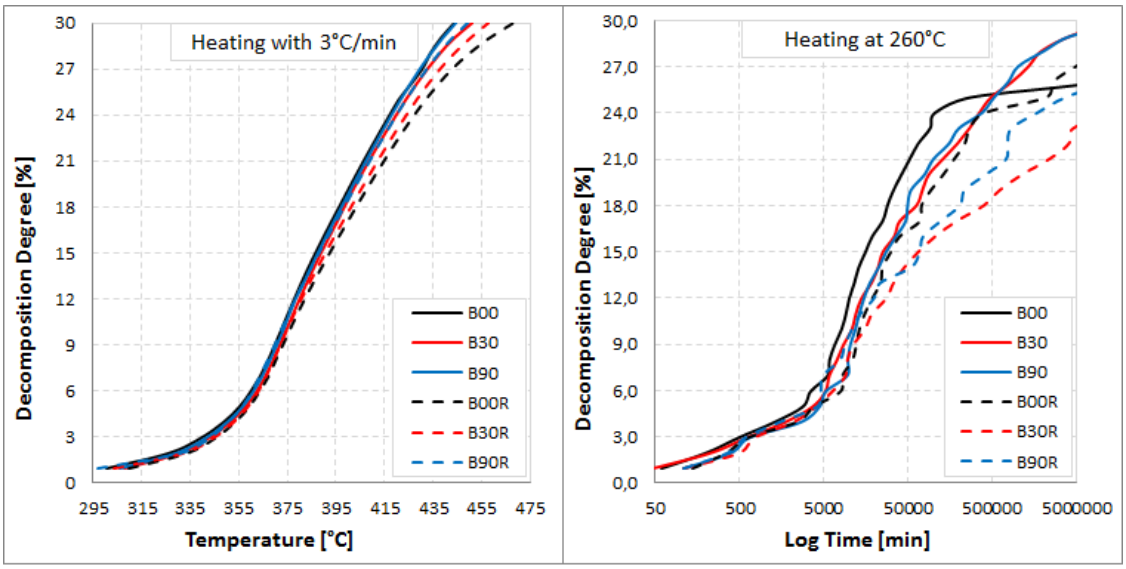

(a) (b)

Figure 5-46 Model-free decomposition kinetics prediction: (a) non-isothermal with 3°C/min heating rate and (b) isothermal at 260°C

5.3.3 Fracture mechanics

5.3.3.1 Monotonic DCB test

Figure 5-47 presents the load-displacement curves for all the DCB samples. Generally, all groups of samples were very brittle since all curves exhibit a sharp peak at the maximum loading force (P_{max}). This also explains the reason that all CT samples failed during sample preparation as described in chapter 4.4.5. Two early failures, which are marked with arrows, were caused by the delamination between the copper surface of the core and the prepreg surface. All other failures occurred in the interlaminar interface of two prepregs. Except B90R, the maximum loads (P_{max}) of each group are similar (~30N), which were influenced mainly by the initial crack length, as shown in Figure 5-48.

The evolution of compliance along with the crack propagation for all samples are depicted in Figure 5-49. It can be seen that they are quite independent from the sample conditions. Even between group B90 and B90R, which have the greatest Tg difference as shown in Figure 5-41, no significant difference can be observed.

Three data reduction methods (BT, CBT and MCC) for calculation G_{Ic} values have been performed according to ASTM standards [85] and examples from B00 and B00R are presented in Figure 5-50. The G_{Ic} values from BT are generally higher than the ones from the other two, because BT assumes that the loading arm is equivalent to the crack length. However, the loading arm becomes smaller due to the bending of the specimen, which is corrected by CBT. The results from CBT and MCC are very well aligned.

Finally, the delamination resistance (R curves) in Figure 5-51 display the averaged G_{Ic} values for each group as a function of the crack length based on MCC. Considering the deviation from the sample/experiment, all groups behaved rather similarly (except B00R), which grows slowly from 350-400J/m^2 and ends at 425-475J/m^2. Similar observations of the fracture toughness of epoxy laminates were also addressed in the literature [134, 135]. No further investigation was carried out for B00R. The fracture toughness of all groups is believed to be the same under the applied monotonic tensile test conditions.

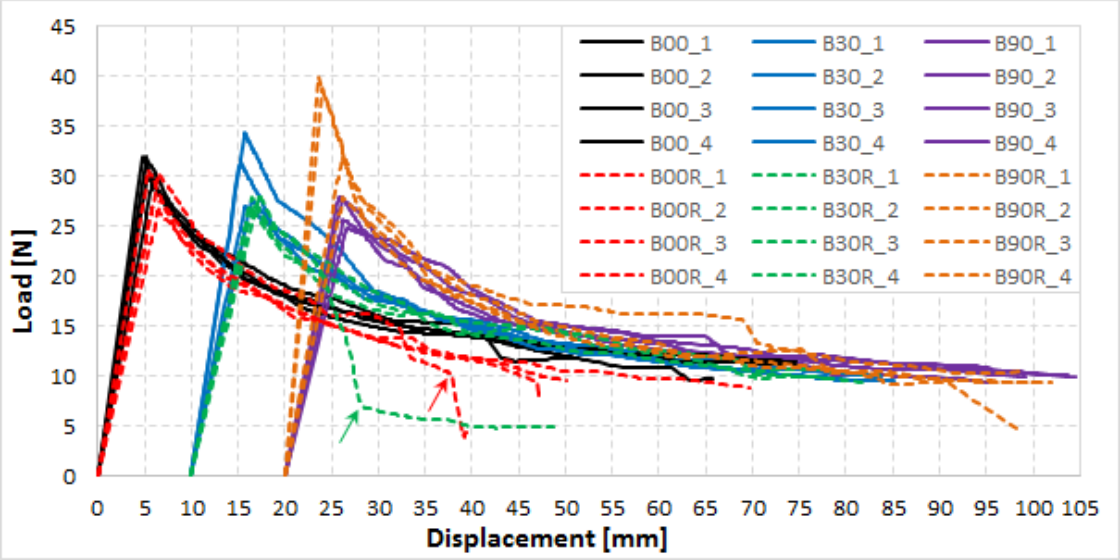

Figure 5-47 Load-displacement curves for all DCB samples. In order to compare all data in one figure, the displacements of B30/B30R and B90/B90R are shifted by 10mm and 20mm respectively.

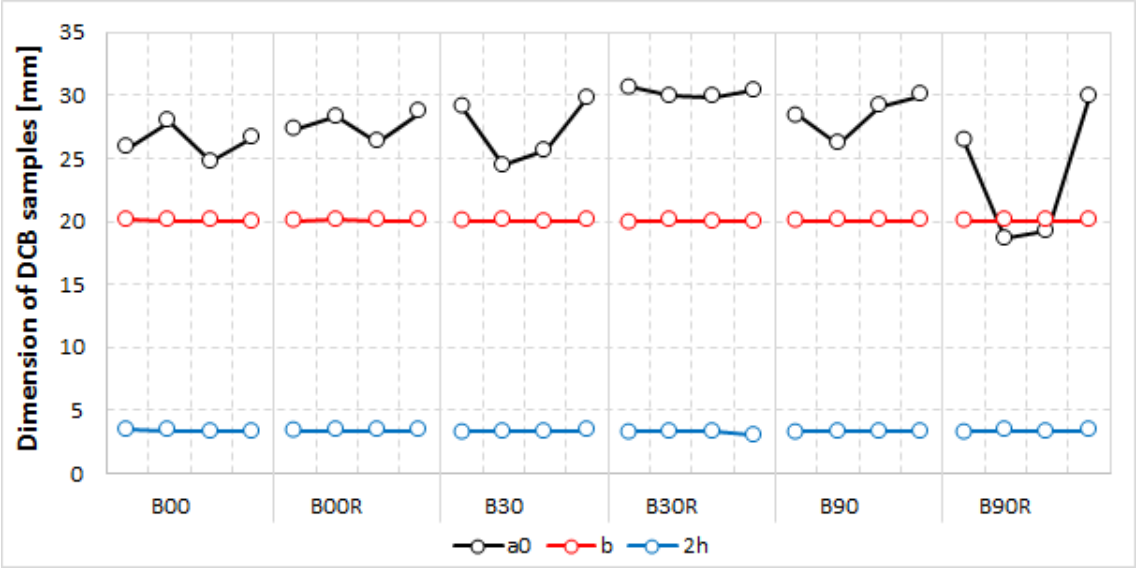

Figure 5-48 Dimension variation of DCB samples in terms of initial crack length, a0, sample width, b, and sample thickness, 2h

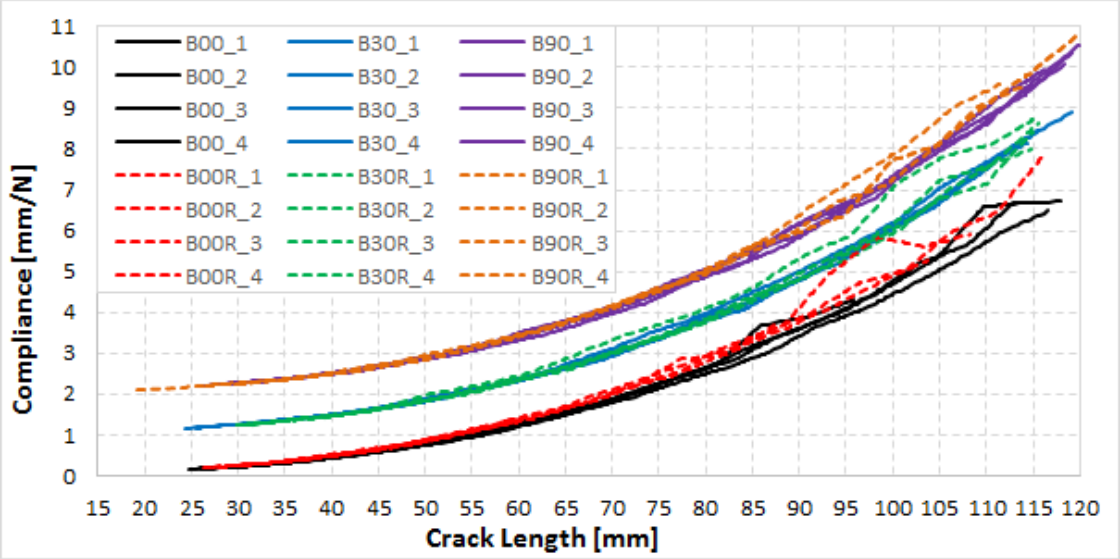

Figure 5-49 Compliance-Crack length curves for all DCB samples. In order to compare all data in one figure, the compliance values of B30/B30R and B90/B90R are shifted by 1mm/N and 2mm/N respectively.

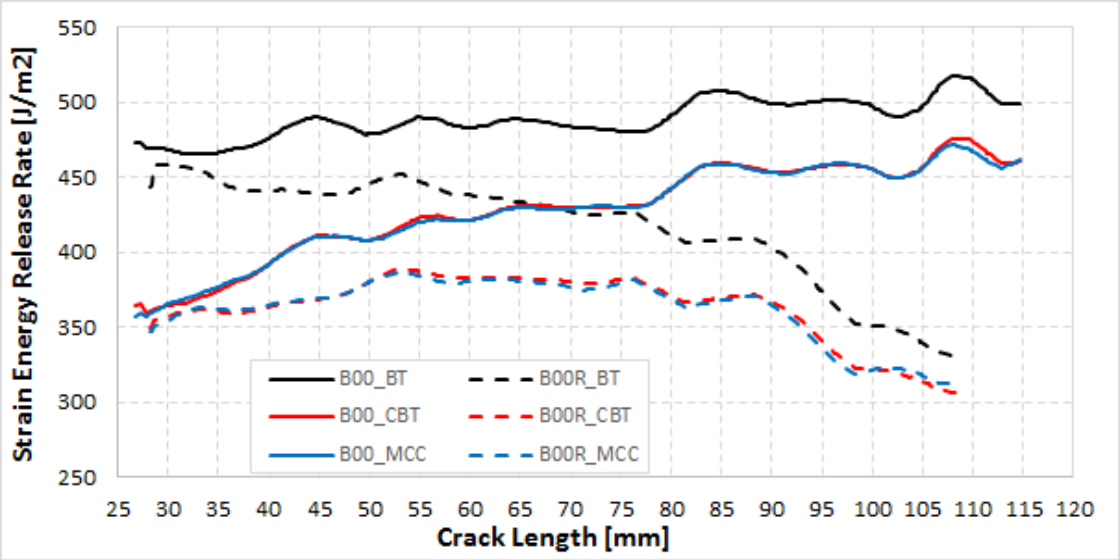

Figure 5-50 Comparison of strain energy release rate, G_{Ic}, evaluated based on different methods for B00 and B00R

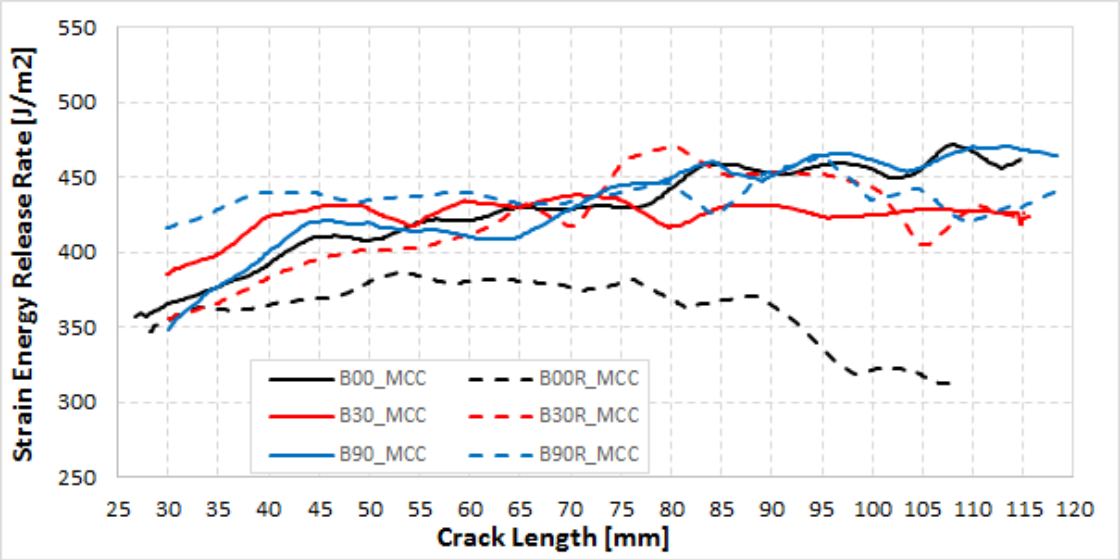

Figure 5-51 Averaged delamination resistance curves (R curves) for each group based on MCC

5.3.3.2 Cyclic DCB test

Figure 5-52, Figure 5-53 and Figure 5-54 show the delamination growth rate for B00 and B00R, B30 and B30R, and B90 and B90R, respectively. Only the samples which have complete data records are shown in the figures. Others, due to records missing or other reasons, are not presented.

Generally, all curves consist of three regions [136]: 1) Region I is the near threshold region and indicates a threshold value below which no crack will grow. It is believed that the threshold consists of two components, i.e., an intrinsic and an extrinsic threshold. The former represents the material property, the latter is a function of loading variables such as the R ratio. 2) Region II corresponds to a stable macroscopic crack growth and shows essentially a linear relationship between *da/dN* and G_{max} which can be described by the Paris Law (Equation 5-2). Parameters A and m are determined experimentally. 3) In region III, the fatigue crack growth rate is very high as G_{max} approaches G_{Ic}. Some researchers believe that the acceleration of *da/dN* should be linked to the microscopic fracture events which results in a higher overall growth rate; some hypothesize that the linear elastic fracture mechanics is no longer valid at high G_{max} values.

$$\frac{da}{dN} = A(G_{max})^m$$

Equation 5-2

Where, A is a material constant, [m^3/cycle/J].

m is a material constants, [-]

G_{max} is the maximum value of the applied energy release-rate in the fatigue cycle, [J/m^2].

Not all the curves in the three figures present the threshold value of the strain energy release rate and no curve shows the boundary of fracture toughness, which should be in the range of 350-400J/m^2 as shown in Figure 5-51. The two parameters of the Paris law according to each da/dN – G_{max} curve are calculated and shown in Table 5-2.

Since the scatter of the thresholds are larger, such as the four measurements for B00 shown in Figure 5-52, due to insufficient sample quantity, the only conclusion which can be drawn from those tests is that the 10x reflow has no influence on the delamination growth rate under cyclic loadings for the CE688 prepregs. However, a further investigation beyond this work is suggested: 1) more samples should be used in order to reduce the scattering effect; 2) some other ways of presenting the data can be tried, such as to express da/dN as a function of $\sqrt{G_{max}}$ instead of G_{max} because some authors [137] claimed that it is more logical to extend the Paris' fatigue crack growth law for metals to delamination growth in polymer-matrix fiber composites.

Table 5-2 DCB test results regarding the parameters of Paris law

Sample	A	m
B00_1	3E-17	5.70
B00_2	2E-12	3.91
B00_3	2E-18	6.59
B00_4	9E-13	4.01
B00R_1	1E-13	4.50
B30_1	1E-15	5.26
B30_2	4E-19	6.38
B30R_1	5E-18	6.34
B90_1	6E-15	4.94
B90R_1	1E-13	4.28
B90R_2	4E-12	3.57

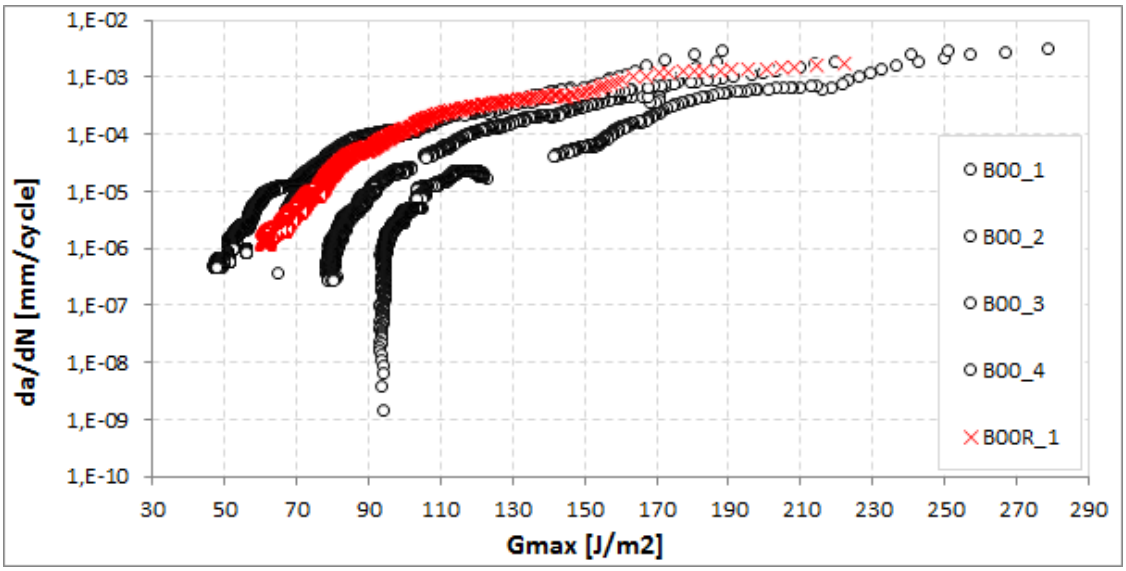

Figure 5-52 Delamination growth rate (Paris Law) for B00 and B00R

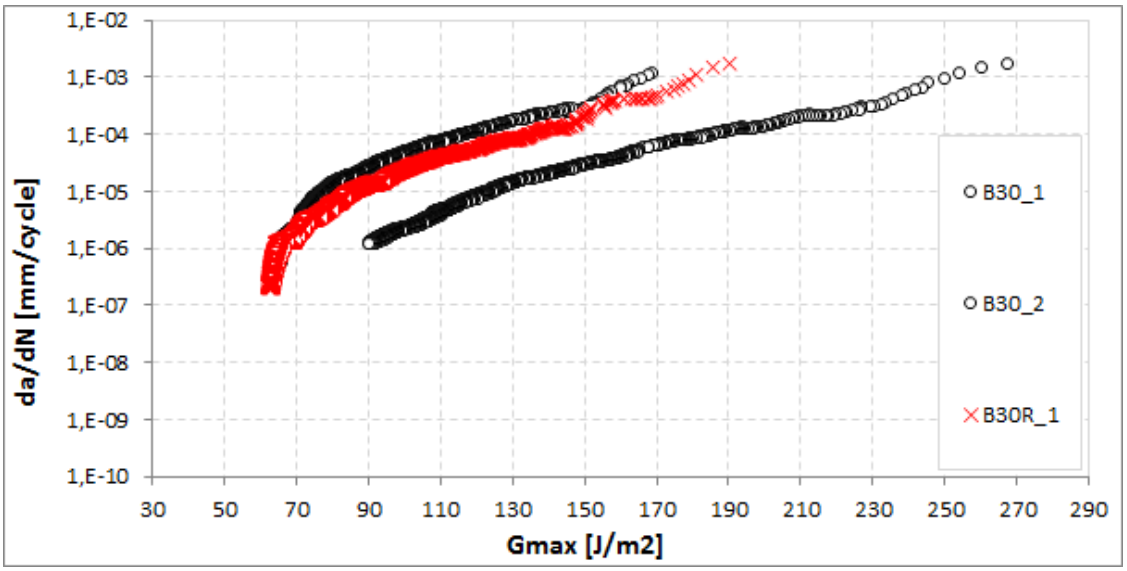

Figure 5-53 Delamination growth rate (Paris Law) for B30 and B30R

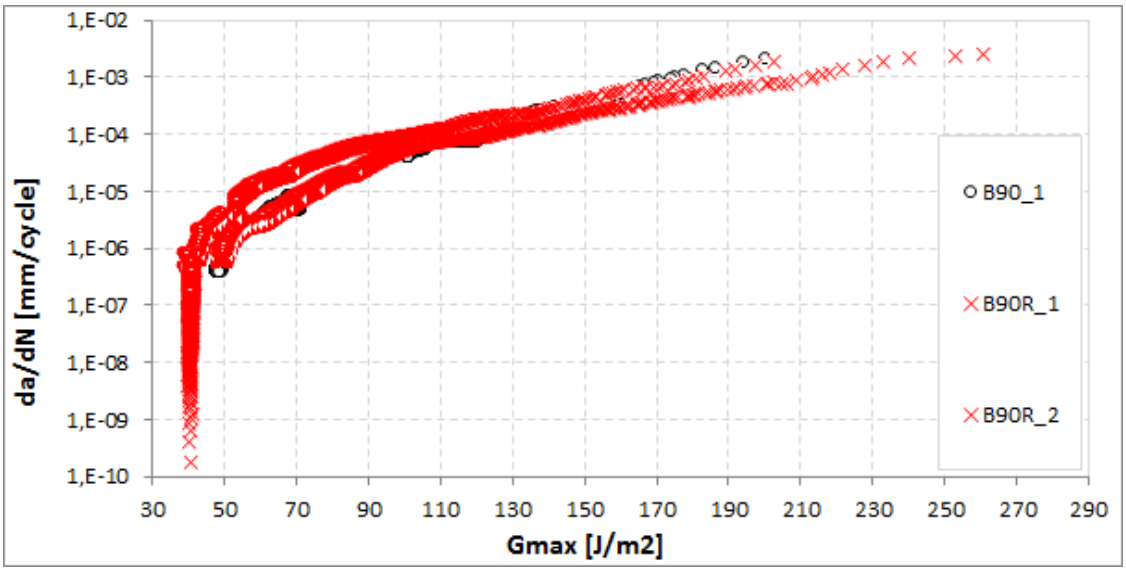

Figure 5-54 Delamination growth rate (Paris Law) for B90 and B90R

5.3.4 Reliability

5.3.4.1 Moisture uptake

Figure 5-55 shows the averaged moisture uptake of the prepreg samples under the hydrothermal condition of 85°C/85%RH. It can be clearly seen from Figure 5-55 (a) that it took about 20 days to reach the plateau and most of the moisture uptake occurred in the first 24 hours. There was no difference among B00, B30 and B90 in the first 8 days regarding moisture-sorption kinetics. Afterwards, B90 absorbed slightly more moisture than the other two and saturated at around 0.79%. The absorption curves of B00 and B30 are basically identical, both present 0.75% moisture uptake at the end of the experiments. The tendency of the curves for the samples after 10x reflowed are similar to those as received as depicted in Figure 5-55 (b): B00R and B30R show no significant difference, and B90R has higher moisture uptake.

Moisture absorption is related to the free volume [46, 138]: more water molecules can be contained with the increasing free volume of an epoxy. That means, B90 and B90R have higher free volumes compared to B00/B30 and B00R/B30R respectively, which is caused by their relatively lower crosslinking densities.

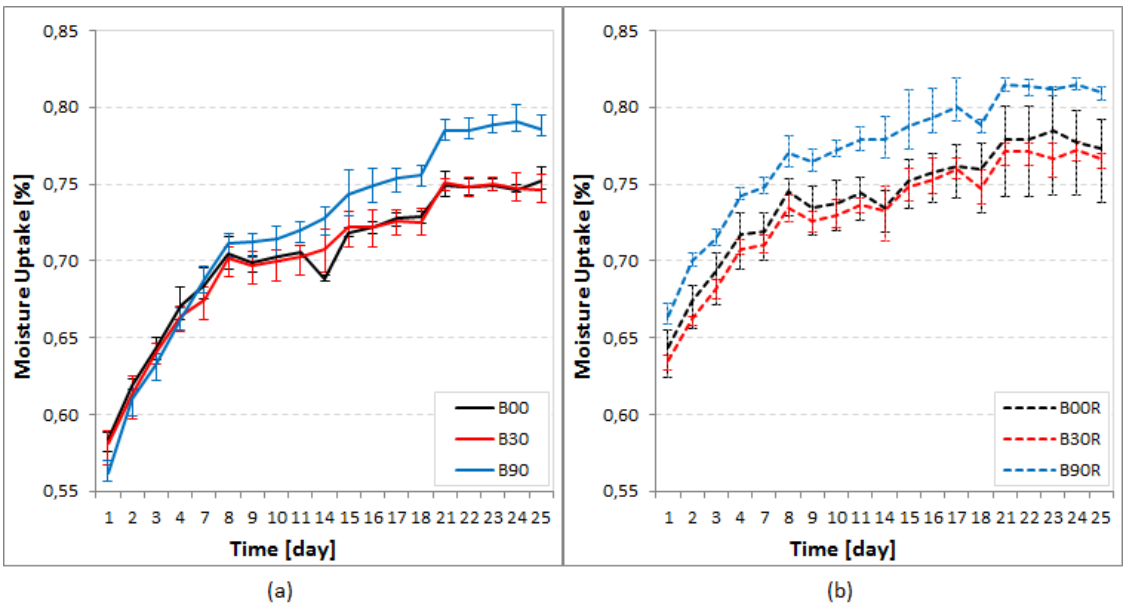

Figure 5-55 Moisture uptake of the prepreg samples (a) as received and (b) after 10x reflowed

5.3.4.2 Peel strength

Peel strength results of the external copper layers for each PCB group are summarized in Figure 5-56 as boxplots. The copper foils were peeled off without breaking as shown by the inset. It is obvious that the difference between as received and after 10x reflowed samples is greater than the variation within a group (i.e., the group of as received or after 10x reflowed samples). C30 showed a slightly higher peel strength than C00, but after reflow both were at the same level. 10x reflow improved the peel strength of C60 most significantly. It is widely accepted that the mechanical interlocking (e.g., the "anchoring" effect) is the primary adhesion mechanism between a polymer and a metal, and the degree and shape of roughness are thought to affect peel strength [139]. However in this case the roughness of the samples is believed to be the same. Therefore, the main contribution to the improvement of the peel strength after reflow is the increased crosslinking density.

Furthermore, it can be seen from Figure 5-56 that although most of the samples were below the specification (1050 N/m) which has raised concerns by the relevant quality assurance, it is obviously not caused by the press cycle time reduction. Hence, no further investigation was done in this study.

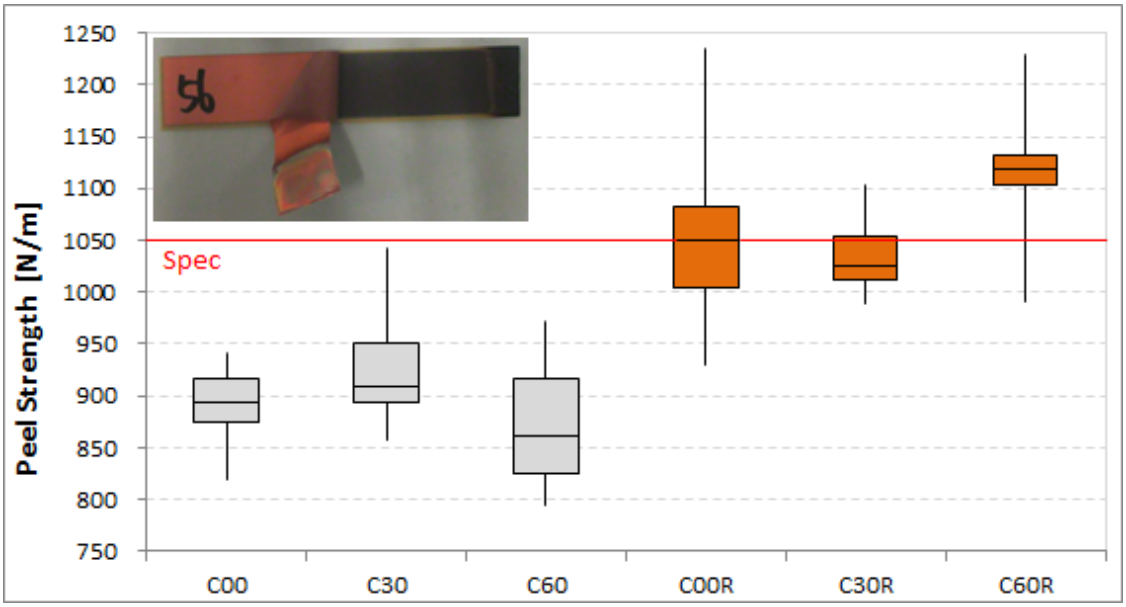

Figure 5-56 Peel strength of the PCB samples (The inset is an example of the sample after testing)

5.3.4.3 Delamination

Delamination of a PCB is the separation of either the fiberglass from the resin or the resin from the laminate or Cu foil, which might be caused by thermal shock, moisture absorption, poor material or the lamination process [140]. Visual inspection is the conventional way to check the delamination, which is inefficient and not accurate. Figure 5-57 presents the capacitance between each adjacent pair of layers and its change over heating time at 300°C for C00 and C00R respectively. It is clear that the capacitances increased after 10x reflow and remained constant before the occurrence of delamination. After 5-6 min heating, both had serious delamination in the layers of L3-L4, L5-L6 and L6-L7 as shown in Figure 5-58. One notable point was that these inner layer delaminations were not discernable by means of visual inspection, even though they were obvious in the cross-sections.

Therefore, a further investigation might be valuable. For example, delamination kinetics could be developed with a suitable automated device as a complementary method to the decomposition kinetics described in the previous chapters.

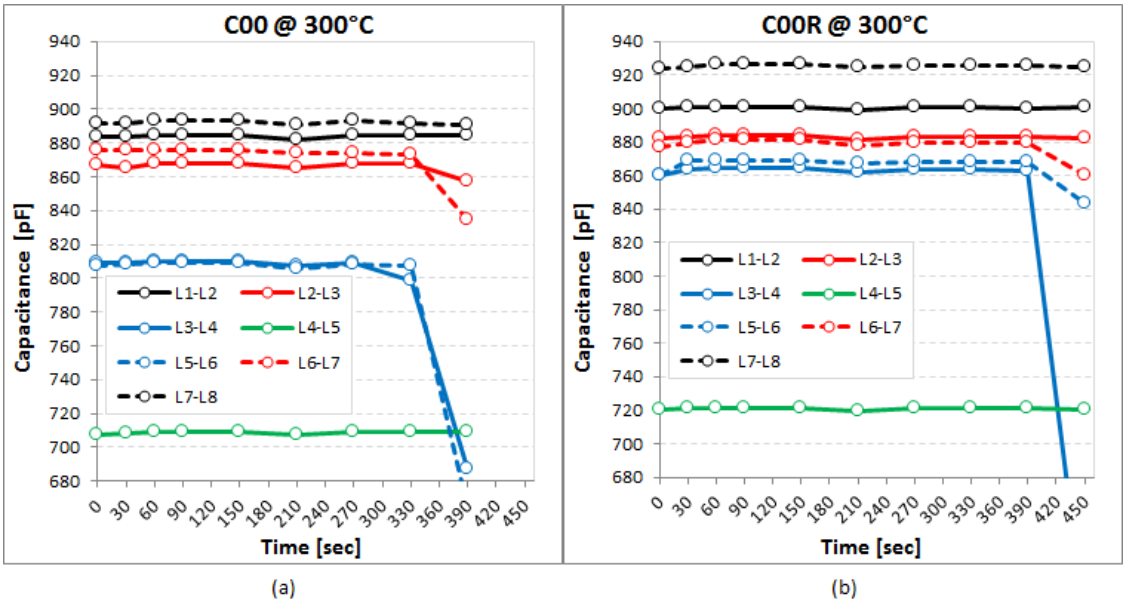

Figure 5-57 Delamination of normal pressed PCB at 300°C for (a) as received and (b) after 10x

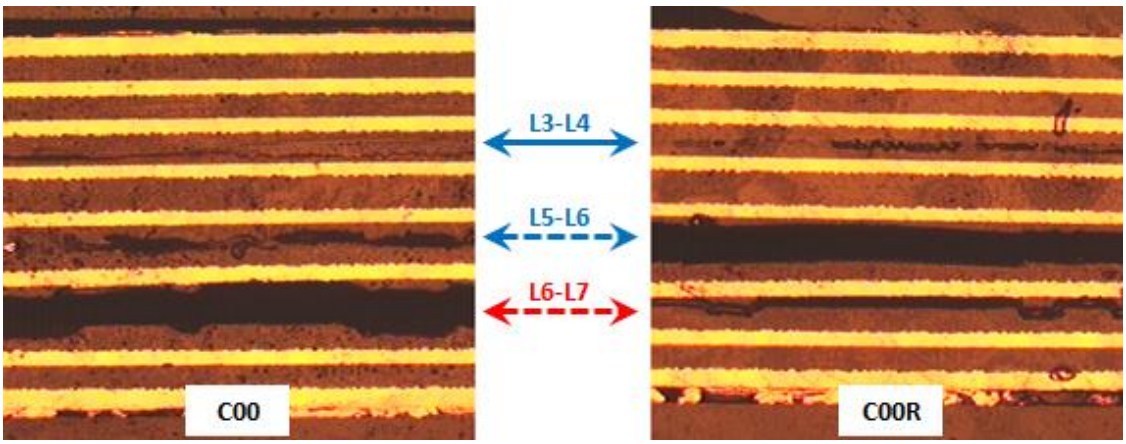

Figure 5-58 Cross section of the failure samples after delamination test

5.3.4.4 Interconnection Stress Test (IST)

The Weibull distribution is one of the most commonly used [141, 142, 143] reliability distributions in the electronics industry for modelling the cycle to failure of electronic components or devices. The most often found two-parameter Weibull distribution, or the so-called scale-shape-version was used in this study, which is given by [144]:

$$f(t) = \frac{\beta}{\eta}\left(\frac{t}{\eta}\right)^{\beta-1} e^{-\left(\frac{t}{\eta}\right)^{\beta}}$$

Equation 5-3

Where, f(t) is the probability density function (pdf) of failure at t number of cycles, [%];
β is the shape parameter (β>0), [-];
η is the scale parameter (η>0), [-].

The Weibull charts shown in Figure 5-59 were plotted in the statistical software Minitab® 17. The right-censored data were estimated with the maximum likelihood (ML) method. Two-sided 90% confidence bounds were applied in the analysis in order to obtain a closed interval, where 90% of the population is likely to lie. Therefore, the confidence level of the lower bound is 95%. The six groups can be assumed to have the same shape parameter or failure mode, which is 2.37. This has been proven using a hypothesis test which gives a p-value of 0.91 (p>0.05 means that the Null-hypothesis cannot be rejected using a risk level of $\alpha = 0.05$). The Mean-Time-To-Failure (MTTF), which is calculated based on the gamma function [145], was taken as the criteria for evaluating the lifetime of the IST samples and the results are shown in Figure 5-60. The inset in Figure 5-60 shows the typical failure mode of a copper crack in the laser via which was mainly caused by the out-of-plane CTE mismatch between the copper and the prepreg.

The lifetime of these PCB samples should be related to both the CTE mismatch and the stiffness of the prepreg materials. However, in terms of the as-received group, C60 is expected to have a shorter lifetime than C30 and C00 since its CTE is higher than the other two (Figure 5-40) and the three have a similar modulus (Figure 5-29). But C60 has a significantly higher lifetime. The same is true for the after 10x reflowed group. Therefore, the copper plating process cannot be considered as stable. That means the copper in C60/C60R samples might be more ductile than others. Nevertheless, the samples before and after reflow are comparable, because both experienced the same processes. Obviously, the 10x reflowed samples have shorter lifetimes than the as-received samples. It means that the increased stiffness after reflow has a big negative impact on the IST performance and the reduced CTE after reflow does not improve the reliability.

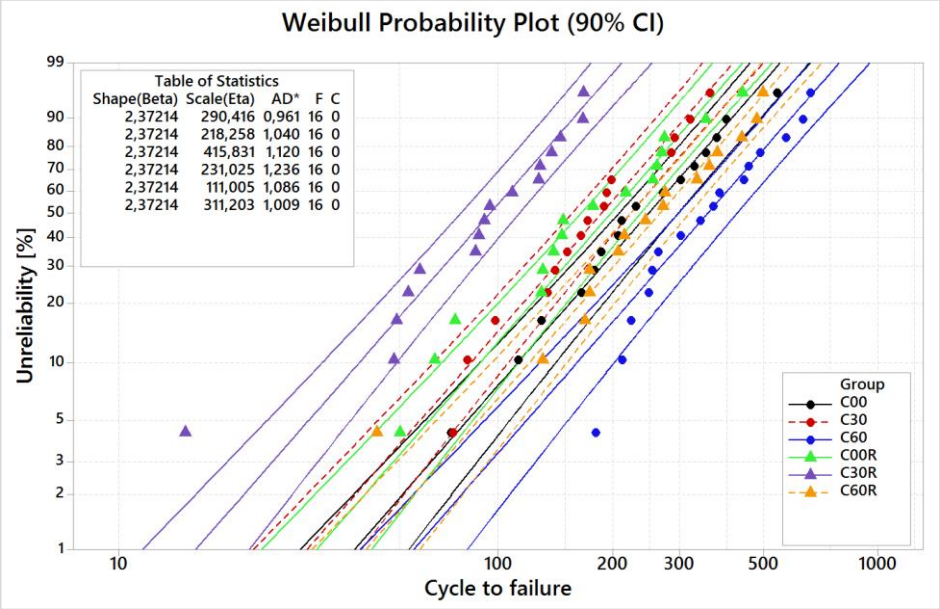

Figure 5-59 Weibull probability plot of IST tested samples with 90% confidence interval

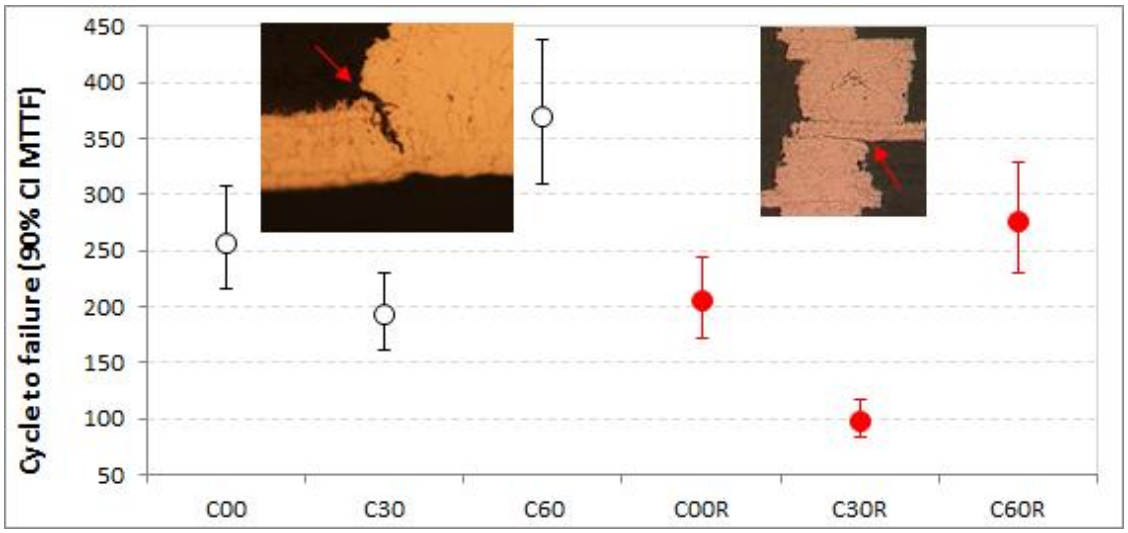

Figure 5-60 IST lifetime based on the Weibull analysis (The insets are examples of typical failures)

5.3.4.5 Highly-Accelerated temperature and humidity Stress Test (HAST)

Conductive anodic filament (CAF) is a term created by Lando et al. (1979) to describe the catastrophic failure modes of conductive bridges between conductors on the PCB surface and conductive shorts through the substrate [146]. In other words, CAF can be used to characterize the electrical insulation resistance of a PCB. The CAF failures can be enhanced under the HAST testing conditions, i.e., high temperature, high humidity and high voltage gradient between anode and cathode. Figure 5-61 confirms that neither the reduced cycle

time (-30min and -60min) nor 10x reflow can introduce the CAF failures even with the harsh test conditions like HAST. The specification requires that the resistance of the comb pattern shall be greater than $10^7\Omega$. And the measured resistances of all samples at both initial and after testing statuses were much higher (~$10^{12.5}\Omega$).

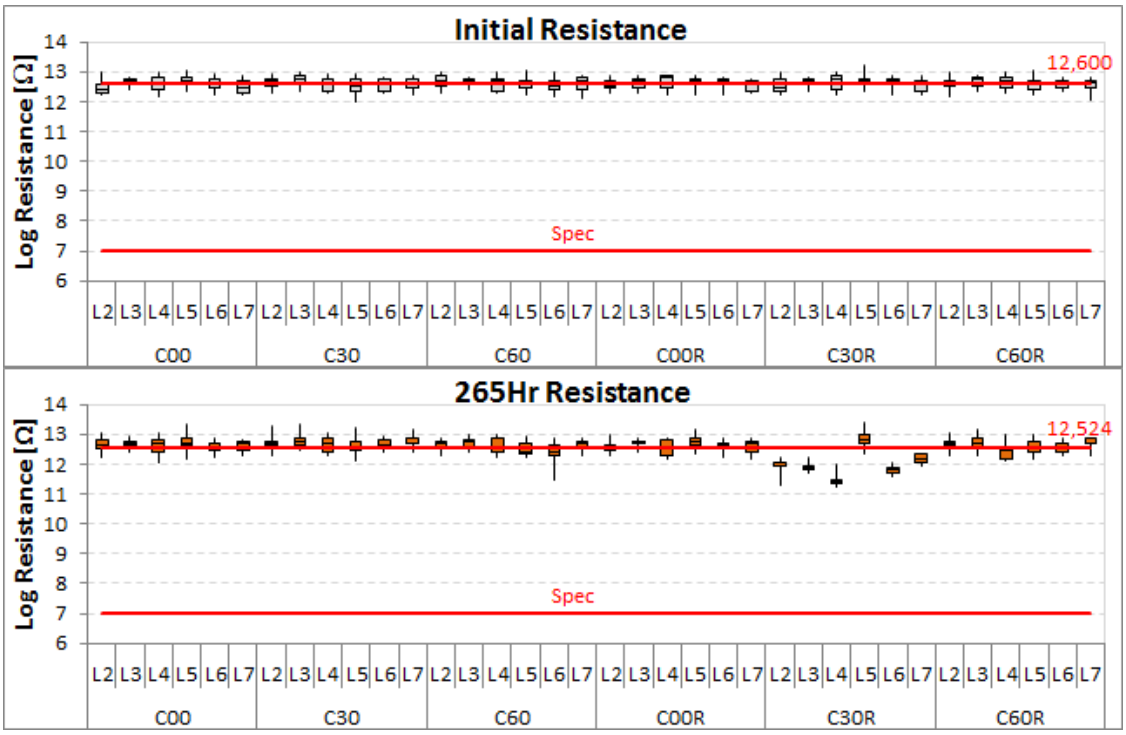

Figure 5-61 Resistances of comb patterns before and after HAST test

5.3.4.6 Warpage

The warpage of the as-received PCB samples (C00, C30 and C60) during a standard lead-free reflow cycle are depicted in Figure 5-62. Initially, C30 and C60 were in a similar range (200-300µm) and were higher than C00 (100-150µm). The coplanarities of all three as-received groups increased as the temperature increased. A bigger change can be seen around the Tg temperature (150°C). However, the magnitude of the changes varied with the press cycle time: C00 showed the least change over heating, and C60 warped most significantly. It is interesting to see in Figure 5-63 that after 10x reflow, C30R was in the similar range as C00R (100-250µm) and was lower than C60R (300-450µm). The coplanarities of all three after 10x reflowed groups decreased as the temperature increased. After Tg temperature, all became relatively stable regarding the out-of-plane dimensional change.

Although in most cases the samples with different conditions were still within the specification (<750µm), a clear conclusion can be drawn based on the warpage behaviors of

the three groups, which were produced with different press cycles: relatively longer press cycle time can reduce the warpage because the epoxy network needs more time at elevated temperatures to relax. Moreover, the highest warpage was observed during the first time reflow, see Figure 5-64.

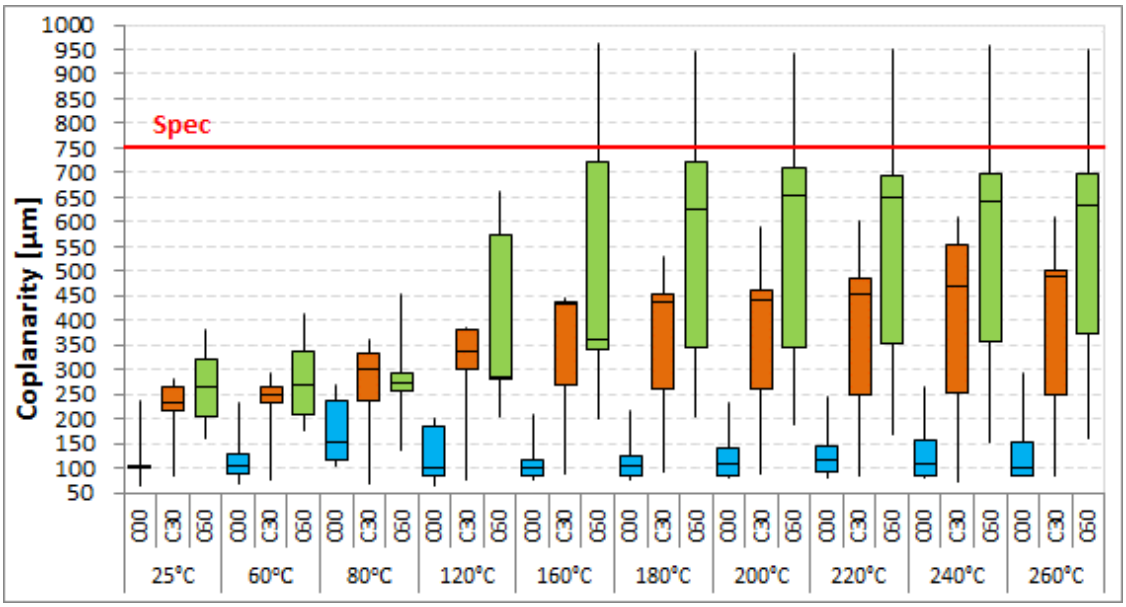

Figure 5-62 Boxplot for the warpage of PCB samples as received

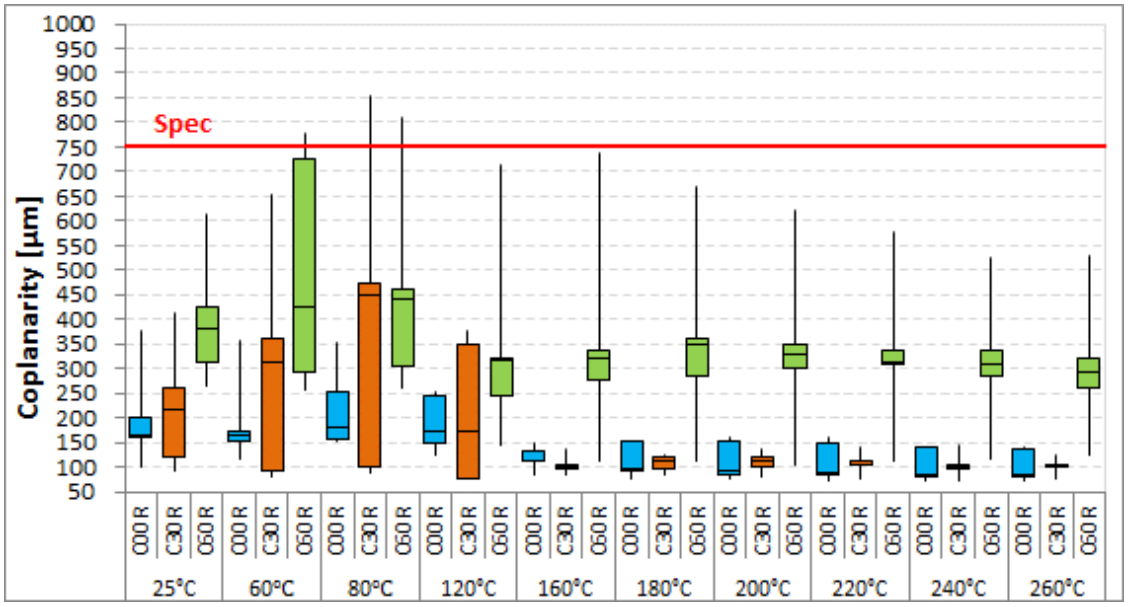

Figure 5-63 Boxplot for the warpage of PCB samples after 10x reflowed

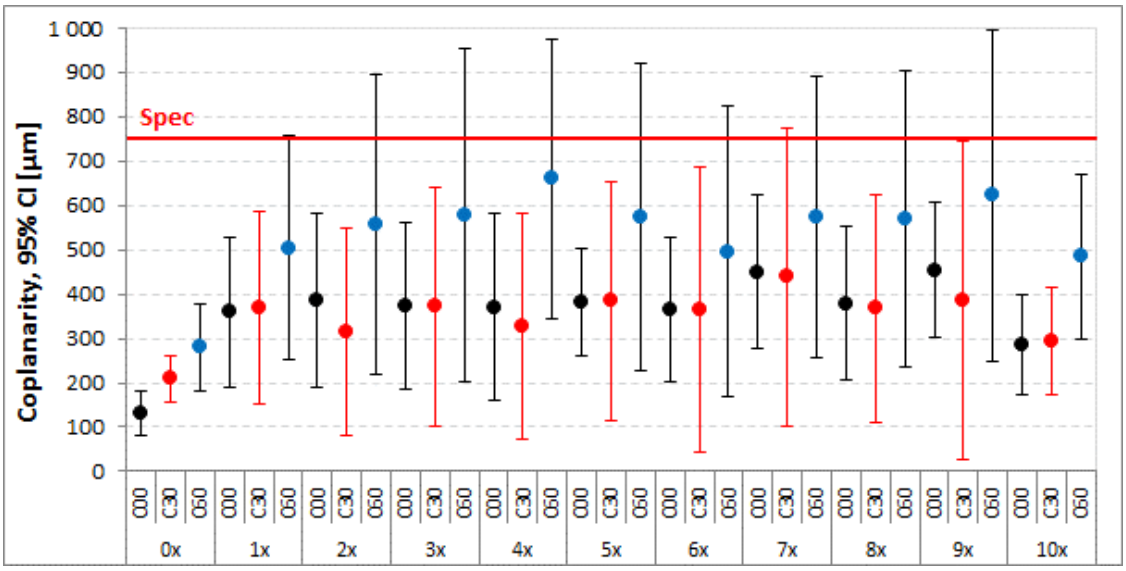

Figure 5-64 Warpage of PCB samples after each reflow measured at room temperature

5.4 General procedure for optimizing the press cycle time of a new material

In order to offer a general guideline for optimizing the press cycle time of a new material with a fast response based on the fundamental studies and the relevant testing results presented in this work, a flowchart has been prepared, as displayed in Figure 5-65.

Normally a reference press program will be provided by the material supplier when they deliver a new material to the PCB manufacturer. Although the program has been studied or optimized at the supplier side, it often needs to be adapted to the lamination process of the manufacturer. However, this press program, which consists of a temperature ramp-up rate, isothermal heating temperature and cooling rate, etc., can be utilized as a reference for the first three steps of the further investigation as described below.

First, the "unknown" material shall be identified by the decomposition kinetics study with TGA for the purpose of obtaining/predicting the thermal stability of the epoxy system, i.e., the decomposition temperature at various heating rates and the time to decomposition at different isothermal heating temperatures. Second, the DSC curing kinetics study is to be performed with the pure resin or prepreg samples depending on the final application (it is not recommended to use the pure resin samples to characterize the curing behavior of the prepreg samples due to the possible influence from the glass fibers, vice versa.). The DSC scanning shall cover the temperature range between RT and the one just before decomposition, which has been revealed by the TGA analysis. Additionally, if the curing

kinetics can be performed in the presence of pressure, which was not the case in this study due to the lack of an appropriate device, the accuracy of the results will be improved. Sometimes FTIR curing kinetics can be used as a complementary method in case certain materials do not produce discernable exothermal peaks in the DSC thermographs. Third, an FEA simulation shall be conducted according to the curing kinetics results. In this step, the real geometry of the press book shall be modeled. Meanwhile, the real temperature profile of the heating plate in the press book shall be measured and be used as a boundary condition of the simulation. Fourth, the design of the experiment (DOE) in terms of varying press cycle time can be devised, because the minimum press cycle time for complete curing and the maximum time before decomposition are given by the simulation and the TGA analysis respectively. Fifth, the warpage coupons can be produced with different press cycle times and performing the warpage measurements afterwards so that the press condition with the best/acceptable warpage performance can be chosen. If the warpage from all the trials is not acceptable, the DOE has to be repeated. Finally, the standard test panels can be produced with the optimized press cycle time on the basis of warpage performance and all the standard reliability tests can be carried out thereafter, such as IST, HAST etc. If the test panels have passed all the tests, the optimal press cycle time can be fixed. Otherwise, a failure analysis has to be carried out in order to figure out the root cause, which might be a process issue or the fact that the press cycle time of this specific material cannot be reduced.

The general procedure described above is mainly focused on the curing status of the material. The warpage performance is defined as the primary criterion for judging the optimization procedure, which is based on the following two facts: (i) The warpage issue is becoming more prominent along with the reduction of the PCB thickness (the reported most common board thickness in 2016 is 3.8mm and its estimated value in five years is 3.1mm [147]), which might cause serious assembly issues or reliability issues in the PCB lifetime. (ii) The diffusion effect, the lamination pressure, the chemical shrinkage and the stress relaxation at the hot stage were not currently considered in the simulation, and thus the warpage cannot be accurately predicted in this study.

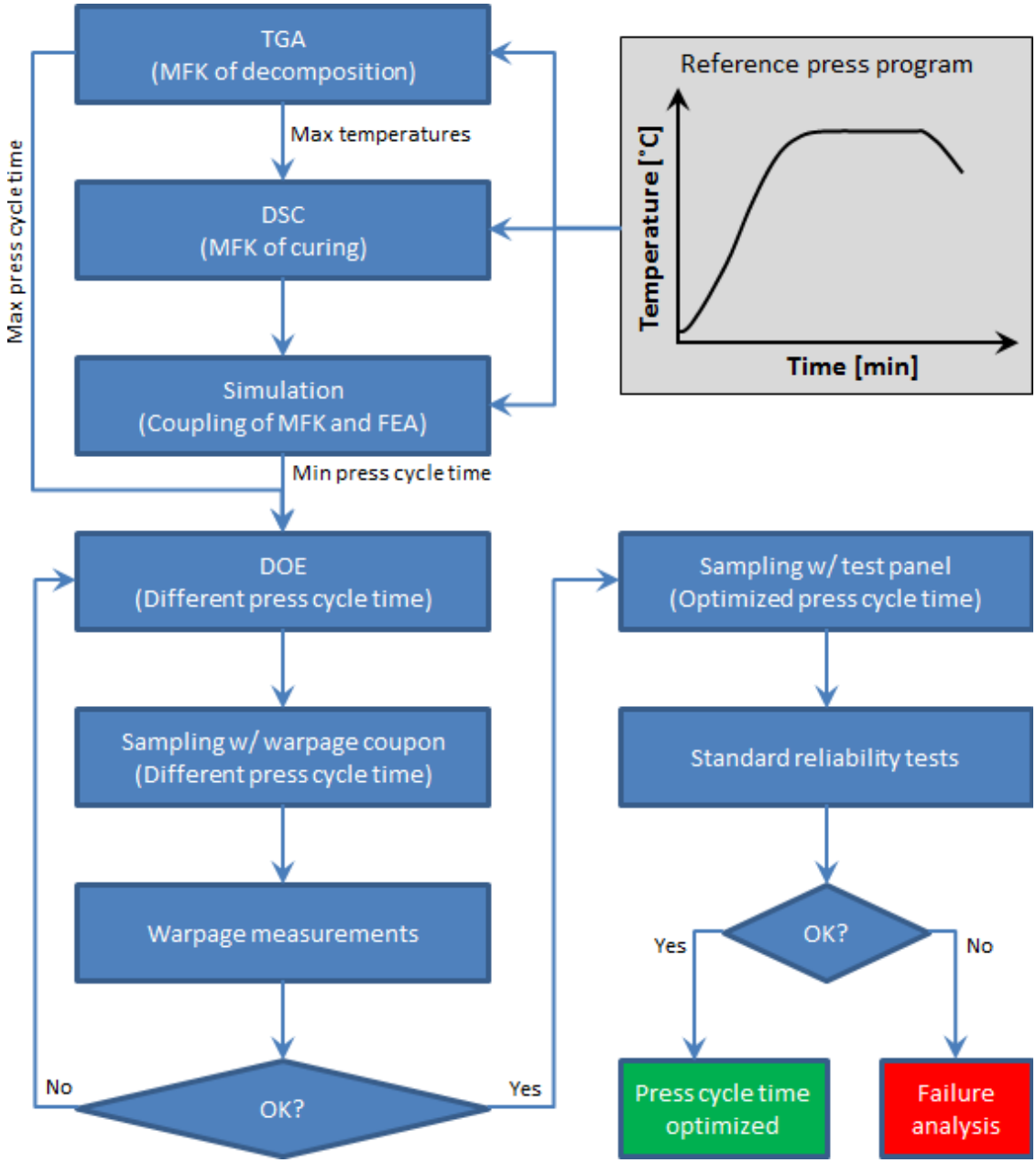

Figure 5-65 Flowchart for optimizing the press cycle time of a new material

6 Conclusion and future work

This PhD work originated from a production-related project whose goal was to evaluate if the press cycle time, relative to the manufacturer's recommended cure cycle (Figure 4-2), can be reduced in the lamination processes for the new CE688 prepreg material with acceptable quality for final PCBs.

Instead of trial-and-error methods typically used by manufacturers for tackling engineering problems, a deep understanding of the epoxy curing process was first developed based on the simple model epoxy resin system. It turned out that the well-known MFK methodology can be applied for predicting the curing behavior of the model resin for both non-isothermal (Figure 5-9) and isothermal (Figure 5-11) conditions with appropriate experimental parameters. This MFK approach was applicable for the commercial epoxy CE688 as well (see Figure 5-15 and Figure 5-16). However, the real heating profile, as shown in Figure 4-2, was neither non-isothermal nor isothermal. That means the conventional MFK approach cannot be used for predicting the real-time curing procedure. Meanwhile, due to the lag of the heat transfer within a press book, the curing degree of the epoxy will vary depending on the location. For instance, the epoxy resins in the outer layers will cure faster than those in the inner layers since the heat has to travel from outside inwards. Therefore, a mathematical algorithm was proposed (chapter 3.5) to couple MFK with FEA so that the curing degree of an epoxy at arbitrary heating rates as well as the geometry of the whole heating system can be simulated. Second, a series of comparison tests regarding thermo-mechanics, fracture mechanics and reliability between the normal and cycle time reduced samples were performed in order to investigate the effect of press cycle time reduction. Third, validation trials based on the real boards (C00, C30 and C60) were carried out. In the end, a reduction of 30min (C30) in the lamination process can be achieved for the boards using CE688 material with guaranteed quality.

This project has been successfully completed and a general procedure for optimizing the press cycle time of new materials has been derived based on those fundamental studies in the frame of this work. But the value of this study is not limited to the application for this specific CE688 material. Some of the key findings/developments and suggestions for future work are listed below:

1) The MFK approach was integrated into the Abaqus® finite element package for the epoxy curing simulation via a utilization of user subroutines. With the coupling of MFK with FEA, it is possible to simulate the curing behavior of epoxy resin systems

in the real manufacturing press book. Although the model (Figure 4-7) used in this study is two dimensional and no curing degree-dependent material properties were considered due to the lack of material data, the developed methodology can be applied to three dimensional models with arbitrary geometries as well as advanced curing degree-dependent material properties, such as density, coefficient of thermal expansion, thermal conductivity, specific heat and even chemical shrinkage during polymerization. These advantages will facilitate the procedures for the curing simulation and widen the application field.

2) Although the study of curing kinetics without consideration of the diffusion effect and in the absence of pressure is quite common in the PCB industry and the results (see chapter 5.1.3 and 5.2.1) presented in this study are quite satisfactory, it might still be interesting to improve the MFK model by involving the diffusion effect in future work, especially in the presence of pressure since the applied pressure will slow down the reaction rate further [39].
3) Thanks to the technology advancement and the miniaturization of electronic devices, PCBs are getting thinner and thinner. Consequently, the criteria for PCBs regarding warpage performance is becoming more difficult to fulfill, especially combined with the reduction of the press cycle time and the critical reflow conditions as shown in Figure 5-62, Figure 5-63 and Figure 5-64. This situation gives rise to the ever higher demand for warpage simulation in order to figure out an optimal condition in PCB design, material selection and process parameters, etc. Therefore, except the CTE mismatch among different materials in PCBs which is a factor being considered ubiquitously, the factors of chemical shrinkage during the polymerization of the epoxy resin and stress relaxation at the hot stage of the lamination process should also be incorporated into the framework of the user subroutines developed for the coupling of MFK with FEA in this study.
4) It is possible that due to the excellent performance of the thermal stability of CE688 used in this study, as shown in Figure 5-46, the TGA model free decomposition kinetics seems less important than the DSC model free curing kinetics. An emphasis should be placed on the fact that the MFK methodology can be applied for both curing and decomposition kinetics studies. Hence an excel-based software was developed in this PhD work for the purpose of facilitating both kinetics studies in a fast and easy way.

5) The dual-effect of cooling rate and annealing has a significant influence on the endothermic peaks in the DSC thermograms, as presented in Figure 5-34, which will result in under-estimated Tg values consequently [99]. An improved DSC program was therefore developed in order to minimize/eliminate the influence of endothermic peaks on the Tg evaluation for general applications. This improvement can be clearly seen by comparing the results in Figure 5-33 with those in Figure 5-35.
6) The FTIR curing kinetics study showed that it has a good potential to be developed as a complementary method to the DSC curing kinetics method. In certain cases, the endothermic peaks of the epoxy resin systems in the DSC thermography are not obvious due to the high filler content or other reasons, in these cases the utilization of the FTIR method will be one of the best alternatives. Because of the lack of the heating function of the existing FTIR equipment used in this study, the curing kinetic curves characterized by FTIR cannot be directly compared to those obtained from DSC due to the temperature/time delay as described in chapter 5.2.2. Therefore, an online FTIR measurement system for the study of curing kinetics is recommended for further work. For instance, the steel sample holder, as shown in Figure 4-6 (D), can be replaced by two PCBs which act as small heaters. The prepreg sample is then placed between the PCB heaters and the heating function shall be controlled by a temperature controller, as presented in Figure 6-1.

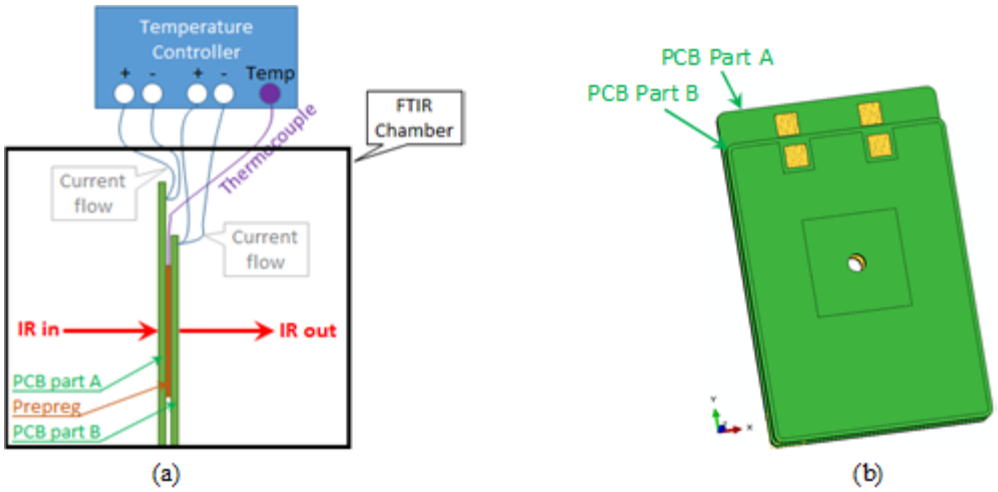

Figure 6-1 Schematic drawing of the FTIR online measurement system (a) and the PCBs which are used as heaters (b)

7) The characterization of the fracture toughness for the CE688 pure resin was not successful due to the brittleness of the material and the lack of experience. Meanwhile no significant difference was found for the prepreg samples regarding G_{Ic} because the

sample quantity was not sufficient to eliminate the big influence from the scattering of the measurement. However, this DCB testing related methodology is very valuable and more attention should be paid to characterize the crack propagation not only on the prepreg/prepreg interfaces, but also on the interfaces of copper/prepreg and copper/copper. An example is given in Figure 6-2 schematically regarding the latter case: the upper DCB sample is designed for characterizing the Cu/PP interface and the lower one is for the mixture of Cu/PP and Cu/Cu of laser via. The crack propagation on the Cu/Cu interface can be calculated subsequently by deducting the Cu/PP part from the mixture.

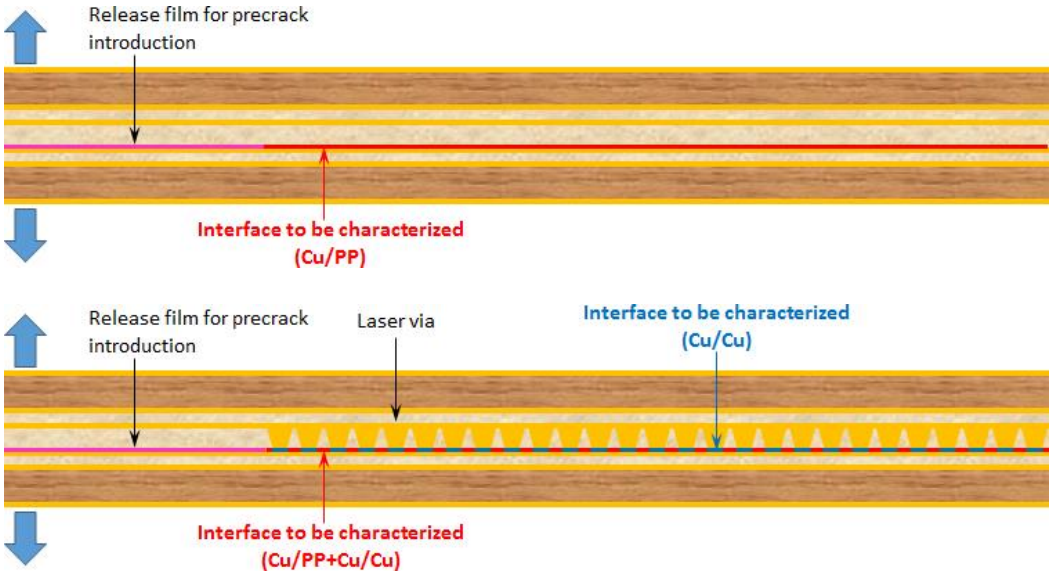

Figure 6-2 DCB samples for characterizing the crack propagation on the interface of Cu/PP and Cu/Cu of laser via

8) Currently, there is no method to check non-destructively the material delamination, especially for the inner layers of a PCB. Therefore, monitoring delamination by capacitance is a very promising method for characterizing the ageing of the material under various environmental conditions, such as reflow, cyclic thermal shock, hygrothermal and so on. Moreover, delamination kinetics, as schematically depicted in Figure 6-3, should be developed in order to predict the lifetime of the material under service environments.

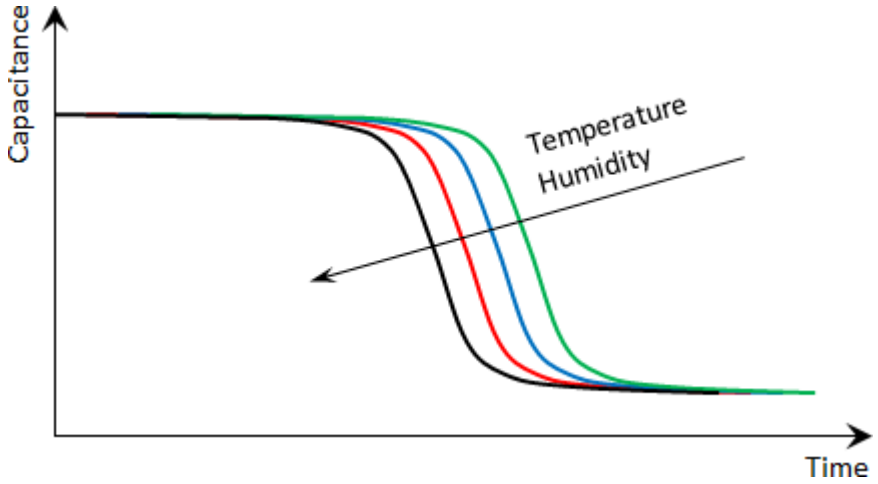

Figure 6-3 Schematic delamination kinetic curves

Using a comprehensive experimental characterization of PCB laminates in combination with modeling techniques paves the way for ensuring the reliability of electronic components for many years of service.

References

[1] P. Glenn, „7 most anticipated tech trends in the 2016 consumer electronics,“ AOL Inc., 6 3 2016. [Online]. Available: https://www.engadget.com/2016/06/03/7-most-anticipated-tech-trends-in-the-2016-consumer-electronics/. [Access on 29 1 2017].

[2] M. Djuric, „Nokia N8 teardown,“ Ifixit, 7 10 2010. [Online]. Available: https://www.ifixit.com/Teardown/Nokia-N8-Teardown/3641/1. [Access on 8 2 2017].

[3] F. Arnold und S. Thoman, „Think Composites, LLC. -- What is B-stage?,“ 09 02 2001. [Online]. Available: http://www.thinkcompositesllc.com/index.php/faq. [Access on 27 03 2017].

[4] A. P. Mouritz, „Manufacturing of fibre-polymer composite materials,“ in *Introduction to Aerospace Materials*, Cambridge, Woodhead Publishing Limited, 2012, p. 317.

[5] J. Gotro, „Thermoset characterization part 6: Practical considerations for gelation,“ 19 5 2014. [Online]. Available: https://polymerinnovationblog.com/thermoset-characterization-part-6-practical-considerations-gelation/. [Access on 12 5 2017].

[6] AT&S, "HDI Any-Layer PCBs," AT&S Austria Technologie & Systemtechnik AG, 2016. [Online]. Available: http://www.ats.net/products-technology/product-portfolio/hdi-any-layer-pcbs. [Accessed 24 12 2016].

[7] IPC/JEDEC, „Moisture/Reflow sensitivity classification for nonhermetic solid state surface mount devices“. Wilson Boulevard Patent J-STD-020D.1, March 2008.

[8] J. Brown, „The history of Printed Circuit Boards,“ PCB Solutions, 3 1 2013. [Online]. Available: http://www.pcb-solutions.com/pcb-market-monitor/the-history-of-pcb-infographic/. [Access on 29 1 2017].

[9] E. G. Fernandes, C. Tramidi, G. M. D. Gregorio, G. Angeloni and E. Chiellini, "Effect of temperature-pressure cycles on structural properties of epoxy-based composites for printed circuit boards applications," *Journal of Applied Polymer Science,* vol. 110, p. 1606–1612, 2008.

[10] M.R.Wisnom, M.Gigliotti, N.Ersoy, M.Campbell und K.D.Potter, „Mechanisms generating residual stresses and distortion during manufacture of polymer–matrix composite structures," *Composites: Part A,* Bd. 37, p. 522–529, 2006.

[11] IPC, „Performance test methods and qualification requirements for surface mount solder attachments". Northbrook, USA Patent IPC-9701, 1 2002.

[12] M. Urbaniak, „A relationship between the glass transition temperature and the conversion degree in the curing reaction of the EPY® epoxy system," *Polimery,* Bd. 56, pp. 240-243, 2011.

[13] A. DiBenedetto, „Prediction of the glass transition temperature of polymers: A model based on the principle of corresponding states," *Journal of Polymer Science: Part B: Polymer Physics,* Bd. 25, pp. 1949-1969, 1987.

[14] M. Zarrelli, A. A. Skordos und I. K. Partridge, „Investigation of cure induced shrinkage in unreinforced epoxy resin," *Plastics, Rubber and Composites Processing and Applications,* Bd. 31, pp. 377-384, 2002.

[15] S.R.White, P.T.Mather und M.J.Smith, „Characterization of DGEBA-DDS epoxy using ultrasonic, dynamic mechanical, and thermal probes," *Polymer Engineering and Science,* Bd. 42, Nr. 1, pp. 51-67, 2002.

[16] J.Zhang, Y.C.Xu und P.Huang, „Effect of cure cycle on curing process and hardness for epoxy resin," *eXPRESS Polymer Letters,* Bd. 3, Nr. 9, pp. 534-541, 2009.

[17] S.R.White und H.T.Hahn, „Cure cycle optimization for the reduction of processing-induced residual stresses in composite materials," *Journal of Composite Materials,* Bd. 27, Nr. 14, pp. 1352-1378, 1993.

[18] C. Naito und M. Todd, „The effects of curing parameters on the properties development of an epoxy encapsulant material," *Microelectronics Reliability,* Bd. 42, Nr. 1, pp. 119-125, 2002.

[19] A. K. Gopal, S. Adali und V. E. Verijenko, „Optimal temperature profiles for minimum residual stress in the cure process of polymer composites," *Composite Structures,* Bd. 48, pp. 99-106, 2000.

[20] J. R. Fried, „Introduction to Polymer Science," in *Polymer Science and Technology*, New Jersey, USA, Pearson Education Inc., 2014, pp. 1-20.

[21] M. A. Boyle, C. J. Martin und J. D. Neuner, „Epoxy resin," in *ASM Handbook Volume 21, Composites*, Materials Park, Ohio, ASM International, 2001, pp. 78-89.

[22] D. Ratna, Handbook of thermoset resins, Shawbury, Shropshire: iSmithers, 2009, pp. 155-174.

[23] M. G. González, J. C. Cabanelas und J. Baselga, „Applications of FTIR on epoxy resins – identification, monitoring the curing process, phase separation and water uptake," in *Infrared Spectroscopy - Materials Science, Engineering and Technology*, Rijeka, Croatia, InTech Europe, 2012, pp. 261-284.

[24] E. Petrie, „Epoxy resin types," SpecialChem, 2017. [Online]. Available: http://adhesives.specialchem.com/selection-guide/epoxy-resins-for-adhesives-and-sealants/epoxy-resin-types#. [Access on 30 4 2017].

[25] Ourpcb.com, „PCB base material," 10 2 2017. [Online]. Available: https://www.ourpcb.com/pcb-base-material-types.html. [Access on 30 4 2017].

[26] Y. Osumi, „One-part epoxy resin," *Three Bond Technical News (19),* p. 10, 1 10 1987.

[27] O. Hara, „Curing agents for epoxy resin," *Three Bond Technical News (32),* p. 10, 20 12 1990.

[28] W. J.Hale und F. C.Vibrans, „The constitution of dicyanodiamide," *Journal of the American Chemical Society,* Bd. 40, Nr. 7, p. 1046–1063, 1918.

[29] J.-B. Zhang, Z.-C. Tan, S.-H. Meng, S.-H. Li und L.-M. Zhang, „Heat capacity and thermal decomposition of dicyandiamide," *Thermochimica Acta,* Bd. 307, pp. 11-15, 1997.

[30] P. Richard E. Prince und P. Prince Engineering, „Glass fiber differences and properties," [Online]. Available: http://www.build-on-prince.com/glass-fiber.html. [Access on 4 5 2017].

[31] M. I. Kiron, „Introduction of Glass Fiber | Types of Glass Fiber | Properties of Glass Fiber | Manufacturing Processes of Glass Fiber | Uses of Glass Fiber or Glass Yarn," [Online]. Available: http://textilelearner.blogspot.co.at/2011/08/glass-fiber-types-of-glass-fiber_3834.html. [Access on 4 5 2017].

[32] F. T. Wallenberger, J. C. Watson und H. Li, „Glass fibers," in *ASM Handbook Volume 21, Composites*, Materials Park, Ohio, ASM International, 2001, pp. 27-34.

[33] I. Low, „Effects of residual stresses on the failure micromechanisms in toughened epoxy systems," *Journal of Materials Science,* Bd. 25, pp. 2144-2148, 1990.

[34] D. Chauhan, N. Singhvi und R. Singh, „Effect of geometry of filler particles on the effective thermal conductivity of two-phase systems," *International Journal of Modern Nonlinear Theory and Application,* Bd. 1, pp. 40-46, 2012.

[35] Y.-R. Peng, X. Qi und C. Chrisafides, „The influence of curing systems on epoxide-based PCB laminate peroformance," *Circuit World,* Bd. 31, Nr. 4, p. 14–20, 2005.

[36] J. K. Gillham, „Cure and properties of thermosetting systems," *British Polymer Journal; VOL. 17, NO. 2 ; ,* Bd. 17, Nr. 2, pp. 224-226, 1985.

[37] J. K. Gillham, „Formation and properties of thermosetting and high Tg polymeric materials," *Polymer Engineering and Science,* Bd. 26, Nr. 20, pp. 1429-1433, 1986.

[38] R. A. L. Jones, „Gelation," in *Soft condensed matter*, New York, Oxford University Press, 2002, pp. 95-102.

[39] M. Tarnacka, O. Madejczyk, M. Dulski, M. Wikarek, S. Pawlus, K. Adrjanowicz, K. Kaminski und M. Paluch, „Kinetics and dynamics of the curing system. High pressure studies," *Macromolecules,* Bd. 47, Nr. 13, p. 4288–4297, 2014.

[40] J.-P. Pascault und R. J. J. Williams, „General concepts about epoxy polymers," in *Epoxy Polymers: New Materials and Innovations*, Online, Wiley-VCH Verlag GmbH & Co. KGaA, 2010, pp. 1-12.

[41] M. Lé-Magda, E. Dargent, J. A. S. Puente, A. Guillet, E. Font und J.-M. Saiter, „Influence of very long aging on the relaxation behavior of flame-retardant PCB epoxy composites under mechatronic conditions," *Journal of Applied Polymer Science,* Bd. 130, pp. 786-792, 2013.

[42] A. S. Maxwell, W. R. Broughton, G. Dean und G. D. Sims, „Review of accelerated ageing methods and lifetime prediction techniques for polymeric materials," National Physical Laboratory, Teddington, 2005.

[43] D. Wright, „Failure of plastics and rubber products: Causes, effects and case studies involving degradation,“ Rapra Technology Limited, Shawbury, Shrewsbury, Shropshire, SY4 4NR, United Kingdom, 2001.

[44] R. Polanský, P. Prosr und M. Čermák, „Determination of the thermal endurance of PCB FR4 epoxy laminates via thermal analyses,“ *Polymer Degradation and Stability,* Bd. 105, pp. 107-115, 2014.

[45] M. Lé-Magda, E. Dargent, B. Youssef, A. Guillet, J. Idrac und J.-M. Saiter, „Thermal properties evolution of PCB FR4 epoxy composites for mechatronic during very long ageing,“ *Macromolecular Symposia,* Bd. 315, p. 143–151, 2012.

[46] C. Bockenheimer, D. Fata und W. Possart, „New aspects of ageing in epoxy networks. II. Hydrothermal ageing,“ *Journal of Applied Polymer Science,* Bd. 91, pp. 369-377, 2004.

[47] Y. Zheng, R. D. Priestley und G. B. Mckenna, „Physical aging of an epoxy subsequent to relative humidity jumps through the glass concentration,“ *Journal of Polymer Science: Part B: Polymer Physics,* Bd. 42, p. 2107–2121, 2004.

[48] G. M. Odegard und A. Bandyopadhyay, „Physical aging of epoxy polymers and their composites,“ *Journal of Polymer Science Part B: Polymer Physics,* Bd. 49, Nr. 24, p. 1695-1716, 2011.

[49] Y. Huang, X. Wang und D. R. Paul, „Physical aging of thin glassy polymer films: Free volume interpretation,“ *Journal of Membrane Science,* Bd. 277, p. 219–229, 2006.

[50] A. J. Kovacs, „Glass transition in amorphous polymers. Phenomenological study,“ *Fortschr. Hochpolym.-Forsch.,* Bd. 3, pp. 394-507, 1963.

[51] L. C. E. STRUIK, „Physical aging in amorphous polymers and other materials,“ TU Delft, Delft University of Technology., Delft, 1977.

[52] E. S. Watson und M. J. O'Neill, „Differential microcalorimeter“. New York Patent US Patent 3,263,484, 2 8 1966.

[53] ASTM, „Standard terminology relating to thermal analysis and rheology“. West Conshohocken, USA Patent ASTM E473-06, 1 3 2006.

[54] J. D. Menczel, L. Judovits, R. B. Prime, H. E. Bair, M. Reading und S. Swier, „Differential Scanning Calorimetry (DSC),“ in *Thermal Analysis of Polymers:*

fundamentals and applications, New Jersey, John Wiley & Sons, Inc., 2008, pp. 7-239.

[55] Hitachi, „Description of differential scanning calorimetery (DSC),“ Hitachi High-Technologies GLOBA, [Online]. Available: http://www.hitachi-hightech.com/global/products/science/tech/ana/thermal/descriptions/dsc.html. [Access on 26 5 2017].

[56] M. Rady und E. Arquis, „A comparative study of phase changing characteristics of granular phase change materials using DSC and T-History methods,“ *Fluid Dynamics & Materials Processing,* Bd. 6, Nr. 2, pp. 137-152, 2010.

[57] G. V. Assche, A. V. Hemelrijck, A. H. Rahier und B. V. Mele, „Modulated differential scanning calorimetry: isothermal cure and vitrification of thermosetting systems,“ *Thermochimica Acta,* Bd. 268, p. 121–142, 1995.

[58] J. McHugh, P. Fideu, A. Herrmann und W. Stark, „Determination and review of specific heat capacity measurements during isothermal cure of an epoxy using TM-DSC and standard DSC techniques,“ *Polymer Testing,* Bd. 29, p. 759–765, 2010.

[59] R. Rudolf, Application handbook thermal analysis - thermosets, Shanghai: DongHua University Press Co., 2011.

[60] T. I. Thermal Analysis & Rheology, „A review of DSC kinetics methods,“ TA Instruments, New Castle, USA.

[61] B. C. Smith, „Introduction of infrared spectroscopy,“ in *Fundamentals of Fourier Transform Infrared Spectroscopy*, Boca Raton, Taylor & Francis Group, LLC, 2011, pp. 1-18.

[62] T. Nicolet, „FT-IR vs. dispersive infrared-Theory of infrared spectroscopy instrumentation,“ [Online]. Available: http://www.thermo.com.cn/resources/200802/productpdf_21615.pdf. [Access on 2 6 2017].

[63] J. Zhao, „The power of the Fourier transform for spectroscopists,“ 23 8 2014. [Online]. Available: https://chem.libretexts.org/Core/Physical_and_Theoretical_Chemistry/Spectroscopy/Fundamentals_of_Spectroscopy/The_Power_of_the_Fourier_Transform_for_Spectroscopists. [Access on 2 6 2017].

[64] N. Poisson, G. Lachenal und H. Sautereau, „Near- and mid-infrared spectroscopy studies of an epoxy reactive system," *Vibrational Spectroscopy,* Bd. 12, pp. 237-247, 1996.

[65] G. Nikolic, S. Zlatkovic, M. Cakic, S. Cakic, C. Lacnjevac und Z. Rajic, „Fast Fourier Transform IR characterization of epoxy GY systems crosslinked with aliphatic and cycloaliphatic EH polyamine adducts," *Sensors,* Bd. 10, pp. 684-696, 2010.

[66] C. M. Earnest, „The modern thermogravimetric approach to the compositional analysis of materials," in *Compositional analysis by thermogravimetry*, Philadelphia, American Society for Testing and Materials, 1988, pp. 1-18.

[67] R. B. Prime, H. E. Bair, S. Vyazovkin, P. K. Gallagher und A. Riga, „Thermogravimetric Analysis (TGA)," in *Thermal Analysis of Polymers: fundamentals and applications*, New Jersey, John Wiley & Sons, Inc., 2008, pp. 241-317.

[68] S. Zhang, L. Li und A. Kumar, „Thermogravimetric analysis," in *Material characterization techniques*, Boca Raton, Taylor & Francis Group, LLC, 2008, pp. 286-292.

[69] L. Zhang, J. Ma, X. Zhu und B. Liang, „Kinetics of thermal degradation of thermotropic poly(poxybenzoate-co-ethylene-2,6-naphthalate) by single heating rate methods," *Journal of Applied Polymer Science,* Bd. 91, p. 3915–3920, 2004.

[70] S. Vyazovkin, A. K. Burnham, J. M. Criado, L. A. Pérez-Maqueda, C. Popescu und N. Sbirrazzuoli, „ICTAC Kinetics Committee recommendations for performing kinetic computations on thermal analysis data," *Thermochimica Acta,* Bd. 520, pp. 1-19, 2011.

[71] S. Vyazovkin und C. A. Wight, „Isothermal and non-isothermal kinetics of thermally stimulated reactions of solids," *International Review In Physical Chemistry,* Bd. 17, Nr. 3, pp. 407-433, 1998.

[72] M. S. Silberberg, Chemistry: The Molecular Nature of Matter and Change, New York: McGraw-Hill, 2006, p. 696.

[73] E. Moukhina, „Initial kinetic parameters for the model-based kinetic method," *High Temperatures-High Pressures,* Bd. 42, p. 287–302, 2013.

[74] V. SV und L. AI, „Transformation of "degree of conversion against temperature" into "degree of conversion against time" kinetic data,“ *Russian Journal Physical Chemistry,* Bd. 62, pp. 1535-1537, 1988.

[75] ASTM, „Standard test method for tensile properties of plastics“. West Conshohocken, USA Patent ASTM D638-10, 15 7 2010.

[76] ISO, „Plastics - Determination of the tensile properties - Part 1: General principles“. Brussels, Belgium Patent EN ISO 527-1, 8 2012.

[77] M. A. Maleque und M. S. Salit, „Mechanical failure of materials,“ in *Materials Selection and Design*, New York, Springer, 2013, pp. 17-38.

[78] T. Anderson, „The fracture mechanics approach to design,“ in *Fracture Mechanics - Fundamentals and applications, Third Edition*, 3rd Hrsg., Boca Raton, USA, Taylor & Francis Group, 2005, pp. 12-16.

[79] G. Swallowe, „Toughening,“ in *Mechanical Properties and Testing of Polymers: An A–Z Reference; ; London :; .* , Dordrecht, Kluwer Academic Publishers, 1999, pp. 257-259.

[80] A. C. Fischer-Cripps, „Linear elastic fracture mechanics,“ in *Introduction to contact mechanics*, New York, Springer Science+Business Media, LLC, 2007, pp. 31-48.

[81] A. Griffith, „Phenomena of rupture and flow in solids,“ *Philosophical Transactions of the Royal Society of London. Series A, Containing Papers of a Mathematical or Physical Character,* Bd. 221, p. 163–198, 1920.

[82] W. F. Hosford, „Fracture mechanics,“ in *Mechanical Behavior of Materials*, New York, Cambridge University Press, 2005, pp. 227-246.

[83] G. Irwin, „Analysis of stresses and strains near the end of a crack traversing a plate,“ *Journal of Applied Mechanics,* Bd. 24, pp. 361-364, 1957.

[84] H. Westergaard, „Bearing pressures and cracks,“ *Journal of Applied Mechanics,* Bd. 6, pp. A49-53, 1939.

[85] ASTM, „Standard test methods for plane-strain fracture toughness and strain energy release rate of plastic materials“. West Conshohocken, USA Patent ASTM D5045-99, 10 3 1999.

[86] J. Whitney, C. Browning und W. Hoogsteden, „A double cantilever beam test for characterizing mode I delamination of composite materials," *Journal of Reinforced Plastics and Composites,* Bd. 1, pp. 297-313, 1982.

[87] Y. Xu und S. V. Hoa, „Mechanical properties of carbon fiber reinforced epoxy/clay nanocomposites," *Composites Science and Technology,* Bd. 68, p. 854–861, 2008.

[88] L. Canal, G. Pappas und J. Botsis, „Large scale fiber bridging in mode I intralaminar fracture. An embedded cell approach," *Composites Science and Technology,* Bd. 126, pp. 52-59, 2016.

[89] ASTM, „Standard test method for mode I interlaminar fracture toughness of unidirectional fiber-reinforced polymer matrix composites". West Conshohocken, USA Patent ASTM D5528-01, 1 5 2007.

[90] ASTM, „Standard test method for mode I fatigue delamination growth onset of unidirectional fiber-reinforced polymer matrix composites". West Conshohocken, USA Patent ASTM D6115-97, 1 3 2004.

[91] C. J. Biermann, „Physical properties of paper," in *Handbook of Pulping and Papermaking*, London, UK, Academic Press Limited, 1996, p. 169.

[92] J. Borch, M. B. Lyne, R. E. Mark und J. Charles C. Habeger, „Thermal properties," in *Handbook of Physical Testing of Paper; Volume 2; 2nd Edition* , New York, USA, Marcel Dekker, Inc., 2002, p. pp400.

[93] J. Kouko, E. Retulainen und P. Kekko, „Straining and relaxation properties of wet paper during heating," *Mech Time-Depend Mater,* Bd. 18, p. 697–719, 2014.

[94] A. J. Hebra, „Density of solids, liquids, and gases," in *The Physics of Metrology: All about Instruments: From Trundle Wheels to Atomic Clocks*, Mörlenbach, Germany, Springer Science + Business Media, 2010, p. 218.

[95] F. Cvema, „Thermal conductivity," in *ASM Ready Reference: Thermal Properties of Metals*, Ohio, USA, ASM International, 2002, p. 340.

[96] F. Cvema, „Specific heat capacity," in *ASM Ready Reference: Thermal Properties of Metals*, Ohio, USA, ASM International, 2002, p. 223.

[97] ISO, „Determination of the tensile properties of plastics". Geneva, Switzerland Patent EN ISO 527-2, 7 1996.

[98] IPC, „Glass transition temperature and cure factor by DSC“. Northbrook, USA Patent IPC-TM-650 2.4.25C, 12 1994.

[99] Q. Tao, G. Pinter und T. Krivec, „Influence of cooling rate and annealing on the DSC Tg of an epoxy resin,“ *Microelectronics Reliability,* Bd. 78, p. 396–400, 2017.

[100] IPC, „Glass transition temperature and z-axis thermal expansion by TMA“. Northbrook, USA Patent IPC-TM-650 2.4.24C, 12 1994.

[101] IPC, „Peel strength of metallic clad laminates“. Northbrook, USA Patent IPC-TM-650 2.4.8C, 12 1994.

[102] IPC, „Capacitance of printed board substrates after exposure to assembly, rework, and/or reliability tests (Draft Pending)“. Northbrook, USA Patent IPC-TM-650 2.5.35, 9 2005.

[103] IPC, „DC current induced thermal cycling test“. Bannockburn, USA Patent IPC-TM-650 2.6.26, 5 2014.

[104] EIA/JEDEC, „Highly-accelerated temperature and humidity stress test (HAST)“. wilson boulevard, USA Patent JESD22-A110-B, 2 1999.

[105] C. Qian, K. Jansen, L. Ernst, C. Bohm, A. Kessler, H. Preu und M. Stecher, „Characterization and modelling of cure kinetics of a molding compound,“ in *8th International Conference on Electronic Packaging Technology*, New York, USA, 2007.

[106] R. Hardis, *Cure kinetics characterization and monitoring of an epoxy resin for thick composite structures,* Iowa State University, 2012.

[107] M. Jovičić, R. Radičević, J. Pavličević und O. Bera, „Isoconversional kinetic analysis of the alkyd/melamine resins curing,“ *Chemical Industry & Chemical Engineering Quarterly,* Bd. 19, Nr. 2, p. 253−262, 2013.

[108] X. Huang und B. Patham, „Experimental characterization of a curing thermoset epoxy-anhydride system — isothermal and nonisothermal cure kinetics,“ *Jouranal of Applied Polymer Science,* Bd. 127, p. 1959–1966, 2013.

[109] Q. Tao, G. Pinter, T. Antretter, T. Krivecc und P. Fuchs, „MFK coupled with FEM for curing simulation of thermosetting epoxy resins,“ *Journal of Applied Polymer Science,* 2018.

[110] M. R. Kamal und S. Sourour, „Kinetics and thermal characterization of thermoset cure," *Polymer Engineering & Science,* Bd. 13, Nr. 1, pp. 59-64, 1973.

[111] M. Gundjian und K. C. Cole, „Effect of copper on the curing and structure of a DICY-containing epoxy composite system," *Journal of Applied Polymer Science,* Bd. 75, p. 1458–1473, 2000.

[112] S.-G. Hong und C.-S. Wu, „DSC and FTIR analysis of the curing behaviors of epoxy/DICY/solvent open systems," *Thermochimica Acta,* Bd. 316, pp. 167-175, 1998.

[113] N. Rabearison, C. Jochum and J. C. Grandidier, "A cure kinetics, diffusion controlled and temperature dependent, identification of the araldite LY556 epoxy," *Journal of Materials Science,* vol. 46, no. 3, pp. 787-796, 2011.

[114] M. R. Keenan, „Autocatalytic cure kinetics from DSC measurements: Zero initial cure rate," *Journal of Applied Polymer Science,* Bd. 33, pp. 1725-1734, 1987.

[115] M. R. Kamal, „Thermoset characterization for moldability analysis," *Polymer Engineering & Science,* Bd. 14, Nr. 3, pp. 231-239, 1974.

[116] J. Fournier, G. Williams, C. Duch und G. A. Aldridge, „Changes in molecular dynamics during bulk polymerization of an epoxide-amine system as studied by dielectric relaxation spectroscopy," *Macromolecules,* Bd. 29, pp. 7097-7107, 1996.

[117] U. Khanna und M. Chanda, „Kinetics of anhydride curing of isophthalic diglycidyl ester using differential scanning calorimetry," *Journal of Applied Polymer Science,* Bd. 49, pp. 319-329, 1993.

[118] V. Pistor, S. S. d. S. d. S. Soares, H. L. O. JúniorI, R. Fiorio und A. J. Zattera, „Influence of glass and sisal fibers on the cure kinetics of unsaturated polyester resin," *Materials Research; vol.15 no.4; 2012,* Bd. 15, Nr. 4, pp. 650-656, 2012.

[119] G. Palmese, O. Andersen und V. Karbhari, „Effect of glass fiber sizing on the cure kinetics of vinyl-ester resins," *composites Part A: applied science and manufacturing,* Bd. 30, pp. 11-18, 1999.

[120] Y. Lin, H. Sautereau und J. Pascault, „BDMA-catalyzed DDA-epoxy resin system: Temperature and composition effects on curing mechanism," *Journal of Polymer Science: Part A: Polymer Chemistry,* Bd. 24, pp. 2171-2184, 1986.

[121] M. D. Gilbert, N. S. Schneider und W. J. MacKnight, „Mechanism of the dicyandiamide/epoxide reaction," *Macromolecules,* Bd. 24, Nr. 2, pp. 360-369, 1991.

[122] R. P. Theriault und T. A. Osswald, „Measurement and prediction of the glass transition temperature during processing of copper-clad epoxy resin systems," *Polymer Composites,* Bd. 20, Nr. 6, pp. 789-795, 1999.

[123] W. Grellmann und S. Seidler, „Mechanical Properties of Polymers," in *Polymer Testing (2nd Edition)*, Munich, Germany, Hanser Publishers, 2013, pp. 73-231.

[124] ASTM, „Standard test method for assignment of the glass transition temperature by dynamic mechanical analysis". West Conshohocken, USA Patent ASTM E1640-04, 1 6 2004.

[125] J. Foreman, S. Sauerbrunn und C. Marcozzi, „Exploring the sensitivity of thermal analysis techniques to the glass transition," TA Instruments, Inc., New Castle, USA, 2006.

[126] S. Alessi, D. Conduruta, G. Pitarresi, C. Dispenza und G. Spadaro, „Accelerated ageing due to moisture absorption of thermally cured epoxy resin/polyethersulphone blends. Thermal, mechanical and morphological behaviour," *Polymer Degradation and Stability,* Bd. 96, pp. 642-648, 2011.

[127] K. Nakamae, T. Nishino, X. AiRu and K. Takatsuka, "Pressure dependence of the curing behavior of epoxy resin," *Polymer Journal,* vol. 23, pp. 1157-1162, 1991.

[128] M. Salam, S. Z. M.V. Hosur und S. Jeelani, „Improvement in mechanical and thermo-mechanical properties of epoxy composite using two different functionalized multi-walled carbon nanotubes," *Scientific Research, Open Journal of Composite Materials,* Bd. 3, pp. 1-9, 2013.

[129] S. Li, J. Shen, X. Chen, R. Chen und X. Luo, „Studies on relaxation and thermal expansion behavior of polysiloxane-modified epoxy resin," *Journal of Macromolecular Science, Part B: Physics,* Bd. 36, Nr. 3, pp. 357-366, 1997.

[130] J. Y. Lee, M. J. Shim und S. W. Kim, „Thermal decomposition kinetics of an epoxy resin with rubber-modified curing agent," *Journal of Applied Polymer Science,* Bd. 81, p. 479–485, 2001.

[131] J. H. Flynn und L. A. Wall, „A quick, direct method for the determination of activation energy from thermogravimetric data," *Polymer Letters,* Bd. 4, pp. 323-328, 1966.

[132] Y. Li, „Atomistic modeling of environmental aging of epoxy resins," School of Materials Science and Engineering, Georgia Institute of Technology , Georgia, USA, 2012.

[133] IPC, „Decomposition temperature (Td) of laminate material using TGA". Bannockburn, USA Patent IPC-TM-650 2.4.24.6, 4 2006.

[134] P. Prabhu, M. Liben und A. Wakjira, „Improving fracture toughness of glass/epoxy composites by using rubber particles together with zirconium toughened alumina (ZTA) nanoparticles," *Research and Reviews: Journal of Engineering and Technology,* Bd. 3, Nr. 1, pp. 21-28, 2014.

[135] E. Borowski, E. Soliman, U. F. Kandil und M. R. Taha, „Interlaminar fracture toughness of CFRP laminates incorporating multi-walled carbon nanotubes," *Polymers,* Bd. 7, pp. 1020-1045, 2015.

[136] T. Anderson, „Fatigue crack propagation," in *Fracture Mechanics - Fundamentals and applications , Third Edition*, Boca Raton, USA, Taylor & Francis Group, 2005, pp. 453, 464.

[137] R. Jones, A. Kinloch, J. Michopoulos, A. J. Brunner und N. Phan, „Delamination growth in polymer-matrix fibre composites and the use of fracture mechanics data for material characterisation and life prediction," *Composite Structures,* 2017.

[138] S. L. Case, „Fundamental importance of fillers, cure condition, and crosslink density on model epoxy properties," Virginia Polytechnic Institute and State University, Blacksburg, USA, 2003.

[139] M. Suzuki, M. Kawamoto und A. Takahashi, „The adhesion between electrolessly deposited copper and a photoimageable polymer," *Polymer Engineering and Science,* Bd. 39, Nr. 2, pp. 321-326, 1999.

[140] L. Lambert, „Delamination, causes and cures?," in *EPTAC webinar*, Manchester, USA, 2008.

[141] F. X. Che und J. H. L. Pang, „Thermal fatigue reliability analysis for PBGA with Sn-3.8Ag-0.7Cu solder joints," in *6th Electronics Packaging Technology Conference*, Pan Pacific Hotel, Singapore, 2004.

[142] L. C. Méndez-González, L. A. Rodríguez-Picón, D. J. Valles-Rosales, R. Romero-López und A. E. Quezada-Carreón, „Reliability analysis for electronic devices using beta-Weibull distribution," *Quality and Reliability Engineering International,* pp. 1-10, 2017.

[143] H. Cui, „Accelerated temperature cycle test and Coffin-Manson model for electronic packaging," in *Annual Reliability and Maintainability Symposium - Product Quality & Integrity (RAMS)*, Hilton Mark Plaza Alexandria, USA, 2005.

[144] H. Rinne, „Definition and properties of the Weibull distribution," in *The Weibull Distribution - A Handbook*, Boca Raton, USA, CRC Press Taylor & Francis Group, 2013, pp. 27-97.

[145] H. Rinne, „Weibull goodness-of-fit testing and related problems," in *The Weibull Distribution - A Handbook*, Boca Raton, , CRC Press Taylor & Francis Group, 2013, pp. 651-690.

[146] L. J. Turbini, „Conductive anodic filament (CAF) formation: an historic perspective," *Circuit World,* Bd. 32, Nr. 3, p. 19–24, 2006.

[147] IPC, „PCB technology trends 2016," IPC-Association Connecting Electronics Industries, Bannockburn, USA, 2017.

[148] J.-P. Pascault, H. Sautereau, J. Verdu und R. J. J. Williams, „Yielding and fracture of polymer networks," in *Thermosetting Polymers*, New York, USA, Marcel Dekker, Inc., 2002, pp. 350-388.

[149] R. Naik, J. Crews und K. Shivakumar, „Effects of T-tabs and large deflections in double cantilever beam specimen tests," in *Composite Materials: Fatigue and Fracture (Third Volume)*, Philadelphia, USA, American Society for Testing and Materials, STP 1110, 1991, p. 169–186.

[150] N. Causse, E. Dantras, C. Tonon, M. Chevalier, H. Combes, P. Guigue and C. Lacabanne, "Enthalpy relaxation phenomena of epoxy adhesive in operational configuration: thermal, mechanical and dielectric analysis," *Journal of Non-Crystalline Solids,* vol. 387, pp. 57-61, 2014.